Neutron scattering studies on multiferroic and frustrated systems

Inaugural-Dissertation

zur

Erlangung des Doktorgrades

der Mathematisch-Naturwissenschaftlichen Fakultät

der Universität zu Köln

vorgelegt von

Sebastian Biesenkamp

aus Troisdorf

Köln, 2022

Diese Arbeit stellt eine von der Mathematisch-Naturwissenschaftlichen Fakultät der Universität zu Köln angenommene Dissertation dar.

Berichterstatter: Prof. Dr. Markus Braden
Prof. Dr. Markus Grüninger

Vorsitzender
der Prüfungskommission: Prof. Dr. Stephan Schlemmer

Tag der mündlichen Prüfung: 18.08.2022

„Si sapis, alterum alteri misce: nec speraveris sine desperatione nec desperaveris sine spe.“

„Bist du weise, so mischst du das eine mit dem anderen und wirst weder hoffen ohne zu zweifeln, noch verzweifeln ohne zu hoffen.“

Seneca, Epistulae morales ad Lucilium, 62 n. Chr. 104. Brief. Übersetzt von Otto Apelt (1924)

Contents

Abbreviations

4F1	Cold neutron three-axis spectrometer (located at the LLB)
4F2	Cold neutron three-axis spectrometer (located at the LLB)
6T2	Thermal neutron four-circle diffractometer (located at the LLB)
BERII	Berlin experimental reactor
D10	Four-circle diffractometer (located at the ILL)
D23	Thermal neutron two-axis diffractometer (located at the ILL)
DMI	Dzyaloshinskii-Moriya interaction
EXED	Extreme environment diffractometer (located at the HZB/BERII)
FR	Flipping ratio
FRMII	Forschungs-Neutronenquelle Heinz Maier-Leibnitz
HEiDi	Single crystal diffractometer on hot source (located at the FRMII)
HFM	High-field magnet (located at the HZB/BERII)
HZB	Helmholtz-Zentrum Berlin
ILL	Institut Laue-Langevin
IN12	Cold neutron three-axis spectrometer (located at the ILL)
KOMPASS	Three-axes spectrometer with polarisation analysis (located at the FRMII)
LLB	Laboratoire Léon Brillouin
MF	Multiferroic
MLZ	Heinz Maier-Leibnitz Zentrum
NRSE	Neutron resonance spin echo spectroscopy
NSE	Neutron spin echo spectroscopy
NSF	Non-spin-flip
PTFE	Polytetrafluoroethylene
QCP	Quantum critical point
RF	Radio frequency
SDW	Spin-density wave
SF	Spin-flip
SHG	Second-harmonic generation
TC1-TC4	Positions of RF-coils
TFI	Transverse-field Ising
TLL	Tomonaga-Luttinger liquid
TRISP	Three-axes spin echo spectrometer (located at the FRMII)
uudd	Up-up-down-down

Preface

The family of multiferroic materials attracted a manifold of research activities not only because of the fundamental interest in the variety of mechanisms that lead to the interplay between different ferroic ordering parameters but also because of their application potential. In particular, the coupling of ferroelectric and magnetic ordering can be seen promising for future technologies as the electric control of magnetic ordering is for instance auspicious for its utilization in novel memory devices. Obviously, this not only requires the search for new multiferroic materials, but it also necessitates a profound understanding about multiferroic domain dynamics and how the switching behavior is impacted by different properties of respective multiferroic systems. Thus, this research field not only motivates the investigation of the relaxation behavior, but it also encourages to study the peculiarities of respective nuclear and magnetic structures in different multiferroics. The aim of this thesis is to gain further understanding about multiferroic domain dynamics and the potential mechanisms that can impact the relaxation behavior. For this purpose, neutron scattering technologies were utilized as this experimental technique is unique in sensing complex magnetic and in particular chiral magnetic arrangements that play a major role in the field of multiferroics. The thesis is organized as follows:

The first two chapters present a brief and general introduction to multiferroics and neutron scattering techniques, respectively. However, the theory and the experimental procedure that is specific to a certain project will be thoroughly discussed in the framework of the respective chapter.

Chapter 3 includes the embedded publication [1], which reports on the structural dimerization in the related materials $NaFe(WO_4)_2$ and $MnWO_4$. Here, the motivation was to investigate the details of magnetoelastic coupling that arises with the onset of commensurate spin up-up-down-down ordering and to analyse anharmonic contributions and their impact on the relaxation behavior in the incommensurate multiferroic phase of $MnWO_4$. In view of the desired investigation of the multiferroic relaxation behavior in a variety of materials, the respective outcome of this work on $NaFe(WO_4)_2$ and $MnWO_4$ motivated the analysis of domain dynamics in multiferroics that exhibit simple phase diagrams without interfering incommensurate and commensurate order.

In this context, the subsequent chapter 4 includes the publication [2], which reports single-crystal studies on the multiferroic double-tungstate $LiFe(WO_4)_2$ and which presents a thorough analysis of its phase diagram. Finite conductivity of respective samples hindered the application of electric-fields and thus an investigation of their relaxation behavior, wherefore the following course of this thesis reports respective studies of the multiferroic domain kinetics in other multiferroic systems.

First, the multiferroic domain inversion, as well as a detailed analysis of developing magnetic components is discussed for $NaFeGe_2O_6$, whereby the respective results are presented in the publication [3], which is embedded in chapter 5. Subsequently, the relaxation behavior is also discussed for $(NH_4)_2[FeCl_5\,(H_2O)]$ in chapter 6 and for $Ni_3V_2O_8$ and CuO in chapter 7. Eventually, the relaxation behavior among the different investigated materials is summarized and discussed in chapter 8.

Complementary to the reported relaxation behavior of the multiferroic domain population, chapter 9 documents Larmor diffraction experiments on the multiferroic domain sizes.

Beside the thorough investigations on multiferroic systems, the last part of this thesis reports on magnetic-field and temperature dependent measurements on the Ising-like spin-1/2 chain material $BaCo_2V_2O_8$, which was exposed to a transverse field along [1 1 0] direction. In this context, the transition to an incommensurate high-field phase is discussed in the framework of a Tomonaga-Luttinger liquid phase.

1. Introduction

The motivation for this thesis was to gain further understanding about the multiferroic domain kinetics and for this purpose, not only the switching behavior of several multiferroics were studied but also open questions concerning their magnetic structure were answered. Obviously, the discussion of the conducted experiments and the following presentation of results necessitate a basic knowledge about the magnetoelectric effect and about multiferroic behavior. Therefore, the following sections comprise the required overview of the underlying theory and also highlight important historical milestones, which led to the present-day understanding of multiferroics. The principle of magnetoelectric coupling is explained in the first section and subsequently the principle of multiferroics as well as the microscopic mechanisms, which drive the coupling of electric and magnetic ordering parameters are explained. Eventually, in the last part of this introductory chapter specific focus is put on the present-day understanding of multiferroic domain kinetics and on the open questions in this field.

1.1. Magnetoelectric behavior

The magnetoelectric effect describes the polarizability of a material by external magnetic fields or vice versa the magnetizability of a sample by external electric fields. A first report of this magnetoelectric behavior was published by W. Röntgen in 1888 [4], when he observed that a moving dielectric gets magnetized in an applied static electric field. The reverse effect, namely the polarizability of a moving dielectric in an external magnetic field was discovered by H. A. Wilson nearly two decades later [5]. It has to be noted that the terminology 'magnetoelectric' was actually introduced not before 1926, when P. Debye established it [6]. In 1894, between the execution of both afore mentioned experiments, P. Curie made theoretical considerations on the basis of symmetry that magnetoelectric coupling should be intrinsically possible even in non-moving systems [7]. However, it took almost half a century before L. D. Landau and J. M. Lifschitz specified the symmetry restrictions that have to be fulfilled for the occurrence of magnetoelectric coupling [8]. These restrictions can be derived from the free energy expansion

$$F = F_0 - P_i^{\mathrm{S}} E_i - M_i^{\mathrm{S}} H_i - \frac{1}{2}\epsilon_0 \epsilon_{ij}^{\mathrm{e}} E_i E_j - \frac{1}{2}\mu_0 \chi_{ij}^{\mathrm{m}} H_i H_j - \alpha_{ij} E_i H_j + \ldots . \tag{1.1}$$

Here, P_i^{S} and M_i^{S} denote the ith component ($i = x, y, z$) of the spontaneous polarization and magnetization, whose orientation can be inverted by the external electric or magnetic fields, **E** and **H**, respectively. The second order terms in equation 1.1 account for the induced polarization and magnetization by the conjugate fields with ϵ^{e} and χ^{m} being the electric and magnetic susceptibility. Moreover, the second order terms in equation 1.1 include a mixed term $\alpha_{ij}^{\mathrm{em}} E_i H_j$ with α^{em} being the magnetoelectric tensor and by considering the total derivative of the free energy, it can be seen that the ith component of the electric polarization or the magnetization is indeed coupled to the jth component of both conjugate fields

$$P_i = -\frac{\partial F}{\partial E_i} = P_i^{\mathrm{S}} + \frac{1}{2}\epsilon_0 \epsilon_{ij} E_j + \alpha_{ij} H_j \tag{1.2}$$

$$M_i = -\frac{\partial F}{\partial H_i} = M_i^{\mathrm{S}} + \frac{1}{2}\mu_0 \mu_{ij} H_j + \alpha_{ij} E_j . \tag{1.3}$$

From the expansion it can be concluded that magnetoelectric coupling is only allowed when both, time- and space-inversion symmetry are broken simultaneously. This is because the magnetization and the electric polarization transform differently under both mentioned symmetry operations. Their orientation is described by polar and axial vectors respectively, which is illustrated in Fig. 1.1. The direction of the magnetic moment is determined by the sense of rotation of the electron, which means that the moment is invariant under space inversion but changes its orientation under time-reversal. The opposite holds for the dipole moment, which is invariant under time reversal but changes sign under space inversion. As these symmetry arguments also hold for the respective conjugate fields, both symmetries, time reversal and space inversion need to be broken to keep the free energy invariant under respective transformations.

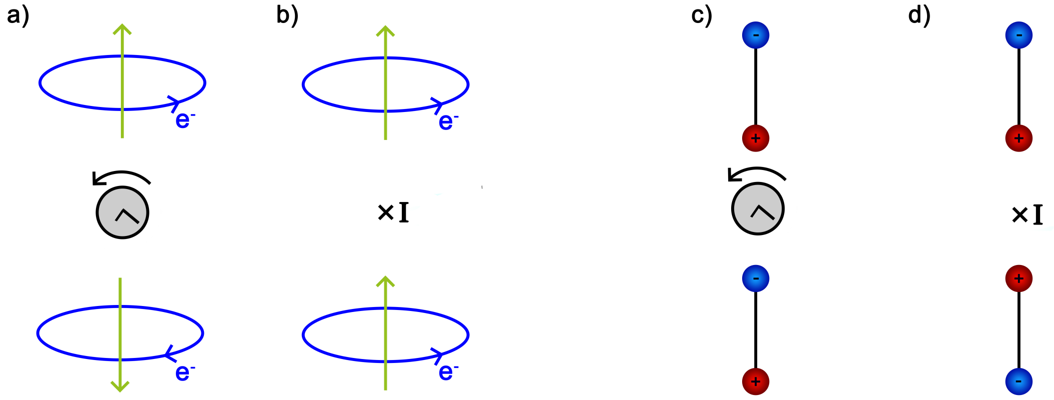

Figure 1.1.: The figure sketches the symmetry transformation of axial and polar vectors under time- and space-inversion. In a) and b) the respective transformations are visualized for the magnetic moment, which is induced by a circulating electron. The opposite symmetry behavior of the electric dipole moment is shown in c) and d).

For the experiments from W. Röntgen and H. A. Wilson [4,5] the time-reversal symmetry was broken by the sample motion itself, but for static samples the magnetic symmetry of the system is decisive. It was shown that from 122 magnetic point groups (Shubnikov groups [9]) only 58 fulfill the symmetry conditions, which are necessary for the linear magnetoelectric behavior [10, 11]. It has to be noted that this holds only for the linear effect, whereas higher order terms in the expansion (e.g. which are responsible for the bilinear magnetoelectric effect) enforce different symmetry restrictions [12–15]. However, the following discussion is solely restricted to the linear magnetoelectric coupling.

A first theoretical prediction for the occurrence of linear magnetoelectric coupling in a real and non-moving system was done by I. E. Dzyaloshinskii in 1959 [16]. He proposed it for Cr_2O_3 and it took only two more years until D. N. Astrov successfully presented the experimental proof [17]. His discovery triggered a growing research activity in this field due to the application potential of magnetoelectrics [18, 19], but nevertheless, the interest rapidly disappeared again because of the rather weak observed couplings. Here, a deeper comprehension of the effect is necessary to understand the limited coupling strength. So far, the occurrence of a magnetoelectric effect was discussed in terms of symmetries that have to be broken, whereas information about the strength can only be gained from the microscopic mechanism, which drives the magnetoelectric coupling. Common to all mechanisms is that the electric or magnetic fields act as external perturbations, which impact the magnetic and electronic environment of the system. A typical example is single ion anisotropy for which an external electric field induces a shift of ions, which itself can change the anisotropy and thus potentially the easy-axis for the magnetic moments. Other microscopic mechanisms that can lead to a magnetoelectric coupling are the symmetric or antisymmetric superexchange, dipolar interactions and the Zeeman effect [20]. As the magnetoelectric effect arises for all named mechanisms only from perturbative effects, it explains the small observed couplings. In this context, W. F. Brown *et. al.* derived an upper limit for the coupling strength of magnetoelectric behavior [21]

$$\sqrt{\alpha_{ij}^{\mathrm{em}}} < \epsilon_{ij}^{\mathrm{e}} \chi_{ij}^{\mathrm{m}}. \tag{1.4}$$

It is thus obvious that materials possessing large electric and magnetic susceptibilities should enforce larger magnetoelectric coupling. Respective larger values for the susceptibilities can naturally be found in ferroelectrics and ferromagnets, wherefore the simultaneous presence of both ferroic ordering parameters in the same phase was seen promising for larger magnetoelectric coupling and hence leads literally to the basic concepts of multiferroic materials.

1.2. Multiferroic behavior

1.2.1. Ferroics

As the name already suggests, multiferroics comprise at least two ferroic ordering types in the same phase. The general features of ferroics were highlighted by Aizu et al [22, 23]. It was pointed out that ferroics are characterized by spontaneous ordering of an ordering parameter $\hat{O}$, for which domains of opposite orientation are forming, when passing the transition temperature to the ferroic phase. This can be motivated in the framework of a Landau theory in which the free energy $F(\hat{O})$ is expanded as a function of the ordering parameter

$$F(\hat{O}) = F_0 + a_2\hat{O}^2 + a_4\hat{O}^4. \tag{1.5}$$

In the absence of an external field, the free energy exhibits only even order terms, which is due to symmetry reasons as the free energy must be equivalent for an inverted sign of the ordering parameter. In addition, a_4 must be positive for thermodynamic stability and a_2 is set to be proportional to $(T - T_\mathrm{C})$ with T_C being the transition temperature to the ferroic phase. The temperature dependence of this free energy function is illustrated in Fig. 1.2 a) and b). Above the phase transition a single minimum is located at $F(\hat{O} = 0)$, but below the transition temperature two energetically equivalent minimas are located at $+\hat{O}$ and $-\hat{O}$. The minimas belong to the two orientations of the ordering parameter and due to the degeneracy, both states are equally preferred. Thus, domains of both states are forming and in the absence of external fields both types are usually equally populated. However, the formation of domains is further provoked and affected from the competition between the energy costs for the creation of domain walls and the energy gain from demagnetizing or depolarizing fields. Also defects and effective pinning of the ferroic structure play an important role in the course of domain formation and domain dynamics. The conjugate field η of the ordering parameter can induce an asymmetry for the free energy function, wherefore the term $-\eta\hat{O}$ is added to the free energy function in equation 1.5. Thus, depending on its orientation, the applied conjugate field lowers one minima, while lifting the second one. Consequently, the domain population becomes imbalanced and for strong enough fields, the system transforms into a monodomain. Hence, driving the field continuously between its polarities results in a hysteresis (see Fig 1.2 c)), which is another important characteristic feature of a ferroic phase. It entails that the domain distribution persists even in the absence of external fields and can be inverted not only before an opposite field exceeds the coercive field strength. It goes without mentioning that the characteristic switchability of ferroic ordering parameters between two states entails tremendous application potential e.g. for memory devices.

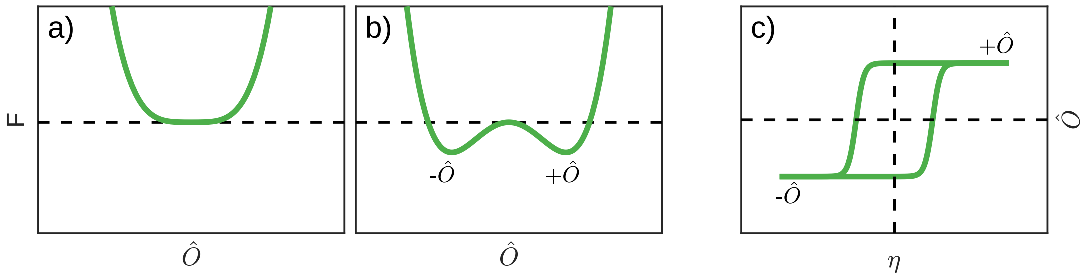

Figure 1.2.: The first panel a) and the second panel b) illustrate the change of the free energy function $F(\hat{O})$, when driving the temperature below the ferroic phase transition. The hysteresis of the ferroic ordering parameter under influence of an applied finite conjugate field η is shown in c).

The well-known ferroic ordering types refer to ferroelasticity, ferroelectricity, ferromagnetism and ferrotoroidicity, whereby the ordering parameters are respectively given by the elastic tensor, the polarization vector, the magnetization and the toroidal moment. The corresponding conjugate fields are the external stress field, the electric field, the magnetic field and the toroidal field. Unique for each ferroic ordering type is the underlying symmetry, whereby it was already discussed in the previous section that for the electric polarization and the magnetization both, space inversion and time reversal have different impact on the ordering parameter. The electric polarization changes sign upon space inversion but remains the same after time reversal. The opposite holds for the magnetization and in contrast, for ferrotoroidal and ferroelastic ordering both symmetries are either broken or preserved, respectively. The subsequent table summarizes the impact of respective symmetry operations on the ordering parameter for all named ferroics.

	Time reversal	Space inversion
Ferroelectric	invariant	non-invariant
Ferromagnetic	non-invariant	invariant
Ferroelastic	invariant	invariant
Ferrotoroidal	non-invariant	non-invariant

Table 1.1.: For all ferroic ordering types it is noted, whether the ordering parameter is kept invariant or not under time reversal or space inversion.

The discussion of ferroics automatically leads also to related antiferroic ordering. For the latter type, the macroscopic ordering parameter, e.g. the magnetization or the electric polarization remains zero as adjacent moments or dipoles in the lattice are not parallel aligned but alternate their orientation between neighboring sites. It is thus not obvious how to define the ordering parameter for antiferroics, but for example in case of an antiferromagnet, the ordering parameter can be described by the staggered magnetization and in a simplified picture, the antiferroic lattice can be viewed as a superposition of two ferroic sublattices with respectively opposite orientation. Consequently, a conjugate field is technically difficult to realize for antiferroics as its orientation has to be reversed at each adjacent lattice site and thus must possess a spatial periodicity in the range of several ångström. However, as it will be shown in the further course of this thesis, the control of antiferromagnetic domains can nevertheless be achieved via a crosscoupling between different ferroic ordering parameters. This is for example realized, when antiferromagnetic ordering is coupled to a ferroelectric polarization, which itself can be controlled by external electric fields. Also in the scope of toroidal ordering it was shown that antiferromagnetic ordering can be controlled by crossed electric and magnetic fields (see section A and Ref. [24])

1.2.2. Type-I Multiferroics

As mentioned in the previous section, the simultaneous presence of ferroelectric and magnetic ordering entails larger electric and magnetic susceptibilities, which hence allow for much higher magnetoelectric coupling constants. Therefore, within the framework of multiferroics, the following course of this introductory chapter is focused only on the multiferroic coupling of ferroelectric and magnetic ordering.

The occurrence of ferroelectric and magnetic ordering in the same phase requires several conditions to be fulfilled. First, the symmetry restrictions for coexisting ferroelectric and magnetic ordering have to be satisfied, which entails that further to the discussed symmetry restrictions for magnetoelectric behavior, the product of time and space inversion needs to be broken. It was shown that only 13 point groups allow for a multiferroic state [25] and beside the symmetry restrictions it is also obvious that the presence of a finite ferroelectric polarization necessitates an insulating host system. The development of respectively both ferroelectric and magnetic ordering is based on different microscopic mechanisms [26], which additionally complicates the creation of a multiferroic state. A prominent example for this difficulty can be found in the family of perovskites. This material class comprises a variety of magnetic and ferroelectric materials, but the coexistence of both ordering types in the same phase is rarely seen [27, 28]. This is because a large amount of ferroelectric perovskites exhibit positively charged transition metal ions, which tend to form covalent bonds with surrounding negatively charged oxygen ions [26]. The respective shift of both ions towards each other forms a local dipole and eventually the macroscopic electric polarization. However, the repulsion as a result of their overlapping electron clouds counteract with the bond formation and impedes the development of the ferroelectric polarization. In this context, it was discussed that the short-range repulsion can be significantly suppressed for transition-metal cations that are exhibiting empty d-shells, as for these systems a hybridization of empty d-orbitals and filled oxygen $2p$-orbitals weakens the repulsion, which thus promotes the shift of both ions towards each other and eventually the development of a finite ferroelectric polarization [29, 30]. However, the necessity of empty d-shells for ferroelectricity highlights the difficulty to obtain both ordering types simultaneously, as magnetic ordering obviously requires partially filled d-shells for the ions to carry a finite magnetic moment [31]. One possible solution to circumvent these mutually excluding requirements was seen in mixed systems, which exhibit both, ions with partially filled d^n-shells (n equals the number of electrons in the d-shell) and atoms with d^0 configuration [32, 33]. The condition of a partially filled shell is a basic requirement for magnetic ordering, whereas the development of ferroelectric polarization is in general not solely based on the formation of covalent bonds. For example in $\mathrm{BiFeO_3}$ the two outer $6s$ electrons (lone pairs) of the $\mathrm{Bi^{3+}}$ cation do not contribute to the chemical bonding, wherefore they naturally exhibit a higher polarizability and thus also the tendency to form local dipoles [34, 35]. Indeed, these dipoles are collectively oriented along [1 1 1] direction, which stabilizes a macroscopic polarization and thus a ferroelectric phase [34–37]. In addition, the magnetic $\mathrm{Fe^{3+}}$ moments also order, which thus forms a multiferroic state at room temperature [38,39]. A key feature of this multiferroic behavior is that ferroelectric polarization as well as magnetic ordering indeed coexist but develop independently from each other. This performance was also observed for multiferroics, whose driving mechanism does not have its origin in lone pairs of outer *s* electrons [19,26,40,41]. Similar multiferroic behavior was found as a result of charge ordering or because of geometrically driven ferroelectricity [19,26,40,41]. In general, all multiferroics that exhibit this kind of behavior are classified as type-I multiferroics [26] and it is obvious that the respective autonomous development of ferroelectric and magnetic order inherently implies rather weak coupling.

Much stronger coupling is expected, when the onset of magnetic ordering itself enforce the development of a finite ferroelectric polarization. Corresponding systems are classified as type-II multiferroics [26] and such induced improper ferroelectricity was first observed in the rare-earth manganate system $\mathrm{TbMnO_3}$ [42]. In the following two subsections several prominent mechanisms for the onset of multiferroic type-II ordering are elucidated.

1.2.3. Type-II Multiferroics

1.2.3.1. Spin-spiral driven multiferroics

For many type-II multiferroic phases, the underlying physics is based on spiral spin structures that are evolving below the multiferroic transition temperature [19,26,40,41,43]. A prominent mechanism for this spin-spiral driven multiferroic behavior arises from the Dzyaloshinskii-Moriya interaction, which was initially proposed to described the observed weak ferromagnetism in α-$\mathrm{Fe_2O_3}$ [44,45]. It was shown by a phenomenological approach that a canting of neighboring spins is favored and responsible for the weak ferromagnetic moment [44]. Beyond the phenomenological approach, T. Moriya developed a more general theory of this mechanism by extending the superexchange interaction with spin-orbit coupling, which thus renders the Dzyaloshinskii-Moriya interaction to be a relativistic correction to this exchange [45]. The referring Hamiltonian that is describing the Dzyaloshinskii-Moriya interaction is given by

$$H_{\mathrm{DMI}} = \mathbf{D}\left(\mathbf{S_i} \times \mathbf{S_j}\right), \tag{1.6}$$

and its underlying principle is sketched for two neighboring spins in Fig. 1.3. The vectors, $\mathbf{S_i}$ and $\mathbf{S_j}$ correspond to the spins of two neighboring magnetic (M) ions on site i and j that are separated by $\mathbf{r_{ij}}$. The ligand (L) ion is shifted by the vector $\mathbf{x}$ from the straight connection $\mathbf{r_{ij}}$ between both magnetic ions and the interaction vector

$$\mathbf{D} \propto \mathbf{r_{ij}} \times \mathbf{x}, \tag{1.7}$$

is proportional to their cross product.

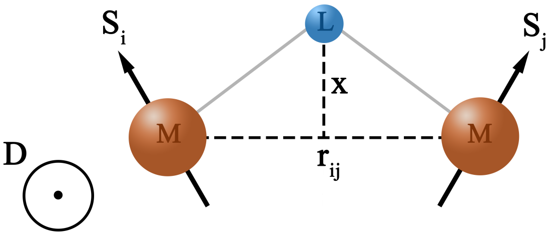

Figure 1.3.: This schematic sketch of two neighboring magnetic (M) ions with canted spins $\mathbf{S_i}$ and $\mathbf{S_j}$ visualizes the parameters that impact the Dzyaloshinskii-Moriya interaction. Here, the interaction vector $\mathbf{D} \propto \mathbf{r_{ij}} \times \mathbf{x}$ describes the displacement of the nonmagnetic ligand ion (L) from the straight line between the magnetic ions, whereby its sign and magnitude depends on both, the amount of displacement and its direction.

In the framework of the developed theory for the Dzyaloshinskii-Moriya interaction, the interaction vector depends on both, the orbital states and spin-orbit coupling [44, 45]. For a non-vanishing value of $\mathbf{D}$ and in the presence of spin canting, the Hamiltonian in 1.6 becomes finite. It is clear that this exchange interaction is antisymmetric as the Hamiltonian in 1.6 entails that a sign change of the canting angle i.e. a sign change of $(\mathbf{S_i} \times \mathbf{S_j})$ leads to energetically nonequivalent states. Thus, depending on $\mathbf{D}$, a respective system exhibits a preference for a particular sense of rotation for the spins, which is closely connected to the displacement $\mathbf{x}$ of the ligand ion. In this context one refers to the chirality $\chi = \mathbf{S_i}\,(\mathbf{S_j} \times \mathbf{S_k})$ of the magnetic structure, whereby the sign of the scalar quantity is assigned to a particular handedness. However, it is obvious that the expression for the scalar chirality is not reasonable for the two-dimensional spirals that are visualized in Fig. 1.4, wherefore in this case a vector chirality is assigned to the handedness.

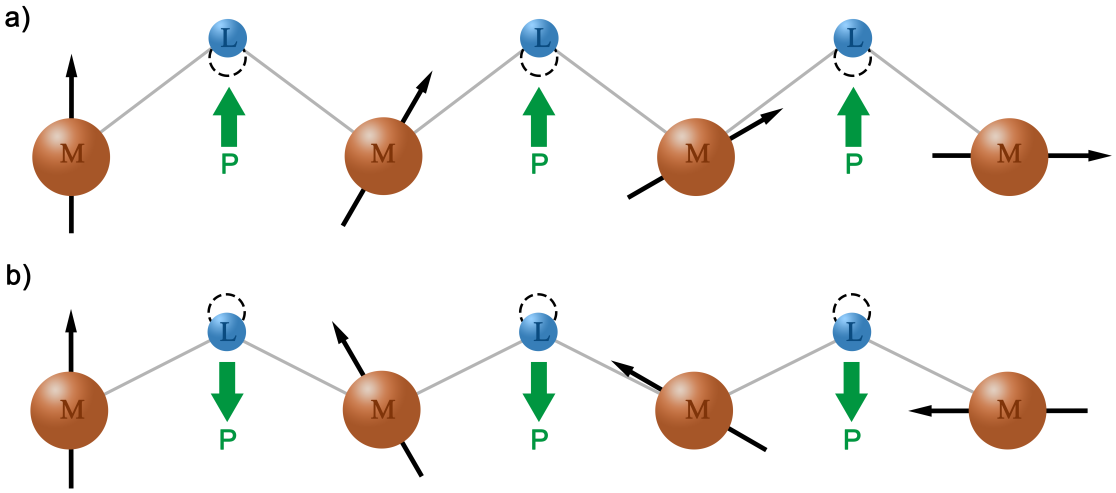

Figure 1.4.: In both, a) and b) two spirals with respectively opposite handedness are shown. Considering the inverse DMI interaction, a uniform shift of all ligand ions from their original position (see dashed circle) is induced and thus, depending on the sense of rotation, the improper ferroelectric polarization $\mathbf{P}$ in a) and b) is pointing in opposite direction.

The displacement of the ligand ion from the direct connection line between neighboring magnetic ions implies a finite value for **D** and thus favors a spin canting. In the framework of multiferroics, the inverse Dzyaloshinskii-Moriya interaction is used to describe the onset of improper ferroelectric polarization. Here, the terminology of an inverse interaction causes that first the onset of spiral ordering induces a shift of the nonmagnetic ligand ions and thus, depending on the underlying symmetry, an improper macroscopic polarization, which is coupled to the spiral handedness.

Utilizing symmetry arguments and a Ginzburg-Landau theory, it was shown by M. Mostovoy [46] that the direction of the induced polarization can be described by

$$\mathbf{P} \propto \mathbf{r_{ij}} \times \left(\mathbf{S_i} \times \mathbf{S_j}\right). \tag{1.8}$$

It entails that a spiral spin configuration with moments rotating in a plane parallel to the spiral propagation vector induces a polarization that is directed perpendicular to the propagation vector and the rotation axis. This is illustrated in Fig. 1.4 a) and b), where spirals with opposite rotation sense induce a ferroelectric polarization with respectively reversed sign. Thus, an external electric field, which is applied parallel to the polarization is capable to invert the handedness of the spiral. This behavior was indeed observed for $\mathrm{TbMnO_3}$, for which a spin spiral in the *bc*-plane develops and propagates along *b*-direction [42, 47, 48]. Here, an evolving ferroelectric polarization along *c* arises from inverse Dzyaloshinskii-Moriya interaction and its direction is in accordance with equation 1.8 [42]. A brief summary of the observed switching dynamics in $\mathrm{TbMnO_3}$ is given in section 1.2.4 and Ref. [47, 49].

In contrast to the cycloidal arrangement of moments, the helicoidal ordering of spins does not lead to a finite ferroelectric polarization, as here the direction of the propagation vector coincides with the spin rotation axis. Thus, following equation 1.8, the polarization is zero. The same outcome for the direction of the induced improper ferroelectric polarization can be obtained by considering the spin-current mechanism that was developed and proposed by Katsura, Nagaosa and Balatsky (KNB model) [50]. Here, the polarization is not formed by a shift of the ligand ions but by pure a shift of electrons.

Another mechanism that enforces multiferroic behavior as a consequence of noncollinear spin ordering is given by the so-called *d*-*p* hybridization mechanism [51, 52], which is proposed to induce a ferroelectric polarization that is described by

$$\mathbf{P} \propto \left(\mathbf{S_i} \cdot \mathbf{r_{ij}}\right) \mathbf{S_i} - \left(\mathbf{S_j} \cdot \mathbf{r_{ij}}\right) \mathbf{S_j}. \tag{1.9}$$

Here, the the mechanism is based on the spin-dependent *d*-*p* hybridization of neighboring magnetic metal and non-magnetic ligand ions. The spin orientation impacts the hybridization of respective *d* and *p* orbitals, which potentially varies the charge distribution between the ligand and the metal ion. This can induce a local electric dipole and depending on the lattice, this local electric polarization does not cancel but adds up to a finite ferroelectric polarization.

Common to the three named mechanisms that drive a type-II multiferroic phase is the requirement of a spiral magnetic structure and the presence of spin-orbit coupling. However, also collinear magnetic structures are capable to evolve a multiferroic state, which is discussed in the following subsection.

1.2.3.2. Symmetric Heisenberg interaction

The mechanism that evokes multiferroic behavior by collinear ordered magnetic structures is driven by the symmetric exchange interaction [19,26,40,41,43,53], for which the principle is sketched in Fig. 1.5. Following the Goodenough-Kanamori rules [54–56] for magnetic superexchange entails that the bonding angle between magnetic ions and the ligands in between depends on the parallel or antiparallel alignment of the neighboring magnetic moments. A ferromagnetic alignment favors a 90° exchange, whereas the antiparallel setup prefers a 180° exchange. Thus, a spin up-up-down-down (*uudd*) arrangement as shown in Fig. 1.5 enforces a bond-angle modulation. In this case a local dipole is formed and with an appropriate underlying symmetry, a macroscopic polarization sums up. As this mechanism is based on symmetric Heisenberg interaction with

$$H_{\mathrm{Heis}} = J\mathbf{S_i}\mathbf{S_j}, \tag{1.10}$$

and not on spin-orbit coupling it promotes stronger coupling compared to the antisymmetric exchange.

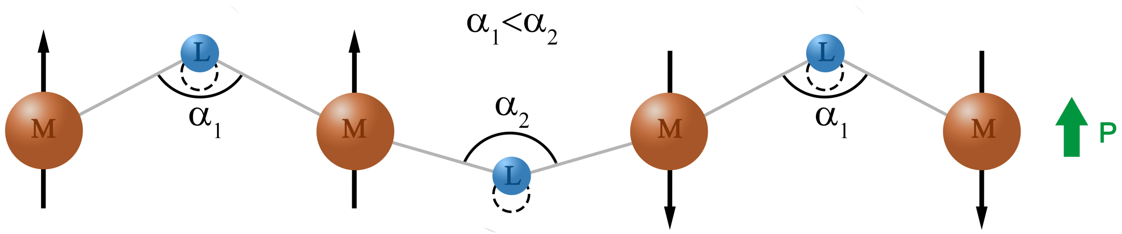

Figure 1.5.: The principle of symmetric exchange based multiferroic coupling is visualized in this figure. Here, the spin up-up-down-down arrangement enforces a bond-angle modulation as the superexchange mechanism entails different bond angles α_1 and α_2 along the superexchange path between magnetic (M) and non-magnetic ligand (L) ions. This modulation causes a shift of ions, which is sketched in this particular case exemplary by a movement of ligand ions with respect to their equilibrium position (dashed circle).

1.2.4. Multiferroic domain kinetics

For the potential application of multiferroics in memory devices, a comprehensive understanding of their domain relaxation is necessary, wherefore previous results on that topic are summarized below. As it will be touched in this subsection and thoroughly discussed in the following course of this thesis, the multiferroic relaxation behavior significantly contrasts the rather complex switching behavior that was observed for pure ferroelectrics [57]. In 1958, W. J. Merz proposed the relaxation time τ in $BaTiO_3$ to be proportional to $\exp(\alpha(T)/E)$ [58]. Hereby, the law named after Merz comprises a temperature-dependent activation field $\alpha(T)$, which was proposed by Hayashi, Lines and Glass to be proportional to the third power of the ferroelectric polarization divided by the temperature [59, 60]. The difficulty to derive a general law that describes both, the temperature and electric field dependence of the relaxation time becomes obvious, when considering the reported different scaling of the relaxation time with temperature and electric field strength [61, 62].

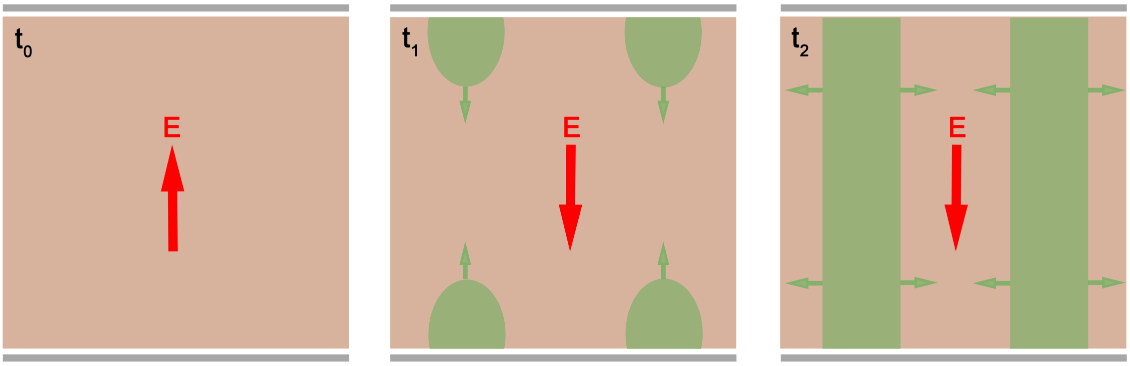

Figure 1.6.: These three panels display the principle sequence of processes that are relevant after field inversion for domain kinetics in ferroelectric or multiferroic materials. Here, the chronology of events is defined by $t_0 < t_1 < t_2$ and the brown and green colored areas visualize domains of opposite polarity and the electrodes are illustrated by the grey colored lines.

The complex and among different ferroelectrics non-uniform temperature- and electric-field dependent description of domain inversion is mainly rooted in the similar timescales, in which different processes during the switching procedure are acting [57]. The principal sequence of a triggered domain inversion is sketched in Fig. 1.6, where the green and brown colored areas represent the different domain types. The initial state at $t = t_0$ for a ferroelectric material in Fig. 1.6 is assumed to be a monodomain state (brown area), while a constant electric field is applied parallel to the electric polarization. At $t = t_1$ the applied electric field is inverted, which subsequently prompts the development of small germs (green spots) of the opposite domain type at the electrodes. The initial nuclei start to growth in forward direction to form needle shaped domains along the direction of the applied electric field. At $t = t_2$, these spicular domains then growth along the direction perpendicular to the applied field direction, which eventually leads to a monodomain state with opposite orientation compared to the initial domain type. It was shown that these three processes all act on the same time-scale, which naturally complicates the description of the temperature and electric-field dependent relaxation behavior [57].

Following the Ishibashi and Takagi treatment of ferroelectric domain kinematics [63–65], which is based on the Avrami model for the kinetics of phase change [66–68], the fraction of inverted domains Q as a function of time is described by

$$Q(t) = 1 - \exp\left(-\left(\frac{(t-t_0)}{\tau}\right)^b\right). \tag{1.11}$$

In this formula, the time t_0 corrects for the latent germs at the beginning of the switching procedure and the exponent b depends on the dimensionality d of the domain growth. In the framework of this model, two cases for domain size development are distinguished. For nucleation of small germs only at the beginning of the inversion process, the exponent b equals the dimensionality of the domain growth. However, for the continuous development of new germs throughout the whole domain inversion, the b value equals $d + 1$.

In contrast to pure ferroelectrics, it was observed for multiferroic switching that the different mentioned processes during domain inversion are mainly dominated by the sideways-motion of domains [69]. It was also seen that only at the beginning of the inversion process new germs are forming and thus, as only one process is dominant for multiferroic domain kinetics, it promised a simplified description for the domain inversion compared to pure ferroelectric switching [49, 69].

However, first time-resolved measurements on the multiferroic domain kinetics in the prominent multiferroic tungstate system $MnWO_4$ revealed the opposite [70, 71]. For this system, the relaxation slows down when reducing the temperature, but close to the lower transition to its commensurate E-type *uudd* phase, the domain kinetics become faster again. Here, the anomalous speeding up of domain inversion becomes even more astonishing, when comparing the multiferroic switching in $MnWO_4$ to the recently reported relaxation behavior in $TbMnO_3$ [49, 70, 71]. For the latter compound, the assumption of a simplified relaxation description for multiferroic switching indeed holds. It was shown that the multiferroic domain relaxation follows a simple combined Arrhenius-Merz law, which necessitate only the two fit parameters A_0 and τ^* to describe the temperature and electric-field dependent relaxation time [49]

$$\tau(E,T) = \tau^* e^{\frac{A_0}{E}\left(\frac{1}{T}-\frac{1}{T_{\mathrm{MF}}}\right)}. \tag{1.12}$$

The characteristic relaxation time τ^* equals the fastest possible relaxation time at the multiferroic transition temperature T_{MF} and the parameter A_0 refers to the activation constant [49]. It was discussed in Ref. [49] that with arguments from Landau theory and with relation 1.12, the activation constant is proportional to the square of the electric polarization, which contrasts the situation in pure ferroelectrics [49, 59, 60]. At least it was shown in Ref. [49] that this simple law describes the multiferroic domain inversion in $TbMnO_3$ over at least 6 orders of magnitude in time and over a broad temperature and electric field range. Only close to the transition temperature the relaxation becomes faster than predicted as further germ nucleation takes place. This has significant impact on the domain inversion process, especially when the nucleation becomes continuous very close to the multiferroics transition temperature. As already explained in Ref. [49], this behavior arises because the condensation energy of the multiferroic phase is small. This is also conform with the observed enhancement of the b parameter, when approaching the multiferroic transition. Without any change of the domain growth dimensionality, the b parameter only increases, when the development of new germs become a continuous process during the inversion process [49]. However, there are also further effects, which can enforce a deviation from the Arrhenius-Merz description.

In the framework of this combined law it is considered that the domain inversion is not driven by sudden inversion of entire domains at once but rather by thermally activated domain-wall motion [49]. The description is thus based on classical domain-wall motion, which necessitates enough energy to overcome the potential barrier that energetically separate the different domain types. Nevertheless, the relaxation of domains can also be powered by quantum tunneling, for which the relaxation time is independent of temperature. Here, the domain does not need to classically overcome the energy barrier but can tunnel through it. Indeed, this effect was observed to impact magnetic and ferroelectric domain inversion, for which a constant relaxation time was observed at low temperature [72–74]. However, such an effect was so far not observed to be relevant for multiferroic switching, which does not entail that the effect cannot become essential at lower temperature, when thermal fluctuations are naturally weakened and quantum fluctuation reinforced.

In summary, to the present day it was observed that multiferroic domain kinetics can principally be described by a simple combined Arrhenius law [49]. However, it was also observed that the relaxation behavior in $MnWO_4$ strongly deviates from this law as the system exhibits a speeding up of domain inversion at the lower transition to commensurate *uudd* ordering [70, 71]. For a comprehensive understanding of multiferroic domain inversion it is thus mandatory to determine the underlying physics that drives the divergence towards an anomalous relaxation behavior as reported for $MnWO_4$ [70, 71]. This necessitates not only the investigation of potential disturbances for the domain kinetics, but it also requires the comparison to the relaxation behavior of other multiferroic systems. The latter exigency motivates the studies of multiferroic switching in a variety of know multiferroics, but it also enforces the characterization of new multiferroic systems, which can serve as potential model systems with different properties for the research on multiferroic domain dynamics. The appropriate tool to investigate not only the multiferroic domain kinetics, but also the details of magnetic structure is provided by neutron scattering techniques. Therefore, the following chapter will give a brief introduction to the basics of neutron scattering, before the respective studies on multiferroic systems are presented in subsequent chapters.

2. Neutron scattering

The discovery of the neutron was finally reported by J. Chadwick in 1932 [75], for which he was honored by the grant of the Nobel Prize in 1935. As it will be discussed below, the discovery not only revolutionized the fundamental understanding of particle and atomic physics but it also provided a new and highly versatile probe for scattering experiments. After a few words to the properties and peculiarities of the neutron and its application potential as a measuring probe, this chapter will give a brief introduction to the concept of neutron scattering, so that the essential basis of understanding is provided for the reader of this thesis. Respective explanations are based on standard literature for neutron scattering [76–80].

Mass	$m_\mathrm{n} \approx 1.67 \times 10^{-27}\,\mathrm{kg}$
Charge	0
Magnetic moment	$\mu_\mathrm{n} \approx -9.66 \times 10^{-27}\,\mathrm{J\,T^{-1}}$
Spin	1/2
Quark configuration	udd
Lifetime	$\tau_\mathrm{n} \approx 879\,\mathrm{s}$

Table 2.1.: This table summarizes the important properties of the neutron.

Together with the positively charged proton, the neutron builds up the atomic nuclei and as the name already implies, it possesses zero charge. However, although the neutron carries no net charge, it nevertheless possesses a finite magnetic moment, which arises from the fact that the neutron is not an elementary particle but comprises one up- and two down-quarks. They respectively exhibit a charge and a spin, wherefore the neutron becomes a spin-1/2 particle with a non-zero magnetic moment. All determined properties and in particular the approximate values of its mass, its magnetic moment and its lifetime are summarized in table 2.1. It must be noted that the latter value refers to a free and unbound neutron, which is inherently not stable and decays into a proton, an electron and an electron antineutrino. It goes without saying that the finite lifetime of a free and unbound neutron naturally complicates its isolated investigation and its handling for scattering experiments.

In view of its scientific impact, the narrative of neutron research did not end with the discovery of the neutron and the classification of its role in nature. Far from it, the neutron was also seen to be a potential probe for scattering experiments and during the last decades this experimental field developed unique tools for high-level research in condensed matter physics, biology, chemistry and engineering. By considering particle-wave duality and the neutron properties, which are summarized in table 2.1, it becomes obvious why neutron scattering can be applied in a variety of fields and why it plays a very important and irreplaceable role in today's experimental landscape.

In view of the crystal structure determination the most obvious difference to established X-ray scattering is that the uncharged neutron does not interact with the electric charge but only with the atomic nuclei via nuclear strong interaction. Thus, the respective scattering strength does not depend on the square value of the atomic number (respectively the square number of electrons) but on an isotope specific and isotropic nuclear scattering length, whose magnitude varies without any systematics between light and heavy elements. This implies the benefit that light atoms e.g. hydrogen can be equally sensed, while coexisting beside heavy atoms within a structural arrangement. As appropriate wavelengths for diffraction studies (in the range of several ångström) exceed by far the interaction region of the strong nuclear force (in the range of femto meters), the respective nuclei can be viewed as weak point scatterer for the neutron. This weak scattering potential allows the theoretical description of scattering events in the framework of the Born approximation and it also further entails high penetration depths, which facilitates the utilization of elaborate sample environments as cryostats, magnets or pressure cells around the sample. However, the rather simple handling of complex setups that are mounted around the sample is opposed to the challenging effort for providing a high incoming flux of free and unbound neutrons. Here, it has to be kept in mind that the weak scattering potential entails weak scattering, wherefore high brilliance sources are needed to obtain scattering data with appropriate statistic.

Nowadays, free neutrons for scattering experiments are provided by nuclear fission or by spallation processes. As explained in the following lines, the key difference between both methods is visible in the time-dependence of the supplied neutron flux. Nuclear fission is based on the capture of neutrons by fissile materials (e.g. ^{235}U), whose excited nuclei decay into two smaller fractions by the emission of 2-3 neutrons. Once initially triggered, the nuclear fission can thus become a continuous self-sustaining process. To maintain the fission process, neutrons are moderated to thermal energies as the cross-section of neutron capture and hence the probability of nuclear fission becomes higher for low-energy neutrons. As the neutron possesses a similar mass compared to light elements, the moderation can easily be done by elastic collisions in water. The supercritical state of a nuclear reactor is avoided by neutron absorbing control rods and finally the controlled nuclear fission provides a continuous flux of neutrons.

This latter point does not hold for the spallation technique, which is based on the bombardment of a heavy target material by highly accelerated protons. Due to their high energy and the respective short wave-length, the impinging protons excite the individual constituents of the target nuclei so that they subsequently strongly interact among each other. This causes a cascade of intra-atomic particle interactions, which finally leads to the ejection of particles and in particular of neutrons. It is obvious that the spallation process is not self-sustaining but contingent on the striking of accelerated high-energy protons. The spallation technique thus provides intense high brilliance neutron pulses with each proton that hits the target material and it follows that in contrast to nuclear fission, the neutron flux is here not continuous but periodically peaked as function of time. The moderation of ejected neutron is not mandatory for the spallation process but as it will be explained in the following, the thermalisation of neutrons is one of the key advantages in terms of potential scattering experiments.

The energy of so-called thermal neutrons amounts approximately to $E = k_{\mathrm{B}}300\,\mathrm{K} \approx 10\,\mathrm{meV}$, which thus coincides with the typical excitations energies in condensed matter physics. As the neutron is sensitive to both, nuclear and magnetic components of the crystal structure, it is thus clear that the investigation of phonons as well as of magnons is possible with reasonable resolution and thus proposes the neutron to be an ideal probe for studying these fundamental excitations. It further follows from the neutron mass m_{n} and the velocity v_{n} of thermal neutrons that the respective de-Broglie wavelength $\lambda = h/\left(m_{\mathrm{n}}v_{\mathrm{n}}\right)$ lies in the range of typical interatomic distances within a crystal unit cell. Therefore, precise characterizations of crystal structures are likewise possible, when utilizing neutron scattering techniques. The fact that both, elastic and inelastic studies of fundamental crystal properties are practicable with reasonable precision, highlights one huge advantage over X-ray scattering. Hereby, it has to be considered that photons with comparable wavelengths that are matching the interatomic distances possess energies of the order of several keV, wherefore respective inelastic studies are possible only with tremendous effort, respectively extreme high resolution. In case of neutron scattering the energy and thus the wavelength spectrum can be further adapted to high-resolution diffraction or high-resolution spectroscopy by respectively tuning the wavelength with a shift of the Maxwell–Boltzmann distribution peak of produced neutrons with hot or cold moderators.

As already noted, another important advantage of neutron scattering refers to the magnetic moment and the spin of the neutron. It enables the scattering from magnetic arrangements and thus the potential characterization of its structure. For a precise separation of different magnetic and nuclear components, longitudinal or spherical polarization analysis of an initially spin polarized neutron beam can be utilized. As it will be shown in the further course of this thesis, the polarization analysis is a unique tool to analyse chiral magnetic structures, because it allows for an experimentally observable distinction between domains of right- and left-handed spin spirals.

It is needless to highlight that both opportunities, the investigation of static and dynamic properties of nuclear and magnetic structures using the same probe within the course of a scattering experiment are highly attractive for the research field of condensed matter physics. Eventually, the importance of neutron scattering is further emphasized by the award of the Nobel Prize to C. Shull and B. Brockhouse in 1994 for their pioneering contribution to the development and progress of elastic and inelastic neutron scattering instruments respectively.

The following sections will give a brief introduction to the theory of neutron scattering processes, whereby specific focus is put on the coherent nuclear and magnetic scattering as well as on the neutron polarization analysis. As noted, the explanations are based on standard literature for neutron scattering [76–80]. The last section of this chapter moreover outlines the principle of the high-voltage and time-resolved setup that was deployed during neutron scattering experiments for the investigation of multiferroic domain relaxation within the course of this thesis.

2.1. Nuclear scattering

The measured quantity within the course of a scattering experiment is in general expressed by the double-differential cross-section $\mathrm{d}^2\sigma/(\mathrm{d}\Omega_\mathrm{f}\mathrm{d}E_\mathrm{f})$. Here, in the context of neutron scattering it describes the magnitude of neutrons that are scattered into a solid angle range $\Delta\Omega$, whereby the final neutron energy amounts to $E_\mathrm{f} + \mathrm{d}E_\mathrm{f}$. The particular scattering process is related to a change of the neutron state, whose transition probability can be well described in the framework of Fermi's Golden Rule

$$W_{\mathbf{k_i},\lambda_i,\mathbf{s_i}\rightarrow\mathbf{k_f},\lambda_f,\mathbf{s_f}} = \frac{2\pi}{\hbar}\rho_\mathrm{f}\left|\left\langle\mathbf{k}_\mathrm{f}\lambda_\mathrm{f}\mathbf{s}_\mathrm{f}\left|V\right|\mathbf{k}_\mathrm{i}\lambda_\mathrm{i}\mathbf{s}_\mathrm{i}\right\rangle\right|^2 . \tag{2.1}$$

The probability $W_{\mathbf{k_i},\lambda_i,\mathbf{s_i}\rightarrow\mathbf{k_f},\lambda_f,\mathbf{s_f}}$ for a transition of the initial wave-vector $\mathbf{k}_\mathrm{i}$, the initial wavelength λ_i and the initial spin $\mathbf{s}_\mathrm{i}$ towards the respective final states $\mathbf{k}_\mathrm{f}, \lambda_\mathrm{f}$ and $\mathbf{s}_\mathrm{f}$ is here proportional to the interaction matrix element $\left\langle\mathbf{k}_\mathrm{f}\lambda_\mathrm{f}\mathbf{s}_\mathrm{f}\left|V\right|\mathbf{k}_\mathrm{i}\lambda_\mathrm{i}\mathbf{s}_\mathrm{i}\right\rangle$ of the underlying scattering potential V and the density of final states ρ_f. As already discussed, the interaction of the neutron with a scattering potential is only weak, wherefore the theoretical description of the scattering process can be simplified by utilizing the Born-Approximation. In the context of this consideration it is assumed that the neutrons are scattered only once by the underlying scattering potential, which eventually entails that both, the initial wave and the scattered wave can be well described by plane waves of the form

$$\Psi_{\mathbf{k}_\mathrm{i,f}} \propto \exp\left(i\mathbf{k}_\mathrm{i,f}\mathbf{r}\right) . \tag{2.2}$$

Thus, the matrix element in formula 2.1 simplifies to

$$\begin{aligned} \left\langle\mathbf{k}_\mathrm{f}\lambda_\mathrm{f}\mathbf{s}_\mathrm{f}\left|V\right|\mathbf{k}_\mathrm{i}\lambda_\mathrm{i}\mathbf{s}_\mathrm{i}\right\rangle &= \left\langle\lambda_\mathrm{f}\mathbf{s}_\mathrm{f}\left|\exp\left(i\left(\mathbf{k}_\mathrm{i}-\mathbf{k}_\mathrm{f}\right)\mathbf{r}\right)V\right|\lambda_\mathrm{i}\mathbf{s}_\mathrm{i}\right\rangle & (2.3)\\ &= \left\langle\lambda_\mathrm{f}\mathbf{s}_\mathrm{f}\left|\exp\left(i\mathbf{Q}\mathbf{r}\right)V\right|\lambda_\mathrm{i}\mathbf{s}_\mathrm{i}\right\rangle & (2.4) \end{aligned}$$

with $|\mathbf{Q}| = 4\pi\mathrm{sin}(\theta)/\lambda$ and θ being the scattering angle. The general formula for the double-differential cross-section can then be written as

$$\frac{\mathrm{d}^2\sigma}{\mathrm{d}\Omega_{\mathrm{f}}\mathrm{d}E_{\mathrm{f}}} = \frac{|\mathbf{k}_{\mathrm{f}}|}{|\mathbf{k}_{\mathrm{i}}|}\left(\frac{m_{\mathrm{n}}}{2\pi\hbar^2}\right)^2 \sum_{\lambda_{\mathrm{i}},\mathbf{s}_{\mathrm{i}}} p_{\lambda_{\mathrm{i}}} p_{\mathbf{s}_{\mathrm{i}}} \sum_{\lambda_{\mathrm{f}},\mathbf{s}_{\mathrm{f}}} |\langle\lambda_{\mathrm{f}}\mathbf{s}_{\mathrm{f}}\,|V|\,\lambda_{\mathrm{i}}\mathbf{s}_{\mathrm{i}}\rangle|^2\,\delta\left(\hbar\omega + E_{\lambda_{\mathrm{i}}} - E_{\lambda_{\mathrm{f}}}\right). \tag{2.5}$$

Here, both values $p_{\lambda_{\mathrm{i}}}$ and $p_{\mathbf{s}_{\mathrm{i}}}$ specify the probability for the respective initial neutron state and the quotient $|\mathbf{k}_{\mathrm{f}}|/|\mathbf{k}_{\mathrm{i}}|$ takes the density of final states (see equation 2.1) into account.

In the context of scattering theory one often refers to this double-differential cross-section by the so-called scattering function

$$S\left(\mathbf{Q},\omega\right) \propto \frac{\mathrm{d}^2\sigma}{\mathrm{d}\Omega_{\mathrm{f}}\mathrm{d}E_{\mathrm{f}}}, \tag{2.6}$$

which describes the observable intensity as a function of $\mathbf{Q}$ and ω. This will be referred to again in the context of spin-echo spectroscopy (see chapter 9), which gives access to the time-fourier transform of $S(\mathbf{Q},\omega)$ and thus to the so-called intermediate scattering function $I(\mathbf{Q},t)$. The following course will however focus on $S(\mathbf{Q},\omega)$ and in particular on elastic scattering, which is described by $S(\mathbf{Q})$.

In case of pure nuclear scattering, the respective scattering potential V_{nuc} can be described by the isotropic Fermi pseudo-potential

$$V_{\mathrm{nuc}} = \frac{2\pi\hbar^2}{m_{\mathrm{n}}} b\delta\left(\mathbf{r} - \mathbf{r_i}\right). \tag{2.7}$$

The nuclear scattering length b is isotope as well as nuclear spin dependent and describes the scattering strength of the respective nuclei. In general, the scattering length is a complex quantity and can possess a finite imaginary part, which is related to absorption effects. A prominent feature of the nuclear scattering length and hence also the nuclear scattering potential is the fact that its magnitude varies without any systematic between different elements. This is in particular highly beneficial for investigations on materials, in which heavy as well as light elements are coexisting. As the scattering length varies randomly between these elements and do not show a tremendous enhancement of its magnitude for heavy atoms, all elements can be sensed more or less with equal accuracy. This naturally contrasts X-ray experiments for which the scattering potential of a particular element depends on the square value of the number of electrons.

The delta-function in equation 2.7 furthermore enforces the potential to take a finite value only at the atomic site $\mathbf{r} = \mathbf{r_i}$. This is because the interaction between the neutron and the nucleus is mediated by the strong-force interaction, whose interaction range is smaller by several orders of magnitude compared to the wavelength range of thermal neutrons. Hence, the nucleus can be viewed as a point-like scatterer for the impinging neutrons. Due to this, the scattering length does not possess a $\mathbf{Q}$-dependence, which contrasts the conventional X-ray experiments, where the scattering process is provoked by an extended object, namely the electron cloud, which enforces a significant $\mathbf{Q}$ dependence that is described by the atomic form factor.

With the given nuclear scattering potential and by considering solely elastic scattering, the scattered intensity, respectively the differential cross-section becomes

$$\frac{\mathrm{d}\sigma}{\mathrm{d}\Omega} \propto \left| \sum_i b_i \exp\left(i\mathbf{Q}\mathbf{r_i}\right) \right|^2 \tag{2.8}$$

$$= \sum_i \sum_j b_i b_j \exp\left(i\mathbf{Q}\left(\mathbf{r_i} - \mathbf{r_j}\right)\right). \tag{2.9}$$

As noted, the nuclear scattering length is isotope and nuclear spin dependent, wherefore its value varies randomly between different sites. Hence, the product $b_i b_j$ can be replaced by the average $\langle b_i b_j \rangle$, whose value must however be considered differently for $i = j$ and $i \neq j$. By regarding unequal sites $(i \neq j)$, the average becomes $\langle b_i b_j \rangle = \langle b_i \rangle \langle b_j \rangle = \langle b \rangle^2$, which is because the different sites are randomly occupied by different isotopes and further because no correlation persists between the respective sites. This is different for equal sites, for which the average of the product can be paraphrased to

$$\langle b_i b_j \rangle = \left\langle b^2 \right\rangle = \left\langle b^2 - 2\langle b \rangle^2 + 2\langle b \rangle^2 \right\rangle \tag{2.10}$$

$$= \left\langle b^2 - 2b\langle b \rangle + \langle b \rangle^2 \right\rangle + \langle b \rangle^2 \tag{2.11}$$

$$= \left\langle (b - \langle b \rangle)^2 \right\rangle + \langle b \rangle^2. \tag{2.12}$$

Putting the outcome for both cases, namely for $i = j$ and $i \neq j$ into equation 2.9, the differential crossection becomes

$$\frac{\mathrm{d}\sigma}{\mathrm{d}\Omega} \propto \underbrace{\sum_i \langle b \rangle^2 \exp\left(i\mathbf{Q}\left(\mathbf{r_i} - \mathbf{r_j}\right)\right)}_{\text{coherent}} + \underbrace{N\left\langle \left(b^2 - \langle b \rangle\right)^2 \right\rangle}_{\text{incoherent}}. \tag{2.13}$$

It can be seen that the differential cross-section is splitted into two parts, the coherent and incoherent term, whereby N equals the number of atomic sites. Only the coherent part contains a phase factor and arises from interference effects that are caused by scattering events from different sites. This contrast the incoherent part, which is provoked by scattering processes from single atoms, which eventually contributes only to an incoherent background signal. In this context one also refers to the coherent scattering length $b_{\mathrm{coh}} = \langle b \rangle^2$ and the incoherent scattering length $b_{\mathrm{inc}} \left\langle \left(b^2 - \langle b \rangle\right)^2 \right\rangle$. It is obvious that the incoherent and coherent scattering length varies at different sites if they are not occupied by the same element, whereby a thorough listing of respective element-, isotope- and spin-dependent scattering lengths can be found in Ref. [81].

By neglecting the incoherent background contribution, the scattered intensity for a particular reflection, respectively for a distinct h, k, l triple is described by

$$I_{\mathrm{hkl}} \propto \left| \sum_j b_{\mathrm{coh},j} \exp\left(i\mathbf{G}\mathbf{r_j}\right) \exp\left(-W_j\right) \right|^2 = \left|F_{\mathrm{N}}(\mathbf{G})\right|^2, \tag{2.14}$$

which equals the absolute square value of the nuclear structure factor $F_\mathrm{N}\left(\mathbf{G}\right)$ with $\mathbf{G}$ being a reciprocal lattice vector. The additional factor $W_j = \exp\left(1/3|\mathbf{G}|^2\langle u_j^2\rangle\right)$ refers to the Debye–Waller factor with u being the mean square displacement. In literature the latter quantity is commonly referred to the B and U values, which are respectively defined by $B = 8\pi^2\langle u^2\rangle$ and $U = \langle u^2\rangle$. It must be noted that formula 2.14 gives only a theoretical value for respective reflection intensity and does not consider experimental and sample dependent parameters like extinction, absorption or even multiple scattering. However, these processes will not be explained in the course of this brief introductory chapter, wherefore the respective standard literature [76–80] is recommended for a detailed understanding of these effects and their impact on the measured intensity.

2.2. Magnetic scattering

It was already mentioned that the neutron is not solely scattered by the nuclear structure but senses also potential magnetic arrangements. This is because the neutron possesses a finite magnetic moment, which interacts with the magnetic moment that arises from unpaired electrons of magnetic atoms. A thorough description of magnetic neutron scattering can be found in [76–80]. The respective scattering potential is given by

$$V_\mathrm{m} = -\mu_\mathrm{n}\mathbf{B} = -\mu_\mathrm{n}\left(\underbrace{\nabla \times \frac{\mu_\mathrm{e} \times \mathbf{R}}{R^3}}_{\mathbf{B}_\mathrm{S}} \underbrace{- \frac{e}{c}\frac{v_\mathrm{e} \times \mathbf{R}}{R^3}}_{\mathbf{B}_\mathrm{L}}\right), \tag{2.15}$$

whereby the magnetic field is composed of two terms $\mathbf{B_L}$ and $\mathbf{B_S}$, which respectively arise from the orbital motion of the electron and its spin. Here, the parameters μ_e and $\mathbf{v}_\mathrm{e}$ describe respectively the magnetic moment and the velocity of the electron. In contrast to nuclear scattering, the magnetic scattering process is not isotropic and only perpendicular components of the magnetic structure with respect to the scattering vector can contribute to a neutron scattering process, whereby this perpendicular component $\mathbf{M}_\perp(\mathbf{Q})$ can in general be expressed by

$$\mathbf{M}_\perp(\mathbf{Q}) = \hat{\mathbf{Q}} \times \left(\mathbf{M}(\mathbf{Q}) \times \hat{\mathbf{Q}}\right) = \mathbf{M}(\mathbf{Q}) - \hat{\mathbf{Q}}\left(\hat{\mathbf{Q}}\mathbf{M}(\mathbf{Q})\right). \tag{2.16}$$

The anisotropy of magnetic scattering yields thus a simple way to get information about the magnetic arrangement, respectively the magnetic moment orientation. However, for a thorough analysis of the structure and in particular for the determination of the magnetic moment magnitude, a structural refinement that utilizes a set of recorded magnetic reflections is necessary. The magnetic structure factor for respective reflections is defined by

$$|\mathbf{F}_\mathrm{M}(\mathbf{Q})|^2 = p\sum_j f_j(|\mathbf{Q}|)\mathbf{m_j}\exp\left(i\mathbf{Q}\mathbf{r_j}\right)\exp\left(-W_j\right) \tag{2.17}$$

with $\mathbf{m_j}$ representing the magnetic moment given in μ_B at site $\mathbf{r_j}$. The fact that the scattering is caused by unpaired electrons entails that the respective magnetization distribution of the magnetic atom cannot be treated as a point-like scatterer, which is taken into account by the magnetic form factor $f_j(|\mathbf{Q}|)$. This resembles the situation of X-ray scattering from an extended electron cloud, whose charge distribution is considered by the atomic form factor. To relate the product $f_j(|\mathbf{Q}|)\mathbf{m_j}$ to a scattering length, the sum in equation 2.17 is multiplied by $p \approx 2.7$ fm/μ_B, which describes the scattering length per Bohr magneton. From the magnitude of p it becomes obvious that common magnetic moments of about $1\mu_\mathrm{B}$ entail already a similar scattering strength compared to nuclear scattering.

As mentioned above, the magnetic scattering is also accompanied by a transition of the initial neutron spin state towards a final state. For pure nuclear scattering events this was neglected so far because the scattering is here only accompanied by non-spin-flip (NSF) processes. This is however different for magnetic scattering, for which both, spin-flip (SF) and non-spin-flip (NSF) events are possible. The occurrence of respective processes depends on the magnetic arrangement and its orientation with respect to $\mathbf{Q}$, wherefore the respective analysis of potential SF and NSF intensity gives detailed information about the magnetic structure. In particular, for complex chiral magnetic arrangements the analysis of SF and NSF scattering yields a unique tool to sense the handedness of magnetic spirals. This is in particular highly beneficial for the investigation of domain dynamics in chiral type-II multiferroics, wherefore the following section provides a brief overview about neutron polarization analysis. Here, the summary of the essential knowlegde is based on the detailed descriptions of polarized neutron scattering techniques in Ref. [76–78, 80].

2.3. Neutron polarization analysis

It is obvious that the analysis and in particular the separation of NSF and SF processes necessitates an at least partially spin-polarized neutron beam, which can however be provided by several methods. For example, a ^{3}He-gas exhibits a vastly different neutron absorption cross-section for the parallel or antiparallel alignment of the neutron spin with respect to the nuclear spin of ^{3}He. Hence, if the nuclear spins of the underlying gas are polarized (e.g. by optical pumping with lasers), the gas acts as a spin-filter that transmits only neutrons, which exhibit a particular spin orientation. Another employable method bases on the utilization of magnetized mirrors, which possess for opposite neutron spin states a different critical angle for refraction. Eventually also scattering processes from ferromagnetic, respectively magnetized crystals entail a gain of finite polarization for the scattered neutron beam, which is commonly utilized together with the monochromatization of the beam.

In general the magnitude of the initial neutron beam polarization $\mathbf{P}_\mathrm{in} = (P_x, P_y, P_z)^\top$

along a particular quantization axis $i = x, y, z$ is given by

$$P_i = \frac{I_i - I_{\bar{i}}}{I_i + I_{\bar{i}}}. \tag{2.18}$$

Here, I_i denotes the number, respectively the intensity of neutrons, which possess a spin that is aligned along $i = x, y, z$, whereby an overbar of i denotes an antiparallel alignment of the spin with respect to this quantization axis. In this context it also mandatory to define a coordinate system for the polarization analysis. Within the course of this thesis, the common right-handed coordinate system with x parallel to the scattering vector is chosen. This entails that correspondingly the y-direction is perpendicular to x but still confined to the scattering plane, whereas z is perpendicular to both x and y.

It is obvious that in real experiments the beam is not perfectly polarized due to the limited device accuracy of polarizers, spin flippers, guide fields and other mandatory parts of the instrument. In this context one often refers to the so-called flipping-ratio (FR)

$$\mathrm{FR}_i = \frac{I_i}{I_{\bar{i}}}, \tag{2.19}$$

which gives the ratio of neutrons that possess the demanded spin orientation and neutrons that exhibit the opposite (respectively wrong) spin alignment with respect to a particular direction. With this expression, the magnitude of the initial beam polarization along a particular quantization axis can be paraphrased to

$$P_i = \frac{\mathrm{FR}_i - 1}{\mathrm{FR}_i + 1}. \tag{2.20}$$

However, in the framework of neutron polarization analysis one is usually interested in the scattered beam polarization $\mathbf{P}_{\text{out}}$, respectively in the change of the neutron beam polarization that is caused by the scattering potential. Equivalent to 2.18, the scattered beam polarization is described with

$$P_{ij} = \frac{I_{ij} - I_{i\bar{j}}}{I_{ij} + I_{i\bar{j}}}, \tag{2.21}$$

whereby the subscript ij denotes the respective SF or NSF process from i to j.

The outgoing polarization vector $\mathbf{P}_{\text{out}}$ after the scattering event is determined with the polarization matrix $\mathcal{P}$ and the incoming polarization vector $\mathbf{P}_{\text{in}}$ by

$$\mathbf{P}_{\text{out}} = \mathcal{P}\mathbf{P}_{\text{in}} + \mathbf{P_c} \qquad \text{with} \qquad \mathcal{P} = \begin{pmatrix} P_{xx} & P_{xy} & P_{xz} \\ P_{yx} & P_{yy} & P_{yz} \\ P_{zx} & P_{zy} & P_{zz} \end{pmatrix} \tag{2.22}$$

and $\mathbf{P_c}$ being the created beam polarization.

To understand the nuclear and magnetic contributions that trigger the respective SF and NSF processes along particular directions enforces the evaluation of all matrix elements in equation 2.3, while considering the nuclear and magnetic scattering potential. This eventually leads to the so-called Blume-Maleev equations [82, 83], which describe both, the scattered intensity and the final beam polarization for a respective spin transition from i to j. Both equations can be written as

$$I_{\text{out}} = \underbrace{NN^*}_{|F_N|^2} + \underbrace{\mathbf{M}_\perp \mathbf{M}_\perp^*}_{|\mathbf{F}_\mathbf{M}|^2} + \underbrace{\mathbf{P}_{\text{in}} \left(\mathbf{M}_\perp N^* + \mathbf{M}_\perp^* N \right)}_{\text{nuclear-magnetic interference}} - \underbrace{i\mathbf{P}_{\text{in}} \left(\mathbf{M}_\perp \times \mathbf{M}_\perp^* \right)}_{\text{chiral magnetism}} \tag{2.23}$$

and

$$\begin{aligned} \mathbf{P}_{\text{out}} I_{\text{out}} &= \mathbf{P}_{\text{in}} \left(NN - \mathbf{M}_\perp \mathbf{M}_\perp^* \right) \\ &+ \mathbf{M}_\perp \left(\mathbf{P}_{\text{in}} \mathbf{M}_\perp^* \right) + \mathbf{M}_\perp^* \left(\mathbf{P}_{\text{in}} \mathbf{M}_\perp \right) + \mathbf{M}_\perp N^* + \mathbf{M}_\perp^* N \\ &- i\mathbf{P}_{\text{in}} \times \left(\mathbf{M}_\perp N^* - \mathbf{M}_\perp^* N \right) + i \left(\mathbf{M}_\perp \times \mathbf{M}_\perp^* \right)_x . \end{aligned} \tag{2.24}$$

Several features of neutron polarization analysis can be directly read off from both equations. First, it is unambiguously clear that the scattered intensity for a completely unpolarized beam is thoroughly described by the sum of both, the absolute square value of the nuclear structure factor and the absolute square value of the magnetic structure factor. This however changes, when the neutron beam is at least partially polarized. In this case, the scattered intensity also depends on nuclear-magnetic interference effects as well as on potential chiral magnetism. From both equations, it can be further deduced that a partially unpolarized beam gains finite polarization if the underlying scattering process includes the impact of nuclear-magnetic interference or chiral magnetism. The first named effect, namely the nuclear-magnetic interference, is in this context often utilized for polarizing the initial beam with magnetized crystals as it is for example done with Heusler monochromators. The latter mentioned possibility of generating beam polarization becomes relevant for the Larmor-diffraction experiments on chiral magnetic arrangements, which are thoroughly discussed in chapter 9 within the course of time-resolved multiferroic domain-size studies.

Most important for a successful polarization analysis of the scattered beam is to get the knowledge about the respective scattering contributions to different intensity channels. These contributions to the different SF and NSF processes can be deduced by considering the fact that the ith component of I_{out} (see equation 2.23) must equal the sum of the respective NSF and SF channel. Together with equation 2.21, the intensity channel I_{ij} can then be described by

$$I_{ij} = \frac{1}{2}(I_i^{\text{out}} + P_i^{\text{out}} I_i^{\text{out}}). \tag{2.25}$$

Thus, by using this formula together with the Blume-Maleev equations (see equation 2.23 and 2.24), it enables the separate description of all 36 intensity channels in terms of magnetic and nuclear scattering contributions. This can be exemplary shown for the

SF-channel $I_{y\bar{y}}$, for which both Blume-Maleev equations become

$$I_y = NN^* + M_y M_y^* + M_z M_z^* + M_y N^* + M_y^* N \tag{2.26}$$

and

$$P_y^{\text{out}} I_y = -NN^* - M_y M_y^* + M_z M_z^* - M_y N^* - M_y^* N \tag{2.27}$$

Hence, by putting both I_y and $P_y^{\text{out}} I_y$ into equation 2.25, the SF-channel $I_{y\bar{y}}$ becomes

$$I_{y\bar{y}} = M_z M_z^*, \tag{2.28}$$

which highlights the benefits of neutron polarization analysis, because it not only senses a magnetic arrangement but also allows in particular for a precise separation of magnetic components with respect to the scattering vector. In general, it holds that magnetic components cause NSF-scattering if they are oriented parallel to the neutron polarization and SF-scattering if they are oriented perpendicular to the polarization of the neutron beam. Hence, it follows that a parallel alignment of the beam polarization with respect to the scattering vector enforces magnetic scattering to be only SF-scattering. A list of all 36 intensity channels is provided in the appendix B.

In view of the neutron scattering studies on multiferroic domain inversion, both SF-channels $I_{x\bar{x}}$ and $I_{\bar{x}x}$ are of special interest, as they are sensing the potential vector chirality of a magnetic arrangement. Both channels are described by

$$I_{x\bar{x}} = \mathbf{M}_\perp \mathbf{M}_\perp^* - i \left(\mathbf{M}_\perp \times \mathbf{M}_\perp^* \right)_x \tag{2.29}$$

and

$$I_{\bar{x}x} = \mathbf{M}_\perp \mathbf{M}_\perp^* + i \left(\mathbf{M}_\perp \times \mathbf{M}_\perp^* \right)_x . \tag{2.30}$$

The respective quotient of the difference and the sum of both channels gives the so-called chiral ratio

$$r_\chi = \frac{I_{x\bar{x}} - I_{\bar{x}x}}{I_{x\bar{x}} + I_{\bar{x}x}} = \frac{-i \left(\mathbf{M}_\perp \times \mathbf{M}_\perp^* \right)_x}{|\mathbf{M}_\perp|^2}, \tag{2.31}$$

which senses the sign of the vector chirality and also quantifies its fraction with respect to the overall scattering contribution. Thus, both domain types of spiral multiferroics can be distinguished by the sign of r_χ and its magnitude gives information about the respective domain population. However, it must be noted that only for scattering vectors that are aligned perpendicular to the rotation planes of spins, the chiral ratio yields values of ±1 for monodomains. For non-ideal scattering configurations or even for a finite elliptic distortion of magnetic spirals, the absolute value of r_χ is less than one.

The experimental access to both channels $I_{x\bar{x}}$ and $I_{\bar{x}x}$ is usually provided by longitudinal polarization analysis, which was first invented by R. M. Moon, T. Riste and W. C. Koehler in 1969 [84]. Here, the beam gets initially polarized by one of the conventional methods and subsequently the polarization is preserved by guide fields until the neutrons reach the sample environment. The sample can be confined to a Helmholtz-coil setup, whose magnetic fields determine the polarization alignment at the sample position. After the scattering process and symmetric to the first field region, the neutron spins adiabatically turn back to the initial quantization axis. The parallel or antiparallel alignment depends here on the scattering process, which either entailed SF- or NSF-scattering. A polarization analyzer, which works equivalent to the polarizing device, transmits neutrons only with a particular alignment with respect to the quantization axis and hence enables the separation between SF- and NSF scattering processes of the sample. Additional spin-flippers before and behind the sample allow to define the demanded SF and NSF processes for a particular quantization axis, whereby this longitudinal polarization analysis is naturally restricted to the diagonal elements of the polarization matrix in equation 2.22. For a thorough investigation of the respective off-diagonal elements, spherical polarization analysis and thus a more complex setup is needed. Commonly these latter experiments are done with Cryopad or MuPad systems, for which a detailed explanation is given in Ref. [85, 86] and Ref. [87] respectively.

2.4. Time-resolved neutron diffraction

Naturally, the investigation of multiferroic domain dynamics and in particular of the domain relaxation necessitates time-resolved measurements but it is also clear that a demanded study of very fast domain inversion processes collides with the weak scattering of neutrons as an appropriate statistic of detected neutrons within several milli-seconds cannot be achieved by far. However, the lack of detected neutrons within small time intervals can be circumvented by repeating the inversion process periodically, whereby the detected neutrons are summed up in time-bins with respect to the moment, when an inversion process starts. This principle was already discussed in Ref. [88] and its utilization for time-resolved studies on multiferroic domain inversion was reported in Ref. [70] and Ref. [49]. This section briefly presents the basics of this technique and in particular it explains the utilized experimental time-resolved (high-voltage) setup, which was built by J. Stein [49, 89].

Figure 2.1 a) shows a typical sample setup for time-resolved experiments on the multiferroic relaxation behavior. The sample (here a single crystal of $NaFeGe_2O_6$) is cramped between two aluminum plates, which are tightened together by insulating polytetrafluoroethylene (PTFE) screws. These aluminum plates can be connected to a high-voltage generator, respectively a high-voltage switch, whereby the plate normals are aligned parallel to the ferroelectric polarization. Thus, an applied high-voltage generates an electric field, which is capable to switch the orientation of the ferroelectric polarization in the dielectric material. The high voltage is provided by two ISEG modules (ISEG BPP4W and ISEG BPN4W), which respectively supply a high-voltage ($|U| \leq 4\,\mathrm{kV}$) with opposite polarity. The high-voltage setup further includes a fast MOSFET array (BEHLKE HTS-111), which can switch between both polarities and allows for electric-field inversion in the time-range of several μs. It must be emphasized that this range sets also the limit of resolvable multiferroic relaxation processes. The time-resolution is achieved by using a multichannel data collector (MESYTEC MCPD-8), which records the detector events as well as the synchronization signals of all field-inversions together with a time-stamp. Thus, with both kinds of recorded and time-stamped signals, all neutrons can be summed up into time bins with respect to the time of field-inversion. In the context of multiferroic domain inversion, this procedure is subsequently done for both SF-channels $I_{x\bar{x}}$ and $I_{\bar{x}x}$ to eventually calculate the chiral ratio.

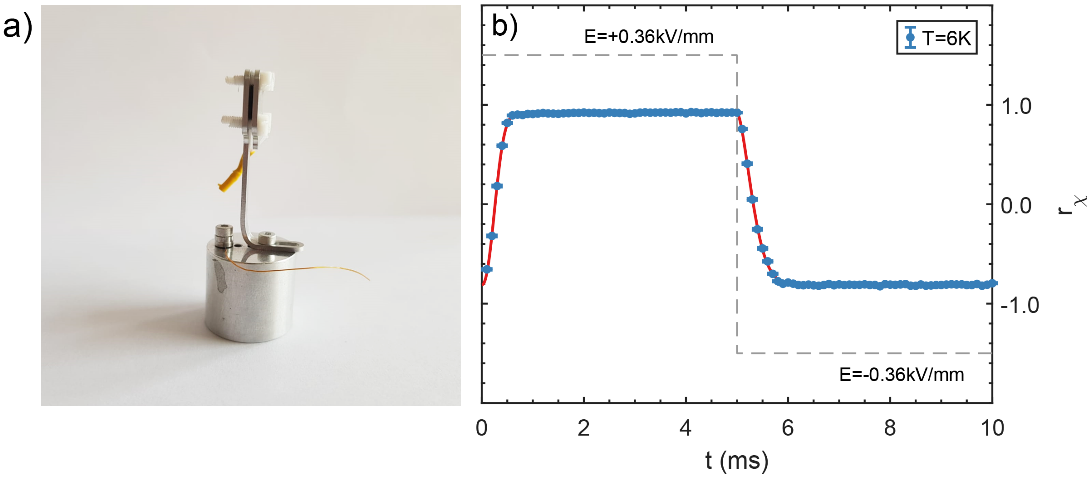

Figure 2.1.: The left panel shows a typical sample setup for time-resolved measurements. This example refers to a mounting of a $NaFeGe_2O_6$ sample, which is squeezed between two aluminum plates that are tightened together by insulating polytetrafluoroethylene (PTFE) screws. A corresponding time-resolved measurement of r_χ is exemplary shown in panel b). The blue data points refer to the measured chiral ratio and the red line corresponds to a respective fit (see equation 2.32). The grey dashed line just sketches the time-dependence of the applied field, whereby its magnitude possesses here an arbitrary scaling with respect to the y-axis. Respective results on $NaFeGe_2O_6$ are thoroughly discussed in chapter 5 and Ref. [3].

The application of high-voltage and also the fast field inversion entails the risk of sudden gas discharges inside the cryostat. To avoid this scenario, respectively to reduce the probability of such processes, the sample setup was commonly confined into a small sample container, which can be evacuated and vented via an external valve. This is facilitated by a small capillary, which goes through the sample stick and allows for a precise control of the atmosphere and in particular of the necessary high-purity exchange gas for the temperature control. However, it must be noted that this kind of sample stick was only available for experiments that were conducted at the IN12 triple-axis spectrometer (located at ILL), whereas experiments at other instruments necessitated a careful adjustment of the atmosphere, respectively the amount of exchange gas in the cryostat and around the sample.

Figure 2.1 b) displays an exemplary switching curve that was obtained within the course of a time-resolved experiment on $NaFeGe_2O_6$ (see chapter 5 and Ref. [3]). It is obvious that the relaxation process of the multiferroic domain inversion, respectively the varying chiral ratio can be well followed after field-inversion. Following the explanations in Ref. [70] and Ref. [49] its time-dependence after field inversion can be well described by an exponential relaxation, respectively by the stretched exponential functions

$$\begin{aligned} r_\chi(t) &= r_\mathrm{a} - (r_\mathrm{a} - r_\mathrm{b})\exp\left[-\left(\frac{t}{\tau_\mathrm{a}}\right)^{b_1}\right] \\ r_\chi(t) &= r_\mathrm{b} - (r_\mathrm{b} - r_\mathrm{a})\exp\left[-\left(\frac{t - t_{1/2}}{\tau_\mathrm{b}}\right)^{b_2}\right]. \end{aligned} \tag{2.32}$$

Here, the parameters r_a and r_b are the potential maximum and minimum values of the chiral ratio after the relaxation process has finished. The time that is needed to switch between both saturation values is described by τ_a and τ_b, whereby the parameter $t_{1/2}$ specifies the time, when the electric field is inverted. In the framework of the Ishibashi-Takagi theory [63–65] and the Avrami model [66–68] both stretching exponents b_1 and b_2 describe the domain-growth dimensionality of germs.

Thus, the description of switching curves by equation 2.32 yields not only the relaxation times τ_a and τ_b for multiferroic domain inversion but it gives also insight into the growth characteristics of the initial nuclei, which develop after field inversion. The respective discussion of the multiferroic relaxation behavior and in particular the analysis of potential differences of its description in different materials is part of this thesis.

3. Structural dimerization in the commensurate magnetic phases of $NaFe(WO_4)_2$ and $MnWO_4$

Beside reliability and storage capacity, one further key feature that sets the benchmark for future storage technologies is their read and write performance. In view of the application potential of multiferroic materials in this field, it is thus of great interest to preserve a thorough understanding and description of the multiferroic relaxation behavior as a function of field amplitude and temperature. In particular, it is of high interest to comprehend the peculiarities that lead to a deviation from a simple relaxation description as from the one that was found for the prototype spiral type-II multiferroic material $TbMnO_3$ [49].

It was already discussed in section 1.2.4 that the observed simple activation behavior for multiferroic domain inversion in $TbMnO_3$ significantly contrasts the reported anomalous domain kinetics in $MnWO_4$ [70, 71], for which the multiferroic switching speeds up again at lower temperatures. The profound understanding of the origin for this discrepancy is highly desirable for the ongoing research on multiferroic domain dynamics and in particular for the design of new multiferroic systems with the potential to be deployed in future memory devices.

Beside the crystallographic disparities [90–92], $TbMnO_3$ and $MnWO_4$ significantly differ by the sequence of their magnetic phases [42, 48, 92–94]. Both systems first develop an incommensurate spin-density wave until below the respective multiferroic transition temperature [42, 95] an incommensurate spiral evolves. In view of the magnetic phase diagrams, the major difference is then given by the low-temperature regime. In $MnWO_4$ the incommensurate spiral transforms into a commensurate *uudd* structure, whereas the magnetic arrangement in $TbMnO_3$ remains incommensurate and only the Tb^{3+} moments additionally order at low temperature. A striking point of this low-temperature transition to commensurate ordering in $MnWO_4$, is the appearance of strong magnetoelastic coupling, which is different from that driving the multiferroic state and it was further shown that already the incommensurate phase develops coupled anharmonic modulations of the magnetic and nuclear structure [96–98]. In view of the anomalous switching kinetics close to the transition to commensurate ordering, it is thus of great interest to investigate the characteristics of magnetoelastic coupling in $MnWO_4$ as well as the anharmonic modulations and their impact on the domain kinetics in the multiferroic phase.

In terms of interfering commensurate and incommensurate ordering, the structurally related double tungstate system $NaFe(WO_4)_2$ exhibits a similar phase diagram [99]. However, in contrast to $MnWO_4$, the system does not develop a multiferroic phase, as in its incommensurate phase the spirals in the upper and lower rows of magnetic zigzag chains are rotating in opposite sense and wherefore the inverse DMI cancels out for this compound [99]. Nevertheless, the similar competition of incommensurate and commensurate order in this system and in particular the reported stronger magnetoelastic coupling rendered $NaFe(WO_4)_2$ to be an ideal system to investigate the essence of this coupling in its commensurate *uudd* phase, which naturally also supports the respective understanding of the behavior in $MnWO_4$. It is expected that the onset of *uudd* ordering causes a structural dimerization in form of a bond-angle modulation due to the alternating ferro- and antiferromagnetic exchange along the magnetic zig-zag chain. This dimerization can be seen to be akin to the one in the Spin-Peierls compound $CuGeO_3$, for which the bond-angle modulation is accompanied by the occurrence of superstructure reflections [100]. For $NaFe(WO_4)_2$, it was further reported that locally tiny commensurate fragments already develop in the incommensurate phase, which was indicated by the onset of odd harmonic reflections [99]. An equivalent occurrence in $MnWO_4$ would enforce depinning effects for multiferroic domains, wherefore a study, respectively the confirmation of this effect in $MnWO_4$ is highly supportive for the understanding of its anomalous relaxation behavior.

Both, the investigation of the structural dimerization and the analysis of anharmonic modulations in the incommensurate phase are ideally suited to neutron diffraction, as the superstructure reflections and the onset of odd harmonics is commonly accessible with this experimental technique. The respective scattering experiments on $NaFe(WO_4)_2$ and $MnWO_4$ were conducted at the ILL [101, 102] and LLB and the respective results were published in the publication

> S. Biesenkamp, N. Qureshi, Y. Sidis, P. Becker, L. Bohatý, and M. Braden, *Structural dimerization in the commensurate magnetic phases of* $NaFe(WO_4)_2$ *and* $MnWO_4$, Phys. Rev. B **102**, 144429 (2020),

which is included into this thesis (see following pages). It turned out that in both materials, $NaFe(WO_4)_2$ and $MnWO_4$, the commensurate *uudd* ordering indeed induces a structural dimerization in form of a sizeable bond-angle modulation due to the alternating ferro- and antiferromagnetic exchange along the magnetic zig-zag chains. Further, it was seen that already in the respective incommensurate phases of both compounds tiny commensurate fragments evolve, which eventually can depin the multiferroic domains in $MnWO_4$. With this result it can be proposed that a simple relaxation behavior (as in $TbMnO_3$ [49]) can be significantly disturbed by the interference of commensurate order in the incommensurate multiferroic phase of a spiral type-II multiferroic. This outcome gave thus a clear selection criteria for potential materials that follow the proposed simple activation law for the domain relaxation and hence motivated the respective investigation of them. Nevertheless, the outcome of this project also encouraged to analyze the multiferroic domain dynamics in compounds, which however are exhibiting interfering commensurate order. This can further disclose to what extend this interference is impacting the relaxation behavior and how the peculiarities of the magnetism and the nuclear structure are influencing an anomalous relaxation behavior.

Contribution to the embedded publication

All reported measurements and the dedicated analysis were done by the author of this thesis. The presented quantitative proof of a dimerization in $NaFe(WO_4)_2$ was part of his master thesis [103] and the subsequent qualitative determination of the related bond-angle modulation was conducted during the course of this doctoral thesis. All measurements and the data analysis on $MnWO_4$ are also part of this doctoral thesis. The experiments that were conducted at the neutron scattering facilities ILL [101, 102] and LLB were respectively supported by the local contacts N. Qureshi and Y. Sidis and the samples for the investigations on $NaFe(WO_4)_2$ and $MnWO_4$ were grown and provided by P. Becker-Bohatý and L. Bohatý. All figures that are shown in the publication were created by the author of this thesis. The first draft of the paper manuscript was written by him and its completion was done in cooperation with M. Braden. The publication was further proofread and corrected by all named co-authors. The whole project was supervised by M. Braden.

PHYSICAL REVIEW B **102**, 144429 (2020)

Structural dimerization in the commensurate magnetic phases of $NaFe(WO_4)_2$ and $MnWO_4$

S. Biesenkamp,[1] N. Qureshi,[2] Y. Sidis,[3] P. Becker,[4] L. Bohatý,[4] and M. Braden[1,*]

[1]*II. Physikalisches Institut, Universität zu Köln, Zülpicher Straße 77, D-50937 Köln, Germany*
[2]*Institut Laue-Langevin, 71 avenue des Martyrs, CS 20156, 38042 Grenoble Cedex 9, France*
[3]*Laboratoire Léon Brillouin, C.E.A./C.N.R.S., F-91191 Gif-sur-Yvette, France*
[4]*Abteilung Kristallographie, Institut für Geologie und Mineralogie, Universität zu Köln, Zülpicher Straße 49b, 50674 Köln, Germany*

(Received 19 June 2020; revised 3 September 2020; accepted 30 September 2020; published 20 October 2020)

The structural distortion and magnetoelastic coupling induced through commensurate magnetism has been investigated by neutron diffraction in structurally related $MnWO_4$ and $NaFe(WO_4)_2$. Both systems exhibit a competition of incommensurate spiral and commensurate spin up-up-down-down ordering along the magnetic chains. In the latter commensurate phases, the alternatingly parallel and antiparallel arrangement of Fe^{3+} or Mn^{2+} moments leads to sizable bond-angle modulation and thus to magnetic dimerization. For $NaFe(WO_4)_2$ this structural distortion has been determined to be strongest for the low-field up-up-down-down arrangement, and the structural refinement yields a bond-angle modulation of $\pm 1.15(16)$ degrees. In the commensurate phase of $MnWO_4$, superstructure reflections signal a comparable structural dimerization and thus strong magnetoelastic coupling different to that driving the multiferroic order. Pronounced anharmonic second- and third-order reflections in the incommensurate and multiferroic phase of $MnWO_4$ result from tiny commensurate fractions that can depin multiferroic domains.

DOI: 10.1103/PhysRevB.102.144429

I. INTRODUCTION

Since the discoveries of giant magnetoelectric coupling in $TbMnO_3$ [1] and of functional responses in thin film $BiFeO_3$ [2], the research interest on multiferroic materials has tremendously increased [3–6]. In type-II multiferroics a ferroic arrangement directly induces a second ferroic order, which implies a strong coupling and thus the potential of manipulating one ferroic parameter by the conjugate field of the coexisting order [3–5]. There are various magnetoelectric mechanisms known to induce type-II multiferroicity [7], and also the multiferroic coupling in $BiFeO_3$ is quite complex [8].

In many type-II multiferroics the microscopic coupling mechanism is described by the inverse Dzyaloshinskii-Moriya interaction (DMI) [9,10] relating the ferroelectric polarization to the cross product of two spins and the direction of their connecting vector $\boldsymbol{e}_{ij}$: $\boldsymbol{P} \propto \boldsymbol{e}_{ij} \times (\boldsymbol{S}_i \times \boldsymbol{S}_j)$ [11–14]. However, due to its origin from spin-orbit coupling, this effect and especially the induced ferroelectric polarization remain small compared to conventional ferroelectrics [4]. In contrast, larger ferroelectric polarization and more generally larger magnetoelastic coupling can be generated by symmetric-exchange striction in a collinear magnetic structure [15]. Indeed, exchange striction was observed to induce large ferroelectric polarization in rare-earth manganates $RMnO_3$, where a small R ionic radius causes a change of the magnetic structure from an incommensurate spiral to commensurate E-type spin up-up-down-down (*uudd*) arrangement [15–17].

The same kind of magnetic competition between incommensurate and commensurate magnetic order can also be found in the phase diagrams of the two tungstates $MnWO_4$ and $NaFe(WO_4)_2$ [18–21]. But only in $MnWO_4$ is the incommensurate phase multiferroic arising from the inverse DMI. In contrast, both materials exhibit strong magnetoelastic coupling in their commensurate phases with *uudd* spin arrangement. Characterizing the magnetoelastic coupling associated with the commensurate *uudd* order in these tungstates is the aim of this work.

The crystal and magnetic structures are illustrated in Fig. 1. Both materials are characterized by zigzag chains of edge-sharing MnO_6 or FeO_6 octahedra along c that are adjacent along b. Along the third direction a, the magnetic chains are separated by layers of WO_6 octahedra in $MnWO_4$. This separation is enhanced in $NaFe(WO_4)_2$, whose structure results from that of $MnWO_4$ by substituting the Mn in the zigzag chain layers alternatingly with Fe and nonmagnetic Na. Therefore, every second layer is magnetic in $MnWO_4$, while only every fourth layer is magnetic in $NaFe(WO_4)_2$. Concerning the magnetic structures it is most important to analyze the intrachain arrangements depicted in Fig. 1. $MnWO_4$ undergoes first a transition into a collinear incommensurate phase AF3 and then into an incommensurate spiral phase, AF2. This AF2 phase can be compared to the low-field incommensurate phase (LF-IC) that $NaFe(WO_4)_2$ directly reaches upon cooling. While the AF2 phase in $MnWO_4$ is multiferroic with finite ferroelectric polarization, the LF-IC phase remains paraelectric in $NaFe(WO_4)_2$. The difference between the two magnetic structures concerns the rotation of the magnetic moments in the cycloid plane [18,20,21]. The upper and lower magnetic moments in one zigzag chain rotate in the same sense in

---

[*] braden@ph2.uni-koeln.de

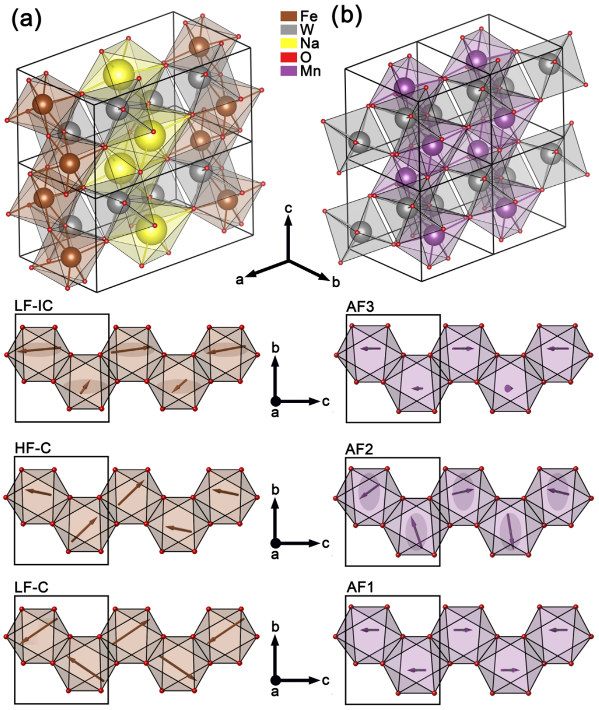

FIG. 1. (a), (b) Displays the nuclear and magnetic structure of $NaFe(WO_4)_2$ and $MnWO_4$, respectively. The unit cells are marked by black boxes and arrows indicate the direction of magnetic moments within the respective magnetic phases. Note the similarities between the incommensurate spiral phases AF2 and LF-IC, as well as between the commensurate *uudd* phases AF1 and HF-C/LF-C.

$MnWO_4$ and in opposite sense in $NaFe(WO_4)_2$. Therefore, the contributions to the polarization according to the inverse DMI cancel out for the Fe compound. $MnWO_4$ reaches a commensurate phase, AF1, at low temperature characterized by *uudd* order within a chain [18,20], and also $NaFe(WO_4)_2$ exhibits commensurate phases, low-field commensurate (LF-C), and high-field commensurate (HF-C), that, however, differ for high and low magnetic fields. In addition there is a strong hysteresis so that the magnetic structure depends on how a point in the B, T phase diagram (see inset of Fig. 3) is reached [21]. In contrast to the E-type manganates, the *uudd* structures occurring in $MnWO_4$ and in $NaFe(WO_4)_2$ are not multiferroic as there is no finite polarization. Nevertheless, we will show that also these *uudd* phases show a strong magnetoelastic coupling characterized by prominent structural dimerization. Note that the ferroelectric polarization in RMnO$_3$ only arises from the interplay between bond-angle-driven dimerization and octahedron rotation, which causes a shift of all bridging oxygen ions in the same direction [15,16].

The first-order transition to the commensurate AF1 phase in $MnWO_4$ is accompanied by sizable thermal expansion anomalies ($\frac{\Delta b}{b} \approx -1 \times 10^{-5}$) [22]. Already in the multiferroic AF2 phase a considerable magneto-elastic coupling was observed [23,24] in the form of magnetic and nuclear anharmonic modulations. Every incommensurate-modulated magnetic structure enforces a nuclear modulation of half the period in real space and of two times the propagation vector. Indeed a strong second-order reflection appears in the multiferroic phase [25], and neutron polarization analysis separates the magnetic and nuclear contribution revealing a strong nuclear fraction and a small magnetic part [23]. The same competition of incommensurate and *uudd* ordering also appears in the double tungstate $NaFe(WO_4)_2$, in which transitions to the commensurate phases are accompanied by thermal expansion anomalies that are at least one order of magnitude larger ($\frac{\Delta b}{b} \approx -2.6 \times 10^{-4}$) compared to the observed anomalies in $MnWO_4$ [21,22]. Independently of the absence of multiferroicity in $NaFe(WO_4)_2$, the similar competition of incommensurate spiral and *uudd* ordering as well as the very strong magneto-elastic coupling to the commensurate phases render $NaFe(WO_4)_2$ an ideal candidate to investigate the magneto-elastic coupling in the form of a structural dimerization effect when entering the commensurate *uudd* phases.

The research field of multiferroics not only concerns fundamental aspects but also the development of new sensor and memory devices utilizing multiferroicity [26–28]. For memory devices the writing speed is an important factor, which in the case of a multiferroic material relates to the relaxation and inversion processes of antiferromagnetic domains, that are controlled by electric fields. The electric-field-dependent behavior of multiferroic domains was studied intensively for the prototype multiferroic materials $TbMnO_3$ and $MnWO_4$ [29–34]. A time-resolved neutron scattering investigation as well as second-harmonic generation imaging of multiferroic domain inversion in $MnWO_4$ revealed a rather complex switching behavior, as the inversion process is speeding up towards the lower first-order transition to the commensurate *uudd* phase [32,35].

In this paper we report studies of the structural dimerization appearing in the commensurate *uudd* phases in $NaFe(WO_4)_2$ and in $MnWO_4$. The paper is organized as follows. After the experimental methods, we first discuss the results for $NaFe(WO_4)_2$, where a stronger dimerization is suggested by the larger thermal expansion anomalies [21,22]. Besides a qualitative proof of structural dimerization, we present a structural refinement that quantifies the structural distortion in $NaFe(WO_4)_2$. In the last part of this paper we discuss the structural dimerization in $MnWO_4$ and its relation to the higher harmonic reflections in the incommensurate phase as well as its role in depinning multiferroic domain walls.

II. EXPERIMENTAL METHODS

The experiments on the structural dimerization in $NaFe(WO_4)_2$ were performed on the D10 diffractometer at the Institut Laue-Langevin (ILL). For the expected bond-angle modulation within the magnetic zigzag chain the shift of light oxygen ions is crucial, and therefore neutron diffraction is the appropriate tool. The effect is expected to be small and hence, it was essential to obtain the best possible signal to background ratio. Thus the instrument had to be equipped with the vertically focusing pyrolytic graphite analyzer, which reduces the background significantly, and a single He^3 detector was used. The commensurate phases of $NaFe(WO_4)_2$ are only accessible by applying a magnetic field along b. Thus, the sample was mounted in the (1 0 0)/(0 0 1) scattering plane and a vertical cryomagnet was used ($\mu_0 H <$ 6 T). All temperature and magnetic-field-dependent measurements were performed with $\lambda = 2.36$ Å (pyrolithic graphite monochromator) yielding high flux, and the data collection for a structural refinement was done with $\lambda = 1.26$ Å (copper monochromator) to reach more reflections. The single crystal with dimensions 1 mm × 5 mm × 10 mm was grown as described in reference [21], which also presents the characterization by various macroscopic methods.

The measurements on $MnWO_4$ were performed on the triple-axis spectrometer 4F2 at the Laboratoire Léon Brillouin (LLB) using a wavelength $\lambda = 4.05$ Å extracted with a highly oriented pyrolithic graphite doublemonochromator. Higher-order contaminations were suppressed by a cooled Be filter and the sample was cooled in a closed-cycle refrigerator. The crystal had dimensions of 2 mm × 4 mm × 9 mm and was mounted in an aluminium can containing He exchange gas. The scattering geometry was (1 0 0)/(0 0 1). Information concerning the crystal growth and characterization are given in Refs. [23,24,34].

III. RESULTS AND DISCUSSION

A. Structural dimerization in $NaFe(WO_4)_2$

$NaFe(WO_4)_2$ crystallizes in the $P2/c$ space group with $a \approx 9.88$ Å, $b \approx 5.72$ Å, $c \approx 4.94$ Å, and $\beta \approx 90.33^\circ$ (at 298 K) [36].

The crystallographic unit cell of $NaFe(WO_4)_2$ is doubled along a with respect to the unit cell of $MnWO_4$ [see Fig. 1(a)]. Due to the enhanced distance between adjacent $[FeO_6]$-octahedra chains along a, the magnetic interaction is significantly reduced in this direction, which provokes a more two-dimensional nature of magnetic ordering in $NaFe(WO_4)_2$. Nevertheless, the system exhibits a cascade of magnetically ordered phases [see Fig. 1(a)] [21]. First, below $T_N \approx 4$ K an incommensurate three-dimensional magnetic order with $\boldsymbol{k} = (0.485, \frac{1}{2}, 0.48)$ develops. The moments are rotating in a plane, which is spanned by the easy plane e_{ac} and a small b component. However, as neighboring spirals rotate in the opposite sense with respect to each other, the DMI effect cancels and no multiferroic state develops in the low-field incommensurate (LF-IC*) phase. Below $T \approx 3$ K emerging third-order reflections signal a squaring up of the magnetic structure but the spiral magnetic structure remains incommensurate in zero field at low temperatures (LF-IC phase). When applying a magnetic field at low temperatures ($\mu_0 H \approx 2$ T at $T \approx 2.5$ K), the system undergoes a spin-flip transition to a high-field commensurate *uudd* arrangement with $\boldsymbol{k} = (\frac{1}{2}, \frac{1}{2}, \frac{1}{2})$ (HF-C phase). While decrasing the magnetic field again (below $\mu_0 H \approx 2$ T at $T \approx 2.5$ K), a spin-flop transition forces a spin-canting but the structure remains commensurate and still exhibits an *uudd* arrangement. This LF-C phase has been determined to be the ground state of the system and all transitions from incommensurate to commensurate order are reported to be of first order [21].

Astonishingly, it is not the onset of magnetic ordering that is accompanied by strong magnetoelastic anomalies, but rather the emergence of anharmonic modulations and especially the transitions from incommensurate to the commensurate phases, which emphasizes a strong magnetoelastic coupling to them [21].

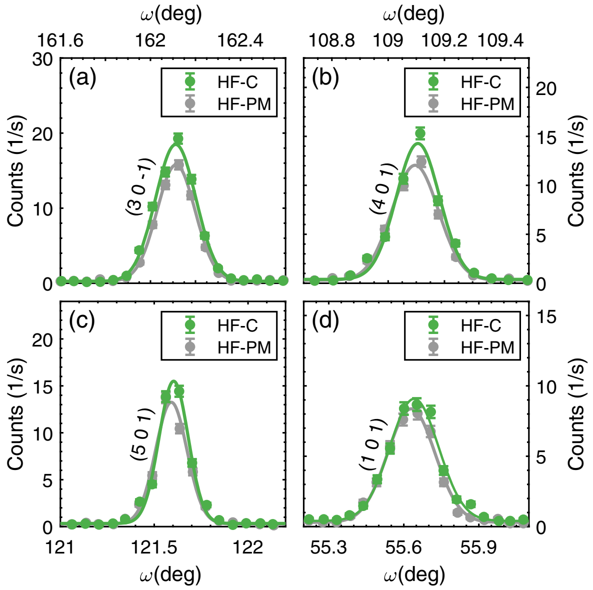

FIG. 2. $NaFe(WO_4)_2$: (a)–(d) Rocking-scans over the Q-space position of superstructure reflections are shown. For all measured reflections, the respective rocking scans were executed in the high-field paramagnetic phase (HF-PM) at $T \approx 10$ K and $\mu_0 H = 6$ T as well as within the high-field commensurate phase (HF-C) at $T \approx 2.4$ K and $\mu_0 H = 6$ T.

The main goal of the neutron experiments was to determine the structural distortion within the commensurate phases of the system. A bond-angle variation along the Fe chain due to alternating exchange interaction violates the glide plane and the twofold rotation symmetry, but it does not break translation symmetry. Therefore, superstructure reflections [37] will appear at $Q = (h\,0\,l)$ with $l =$ odd. Figure 2 displays recorded rocking scans across several superstructure reflections. All reflections were measured inside the HF-C phase at $T \approx 2.4$ K and within the paramagnetic phase at $T \approx 5.2$ K, while applying a magnetic field of $\mu_0 H = 6$ T. Even in the paramagnetic phase a reflection is detectable, whose presence should actually be forbidden due to the $P2/c$ symmetry. The field-induced moment cannot contribute a magnetic signal at these Q values because it does not break the glide-mirror symmetry. This is also visible in the magnetic-field-dependent measurements in Figs. 3 and 4 for $Q = (3\,0\,-1)$ and $Q = (4\,0\,1)$, respectively. This Bragg-signal in the paramagnetic phase can arise from either $\lambda/2$-contamination or multiple scattering. The $\lambda/2$-contamination was determined through rocking scans across the allowed (5 0 2) reflection and the resulting $\lambda/2$-contamination at $Q = (2.5\,0\,1)$. The fraction of $\lambda/2$-contamination with respect to the main reflection amounts to $\approx 6 \times 10^{-4}$ and is too small to explain the observed $Q = (3\,0\,-1)$ and $Q = (4\,0\,1)$ intensities in the paramagnetic state. By measuring the intensity at $Q = (6\,0\,-2)$, we can conclude that the $\lambda/2$-contamination at $Q = (3\,0\,-1)$ only approaches ≈1.32 counts per seconds.

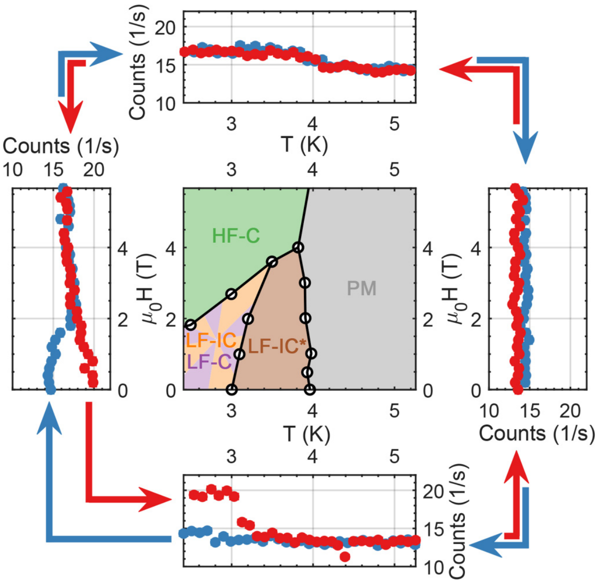

FIG. 3. NaFe(WO$_4$)$_2$: For analyzing the occurrence and strength of superstructure reflections in a particular phase, temperature and magnetic-field-dependent measurements were performed for the superstructure reflection $Q = (3\,0\,\text{-}1)$. The temperature and magnetic-field-dependent sweep path is here defined by the axes of the phase diagram (the white marked phase boundaries are extracted from [21]), which is plotted in the middle of this figure. The sweep path was traversed clockwise (blue path) and also anticlockwise (red path), as the accessibility of the LF-IC and LF-C phases depends on prehistory of applied fields. The T- and μ_0H-sweep speed was low, as the weak signal required a counting time of ≈3 minutes per point.

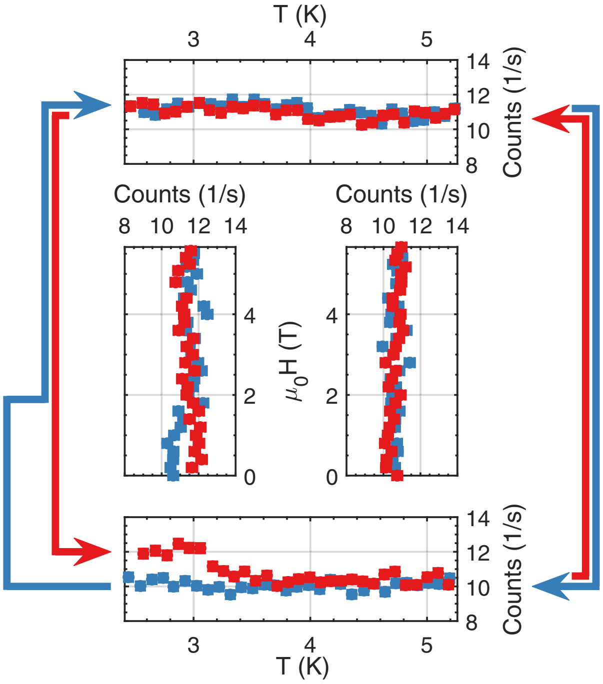

FIG. 4. NaFe(WO$_4$)$_2$: Similar to Fig. 3 this figure presents the temperature and magnetic-field dependence of the peak intensity for the superstructure reflection $Q = (4\,0\,1)$ in NaFe(WO$_4$)$_2$. The blue and red arrows indicate the clockwise or anticlockwise paths in the B, T space, respectively.

Thus, multiple scattering almost entirely causes the finite intensities at $Q = (3\,0\,-1)$ and $Q = (4\,0\,1)$ outside the commensurate phases, but the enhancement of these signals in the commensurate phases cannot stem from multiple diffraction [38]. In Fig. 2, it can be seen that the integrated intensity of all reflections increases, when forcing the system to the HF-C phase. Therefore, we can conclude that the glide plane symmetry is broken, when entering the HF-C phase.

To investigate the occurrence and the strength of superstructure reflections in all phases, we performed temperature and magnetic-field-dependent sweeps through the phase diagram. Due to the weakness of the signal and the corresponding long counting time, we restricted the data collection on recording only the intensity at the maximum position of the peak. Nevertheless, we checked by some rocking scans, whether the Bragg-peak shifts for different fields and temperatures. As this was not the case, we can exclude a maximum peak intensity modulation due to a shift of the Bragg-reflection in Q-space. Exemplary for the $Q = (3\,0\,-1)$ superstructure reflection, the temperature and magnetic-field-dependent intensity is shown in Fig. 3. Because the commensurate or incommensurate character of the low-field phases strongly depends on the prehistory of applied magnetic fields in this system, we performed clockwise and anticlockwise sweeps through the phase diagram of NaFe(WO$_4$)$_2$. The temperature and magnetic-field-dependent sweep paths are marked by the axes of the B, T phase diagram in the middle of Fig. 3.

Starting the clockwise cycle (blue symbols in Fig. 3) in the paramagnetic phase at $\mu_0H = 0\,\text{T}$ and $T \approx 5.2\,\text{K}$, a reduction of the temperature does not change the peak intensity of the superstructure reflection, when passing the two transitions to the incommensurate phase (LF-IC*) and to the anharmonic distorted incommensurate phase (LF-IC), respectively. Increasing the magnetic field at low temperatures leads to a sudden intensity enhancement at $\mu_0H = 1.8\,\text{T}$. At that field value, the system undergoes a transition from an incommensurate magnetic ordering to a commensurate *uudd* arrangement. The intensity enhancement, and hence, the occurrence of a superstructure reflection coincides with the onset of an alternating ferro- and antiferromagnetic exchange along the magnetic zigzag chains. When increasing the temperature at high fields, the intensity drops back again to its initial value right at the transition to the paramagnetic phase at $T \approx 4\,\text{K}$ and lowering the field at 5.2 K does not further change the intensity.

The anticlockwise sweep (red symbols in Fig. 3) through the phase diagram recovers the measured intensity of the clockwise sweep, when starting again from the paramagnetic phase in zero field at $T \approx 5.2\,\text{K}$ ramping the field up and then cooling at high field. This is not surprising, as the same high-field phase is reached, when cooling below $T \approx 4\,\text{T}$ in high fields at $\mu_0H = 6\,\text{T}$. However, when decreasing the field at low temperatures, the magnetic arrangement does not return

TABLE I. The left part of this table contains the structural parameters that were determined in the paramagnetic phase at $T = 12\,\mathrm{K}$ by Holbein *et al.* [21]. All positions were converted to space group $P\bar{1}$ as given in the middle part of this table. The right part consists of the refined structural parameters within the LF-C phase and by assuming $P\bar{1}$ symmetry. For the refinement, 26 unique superstructure reflection of which 24 are independent were used. Moreover, 13 uniquely allowed reflections of which 7 are independent were added to the refinement. To reduce the number of variables, the following constraints were utilized: $x[\mathrm{O}2a] = x[\mathrm{O}2b] - 0.78224$, $x[\mathrm{W}1] = x[\mathrm{W}2] - 0.52592$, $z[\mathrm{O}2a] = z[\mathrm{O}2b] - 0.3154$, and $z[\mathrm{W}1] = z[\mathrm{W}2] + 0.0144$. The structural refinement yielded reliability factors of $R_{\mathrm{obs}} = 7.07$, $wR_{\mathrm{obs}} = 16.44$, $R_{\mathrm{all}} = 9.13$, and $wR_{\mathrm{all}} = 18.54$ for structure factors.

	Paramagnetic phase (spacegroup $P2/c$)					Paramagnetic phase (spacegroup $P\bar{1}$)			LF-C phase (spacegroup $P\bar{1}$)		
	x	y	z	B_{iso}		x	y	z	x	y	z
Fe	0.0	0.67074(19)	0.25	0.04(2)	Fe	0.0	0.67074(19)	0.25	−0.0002(2)	0.67074	0.2525(7)
Na	0.5	0.6971(6)	0.25	0.35(5)	Na	0.5	0.6971(6)	0.25	0.5	0.6971	0.25
W	0.23704(14)	0.1831(2)	0.2572(3)	0.12(3)	W1	0.23704(14)	0.1831(2)	0.2572(3)	0.2383(3)	0.1831	0.2562(8)
O1	0.35385(12)	0.3813(3)	0.3816(3)	0.25(3)	W2	0.76296(14)	0.1831(2)	0.2428(3)	0.7642(3)	0.1831	0.2418(8)
O2	0.10888(13)	0.6226(3)	0.5923(3)	0.22(2)	O1a	0.35385(12)	0.3813(3)	0.3816(3)	0.35385	0.3813	0.3816
O3	0.33177(13)	0.0897(2)	0.9533(3)	0.22(3)	O1b	0.64615(12)	0.3813(3)	0.1184(3)	0.64615	0.3813	0.1184
O4	0.12606(13)	0.1215(3)	0.5757(3)	0.17(2)	O2a	0.10888(13)	0.6226(3)	0.5923(3)	0.1111(2)	0.6226	0.5935(8)
					O2b	0.89112(13)	0.6226(3)	0.9077(3)	0.8933(2)	0.6226	0.9089(8)
					O3a	0.33177(13)	0.0897(2)	0.9533(3)	0.33177	0.0897	0.9533
					O3b	0.66823(13)	0.0897(2)	0.5467(3)	0.66823	0.0897	0.5467
					O4a	0.12606(13)	0.1215(3)	0.5757(3)	0.12606	0.1215	0.5757
					O4b	0.87394(13)	0.1215(3)	0.9243(3)	0.87394	0.1215	0.9243

to the incommensurate and metastable low-field phase but a spin-flop transition at $\mu_0 H \approx 1.8\,\mathrm{T}$ leads to the LF-C phase with canted moments that are still ordered in a commensurate *uudd* arrangement. The superstructure intensity even further increases, when removing the applied field completely and hence, the superstructure reflection is strongest for the ground-state of the system, which leads to the assumption that also the bond-angle variation is strongest for this LF-C phase. The intensity sharply decreases when the temperature is raised above the transition to the incommensurate LF-IC* phase recovering its initial value, which limits the presence of the structural distortion precisely to the commensurate phases. Qualitatively identical behavior is observed for the superstructure reflection $Q = (4\;0\;1)$ (see Fig. 4).

B. Quantitative determination of the dimerization in NaFe(WO$_4$)$_2$

For a structural refinement and hence the quantitative analysis of the structural distortion, we collected a set of integrated intensities in the dimerized phase on the D10 diffractometer. As the superstructure signal is strongest within the LF-C phase, see Figs. 3 and 4, a structural refinement seems to be most promising to execute within this commensurate phase in zero field. Moreover the data collection in zero field avoids an additional signal contribution from field-induced moments to allowed main reflections. However, the application of a magnetic field was still necessary to drive the system to the LF-C phase.

Before we collected respective superstructure reflections, we measured (with a microstrip detector and without additional analyzer) 108 unique allowed nuclear reflections of which 56 are independent within the LF-IC phase to refine the isotropic extinction coefficient. The refinement was done by using the software JANA [39], which utilizes the Becker-Coppens formalism for the extinction correction. For the corresponding refinement we used the structural parameters that were obtained by Holbein *et al.* [21]. Hereafter we measured with a single He^3 detector and with the analyzer option to improve the intensity over background ratio. To obtain the appropriate scaling factor for the refinement of the superstructure, we measured 13 unique allowed reflections, of which 7 are independent at $T \approx 2\,\mathrm{K}$ and $\mu_0 H = 0\,\mathrm{T}$.

It was already discussed that the intensity of superstructure peaks superposes the multiple scattering signal and the tiny $\lambda/2$-contamination and thus, it was necessary to measure the respective superstructure reflections inside and outside the commensurate phases to extract the integrated intensity that is purely originating from the structural distortion. Hence, we measured these superstructure reflections in the LF-C phase at $T \approx 2\,\mathrm{K}$, $\mu_0 H = 0\,T$, as well as in the LF-IC phase (also at $T \approx 2\,\mathrm{K}$, $\mu_0 H = 0\,\mathrm{T}$). This procedure and the weak signal itself limit the number of collectible reflections and we were able to collect 26 superstructure reflections of which 24 are independent. The required vertical cryomagnet with its magnetic field along b and the analyzer option prevented the collection of reflections with a nonzero k-component and thus the structural refinement will only testify a structural distortion within the ac-plane.

The left part of Table I contains the structural parameters that have been refined by Holbein *et al.* in the paramagnetic phase [21]. All Fe ions are surrounded by edge sharing oxygen octahedra, and when considering the $P2/c$ spacegroup, all oxygen ions along the Fe chain are generated from the general site O2. The distance between two O2's belonging to the same edge alternate in the dimerized phase resulting in alternating enhancement and reduction of the Fe-O2-Fe bond angle and thus in an alternation of the magnetic exchange energy. In the simple picture neglecting ligands, a ferromagnetic arrangement prefers a 90° Fe-O-Fe bond-angle, whereas an antiferromagnetic bond requires the bond angle to approach 180°. Both O2 ions on the same edge are connected through

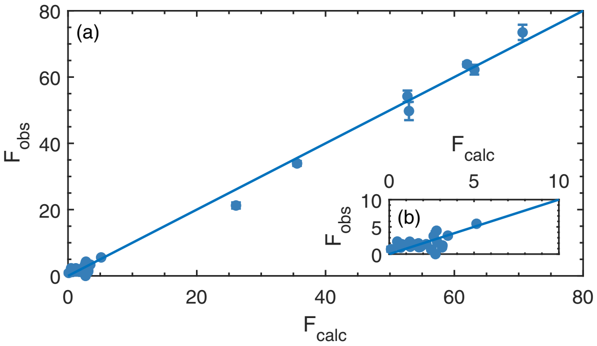

FIG. 5. The observed structure factors are plotted against the calculated ones for the final refinement of the structural dimerization within the LF-C phase.

inversion symmetry, and as they elongate or shorten their distance uniformly, the inversion symmetry is preserved in a dimerized state. However, an alternating exchange interaction along the chain and the corresponding bond-angle modulation violate the two-fold axis and the glide mirror symmetry giving rise to the observed superstructure reflections. Thus, the refinement of the superstructure within the LF-C phase was done by considering a transition from spacegroup $P2/c$ to $P\bar{1}$. The middle part of Table I displays the structural parameters transformed from $P2/c$ to $P\bar{1}$ setting and the right part the refined distortion in the lower symmetry.

The transformation to spacegroup $P\bar{1}$ splits the site of O2 in P2/c into the two independent sites O2a and O2b. The Fe-O-Fe bonding along the chains passes alternatingly through O2a-O2a and O2b-O2b edges. In the refinements we kept the average O2 position fixed and allowed only for alternating O2 shifts. To further reduce the number of variables, equivalent constraints have been also stated for the W1 and W2 positions. Six variables have been refined. The right part of Table I contains the refined parameters of the $P\bar{1}$ structure within the LF-C phase. For the refinement, the isotropic B parameters have been adopted from Ref. [21]. At first glance, the obtained R-values (see Table I) may appear large but one has to keep in mind that only very weak superstructure reflections (almost four orders of magnitude weaker than strong fundamental Bragg peaks) intervene in these refinements. In Fig. 5 we plot the observed structure factors against the calculated ones documenting the reliability of this analysis. The O2a and O2b sites are shifting significantly in opposite directions by 0.0195(32) Å. The Fe ions are only moving along z by 0.0093(31) Å and the position of W1 and W2 is also shifting because of their bonding to the O2a and O2b sites. Within the commensurate LF-C phase, the calculated bond angles amount $\alpha_1 = 97.20(14)^\circ$ for the Fe-O2a-Fe bond and $\alpha_2 = 99.49(14)^\circ$ for the Fe-O2b-Fe bond, whereas the bond angle outside the commensurate phase amounts $\alpha = \alpha_1 = \alpha_2 = 98.35(7)^\circ$ [21]. Hence, a bond-angle variation of $\approx \pm 1.15(16)^\circ$ can be observed, when entering the commensurate *uudd* phase. This modulation includes the shift of oxygen and iron ions within the *ac*-plane. A respective shift along b cannot be studied with the chosen scattering geometry.

The implication of the bond angle, ϕ, on the magnetic exchange interaction was intensively studied for $RMeO_3$ with $Me =$ Fe and Mn finding a $\sin^4(\phi/2)$ relation [40,41]. This strong bond-angle dependence of the magnetic interaction drives the magnetoelectric coupling in E-type RMnO$_3$ [15,16] and causes the dynamic magnetoelectric coupling and the strongest electromagnon modes in chiral RMnO$_3$ [42]. However, this $\sin^4(\phi/2)$ relation applies to a bond angle, which is not too far below 180° , while the O-Fe-O angles in NaFe(WO$_4$)$_2$ amount to 97.2 and 99.5 degrees. Therefore, the arrangement more closely resembles the dimerization in the spin-Peierls compound CuGeO$_3$, in which a bond-angle alternation of only $\pm 0.5^\circ$ around the average value of $\sim 99^\circ$ results in a sizable variation of the magnetic exchange by ± 20 percent [43]. Unfortunately, the magnetic exchange parameters in NaFe(WO$_4$)$_2$ are not known. For MnWO$_4$ the nearest-neighbor intrachain is not dominating and several parameters are of the order of 0.3 to 0.4 meV [44,45] explaining the considerable frustration. The antiferromagnetic Curie-Weiss temperature in NaFe(WO$_4$)$_2$ amounts to -8.5 K (compared to -75 K for MnWO$_4$ [45]), which transforms to a nearest-neighbor intrachain interaction of only 0.06 meV when neglecting all other interactions. NaFe(WO$_4$)$_2$ seems to be less frustrated with a ratio of Néel and Weiss temperatures of only ~ 2, but the next-nearest-neighbor interaction along the chains will stabilize the *uudd* magnetic order. Since the magnetic interaction in NaFe(WO$_4$)$_2$ is quite weak the relative change induced by the sizable structural dimerization through the bond-angle alternation is expected to be rather strong.

The strong reduction of the b lattice parameter upon entering the commensurate magnetic order in NaFe(WO$_4$)$_2$ [21] is not contributing to the dimerization, which can be considered as the primary order parameter of the structural distortion. Note that the strain does not break the glide mirror symmetry. Since both distortions correspond to zone-center phonon modes, one would expect a bilinear coupling, but the coupling with the magnetism renders the analysis more complex. The commensurate magnetic order clearly is the primary order parameter and both structural distortions, dimerization, and strain along b, are coupled to it. The dimerization modulates the nearest-neighbor interaction, thereby rendering the *uudd* structure more favorable. The strain along b acts on the ratio between nearest and next-nearest neighbor interaction. One expects an enhanced second-nearest neighbor interaction for smaller b, which again will favor the commensurate *uudd* order. Since the two types of distortion act differently, one can understand their different relative strengths in NaFe(WO$_4$)$_2$ and MnWO$_4$.

C. Structural dimerization in MnWO$_4$

MnWO$_4$ crystallizes in the monoclinic spacegroup $P2/c$ with $a \approx 4.823$ Å, $b \approx 5.753$ Å, $c \approx 4.992$ Å, and $\beta \approx 91.08^\circ$ (at 1.5 K) [20]. Within the bc-plane, magnetic Mn^{2+} ions are forming edge-sharing [MnO$_6$] octahedra chains along c and those layers, containing the chains are separated along the a direction by nonmagnetic [WO$_6$]-octahedra chains [46]. The crystallographic unit cell of the parent wolframite structure is bisected along a with respect to the structure of

NaFe(WO$_4$)$_2$ due to the missing [NaO$_6$]-layer. Similar to NaFe(WO$_4$)$_2$, the system exhibits also a sequence of magnetic phases with competing commensurate and incommensurate ordering [18,20]. First, below $T_{N3} \approx 13.5$ K an incommensurate modulated spin-density wave with $\boldsymbol{k} = (-0.214, \frac{1}{2}, 0.457)$ emerges (AF3-phase). The magnetic moments point along the easy direction, which lies within the *ac*-plane and forms an angle of about ≈35.5° with the *a*-direction. In this configuration, the magnetic moments cannot saturate and thus due to entropy reasons a spiral with an additional component along the *b*-direction develops at $T_{N2} \approx 12.3$ K but the modulation remains incommensurate (AF2-phase) [18,20]. The spiral arrangements allows for the occurrence of a ferroelectric polarization following DMI and indeed, it was possible to measure an electric polarization along *b*, which is fully switchable by external electric fields [31,32]. The polarization is small but sizable ($P \approx 60\ \mu\text{cm}^{-2}$) and its existence is limited to the spiral phase AF2 [29,47]. However, due to single ion anisotropy the system preferably aligns along its easy direction, which provokes the transition to a commensurate *uudd* arrangement with $\boldsymbol{k} = (-\frac{1}{4}, \frac{1}{2}, \frac{1}{2})$ at $T_{N1} \approx 7.5$ K [18,20].

As in NaFe(WO$_4$)$_2$, the transition to the commensurate phase is of first order and accompanied by a thermal expansion anomaly. It is expected that a structural distortion is here also caused by a bond-angle modulation due to the alternating ferro- and antiferromagnetic exchange interaction along the magnetic Mn^{2+} chain. The observed thermal expansion anomaly in MnWO$_4$ is one order of magnitude smaller compared to NaFe(WO$_4$)$_2$ but its commensurate phase is accessible without the application of a magnetic field. The symmetry consideration from NaFe(WO$_4$)$_2$ can be adopted to MnWO$_4$ and it becomes obvious that corresponding superstructure reflections occur at $Q = (h + \frac{1}{2}\ 0\ l)$ with l = odd for MnWO$_4$. X-ray measurements have already qualitatively confirmed the presence of a respective signal in the context of second harmonic order reflections within the AF1 phase [25].

Neutron scattering experiments were performed on the cold triple-axis spectrometer 4F2, where we first executed longitudinal scans over the Q-space position of the superstructure reflection $Q = (1.5\ 0\ 1)$ for different temperatures. At these noninteger positions no multiple scattering can contribute to the signal. From the measured data, which is displayed in Fig. 6(a) it can be clearly stated that at the transition to the low-lying commensurate phase, a superstructure reflection evolves. We measured the peak intensity, while lowering the temperature from above T_{N1} to far below the transition of the commensurate phase [see Fig. 6(b)]. This temperature-dependent sweep demonstrates that the superstructure reflection is exactly evolving, when passing the later-mentioned transition. Hence, also in MnWO$_4$ the occurrence of the commensurate *uudd* arrangement coincides with an evolving superstructure. In view of the equivalent behavior in NaFe(WO$_4$)$_2$, we conclude that also in MnWO$_4$ a bond-angle modulation is coupled to the onset of commensurate *uudd* ordering. Comparing the intensities of superstructure reflections $Q = (2h\ 0\ l)$ for NaFe(WO$_4$)$_2$ and $Q = (h\ 0\ l)$ for MnWO$_4$ ($h = 1.5$) with respect to the particular strongest allowed reflections ($Q = (0\ 2\ 3)$ [48] in NaFe(WO$_4$)$_2$ and $Q = (1\ 0\ 0)$ in MnWO$_4$) results in almost equal ratios of a few 10^{-4}. This indicates a bond-angle modulation of the same order of magnitude in the two systems.

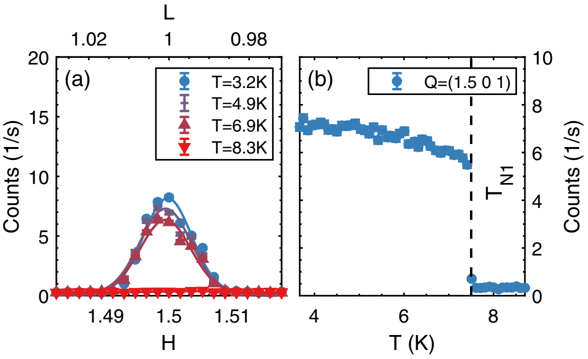

FIG. 6. MnWO$_4$: Panel (a) shows the longitudinal scans over $Q = (H\ 0\ L)$ for four different temperatures. The measured peak intensity for $Q = (1.5\ 0\ 1)$ is displayed in panel (b) as a function of temperature.

Locally, the commensurate *uudd* structure can also evolve within the multiferroic phase and it was proposed for NaFe(WO$_4$)$_2$ that an anharmonic modulation of the incommensurate structure within its incommensurate LF-IC phase corresponds to tiny fragments of commensurate order [21] that are regularly arranged. This assumption is supported by the occurrence of third-order reflections, which signal a squaring up of the cycloid [21].

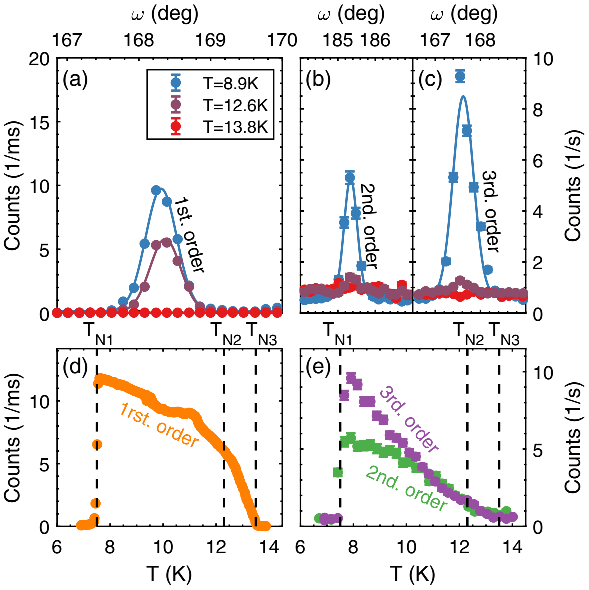

FIG. 7. MnWO$_4$: Panels (a), (b), and (c) present rocking scans over the first [$Q = (-0.214\ \frac{1}{2}\ 0.457)$], second [$Q = (-0.428\ 1\ 0.914)$], and third harmonic reflection [$Q = (-0.642\ \frac{1}{2}\ 1.371)$] for different temperatures. The respective temperature dependence of the peak intensities is shown in (d) and (e).

Figures 7(a) to 7(c) presents rocking scans of the higher harmonic reflections as a function temperature for $MnWO_4$. In Figs. 7(d) and 7(e), the peak intensity is plotted as a function of temperature. The temperature dependence of the first- and of the second-order reflections resembles reported measurements [23], but the occurrence of a third-order reflection has not been reported so far. Fig. 7(e) displays the temperature dependence of the measured peak intensity of the third order reflection $Q = (-0.642\ \frac{1}{2}\ 1.371)$. At low temperatures this reflection becomes even stronger than the second-order reflection and its existence is not limited to the multiferroic phase but a finite signal persists in the AF3 phase. While the second-order intensity clearly follows the intensity of the main magnetic peak, the third-order reflection exhibits a different temperature dependence. The first- and second-order peaks tend to saturate towards the lower temperature limit of the multiferroic AF2 phase, but the growth of the third-order peak continuously increases showing a negative second temperature derivative. This strongly resembles the behavior in $NaFe(WO_4)_2$ [21] and this diverging third-order peak must be considered as a precursor of the phase transition into the commensurate *uudd* phase. Tiny commensurate fragments with the corresponding discommensurations strongly increase upon cooling towards the low-temperature limit of the AF2 phase. These perturbations of the harmonic multiferroic magnetic structure can explain the depinning of multiferroic ordering reported in the various studies on the dynamics of multiferroic domains [31,32,49].

IV. SUMMARY AND CONCLUSION

We present a comprehensive study of a dimerization effect in $NaFe(WO_4)_2$ and $MnWO_4$. It was possible to qualitatively observe the existence of superstructure reflections documenting the loss of symmetry, when entering the respective commensurate magnetic phases of both materials. This loss of symmetry is connected to a bond-angle modulation along the magnetic zigzag chains due to the alternating ferromagnetic and antiferromagnetic arrangement in the respective commensurate *uudd* phases. For $NaFe(WO_4)_2$ a bond-angle modulation is present in the HF-C as well as in the LF-C phase and it turned out that the dimerization effect is strongest for the commensurate phase in zero field. In this phase, a structural refinement of neutron data yields a bond-angle modulation of $\approx \pm 1.15(16)^\circ$ but it has to be noted that this specified bond-angle modulation does not include a possible modulation along the b-direction, as the chosen scattering plane and the utilized cryomagnet and analyzer prevented the collection of reflections with a finite k-component.

Also for $MnWO_4$, a structural dimerization of comparable size was detected by the appearance of superstructure reflections in its commensurate phase. Moreover, strong harmonic third-order reflections were observed within the multiferroic phase that perfectly correspond to the anharmonic modulation reported for $NaFe(WO_4)_2$ [21]. The emerging third-order reflection is connected to a squaring up of the magnetic ordering and indicates the presence of small commensurate fragments already in the incommensurate and multiferroic phase. As the magnetic arrangement of $MnWO_4$ already starts to resemble the *uudd* arrangement within the incommensurate spiral phase, it can lead to depinning of the multiferroic domains and of the corresponding domain walls. The pinning of the multiferroic domains bases on the harmonic modulation, which causes the ferroelectric polarization through the inverse DMI. Therefore, the anomalous speeding up of the multiferroic domain inversion can be attributed to the emergence of the anharmonic modulations. Such effects can even be beneficial for the application of multiferroics.

Single-crystal neutron diffraction data from the D10 diffractometer are available [50].

ACKNOWLEDGMENTS

This work was funded by the Deutsche Forschungsgemeinschaft (DFG, German Research Foundation), Project No. 277146847, CRC 1238, projects A02 and B04.

---

[1] T. Kimura, T. Goto, H. Shintani, K. Ishizaka, T. Arima, and Y. Tokura, Magnetic control of ferroelectric polarization, Nature **426**, 55 (2003).

[2] J. Wang, J. B. Neaton, H. Zheng, V. Nagarajan, S. B. Ogale, B. Liu, D. Viehland, V. Vaithyanathan, D. G. Schlom, U. V. Waghmare, N. A. Spaldin, K. M. Rabe, M. Wuttig, and R. Ramesh, Epitaxial $BiFeO_3$ multiferroic thin film heterostructures, Science **299**, 1719 (2003).

[3] M. Fiebig, Revival of the magnetoelectric effect, J. Phys. D. Appl. Phys. **38**, R123 (2005).

[4] D. Khomskii, Classifying multiferroics: Mechanisms and effects, Physics **2**, 20 (2009).

[5] M. Fiebig, T. Lottermoser, D. Meier, and M. Trassin, The evolution of multiferroics, Nat. Rev. Mater. **1**, 16046 (2016).

[6] N. A. Spaldin and R. Ramesh, Advances in magnetoelectric multiferroics, Nat. Mater. **18**, 203 (2019).

[7] Y. Tokura, S. Seki, and N. Nagaosa, Multiferroics of spin origin, Rep. Prog. Phys. **77**, 076501 (2014).

[8] S. Lee, M. T. Fernandez-Diaz, H. Kimura, Y. Noda, D. T. Adroja, S. Lee, J. Park, V. Kiryukhin, S.-W. Cheong, M. Mostovoy, and J.-G. Park, Negative magnetostrictive magnetoelectric coupling of $BiFeO_3$, Phys. Rev. B **88**, 060103(R) (2013).

[9] I. E. Dzyaloshinskii, A thermodynamic theory of “weak” ferromagnetism of antiferromagnetics, J. Phys. Chem. Solids **4**, 241 (1958).

[10] T. Moriya, Anisotropic Superexchange Interaction and Weak Ferromagnetism, Phys. Rev. **120**, 91 (1960).

[11] H. Katsura, N. Nagaosa, and A. V. Balatsky, Spin Current and Magnetoelectric Effect in Noncollinear Magnets, Phys. Rev. Lett. **95**, 057205 (2005).

[12] M. Mostovoy, Ferroelectricity in Spiral Magnets, Phys. Rev. Lett. **96**, 067601 (2006).

[13] I. A. Sergienko and E. Dagotto, Role of the Dzyaloshinskii-Moriya interaction in multiferroic perovskites, Phys. Rev. B - Condens. Matter Mater. Phys. **73**, 094434 (2006).

[14] T. Kimura, Spiral Magnets as Magnetoelectrics, Annu. Rev. Mater. Res. **37**, 387 (2007).

[15] I. A. Sergienko, C. Şen, and E. Dagotto, Ferroelectricity in the Magnetic E -Phase of Orthorhombic Perovskites, Phys. Rev. Lett. **97**, 227204 (2006).

[16] S. Ishiwata, Y. Kaneko, Y. Tokunaga, Y. Taguchi, T.-H. Arima, and Y. Tokura, Perovskite manganites hosting versatile multiferroic phases with symmetric and antisymmetric exchange strictions, Phys. Rev. B **81**, 100411(R) (2010).

[17] T. Kimura, G. Lawes, T. Goto, Y. Tokura, and A. P. Ramirez, Magnetoelectric phase diagrams of orthorhombic $R\mathrm{MnO}_3$ ($R =$ Gd, Tb, and Dy), Phys. Rev. B **71**, 224425 (2005).

[18] H. Ehrenberg, H. Weitzel, C. Heid, H. Fuess, G. Wltschek, T. Kroener, J. van Tol, and M. Bonnet, Magnetic phase diagrams of MnWO_4, J. Phys. Condens. Matter **9**, 3189 (1997).

[19] O. Heyer, N. Hollmann, I. Klassen, S. Jodlauk, L. Bohatý, P. Becker, J. A. Mydosh, T. Lorenz, and D. Khomskii, A new multiferroic material: MnWO_4, J. Phys. Condens. Matter **18**, L471 (2006).

[20] G. Lautenschläger, H. Weitzel, T. Vogt, R. Hock, A. Böhm, M. Bonnet, and H. Fuess, Magnetic phase transitions of MnWO_4 studied by the use of neutron diffraction, Phys. Rev. B **48**, 6087 (1993).

[21] S. Holbein, M. Ackermann, L. Chapon, P. Steffens, A. Gukasov, A. Sazonov, O. Breunig, Y. Sanders, P. Becker, L. Bohatý, T. Lorenz, and M. Braden, Strong magnetoelastic coupling at the transition from harmonic to anharmonic order in $\mathrm{NaFe(WO_4)_2}$ with $3d^5$ configuration, Phys. Rev. B **94**, 104423 (2016).

[22] R. P. Chaudhury, F. Yen, C. R. dela Cruz, B. Lorenz, Y. Q. Wang, Y. Y. Sun, and C. W. Chu, Thermal expansion and pressure effect in MnWO_4, Phys. B Condens. Matter **403**, 1428 (2008).

[23] T. Finger, D. Senff, K. Schmalzl, W. Schmidt, L. P. Regnault, P. Becker, L. Bohatý, and M. Braden, Polarized-neutron-scattering studies on the chiral magnetism in multiferroic MnWO_4, J. Phys. Conf. Ser. **211**, 012001 (2010).

[24] T. Finger, D. Senff, K. Schmalzl, W. Schmidt, L. P. Regnault, P. Becker, L. Bohatý, and M. Braden, Electric-field control of the chiral magnetism of multiferroic MnWO_4 as seen via polarized neutron diffraction, Phys. Rev. B - Condens. Matter Mater. Phys. **81**, 1 (2010).

[25] K. Taniguchi, N. Abe, H. Sagayama, S. Otani, T. Takenobu, Y. Iwasa, and T. Arima, Magnetic-field dependence of the ferroelectric polarization and spin-lattice coupling in multiferroic MnWO_4, Phys. Rev. B **77**, 064408 (2008).

[26] J. F. Scott, Multiferroic memories, Nat. Mater. **6**, 256 (2007).

[27] M. Bibes and A. Barthélémy, Multiferroics: Towards a magnetoelectric memory, Nat. Mater. **7**, 425 (2008).

[28] J. Zhai, Z. Xing, S. Dong, J. Li, and D. Viehland, Detection of pico-Tesla magnetic fields using magneto-electric sensors at room temperature, Appl. Phys. Lett. **88**, 062510 (2006).

[29] A. H. Arkenbout, T. T. Palstra, T. Siegrist, and T. Kimura, Ferroelectricity in the cycloidal spiral magnetic phase of MnWO_4, Phys. Rev. B **74**, 184431 (2006).

[30] D. Meier, M. Maringer, T. Lottermoser, P. Becker, L. Bohatý, and M. Fiebig, Observation and Coupling of Domains in a Spin-Spiral Multiferroic, Phys. Rev. Lett. **102**, 107202 (2009).

[31] D. Niermann, C. P. Grams, M. Schalenbach, P. Becker, L. Bohatý, J. Stein, M. Braden, and J. Hemberger, Domain dynamics in the multiferroic phase of MnWO_4, Phys. Rev. B **89**, 134412 (2014).

[32] M. Baum, J. Leist, T. Finger, K. Schmalzl, A. Hiess, L. P. Regnault, P. Becker, L. Bohatý, G. Eckold, and M. Braden, Kinetics of the multiferroic switching in MnWO_4, Phys. Rev. B **89**, 144406 (2014).

[33] J. Stein, M. Baum, S. Holbein, T. Cronert, V. Hutanu, A. C. Komarek, and M. Braden, Control of multiferroic domains by external electric fields in TbMnO_3, J. Phys. Condens. Matter **27**, 446001 (2015).

[34] J. Stein, M. Baum, S. Holbein, T. Finger, T. Cronert, C. Tölzer, T. Fröhlich, S. Biesenkamp, K. Schmalzl, P. Steffens, C. H. Lee, and M. Braden, Control of Chiral Magnetism Through Electric Fields in Multiferroic Compounds above the Long-Range Multiferroic Transition, Phys. Rev. Lett. **119**, 177201 (2017).

[35] T. Hoffmann, P. Thielen, P. Becker, L. Bohatý, and M. Fiebig, Time-resolved imaging of magnetoelectric switching in multiferroic MnWO_4, Phys. Rev. B **84**, 184404 (2011).

[36] P. V. Klevtsov and R. F. Klevtsova, Single-crystal synthesis and investigation of the double tungstates $\mathrm{NaR^{3+}(WO_4)_2}$, where $\mathrm{R}^{3+} =$ Fe, Sc, Ga, and In, J. Solid State Chem. **2**, 278 (1970).

[37] A superstructure is commonly connected to a loss of translational symmetry while here only a glide-mirror plane is broken. However, we will use the notation of a superstructure reflection also for the reflections $(h\,0\,l)$ with l odd that are systematically absent in space group $P2/c$ due to the c-glide plane.

[38] We note that due to the usage of the vertical cryomagnet, it was not possible to modify the signal strength of multiple scattering by Renninger scans.

[39] V. Petříček, M. Dušek, and L. Palatinus, Crystallographic computing system JANA2006: General features, Z. Kristallogr. **229**, 345 (2014).

[40] J.-S. Zhou and J. B. Goodenough, Intrinsic structural distortion in orthorhombic perovskite oxides, Phys. Rev. B **77**, 132104 (2008).

[41] S. Dong, R. Yu, S. Yunoki, J.-M. Liu, and E. Dagotto, Origin of multiferroic spiral spin order in the $r\mathrm{mno}_3$ perovskites, Phys. Rev. B **78**, 155121 (2008).

[42] R. Valdés Aguilar, M. Mostovoy, A. B. Sushkov, C. L. Zhang, Y. J. Choi, S.-W. Cheong, and H. D. Drew, Origin of Electromagnon Excitations in Multiferroic $R\mathrm{MnO}_3$, Phys. Rev. Lett. **102**, 047203 (2009).

[43] M. Braden, G. Wilkendorf, J. Lorenzana, M. Aïn, G. J. McIntyre, M. Behruzi, G. Heger, G. Dhalenne, and A. Revcolevschi, Structural analysis of CuGeO_3: Relation between nuclear structure and magnetic interaction, Phys. Rev. B **54**, 1105 (1996).

[44] F. Ye, R. S. Fishman, J. A. Fernandez-Baca, A. A. Podlesnyak, G. Ehlers, H. A. Mook, Y. Wang, B. Lorenz, and C. W. Chu, Long-range magnetic interactions in the multiferroic antiferromagnet MnWO_4, Phys. Rev. B **83**, 140401(R) (2011).

[45] C. Tian, C. Lee, H. Xiang, Y. Zhang, C. Payen, S. Jobic, and M.-H. Whangbo, Magnetic structure and ferroelectric polarization of MnWO_4 investigated by density functional calculations and classical spin analysis, Phys. Rev. B **80**, 104426 (2009).

[46] H. Weitzel, Kristallstrukturverfeinerung von wolframiten und columbiten, Z. Kristallogr **144**, 238 (1976).

[47] K. Taniguchi, N. Abe, T. Takenobu, Y. Iwasa, and T. Arima, Ferroelectric Polarization Flop in a Frustrated Magnet $MnWO_4$ Induced by a Magnetic Field, Phys. Rev. Lett. **97**, 097203 (2006).

[48] The reflection $Q = (0\ 2\ 3)$ was not measurable due to the chosen scattering geometry, however, the respective intensity can be calculated by comparing absolute square values of structure factors with the intensity of both measured and nonmeasured reflections.

[49] Note that the speeding up of domain inversion when approaching the commensurate phases was also observed on large crystals presenting an average of domains.

[50] Data are available at S. Biesenkamp, M. Braden, S. Holbein, and, N. Qureshi, dataset for “Dimerization in the commensurate antiferromagnetic phase of $NaFe(WO_4)_2$”, doi: 10.5291/ILL-DATA.5-41-911, 2017 and S. Biesenkamp, M. Braden, T. Fröhlich, and N. Qureshi, dataset for “Structural refinement of the dimerization in $NaFe(WO_4)_2$”, doi: 10.5291/ILL-DATA.5-41-983, 2018.

4. Single-crystal investigations on the multiferroic material LiFe(WO_4)$_2$

It was discussed in Ref. [1] (see also last chapter) that a simple relaxation behavior of multiferroic domains necessitates a simple phase diagram without interfering commensurate ordering. For the further investigation of multiferroic domain dynamics it is thus desirable to conduct respective experiments on samples that do possess a simple sequence of magnetic phases without interfering commensurate ordering or other perturbative effects that can impact a simple activation behavior. In that case it is possible to study further general details of multiferroic switching i.e. the limiting process for the inversion time, the determining factor of the activation constant, or eventually also the potential occurrence of quantum fluctuation driven domain-wall tunneling.

Recently, Liu *et al.* [104] reported a spiral driven multiferroic phase in the double-tungstate system LiFe(WO_4)$_2$, which is thus beside MnWO_4 [95] only the second multiferroic compound in the family of tungstates. The nuclear structure is closely related to MnWO_4 [91,92], but magnetic zig-zag chains in LiFe(WO_4)$_2$ are not solely occupied by a single magnetic ion [104–106]. In LiFe(WO_4)$_2$ both, non-magnetic Li atoms and magnetic Fe ions are alternating in the same zig-zag chains, which are propagating along c-direction. Comparable to MnWO_4, these magnetic layers are separated by nonmagnetic tungsten layers along the a-direction, which however contrasts the situation in NaFe(WO_4)$_2$ [99], for which magnetic chains are separated by two layers that are respectively occupied by Na ions and W atoms. The material LiFe(WO_4)$_2$ can be seen as a J_1,J_2 chain system, which nevertheless exhibits more extended, but finite interactions that lead to three-dimensional long-range ordering. Liu *et al.* presented investigations of the nuclear and magnetic structure, which revealed a simple sequence of two magnetic phases in LiFe(WO_4)$_2$ [104]. From their neutron powder diffraction (NPD) results, they proposed that the system first develops short-range ordering below the first magnetic transition at $T_\mathrm{N} = 21.6\,\mathrm{K}$ and below the second transition at $T_\mathrm{MF} = 19.7\,\mathrm{K}$ an incommensurate long-range spiral magnetic structure is reported. This lower phase was identified to be multiferroic and by utilizing density functional theory (DFT) calculations, it was claimed that the measured ferroelectric polarization ($\mathbf{P} \approx 15\,\mu\mathrm{C\,m^{-2}}$) is directed along b direction. As no lower transition to commensurate ordering was reported, the system promotes itself to be an ideal candidate for studies on the multiferroic domain kinetics. However, the published results on the nuclear and magnetic structure were all based on measurements on polycrystalline samples [104]. In particular, for complex spiral magnetic structures this method is not sufficient to fully characterize the structure, which thus promoted the respective investigation by single-crystal neutron diffraction. Moreover, it is astonishing that the system directly transforms from short-range ordering to a long-range ordered spiral structure without exhibiting an intermediate phase. Commonly, the transition to a multiferroic spiral type-II phase is preceded by a long-range ordered intermediate phase [46, 107, 108]. Both, the necessity for an accurate description of the magnetic spiral and the characterization of the intermediate phase proposed further studies.

As single crystals were available during the course of this thesis, it highly motivated the respective single-crystal investigation of the temperature-dependent nuclear and magnetic structure for a thorough characterization of the magnetic phase diagram of $\mathrm{LiFe(WO_4)_2}$. For this purpose, X-ray diffraction, specific heat, susceptibility, unpolarized and polarized neutron diffraction experiments were conducted and their results were published in the publication

> S. Biesenkamp, D. Gorkov, D. Brüning, A. Bertin, T. Fröhlich, X. Fabrèges, A. Gukasov, M. Meven, P. Becker, L. Bohatý, T. Lorenz, and M. Braden, *Single-crystal investigations on the multiferroic material* $\mathit{LiFe(WO_4)_2}$, Phys. Rev. B **103**, 134412 (2021),

which is included into this thesis (see following pages). With unpolarized and polarized neutron diffraction it was possible to precisely characterize both magnetic phases. Indeed, it was observed that no short-range ordering but long-range ordering in form of a spin-density wave (SDW) develops below the Néel temperature. This SDW phase is followed by a multiferroic phase with incommensurate spiral ordering. The longitudinal neutron polarization analysis further revealed that this lower phase develops an unbalanced chiral domain distribution even in the absence of applied external electric-fields. Unfortunately, all samples exhibited finite conductivity even at low temperature, wherefore the application of fields and thus the investigation of multiferroic switching was prohibited at least for these samples. Nevertheless, the published results thoroughly characterized the temperature and magnetic-field dependent magnetic phase diagram of $\mathrm{LiFe(WO_4)_2}$ and evidenced its simplicity, which is desirable for studies on the relaxation behavior. Thus, it motivates further experiments on this system, especially, when highly isolating samples are available and allow for the application of electric fields and hence the investigation of multiferroic switching in $\mathrm{LiFe(WO_4)_2}$.

Contribution to the embedded publication

The publication includes the data of several neutron beamtimes, which were conducted at the neutron scattering facilities LLB and FRMII. A neutron scattering experiment at the 6T2 diffractometer (LLB) was performed by the author of this thesis and supported by the local contacts A. Gukasov and X. Fabrèges. A second neutron scattering experiment at the four-circle diffractometer HEiDi (FRMII) was also conducted by the author of this thesis and supported by the local contact M. Meven. In addition to these unpolarized neutron diffraction investigations, a polarized neutron scattering experiment was conducted by D. Gorkov and M. Braden at the cold three axes spectrometer KOMPASS (FRMII). The analysis of all recorded neutron data were done by the author of this thesis. The magnetic-field dependent specific-heat measurements were performed and analyzed by D. Brüning under supervision of T. Lorenz. For a further characterization of the magnetic phase diagram, susceptibility measurements were conducted by the author of this thesis and supported by S. Heijligen. The temperature dependent structural investigation was done by X-ray measurements, which were performed by the author of this thesis, and the labor-intensive low-temperature X-ray experiments were supported by T. Fröhlich and A. Bertin. Except for the specific heat experiment, all recorded data were analyzed by the author of this thesis. All samples were grown and provided by P. Becker and L. Bohatý. The figures that are shown in the embedded publication were all created by the author of this thesis. The first draft of the paper manuscript was written by him and its completion was done in cooperation with M. Braden. All named co-authors proofread and corrected the manuscript. The whole project was supervised by M. Braden.

PHYSICAL REVIEW B **103**, 134412 (2021)

Single-crystal investigations on the multiferroic material LiFe(WO_4)$_2$

S. Biesenkamp,[1,*] D. Gorkov,[1,2] D. Brüning,[1] A. Bertin,[1] T. Fröhlich,[1] X. Fabrèges,[3] A. Gukasov,[3] M. Meven,[4,5]
P. Becker,[6] L. Bohatý,[6] T. Lorenz,[1] and M. Braden[1,†]
[1]*II. Physikalisches Institut, Universität zu Köln, Zülpicher Straße 77, D-50937 Köln, Germany*
[2]*Heinz Maier-Leibnitz Zentrum (MLZ), Technische Universität München, Lichtenbergstr. 1, 85748 Garching, Germany*
[3]*Laboratoire Léon Brillouin, CEA/CNRS, F-91191 Gif-sur-Yvette Cedex, France*
[4]*Institut für Kristallographie, RWTH Aachen University, D-52056 Aachen, Germany*
[5]*Jülich Centre for Neutron Science, Heinz Maier-Leibnitz Zentrum, D-85747 Garching, Germany*
[6]*Abteilung Kristallographie, Institut für Geologie und Mineralogie, Universität zu Köln, Zülpicher Straße 49b, D-50674 Köln, Germany*

(Received 23 November 2020; accepted 25 March 2021; published 8 April 2021)

The crystal and magnetic structures of multiferroic LiFe(WO_4)$_2$ were investigated by temperature and magnetic-field-dependent specific heat, susceptibility, and neutron diffraction experiments on single crystals. Considering only the two nearest-neighbor magnetic interactions, the system forms a J_1, J_2 magnetic chain, but more extended interactions are sizable. Two different magnetic phases exhibiting long-range incommensurate order evolve at $T_{N1} \approx 22.2$ K and $T_{N2} \approx 19$ K. First, a spin-density wave develops with moments lying in the *ac* plane. In its multiferroic phase below T_{N2}, LiFe(WO_4)$_2$ exhibits a spiral arrangement with an additional spin component along *b*. Therefore, the inverse Dzyaloshinskii-Moriya mechanism fully explains the multiferroic behavior in this material. A partially unbalanced multiferroic domain distribution was observed even in the absence of an applied electric field. For both phases only a slight temperature dependence of the incommensurability was observed, and there is no commensurate phase emerging at low temperature or at finite magnetic fields up to 6 T. LiFe(WO_4)$_2$ thus exhibits a simple phase diagram with the typical sequence of transitions for a type-II multiferroic material.

DOI: 10.1103/PhysRevB.103.134412

I. INTRODUCTION

The demand for memory devices with larger storage capacity and lower power consumption pushed the research on multiferroic materials featuring the coupling of magnetic ordering and ferroelectric polarization in the same phase (so-called type-II multiferroics) [1–3]. Over the past few decades a variety of multiferroic systems were discovered, and several different microscopic mechanisms were identified to induce multiferroicity in respective materials [4,5]. Besides symmetric exchange striction, the inverse Dzyaloshinskii-Moriya interaction (DMI) is a frequent mechanism that drives the multiferroic behavior in many type-II multiferroics [6–9]. With this mechanism, a spiral spin canting of neighboring spins induces a shift of nonmagnetic ligand ions and thus a ferroelectric polarization that can be controlled by external electric and magnetic fields. The spiral handedness (or, precisely, the vector chirality) determines the sign of the ferroelectric polarization.

Many multiferroic materials exhibit additional phase transitions at low temperature either due to other magnetic constituents or due to locking into a commensurate phase. Anharmonic modulations of the spiral structure also cause sizable magnetoelastic coupling, which is different from the multiferroic one and which can lead to anomalous relaxation behavior of multiferroic domains [10,11]. Besides the demand for higher transition temperatures and larger ferroelectric polarization it is also necessary to find multiferroic materials exhibiting simpler phase diagrams in order to analyze and describe multiferroic domain dynamics.

Recently, Liu *et al.* reported a type-II multiferroic phase in LiFe(WO_4)$_2$ [12], which is, in addition to $MnWO_4$ [13,14], only the second multiferroic material in the family of tungstates and exhibits higher transition temperatures compared to related compounds [13–21]. In $MnWO_4$, the magnetic ions occupy zigzag chains that lie within the *bc* plane [22] (see Fig. 1). These chains propagate along the *c* direction and are separated along *a* by tungsten layers [22]. In the case of the double-tungstate NaFe(WO_4)$_2$, the magnetic ion is substituted by Na in every second chain stacked along the *a* axis of the $MnWO_4$ structure type. Therefore, the *a* lattice constant and the distance between two magnetic zigzag chains along *a* are doubled, lowering the dimensionality of magnetic interaction (see Fig. 1) [21]. Distinctive for LiFe(WO_4)$_2$ is that the zigzag chains are not entirely occupied by magnetic ions but alternatingly by magnetic Fe^{3+} and nonmagnetic Li^{1+} ions (see Fig. 1) [12,23,24]. Similar to $MnWO_4$, every second layer along *a* is magnetic in LiFe(WO_4)$_2$.

Two successive magnetic anomalies have been reported for LiFe(WO_4)$_2$ at $T_{N1} \approx 22.6$ K and $T_{N2} \approx 19.7$ K, and the first one was associated with the onset of short-range

---

[*] biesenkamp@ph2.uni-koeln.de
[†] braden@ph2.uni-koeln.de

2469-9950/2021/103(13)/134412(10)

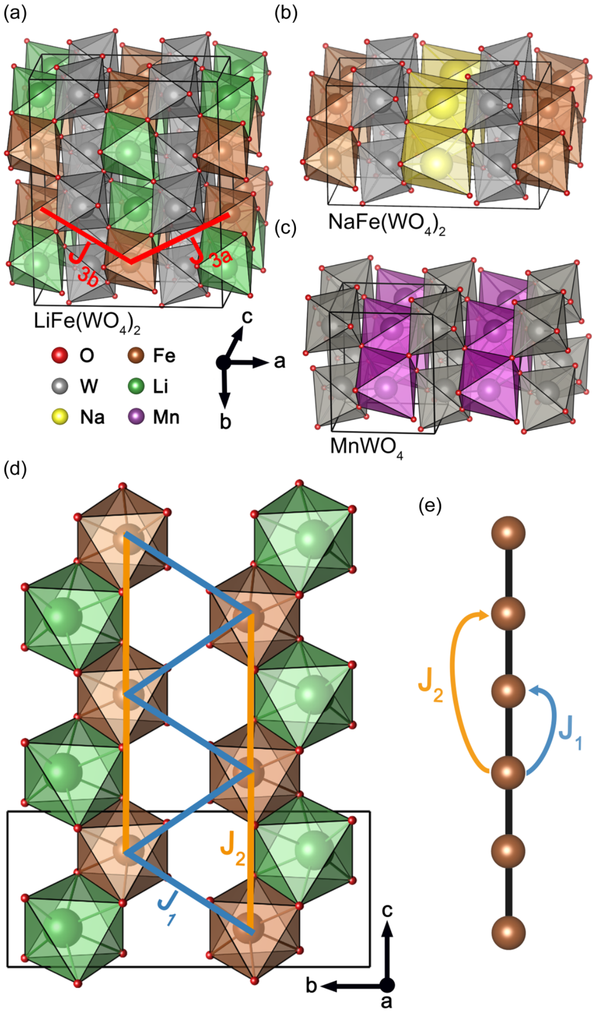

FIG. 1. Crystal structure and magnetic interaction paths in LiFe(WO$_4$)$_2$. (a) displays the nuclear structure of LiFe(WO$_4$)$_2$, for which the structural parameters were adopted from the refinement results based on x-ray diffraction data at 290 K (see Table I). The exchange couplings J_{3a} and J_{3b} are marked in red. For comparison the nuclear structures of related NaFe(WO$_4$)$_2$ and MnWO$_4$ are shown in (b) and (c). In (d) the magnetic zigzag chains along c are visualized together with the respective exchange couplings J_1 and J_2. For the sake of simplicity tungsten ions are hidden in (d). (e) visualizes the configuration of nearest-neighbor interaction J_1 and next-nearest-neighbor interaction J_2 along the magnetic Fe^{3+} chain. For the crystal structure visualization the software VESTA3 [36] was utilized.

TABLE I. The temperature-dependent refinements of the nuclear structure based on singlecrystal data. R(obs), wR(obs), R(all) and wR(all) denote the standard reliability values for structure factors as described in [38]. The temperature-dependent lattice constants were obtained by refining the orientation matrix considering the complete set of recorded x-ray data at the respective temperature. All refinements were done by using the software package JANA2006 [37] and by assuming space group $C2/c$.

	Atom	x	y	z	U_{iso}
290 K[a]	W	0.247505(9)	0.091348(9)	0.246221(18)	0.00299(3)
	Fe	0.0	0.33485(5)	0.25	0.00447(8)
	Li	0.5	0.3421(7)	0.25	0.008(2)
	O1	0.3634(2)	0.05909(18)	0.9240(4)	0.0052(3)
	O2	0.3801(2)	0.18198(19)	0.4114(4)	0.0056(3)
	O3	0.3552(2)	0.54862(18)	0.9452(4)	0.0052(3)
	O4	0.3769(2)	0.69430(19)	0.3928(4)	0.0059(3)
100 K[b]	W	0.24709(3)	0.09137(2)	0.24661(6)	0.00193(9)
	Fe	0.0	0.33466(13)	0.25	0.0019(2)
	Li	0.5	0.344(3)	0.25	0.032(7)
	O1	0.3635(6)	0.0586(5)	0.9252(11)	0.0032(8)
	O2	0.3800(7)	0.1830(5)	0.4121(12)	0.0063(10)
	O3	0.3557(6)	0.5485(5)	0.9446(11)	0.0047(9)
	O4	0.3781(6)	0.6946(5)	0.3936(11)	0.0037(9)
38 K[c]	W	0.24703(3)	0.09137(2)	0.24675(6)	0.00226(8)
	Fe	0.0	0.33474(13)	0.25	0.0025(2)
	Li	0.5	0.346(2)	0.25	0.022(5)
	O1	0.3638(6)	0.0598(5)	0.9245(10)	0.0050(8)
	O2	0.3801(6)	0.1822(5)	0.4115(10)	0.0051(8)
	O3	0.3562(5)	0.5497(5)	0.9437(10)	0.0045(8)
	O4	0.3775(5)	0.6951(5)	0.3933(10)	0.0046(8)

[a] Recorded reflections: 70 005, independent: 2816; $a = 9.2894(5)$, $b = 11.4142(6)$, $c = 4.9026(3)$, $\beta = 90.574(2)$, R(obs) = 2.71, wR(obs) = 3.08, R(all) = 3.64, wR(all) = 3.23.

[b] Recorded reflections: 14 973, independent: 1595; $a = 9.252(4)$, $b = 11.383(4)$, $c = 4.8897(18)$, $\beta = 90.44(2)$, R(obs) = 4.00, wR(obs) = 3.67, R(all) = 6.79, wR(all) = 4.29.

[c] Recorded reflections: 17 924, independent: 1681; $a = 9.2648(11)$, $b = 11.3858(13)$, $c = 4.8918(6)$, $\beta = 90.400(7)$, R(obs) = 3.57, wR(obs) = 3.45, R(all) = 6.30, wR(all) = 4.04.

ordering [12]. At the lower transition an emerging ferroelectric polarization of about 15 μC/m^2 was observed, but the corresponding measurements were performed on polycrystalline samples, thus preventing the determination of the polar axis [12]. Density functional theory (DFT) calculations suggest a ferroelectric polarization along the b direction, whose magnitude is comparable to the one observed in MnWO$_4$ [12,13,25]. Neutron powder diffraction (NPD) revealed an incommensurate spiral ordering of magnetic moments below T_{N2} and thus suggests the inverse DMI as the underlying mechanism for multiferroicity in LiFe(WO$_4$)$_2$ [12]. No transition to a commensurate phase was observed, and specific heat measurements reported only a slight magnetic-field dependence of both transitions, indicating strong antiferromagnetic coupling as well as a simple phase diagram of LiFe(WO$_4$)$_2$ [12].

However, NPD experiments are not sufficient to fully characterize complex magnetic structures in the form of incommensurate spiral arrangements. Furthermore, it is unusual for spiral type-II multiferroics to have short-range magnetic ordering that directly turns into a long-range spiral arrangement of magnetic moments without an intermediate phase [8,26,27]. For multiferroic MnWO$_4$, various magnetic and nonmagnetic chemical substitutions have been studied, and the intermediate antiferromagnetic paraelectric phase is not suppressed for Fe [28], Co [29], Ni [30], Cu [31], Zn [32], Mg [32], Mo [33], In [34], and Ir [35] substitution. For LiFe(WO$_4$)$_2$ a thorough investigation of the first magnetic transition at T_{N1} and confirmation of the spiral character below T_{N2} are thus needed, requiring single-crystal investigations. Here we report on single-crystal investigations concerning the magnetization, the specific heat at the magnetic field, and the nuclear and magnetic structures utilizing different experimental techniques. After an introduction of the experimental methods we will first discuss specific heat data and the temperature-dependent refinements of the nuclear structure before we subsequently discuss both observed magnetic phases, which have been characterized by susceptibility measurements, structural refinements, and neutron polarization analysis.

II. EXPERIMENTAL METHODS

Single crystals about $3 \times 3 \times 0.5\,\mathrm{mm}^3$ in size were grown from a lithium polytungstate melt solution. The samples exhibit a finite conductivity even at low temperature, which prevents the application of electric fields and the direct investigation of the ferroelectric polarization. The measurements, which are discussed below in Sec. III, were performed on the same prepared single crystal (SI). The investigations of a second sample, SII, exhibiting reduced transition temperatures are reported in the Appendix.

The characterizations of the low-temperature phase transitions by susceptibility and by specific heat measurements were done on a commercial superconducting quantum interference device magnetometer and on a commercial calorimeter (physical property measurement system, Quantum Design) by using the thermal relaxation-time method, respectively. For the nuclear and magnetic structure determination, diffraction experiments with x-ray and neutron radiation were executed. The respective single-crystal x-ray data collection for a refinement of the nuclear structure was carried out on a Bruker AXS Kappa APEX II four-circle x-ray diffractometer with Mo K_α radiation ($\lambda = 0.71$ Å). An Oxford N-HeliX cryosystem was additionally deployed for low-temperature measurements. A collection of magnetic reflections and temperature- and magnetic-field-dependent Q space mappings of magnetic reflections were undertaken on the diffractometer 6T2, which is located at the Laboratoire Léon Brillouin. The instrument was equipped with a vertical cryomagnet ($\mu_0 H \leqslant 6\,\mathrm{T}$), a lifting counter detector, and a vertically focusing pyrolytic graphite monochromator yielding wavelength $\lambda = 2.35$ Å. A neutron diffraction experiment utilizing a polarized neutron beam was executed on the cold neutron three-axis spectrometer KOMPASS, which is located at the Heinz Maier-Leibnitz Zentrum (MLZ). Serial polarizing V-shaped multichannel cavities provided an incoming polarized neutron beam, and a highly oriented pyrolytic graphite [HOPG(002)] monochromator was used to select neutrons with $\lambda = 4$ Å. A Helmholtz coil setup for defining the guide-field direction at the sample position was deployed together with a secondary V cavity polarizer in front of the detector, thus enabling longitudinal polarization analysis.

III. RESULTS AND DISCUSSION

A. Nuclear structure

The nuclear structure was determined from x-ray and neutron diffraction data as a function of temperature. All atomic positions and isotropic displacement factors were refined by using the software JANA2006 [37], and the corresponding results are summarized in Table I.

The crystal structure was first discussed in Ref. [23], and it was reported that $\mathrm{LiFe(WO_4)_2}$ crystallizes in the monoclinic space group $C2/c$ [15,24], which is confirmed by our measurements. No superstructure reflections were observed as a function of temperature, indicating no violation of the C centering or a structural transition. The system consists of zigzag chains that propagate along the c direction (see Fig. 1). In contrast to $\mathrm{NaFe(WO_4)_2}$ the nonmagnetic monovalent alkali-metal ion A in $A\mathrm{Fe(WO_4)_2}$ and the magnetic $\mathrm{Fe^{3+}}$ ions do not solely occupy the zigzag chains in $\mathrm{LiFe(WO_4)_2}$ but alternating within the same chain. With respect to $\mathrm{MnWO_4}$, the cell is not only doubled along a direction, as is the case in $\mathrm{NaFe(WO_4)_2}$, but also along the b direction due to a phase shift of the $\mathrm{Li^{1+}}$ and $\mathrm{Fe^{3+}}$ ordering. In $\mathrm{NaFe(WO_4)_2}$ the $[\mathrm{WO_6}]$ octahedra layer separates nonmagnetic $[\mathrm{NaO_6}]$ and magnetic $[\mathrm{FeO_6}]$ layers, whereas in $\mathrm{LiFe(WO_4)_2}$ the layers of $[\mathrm{WO_6}]$ units alternate with layers that contain both $\mathrm{Li^{1+}}$ and $\mathrm{Fe^{3+}}$ ions.

By lowering the temperature to $T = 100\,\mathrm{K}$ the respective inter- and intralayer distances shrink by $\approx 0.3\%$, whereas a refinement at $T = 38\,\mathrm{K}$ reveals no further significant length changes. We do not find any evidence of a structural phase transition, and the low-temperature atomic displacement parameters are not enhanced.

B. Specific heat

Figure 2 displays the temperature dependence of the specific heat for different magnetic fields applied either along b or along c. The c_p anomalies located at $T_{\mathrm{N1}} \approx 22.2$ K and $T_{\mathrm{N2}} \approx 19.0$ K agree with those from Liu *et al.* [12]. As can be seen in Fig. 2(b), no further anomalies were observed for higher temperatures up to room temperature. In magnetic fields up to 14 T along b, T_{N1} is only weakly suppressed, while T_{N2} is significantly reduced to 16.2 K [see Fig. 2(c)]. This indicates that ordering of the b components of the magnetic moments takes place not at the upper transition but only at the lower transition. In contrast a magnetic field along c causes a more pronounced decrease of T_{N1} but a weaker decrease of T_{N2} [see Fig. 2(d)], indicating ordering of c components at the upper transition. This anisotropic behavior clearly documents different magnetic ordering phenomena occur at T_{N1} and T_{N2} and thus the presence of two different phases, IC1 and IC2, which are studied in the following.

C. Susceptibility

The susceptibility was measured for magnetic fields applied along all crystallographic directions. As the crystal structure of $\mathrm{LiFe(WO_4)_2}$ is monoclinic, the a direction is not equivalent to a^*, but because the monoclinic angle is close to 90°, the effect on the respective orientation is negligible. The same holds for c and c^*. A detailed view of the low-temperature region is displayed in Fig. 3(a). At $T_{\mathrm{N1}} \approx 22.2$ K the susceptibility exhibits a kink, indicating the onset of long-range magnetic ordering. The susceptibility for fields applied along the a and c directions starts to decrease below T_{N1}, whereas for a field applied along the b direction, the susceptibility remains at the same level and decreases only

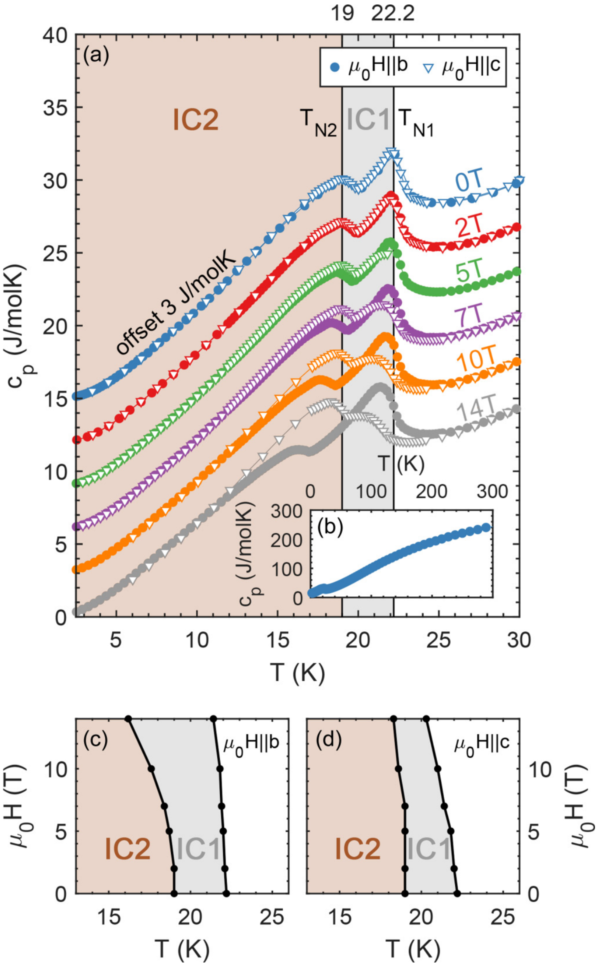

FIG. 2. In (a), the specific heat of LiFe$(WO_4)_2$ in magnetic fields along *b* and *c* is shown. Different fields are offset by 3 J/mol K. Both phases IC1 and IC2 are marked by colored regions, and the respective transition temperatures T_{N1} and T_{N2} refer to the zero-field behavior. The zero-field data for temperatures up to room temperature are shown in (b). Both (c) and (d) display the obtained phase boundaries of the IC1 and IC2 phases for different field directions.

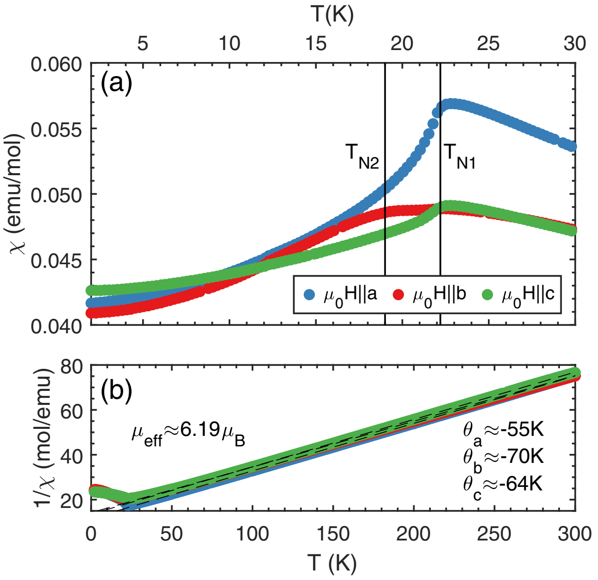

FIG. 3. (a) displays the temperature dependence of the susceptibility χ for all crystallographic directions around the phase transitions T_{N1} and T_{N2}. The susceptibility was measured after zero-field cooling, while heating and applying a constant field of $\mu_0 H = 0.1$ T to the sample. Curie-Weiss fits for $1/\chi$ are shown by dashed black lines in (b) together with the resulting Weiss temperatures θ and the averaged effective moment μ_{eff}.

below the second magnetic transition at $T_{N2} \approx 19$ K. Both transition temperatures agree with the respective temperatures of the specific heat anomalies in Fig. 2, but T_{N1} and T_{N2} are reduced by about 0.6 K compared to the transition temperatures reported by Liu *et al.* [12]. The temperature-dependent susceptibility data suggest that magnetic moments are initially aligning within the *ac* plane and that an additional *b* component of the magnetic ordering is evolving below T_{N2}. This agrees with the different impacts of magnetic fields along *b* and *c* on T_{N1} and T_{N2} (see Fig. 2). The inverse susceptibility of the high-temperature region was fitted by the Curie-Weiss function $C^{-1}(T + \theta)$, yielding antiferromagnetic Weiss temperatures for different field directions in the range of $\theta \approx -70$ to -55 K [see Fig. 3(b)]. From this, the averaged effective magnetic moment $\mu_{\mathrm{eff}} \approx 6.19\mu_B$ was calculated, and its value agrees well with the expected spin-only moment $\mu_{\mathrm{eff}} = 2\sqrt{S(S+1)} = 5.91\mu_B$ for Fe^{3+} ($S = 5/2, L = 0$). The frustration parameter $f = |\theta|/T_N \approx 2.84$ is comparable to that in NaFe$(WO_4)_2$ ($f \approx 2$; see Ref. [21]) and signals a moderate frustration. For comparison, $MnWO_4$ exhibits a larger frustration parameter of about 6 (see Ref. [13]). In contrast to NaFe$(WO_4)_2$ no broad maximum was observed in LiFe$(WO_4)_2$ above the first magnetic transition, thus indicating a more three-dimensional magnetic interaction. Compared to the low-dimensionality in NaFe$(WO_4)_2$ this is not astonishing, as the interlayer distance along *a* is significantly reduced, which enhances the magnetic interaction between layers and explains the higher antiferromagnetic transitions.

D. Incommensurate propagation vector

To trace the temperature and magnetic-field dependence of evolving magnetic reflections and that of the incommensurability in LiFe$(WO_4)_2$ we performed experiments on the 6T2 diffractometer. A vertical cryomagnet ($\mu_0 H \leqslant 6$ T) was utilized together with a lifting counter detector that allows for the collection of reflections with a finite-*k* component of the scattering vector $\boldsymbol{Q}$. For the respective experiment, the sample was mounted in the (100)/(001) scattering plane, thus aligning the *b* direction parallel to the magnetic field.

Figures 4(a) and 4(b) display rocking scans over the magnetic reflections $\boldsymbol{Q} = (0.09\ {-1}\ {-1.3})$ and $\boldsymbol{Q} = (-2.09\ {-1}\ 1.3)$ for $T = 3$ K and $T = 20$ K, respectively. The indexing of both reflections yields similar *h* and *l* components of the incommensurate propagation vector $\boldsymbol{k}_{\mathrm{inc}} = (0.91\ 0\ 0.30)$ that qualitatively agree with Liu *et al.* [12], who

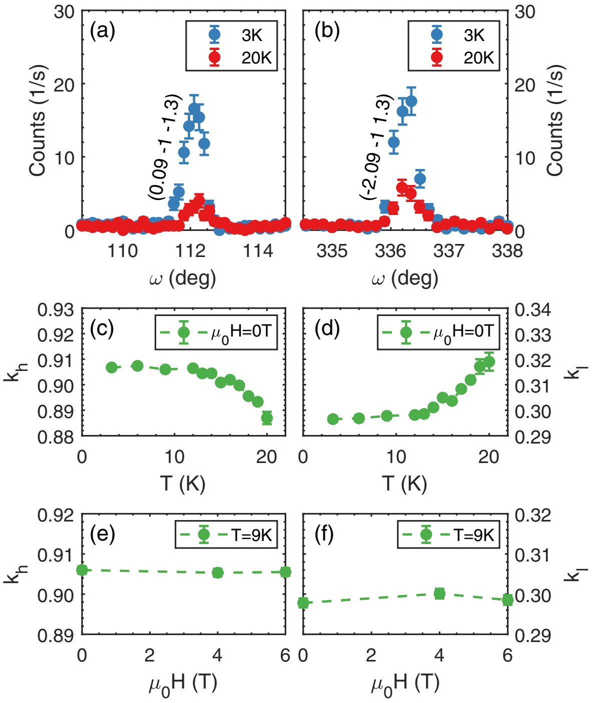

FIG. 4. (a) and (b) display rocking scans over the magnetic reflections $\boldsymbol{Q} = (0.09\ -1\ -1.30)$ and $\boldsymbol{Q} = (-2.09\ -1\ 1.30)$ for $T = 3\,\mathrm{K}$ and $T = 20\,\mathrm{K}$, respectively. The temperature and magnetic-field dependences of the incommensurate propagation vector $\boldsymbol{k}_{\mathrm{inc}} = (k_h\ 0\ k_l)$ are shown in (c)–(f). All respective values have been obtained by fitting the $\boldsymbol{Q}$-space mappings in the h-l plane with a two-dimensional Gaussian function. The magnetic field was applied along the b direction.

reported an almost commensurate $l = 0.332$ component. For both magnetic phases IC1 and IC2 a distinct peak is visible at the respective position in Q space. From this result, it can be stated that long-range magnetic order also persists in the IC1 phase. To trace the incommensurability in the respective magnetic phases, $\boldsymbol{Q}$-space mappings within the h-l plane were recorded around magnetic reflections as a function of temperature and magnetic field. Figures 4(c) and 4(d) show the temperature dependence of the resulting averaged h and l components of the incommensurate propagation vector for $\mu_0H = 0\,\mathrm{T}$, and it can clearly be seen that below T_{N1} the components of $\boldsymbol{k}_{\mathrm{inc}}$ vary with temperature but reach a constant value at low temperature. Incommensurate magnetic long-range order persists down to low temperature, in contrast to $MnWO_4$, which exhibits a first-order transition to a commensurate spin up-up-down-down phase at low temperature [21,22].

The magnetic-field dependence of the incommensurability at $T = 9\,\mathrm{K}$ is presented in Figs. 4(e) and 4(f). In contrast to related $NaFe(WO_4)_2$, no variation of k_h and k_l is visible as a function of magnetic-field strength. The absence of field-dependent alteration of the incommensurability in $LiFe(WO_4)_2$ further illustrates a well-defined antiferromagnetic coupling in accordance with the simplicity of its phase diagram. Just two incommensurate magnetic phases exist at low temperature and persist for finite magnetic fields along the b and c directions. The determination of the appropriate magnetic models and the refinement of the respective magnetic structure will be discussed in the following sections.

TABLE II. Symmetry conditions for the transformation of the complex amplitudes u, v, and w between the two magnetic sites for the little group $G_{\boldsymbol{k}_{\mathrm{ic}}} = \{1, c\}$. The conditions are defined by the irreducible representations Γ_1 and Γ_2 and the corresponding basis vectors Ψ with $a = e^{-i2\pi 0.15}$. Equivalent results were reported in Ref. [12].

Γ	Ψ	(x, y, z)	$(x, \bar{y}, z + 1/2)$
Γ_1	Ψ_1, Ψ_2, Ψ_3	(u, v, w)	$a(u, -v, w)$
Γ_2	Ψ_4, Ψ_5, Ψ_6	(u, v, w)	$a(-u, v, -w)$

E. Magnetic structure of phases IC1 and IC2

In $LiFe(WO_4)_2$, the propagation vector remains incommensurate down to the lowest temperature (see Sec. III D). $\boldsymbol{k}_{\mathrm{inc}}$ and $-\boldsymbol{k}_{\mathrm{inc}}$ are not equivalent for both magnetic phases, and thus, two vectors belong to the star of $\boldsymbol{k}$. By considering space group $C2/c$ and the incommensurate propagation vector $\boldsymbol{k}_{\mathrm{ic}} = (0.91\ 0\ 0.30)$, the little group $G_{\boldsymbol{k}_{\mathrm{ic}}} = \{1, c\}$ can be deduced. The corresponding magnetic representations can be decomposed into two one-dimensional irreducible representations, $\Gamma_{\mathrm{mag}} = 3\Gamma_1 + 3\Gamma_2$. Both magnetic Fe sites on the 4f Wyckoff position are linked via a c glide-plane symmetry and thus belong to one orbit. Therefore, only three complex amplitudes, u, v, and w, are needed to describe the magnetic moment on each site. The phase difference between the two sites amounts to $\phi_{\boldsymbol{k}} = 2\pi \times 0.15$, and the symmetry restrictions referring to the transformation of magnetic moments between the respective sites (x, y, z) and $(x, \bar{y}, z + 1/2)$ are displayed in Table II.

The collection of magnetic reflections in zero field for both phases IC1 and IC2 was carried out on the 6T2 diffractometer by using the same setup as for the temperature- and magnetic-field-dependent study of the incommensurability (see Sec. III D). Due to the instrumental setup the number of accessible reflections in Q space was limited, where only 25 magnetic reflections were recorded in the IC1 phase at $T = 20\,\mathrm{K}$ and 39 magnetic reflections were recorded in the IC2 phase at $T = 3\,\mathrm{K}$. The refinement and testing of different magnetic models were done with the software package FULLPROF [38]. All resulting reliability values for the refinements of respective models in both phases are displayed in Table III, and the observed versus calculated structure factor plots for the best resulting refinements are displayed in Fig. 5.

The best refinement result for the IC1 phase was unambiguously achieved by assuming a magnetic model that is compatible with the single irreducible representation Γ_1. Since for this phase the susceptibility data indicate a magnetic arrangement exclusively lying within the ac plane and in order to reduce the number of parameters, the v component was fixed to zero. With this assumption, the magnetic moment on site 1 was refined to be $\boldsymbol{m} = (2.62(14)\ 0\ 2.26(18))\mu_{\mathrm{B}}$, and thus, the magnetic arrangement of the IC1 phase is described

TABLE III. The reliability values of refinements assuming different magnetic models at $T = 20$ K and $T = 3$ K. The refinement was done by using the FULLPROF suite [38]; measured intensities were corrected for absorption effects.

	20 K		3 K		
	Γ_1	Γ_2	Γ_1	Γ_2	$\Gamma_1 \otimes \Gamma_2$
R_{F^2}	16.2	92.9	25.7	26.6	14.8
R_{wF^2}	20.2	87.6	24.1	28.7	14.6
R_F	19.7	74.1	19.8	17.5	13.2
χ^2	1.43	26.7	7.01	9.95	2.56

by a spin density wave (SDW) that is confined to the *ac* plane with an easy axis $\boldsymbol{e}_{ac}$ that forms an angle of about 41° with the *a* axis (or 9° with the propagation vector). The alignment of moments almost bisecting the *a* and *c* directions nicely agrees with the anomalies appearing in the susceptibility for magnetic fields along *a* and *c*.

Below T_{N2} an additional *b* component develops, and the best refinement result was obtained by combining Γ_1 and Γ_2. The *a* and *c* components are described by Γ_1, whereas Γ_2 describes the *b* component. Moreover, it turned out that choosing *u* and *w* to be real and *v* to be imaginary (corresponding to a $\pi/2$ phase shift) yields the lowest reliability values for the refinement, and thus, the magnetic model following $\Gamma_1 \otimes \Gamma_2$ describes an elliptical spin spiral arrangement for the IC2 phase with moments that are rotating within the plane spanned by $\boldsymbol{e}_{ac}$ and $\boldsymbol{b}$. It has to be noted that the combination of two irreducible representations does not violate Landau theory, considering two consecutive second-order transitions, which is the typical scenario in many type-II multiferroics. The refinement yields $\boldsymbol{m} = (5.05(19)\ i4.21(24)\ 2.93(27))\mu_B$, and the lengths of the major and minor principal axes of the elliptical spiral amount to $m_{\max} = \sqrt{m_a^2 + m_c^2} = 5.84(21)\mu_B$ and $m_{\min} = m_b = 4.21(24)\mu_B$, respectively, and hence depict a moderate deformation with respect to a circular envelope. The fact that the larger axis of this ellipse is even larger than the full spin moment of Fe^{3+} indicates some anharmonicity. The *a*, *c* principal axis of the spiral is now almost parallel to the propagation vector (2°). The averaged magnetic moment of the elliptical spiral amounts to $5.09(11)\mu_B$, in perfect agreement with the Fe^{3+} spin moment of $S = 5/2$. Both magnetic structures are visualized in Fig. 6. Compared to that of the sister compound $NaFe(WO_4)_2$, the order moment is much larger due to the more three-dimensional arrangement of magnetic coupling. Also disorder seems not to play a crucial role in this material (see also the Appendix). $LiFe(WO_4)_2$ does not exhibit a commensurate phase lower than $MnWO_4$, thus making its phase diagram simple and comparable to the zero-field behavior of multiferroic $NaFeGe_2O_6$ and $(NH_4)_2[FeCl_5(H_2O)]$ [18,39–42].

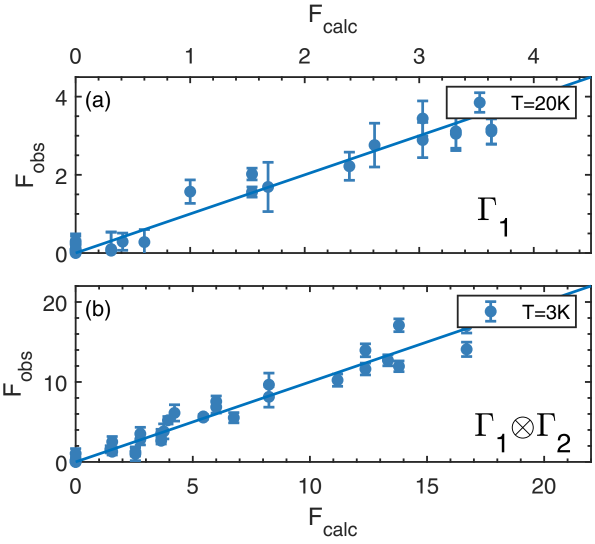

FIG. 5. (a) and (b) display the observed structure factors against the calculated ones for the magnetic models Γ_1 and $\Gamma_1 \otimes \Gamma_2$ at $T = 20$ K and $T = 3$ K, respectively.

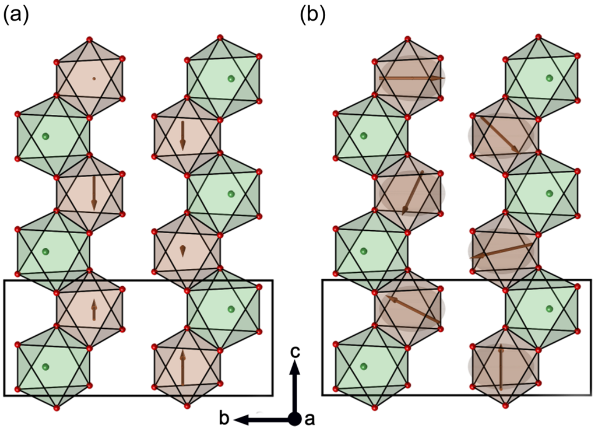

FIG. 6. (a) and (b) visualize the refinement results for the magnetic structure in the magnetic phases IC1 and IC2, respectively. For the sake of simplicity tungsten ions are not shown.

F. Neutron polarization analysis

Neutron polarization analysis can be used to separate the magnetic components and to sense the chirality of the magnetic structure. The respective experiment on $LiFe(WO_4)_2$ was executed at the cold three-axis spectrometer KOMPASS, located at the MLZ. The sample was mounted within the scattering plane (100)/(001), and a Helmholtz coil setup was deployed to define the guide field direction at the sample position. For a longitudinal polarization analysis the common right-handed coordinate system was defined, for which *x* is parallel to $\boldsymbol{Q}$, *y* is perpendicular to *x* but within the scattering plane, and *z* is perpendicular to *x* and *y*. Thus, the crystallographic *b* direction is aligned parallel to the *z* direction. The small sample volume demanded a high neutron flux. Therefore, the horizontal collimation in front of the secondary spin-analyzing cavity was removed. As the efficiency of the V-shaped cavity depends on the incoming beam divergence, the flipping ratio (FR) was reduced significantly to FR = 8–11.

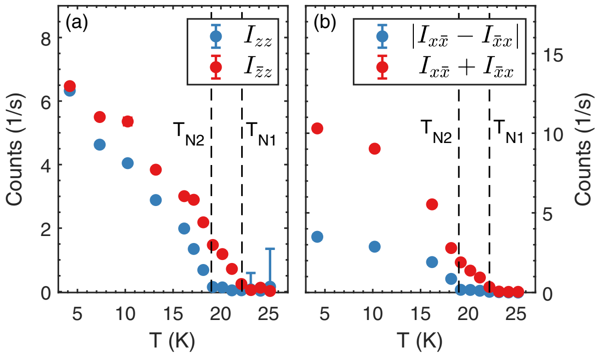

FIG. 7. The displayed intensities in (a) correspond to the recorded NSF and SF channels I_{zz} and $I_{\bar{z}z}$ with $\boldsymbol{P}||z$ and $\boldsymbol{Q} = (-1.09\ 0\ 0.30)$. In (b) the sum and the difference of both SF channels with $\boldsymbol{P}||x$ are plotted.

In the first part of the experiment, the neutron beam polarization $\boldsymbol{P}$ was aligned parallel to z, and a single spin flipper was placed in front of the sample, thus allowing us to measure the spin-flip (SF) channel $I_{\bar{z}z}$ and the non-spin-flip (NSF) channel I_{zz}. The intensities of the respective SF and NSF channels were recorded for the magnetic reflection $\boldsymbol{Q} = (-1.09\ 0\ 0.30)$, and their temperature dependence is displayed in Fig. 7(a). Due to the chosen position in $\boldsymbol{Q}$ space, no nuclear Bragg signal contributes to the scattered intensity. In general, only the magnetization $\boldsymbol{M}_{\perp}(\boldsymbol{Q})$ perpendicular to $\boldsymbol{Q}$ contributes to the scattering process. Moreover, a neutron spin-flip requires a component of the magnetization perpendicular to the neutron polarization, whereas non-spin-flip processes occur when the neutron polarization is collinear to the magnetization. Here it entails the respective SF and NSF channels being described by $I_{zz} = M_b M_b^*$ and $I_{\bar{z}z} = \sin^2(\alpha) M_{ac} M_{ac}^*$, with M_b and M_{ac} being the complex Fourier components of the magnetization along the b direction and within the ac plane, respectively, and $\sin^2(\alpha)$ being the geometry factor. From Fig. 7(a) it can clearly be stated that in the IC1 phase a magnetic component is solely evolving within the ac plane. Below T_{N2} an additional b component develops, and its magnitude approaches a similar size with respect to the ac component when lowering the temperature. The respective temperature-dependent ratios of both components confirm the refinement results for both phases discussed above.

In the second part of the experiment, the neutron beam polarization was set parallel to x (parallel to $\boldsymbol{Q}$), and a second spin flipper was placed behind the sample. With this configuration both SF channels $I_{x\bar{x}} = \boldsymbol{M}_{\perp}\boldsymbol{M}_{\perp}^* - i(\boldsymbol{M}_{\perp} \times \boldsymbol{M}_{\perp}^*)_x$ and $I_{\bar{x}x} = \boldsymbol{M}_{\perp}\boldsymbol{M}_{\perp}^* + i(\boldsymbol{M}_{\perp} \times \boldsymbol{M}_{\perp}^*)_x$ can be measured, giving access to the chiral component $\pm i(\boldsymbol{M}_{\perp} \times \boldsymbol{M}_{\perp}^*)_x$, for which the sign depends on the vector chirality of the spiral. Figure 7(b) displays the sum and the difference of both SF channels, hence presenting the temperature dependence of the overall magnetic scattering contribution $2\boldsymbol{M}_{\perp}\boldsymbol{M}_{\perp}^*$ and that of the chiral signal $-i2(\boldsymbol{M}_{\perp} \times \boldsymbol{M}_{\perp}^*)_x$, respectively. It is clearly visible that the magnetic signal develops below T_{N1}, whereas the chiral structure appears only when passing the lower transition at T_{N2}. This is in accordance with the discussed refinement results, which proposed a SDW and a spiral spin arrangement below T_{N1} and T_{N2}, respectively. Astonishingly, the finite value of $|I_{x\bar{x}} - I_{\bar{x}x}|$ develops without an applied external electric field. The sample crystal thus exhibits an intrinsic preferred vector chirality, which has also been reported for other type-II multiferroics [43].

G. Discussion of magnetic interaction and multiferroic coupling

The transition temperatures for both observed phases, IC1 and IC2, are significantly larger than those reported in $NaFe(WO_4)_2$ and $MnWO_4$. The low transition temperatures in $NaFe(WO_4)_2$ can be attributed to the reduced interlayer coupling arising from the separation through nonmagnetic Na layers. However, the lower transition temperatures in $MnWO_4$ disagree with the higher density of magnetic Mn^{2+} ions compared to that of Fe^{3+} ions in $LiFe(WO_4)_2$, which possess the same $3d^5$ configuration. The lower transition temperatures in $MnWO_4$ result from a higher degree of frustration [44].

The magnetic coupling between Fe^{3+} ions in $LiFe(WO_4)_2$ is mediated through super-superexchange interaction along Fe-O-O-Fe and Fe-O-W-O-Fe paths, which are marked by J_1, J_2 and J_{3a}/J_{3b} in Figs. 1(a), 1(d) and 1(e). The exchange coupling J_3 is split into J_{3a} and J_{3b} due to the monoclinic angle $\beta = 90.574(2)^\circ$. The refinement based on single-crystal x-ray data at room temperature yields the inter- and intralayer distances between nearest-neighbor Fe ions of about 4.4970(10), 4.9026(4), and 5.5773(5)/5.6180(5) Å for the pairs described by J_1, J_2, and J_{3a}/J_{3b}, respectively. The distances of pairs J_1 and J_2 are comparable, so that a single zigzag chain is not the main magnetic unit. Instead, the Fe^{3+} of two neighboring zigzag chains together form a magnetic chain with nearest-neighbor interaction J_1 and next-nearest-neighbor interaction J_2, which is a classical configuration of frustration (see Fig. 1).

DFT calculations find J_1 to be ferromagnetic and J_2 and J_{3a}/J_{3b} to be antiferromagnetic, yielding magnetic frustration [12]. The ferromagnetic coupling for J_1 can be verified by calculating the magnetic exchange energy in the incommensurate phase. For the SDW and the spiral phases the classical exchange energy per Fe resulting from J_1 and J_2 amounts to

$$E_{\mathrm{exch}} = -2J_1\cos(\pi q_c) - 2J_2\cos(2\pi q_c). \tag{1}$$

In this phenomenological simple approach only a ferromagnetic (positive) J_1 with $J_2/J_1 \approx -0.4$ agrees with the observed incommensurability along c of ~0.3 in phases IC1 and IC2 (see Sec. III D), which corresponds to a long wavelength of about six Fe moments. Ferromagnetic coupling between Fe^{3+} moments is rather unusual in view of the half-filled $3d$ shell but arises from cancellation of different superexchange paths. The ferromagnetic nearest-neighbor coupling is, however, much smaller in size than the usual antiferromagnetic couplings, so that the more distant interaction parameters play an important role in $LiFe(WO_4)_2$. Furthermore, $LiFe(WO_4)_2$ is not a highly one-dimensional system as the coupling between the double-zigzag chains is sizable.

One may extend the exchange energy to J_{3a}/J_{3b}, ignoring the small difference arising from the monoclinic angle by adding the term

$$E_{\mathrm{exch}-J_3} = -2J_3[\cos(\pi q_a + \pi q_c) + \cos(\pi q_a - \pi q_c)]. \tag{2}$$

A finite antiferromagnetic J_3 stabilizes antiferromagnetic stacking along the *a* direction corresponding to $q_a = 1$ and reduces the q_c value of minimum exchange energy. For the parameters calculated within density functional theory [12], $J_1 = 2.\,\text{meV}$, $J_2 = -2.44\,\text{meV}$, and $J_3 = -1.13\,\text{meV}$, the minimum occurs at $q_c = 0.347$, close to the experimental value of 0.30, while the minimum appears at 0.425 without taking J_3 into account. In order to explain the incommensurate modulation along *a* one needs to take interaction at even farther distances into account. There are four neighbors at 7.33-Å distance, but this shell corresponds to the *C* centering vector and thus enforces $q_a = 1$ for an antiferromagnetic parameter. The next six Fe-Fe shells are at distances between 8 and 9 Å with, in total, 16 bonds. Therefore, a reasonable estimate of the impact of these interaction parameters cannot be made.

In contrast to $\text{NaFe(WO}_4)_2$ [21], no second intrachain spiral with opposite handedness exists as the upper and lower rows of a zigzag chain are alternatingly occupied by magnetic Fe^{3+} and nonmagnetic Li^{1+}. Furthermore, spirals of neighboring chains possess the same handedness; therefore, the effect of inverse DMI is not canceled in $\text{LiFe(WO}_4)_2$. It is the combination of the two incommensurate magnetic modes that breaks the inversion symmetry in $\text{LiFe(WO}_4)_2$. For the inverse DMI the ferroelectric polarization is given by

$$\boldsymbol{P} \propto \boldsymbol{r}_{ij} \times (\boldsymbol{S}_i \times \boldsymbol{S}_j), \tag{3}$$

with $\boldsymbol{S}_i$ and $\boldsymbol{S}_j$ being two neighboring spins and $\boldsymbol{r}_{ij}$ being their connecting vector [8,9]. With this formalism we can determine the direction of the ferroelectric polarization. With the propagation vector $\boldsymbol{k}_{\text{inc}} = (0.91\ 0\ 0.30)$ being perpendicular to *b* and with the spiral structure arising from the e_{ac} and *b* components it is obvious that the four Fe moments coupled through J_1 and J_2 yield a ferroelectric polarization along the *b* direction. Taking into account all other pairs described by adding translations $\pm(n\boldsymbol{a} + m\boldsymbol{b} + l\boldsymbol{c})$ also shows that any polarization contribution perpendicular to *b* cancels out. The same conclusion can be deduced from the symmetry of the magnetic spiral combining two representations so that the *c* glide mirror plane perpendicular is broken.

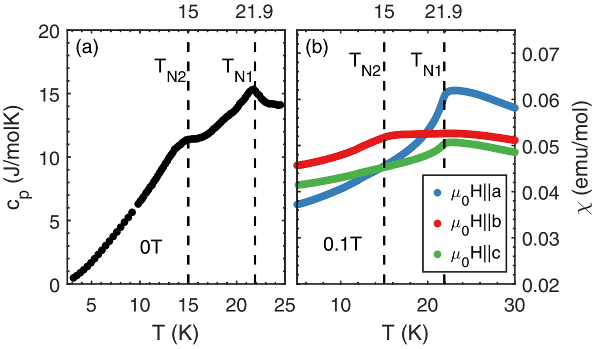

FIG. 8. The specific heat and susceptibility measurements on sample SII reveal reduced transition temperatures T_{N1} and T_{N2} compared to those of sample SI, which are related to Li/Fe site disorder (see text).

IV. CONCLUSIONS

We presented a comprehensive single-crystal investigation of the magnetization, the specific heat under magnetic field, and the nuclear and magnetic structures of the newly discovered multiferroic material $\text{LiFe(WO}_4)_2$ [12]. Temperature-dependent susceptibility and specific heat measurements revealed the magnetic anisotropy. The system undergoes two magnetic transitions at $T_{\text{N1}} \approx 22.2\,\text{K}$ and $T_{\text{N2}} \approx 19\,\text{K}$. With single-crystal neutron diffraction we were able to observe long-range incommensurate magnetic ordering not only in the multiferroic but also in the intermediate phase, which so far has been proposed to exhibit only short-range ordering [12]. The incommensurability in both magnetic phases shows only a slight temperature dependence, whereas magnetic field up to 6 T does not change the magnetic propagation vector at all. It was possible to determine and refine the magnetic structure in both phases IC1 and IC2, revealing a SDW with an easy axis lying within the *ac* plane in phase IC1 and an elliptical spiral with an additional *b* component in phase IC2. Both refinements, in particular the chiral nature of the IC2 magnetic structure, are confirmed by neutron polarization analysis in the respective phases. The refined chiral structure of the IC2 phase is compatible with the proposed ferroelectric polarization along the *b* direction arising from the inverse DMI [8,9,12], and it was observed that in IC2 an unbalanced multiferroic domain distribution appears even in the absence of an applied external electric field. No transitions to commensurate phases were observed, rendering the phase diagram simple and $\text{LiFe(WO}_4)_2$ a well-suited material to study intrinsic multiferroic properties such as domain dynamics. Due to the particular arrangement of magnetic Fe ions in the zigzag octahedron chains, $\text{LiFe(WO}_4)_2$ can be, moreover, considered

TABLE IV. Nuclear refinements based on neutron diffraction data from sample SII for two temperatures. The Li site was refined while assuming a misoccupation of it by Fe ions [≈ 6.7(5)% at 24 K and ≈ 6.2(4)% at 2.5 K]. The refinement was done on structure factors and with the software JANA2006 [37]. The integrated intensities were numerically corrected for absorption, and an extinction correction was applied during the refinements.

	Atom	*x*	*y*	*z*	U_{iso}
24 K[a]	W	0.24755(19)	0.09125(13)	0.2470(4)	0.0029(4)
	Fe	0.0	0.33480(9)	0.25	0.0024(3)
	Li	0.5	0.3495(10)	0.25	0.016(4)
	O1	0.36287(13)	0.05852(10)	0.9250(3)	0.0043(4)
	O2	0.38014(12)	0.18270(11)	0.4102(3)	0.0045(4)
	O3	0.35553(13)	0.54899(10)	0.9431(3)	0.0039(4)
	O4	0.37747(12)	0.69384(10)	0.3926(3)	0.0041(4)
2.5 K[b]	W	0.24754(15)	0.09120(11)	0.2472(3)	0.0029(3)
	Fe	0.0	0.33469(8)	0.25	0.0022(3)
	Li	0.5	0.3493(9)	0.25	0.019(3)
	O1	0.36294(11)	0.05853(9)	0.9252(2)	0.0042(3)
	O2	0.38028(10)	0.18278(9)	0.4102(2)	0.0045(3)
	O3	0.35572(11)	0.54913(9)	0.9429(2)	0.0035(3)
	O4	0.37738(10)	0.69370(9)	0.3924(2)	0.0044(3)

[a] Recorded reflections: 578, independent: 290; R(obs) = 1.99, wR(obs) = 2.19, R(all) = 2.24, wR(all) = 2.22.

[b] Recorded reflections: 1259, independent: 730; R(obs) = 2.42, wR(obs) = 2.37, R(all) = 2.42, wR(all) = 2.37.

a realization of a J_1, J_2 magnetic chain, although the interchain interaction is sizeable and results in a fully ordered structure at low temperature. Both the simple phase diagram and the three-dimensional coupling of magnetic zigzag chains encourage further research on multiferroic domain dynamics and magnetic interactions in $LiFe(WO_4)_2$.

ACKNOWLEDGMENTS

This work was funded by the Deutsche Forschungsgemeinschaft (DFG, German Research Foundation), Project No. 277146847-CRC 1238, Projects A02, B01, and B04, and by the Bundesministerium für Bildung und Forschung, Project No. 05K19PK1.

APPENDIX

Characterization measurements on several $LiFe(WO_4)_2$ samples revealed two different sample types that exhibit different transition temperatures. For some samples the specific heat and the susceptibility measurements display a slightly lowered value for T_{N1}, whereas the T_{N2} value was diminished significantly to ≈ 15 K. Exemplary measurements are shown for sample SII in Fig. 8. Sample SII was investigated furthermore by neutron diffraction at the four-circle instrument HEiDi [45], which is located at the MLZ and jointly operated by Rheinisch-Westfälische Technische Hochschule Aachen (RWTH) University and Forschungszentrum Jülich GmbH within the Jülich Aachen Research Alliance – Fundamentals of Future Information Technology (JARA-FIT) collaboration. A combined set of nuclear reflections was recorded with $\lambda = 0.795$ Å and $\lambda = 1.171$ Å utilizing a germanium monochromator [Ge(422) and Ge(311), respectively]. The refinement of the nuclear structure yields similar results for the atomic positions (see Table IV) compared to the structural refinement of sample SI (see Table I). The onset of magnetic order does not yield a significant change in the crystal structure. However, the structural refinement of sample SII discloses a misoccupation of the Li site by Fe ions of about $\approx 6.7(5)\%$ at 24 K and $\approx 6.2(4)\%$ at 2.5 K, which provokes a strong impact on magnetic interactions and hence on the respective magnetic ordering and transition temperatures. In contrast, the x-ray experiment on sample SI yields an insignificant misoccupation of only about $0.4(5)\%$. Thus, the discrepancy concerning the observed magnetic transition temperatures for both sample types with respect to the reported phase diagram [12] of multiferroic $LiFe(WO_4)_2$ arises from the alteration of the magnetic zigzag chains through a misoccupation by Fe on the Li site. However, in both phases of SII, a magnetic reflection indexed by a propagation vector similar to that for SI was detectable.

---

[1] J. F. Scott, Multiferroic memories, Nat. Mater. **6**, 256 (2007).

[2] M. Fiebig, Revival of the magnetoelectric effect, J. Phys. D **38**, R123 (2005).

[3] N. A. Spaldin and R. Ramesh, Advances in magnetoelectric multiferroics, Nat. Mater. **18**, 203 (2019).

[4] M. Fiebig, T. Lottermoser, D. Meier, and M. Trassin, The evolution of multiferroics, Nat. Rev. Mater. **1**, 16046 (2016).

[5] D. Khomskii, Classifying multiferroics: Mechanisms and effects, Physics **2**, 20 (2009).

[6] I. E. Dzyaloshinskii, A thermodynamic theory of "weak" ferromagnetism of antiferromagnetics, J. Phys. Chem. Solids **4**, 241 (1958).

[7] T. Moriya, Anisotropic Superexchange Interaction and Weak Ferromagnetism, Phys. Rev. **120**, 91 (1960).

[8] M. Mostovoy, Ferroelectricity in Spiral Magnets, Phys. Rev. Lett. **96**, 067601 (2006).

[9] T. Kimura, Spiral Magnets as Magnetoelectrics, Annu. Rev. Mater. Res. **37**, 387 (2007).

[10] M. Baum, J. Leist, T. Finger, K. Schmalzl, A. Hiess, L. P. Regnault, P. Becker, L. Bohatý, G. Eckold, and M. Braden, Kinetics of the multiferroic switching in $MnWO_4$, Phys. Rev. B **89**, 144406 (2014).

[11] S. Biesenkamp, N. Qureshi, Y. Sidis, P. Becker, L. Bohatý, and M. Braden, Structural dimerization in the commensurate magnetic phases of $NaFe(WO_4)_2$ and $MnWO_4$, Phys. Rev. B **102**, 144429 (2020).

[12] M. Liu, L. Lin, Y. Zhang, S. Li, Q. Huang, V. O. Garlea, T. Zou, Y. Xie, Y. Wang, C. Lu, L. Yang, Z. Yan, X. Wang, S. Dong, and J.-M. Liu, Cycloidal magnetism driven ferroelectricity in double tungstate $LiFe(WO_4)_2$, Phys. Rev. B **95**, 195134 (2017).

[13] K. Taniguchi, N. Abe, T. Takenobu, Y. Iwasa, and T. Arima, Ferroelectric Polarization Flop in a Frustrated Magnet $MnWO_4$ Induced by a Magnetic Field, Phys. Rev. Lett. **97**, 097203 (2006).

[14] O. Heyer, N. Hollmann, I. Klassen, S. Jodlauk, L. Bohatý, P. Becker, J. A. Mydosh, T. Lorenz, and D. Khomskii, A new multiferroic material: $MnWO_4$, J. Phys.: Condens. Matter **18**, L471 (2006).

[15] A. G. Anders, A. I. Zvyagin, P. S. Kalinin, E. N. Khats'ko, and V. G. Yurko, Magnetic properties of a low-dimensional magnetic material with monoclinic crystal structure symmetry, Fiz. Nizk. Temp. **1**, 1013 (1975) [Sov. J. Low Temp. Phys. **1**, 485 (1975)].

[16] T. Kimura, T. Goto, H. Shintani, K. Ishizaka, T. Arima, and Y. Tokura, Magnetic control of ferroelectric polarization, Nature (London) **426**, 55 (2003).

[17] G. Lawes, A. B. Harris, T. Kimura, N. Rogado, R. J. Cava, A. Aharony, O. Entin-Wohlman, T. Yildirim, M. Kenzelmann, C. Broholm, and A. P. Ramirez, Magnetically Driven Ferroelectric Order in $Ni_3V_2O_8$, Phys. Rev. Lett. **95**, 087205 (2005).

[18] M. Ackermann, D. Brüning, T. Lorenz, P. Becker, and L. Bohatý, Thermodynamic properties of the new multiferroic material $(NH_4)_2[FeCl_5(H_2O)]$, New J. Phys. **15**, 123001 (2013).

[19] M. Ackermann, L. Andersen, T. Lorenz, L. Bohatý, and P. Becker, Anisotropy study of multiferroicity in the pyroxene $NaFeGe_2O_6$, New J. Phys. **17**, 013045 (2015).

[20] S. Jodlauk, P. Becker, J. A. Mydosh, D. I. Khomskii, T. Lorenz, S. V. Streltsov, D. C. Hezel, and L. Bohatý, Pyroxenes: A new class of multiferroics, J. Phys.: Condens. Matter **19**, 432201 (2007).

[21] S. Holbein, M. Ackermann, L. Chapon, P. Steffens, A. Gukasov, A. Sazonov, O. Breunig, Y. Sanders, P. Becker, L. Bohatý, T. Lorenz, and M. Braden, Strong magnetoelastic coupling at the

transition from harmonic to anharmonic order in NaFe$(WO_4)_2$ with $3d^5$ configuration, Phys. Rev. B **94**, 104423 (2016).

[22] G. Lautenschläger, H. Weitzel, T. Vogt, R. Hock, A. Böhm, M. Bonnet, and H. Fuess, Magnetic phase transitions of $MnWO_4$ studied by the use of neutron diffraction, Phys. Rev. B **48**, 6087 (1993).

[23] G. Le Flem, R. Salmon, and P. Hagenmuller, Sur quelques nouveaux tungstates doubles de structure wolframite, C. R. Acad. Sc. Paris, Ser. C **268**, 1431 (1969).

[24] P. V. Klevtsov and R. F. Klevtsova, Crystallographic investigation of a double tungstate LiFe$(WO_4)_2$, Sov. Phys. Crystallogr. **15**, 294 (1970).

[25] A. H. Arkenbout, T. T. M. Palstra, T. Siegrist, and T. Kimura, Ferroelectricity in the cycloidal spiral magnetic phase of $MnWO_4$, Phys. Rev. B **74**, 184431 (2006).

[26] P. Tolédano, Pseudo-proper ferroelectricity and magnetoelectric effects in $TbMnO_3$, Phys. Rev. B **79**, 094416 (2009).

[27] P. Tolédano, B. Mettout, W. Schranz, and G. Krexner, Directional magnetoelectric effects in $MnWO_4$: Magnetic sources of the electric polarization, J. Phys.: Condens. Matter **22**, 065901 (2010).

[28] F. Ye, Y. Ren, J. A. Fernandez-Baca, H. A. Mook, J. W. Lynn, R. P. Chaudhury, Y.-Q. Wang, B. Lorenz, and C. W. Chu, Magnetic switching and phase competition in the multiferroic antiferromagnet $Mn_{1-x}Fe_xWO_4$, Phys. Rev. B **78**, 193101 (2008).

[29] K.-C. Liang, Y.-Q. Wang, Y. Y. Sun, B. Lorenz, F. Ye, J. A. Fernandez-Baca, H. A. Mook, and C. W. Chu, The complex multiferroic phase diagram of $Mn_{1-x}Co_xWO_4$, New J. Phys. **14**, 073028 (2012).

[30] N. Poudel, B. Lorenz, B. Lv, Y. Q. Wang, F. Ye, J. Wang, J. A. Fernandez-baca, and C. W. Chu, Effects of Nickel Doping on the Multiferroic and Magnetic Phases of $MnWO_4$, Integr. Ferroelectr. **166**, 17 (2015).

[31] C. M. N. Kumar, Y. Xiao, P. Lunkenheimer, A. Loidl, and M. Ohl, Crystal structure, incommensurate magnetic order, and ferroelectricity in $Mn_{1-x}Cu_xWO_4 (0 \leqslant x \leqslant 0.19)$, Phys. Rev. B **91**, 235149 (2015).

[32] L. Meddar, M. Josse, P. Deniard, C. La, G. André, F. Damay, V. Petricek, S. Jobic, M.-H. Whangbo, M. Maglione, and C. Payen, Effect of Nonmagnetic Substituents Mg and Zn on the Phase Competition in the Multiferroic Antiferromagnet $MnWO_4$, Chem. Mater. **21**, 5203 (2009).

[33] L. Meddar, M. Josse, M. Maglione, A. Guiet, C. La, P. Deniard, R. Decourt, C. Lee, C. Tian, S. Jobic, M.-H. Whangbo, and C. Payen, Increasing the Phase-Transition Temperatures in Spin-Frustrated Multiferroic $MnWO_4$ by Mo Doping, Chem. Mater. **24**, 353 (2012).

[34] U. Gattermann, G. Benka, A. Bauer, A. Senyshyn, and S.-H. Park, Magnetic properties of the In-doped $MnWO_4$-type solid solutions $Mn_{1-3x}In_{2x}v_xWO_4$ [v=vacancy; $0 < x < 0.11$], J. Magn. Magn. Mater. **398**, 167 (2016).

[35] H. W. Wang, S. H. Zheng, G. Z. Zhou, P. Z. Chen, L. Lin, Z. B. Yan, X. H. Zhou, X. P. Jiang, H. W. Yu, and J.-M. Liu, The Ir^{4+} substitution dependence of electric polarization as a probe of magnetic phase stability in multiferroic $MnWO_4$, J. Appl. Phys. **126**, 064103 (2019).

[36] K. Momma and F. Izumi, *VESTA3* for three-dimensional visualization of crystal, volumetric and morphology data, J. Appl. Crystallogr. **44**, 1272 (2011).

[37] V. Petříček, M. Dušek, and L. Palatinus, Crystallographic computing system JANA2006: General features, Z. Kristallogr. **229**(5), 345 (2014).

[38] J. Rodríguez-Carvajal, Recent advances in magnetic structure determination by neutron powder diffraction, Phys. B (Amsterdam, Neth.) **192**, 55 (1993).

[39] I. Kim, B.-G. Jeon, D. Patil, S. Patil, G. Nénert, and K. H. Kim, Observation of multiferroic properties in pyroxene $NaFeGe_2O_6$, J. Phys.: Condens. Matter **24**, 306001 (2012).

[40] L. Ding, P. Manuel, D. D. Khalyavin, F. Orlandi, and A. A. Tsirlin, Unraveling the complex magnetic structure of multiferroic pyroxene $NaFeGe_2O_6$: A combined experimental and theoretical study, Phys. Rev. B **98**, 094416 (2018).

[41] J. Alberto Rodríguez-Velamazán, Ó. Fabelo, Á. Millán, J. Campo, R. D. Johnson, and L. Chapon, Magnetically-induced ferroelectricity in the $(ND_4)_2[FeCl_5(H_2O)]$ molecular compound, Sci. Rep. **5**, 14475 (2015).

[42] W. Tian, H. Cao, J. Wang, F. Ye, M. Matsuda, J.-Q. Yan, Y. Liu, V. O. Garlea, H. K. Agrawal, B. C. Chakoumakos, B. C. Sales, R. S. Fishman, and J. A. Fernandez-Baca, Spin-lattice coupling mediated multiferroicity in $(ND_4)_2[FeCl_5(H_2O)]$, Phys. Rev. B **94**, 214405 (2016).

[43] T. Finger, D. Senff, K. Schmalzl, W. Schmidt, L. P. Regnault, P. Becker, L. Bohatý, and M. Braden, Electric-field control of the chiral magnetism of multiferroic $MnWO_4$ as seen via polarized neutron diffraction, Phys. Rev. B **81**, 054430 (2010).

[44] F. Ye, R. S. Fishman, J. A. Fernandez-Baca, A. A. Podlesnyak, G. Ehlers, H. A. Mook, Y. Wang, B. Lorenz, and C. W. Chu, Long-range magnetic interactions in the multiferroic antiferromagnet $MnWO_4$, Phys. Rev. B **83**, 140401(R) (2011).

[45] M. Meven and A. Sazonov, HEiDi: Single crystal diffractometer at hot source, J. Large-Scale Res. Facil. **1**, A7 (2015).

5. Chiral order and multiferroic domain relaxation in $NaFeGe_2O_6$

A rather complex relaxation behavior of multiferroic domains in $MnWO_4$ contrasts the simple description of multiferroic switching in $TbMnO_3$ [49, 70]. For the latter system, the temperature- and electric-field dependent relaxation times can be described by a simple Arrhenius-Merz law, whereas $MnWO_4$ shows a speeding up of multiferroic domain inversion, when approaching its lower phase transition [49, 70] to commensurate ordering. It was thoroughly discussed that this anomalous relaxation behavior is caused by depinning effects due to the interference of tiny commensurate fragments in the multiferroic phase (see Ref. [1] and section 3). As already mentioned within the course of this thesis, it is thus desirable for further studies on domain kinetics to study multiferroic systems, which exhibits simple phase diagrams. A potential candidate was seen to be $LiFe(WO_4)_2$, whose temperature and magnetic-field dependent structure was thoroughly characterized within the course of this thesis (see Ref. [2] and section 4). However, despite the evidence of ideal conditions for multiferroic switching in $LiFe(WO_4)_2$, the available samples exhibited finite conductivity at low temperature, wherefore the electric-field control of multiferroic domains and the respective study of multiferroic domain inversion was prohibited. Hence, another material was needed to deepen the investigations of multiferroic domain kinetics.

The multiferroic pyroxene $NaFeGe_2O_6$ was reported to exhibit such a simple magnetic phase diagram [109–113]. It first develops a SDW at $T_\mathrm{N} = 13\,\mathrm{K}$ until the structure transforms into a spiral arrangement below the multiferroic transition temperature at $T_\mathrm{MF} = 11.6\,\mathrm{K}$. In the latter phase a ferroelectric polarization appears ($\mathbf{P} \approx 32\,\mu\mathrm{C\,m^{-2}}$) and can be described in the framework of inverse DMI [110, 113]. Though, the magnetic phase diagram was thoroughly investigated during the last decade, the details of the spiral structure and in particular the potential presence of a *b*-component for the magnetic spiral were still controversially discussed [111, 112]. This motivated respective studies for clarification by utilizing neutron polarization analysis, as this technique is highly sensitive to the different components of a magnetic structure. The reported simplicity of its zero-field phase diagram also yields an ideal playground for the investigation of domain dynamics, wherefore time-resolved studies were encouraged to conduct on this system. As the available crystals were of sufficient size, it further motivated inelastic studies of the magnon dispersion and in particular of the spin-wave velocity, which was proposed to limit the speed of multiferroic domain inversion.

The results of respective experiments, which were carried out at the facilities ILL [114, 115] and LLB, were published in the publication

> S. Biesenkamp, D. Gorkov, W. Schmidt, K. Schmalzl, Y. Sidis, P. Becker, L. Bohatý and M. Braden, *Chiral order and multiferroic domain relaxation in* $NaFeGe_2O_6$*,* Phys. Rev. B **104**, 174405 (2021),

as an Editors' Suggestion and is included into this thesis (see following pages).

With neutron polarization analysis it was possible to separate magnetic components and thus to characterize the low-temperature structure of $NaFeGe_2O_6$, which develops an additional b-component below the lock-in of the incommensurability of the magnetic structure. The latter point further showed that no commensurate phase appears (at least down to the lowest measured temperature), which in view of the multiferroic relaxation investigation provided ideal conditions for the respective time-resolved studies of the multiferroic domain kinetics. Further to the benefits from a simple phase diagram, the small observed coercive fields at the lowest temperature allowed the investigation of relaxation times in a broad temperature range ($T/T_{\mathrm{MF}} \approx 0.14$) with respect to the multiferroic transition. The respective measurements revealed multiferroic domain inversion that obeys the same simple combined Arrhenius-Merz law, which was shown to describe the domain kinetics in $TbMnO_3$ [49]. However, the relaxation in $NaFeGe_2O_6$ was observed to be much faster by several orders of magnitude in time compared to $TbMnO_3$. This is because both, the activation constant as well as the characteristic relaxation time are much smaller compared to them in $TbMnO_3$. Concerning the activation constant this naturally follows from the fact that the ferroelectric polarization is much weaker in $NaFeGe_2O_6$ and can thus be pinned less effectively with respect to the polarization in $TbMnO_3$ [49]. The fastest possible multiferroic relaxation time can be reached at the multiferroic transition temperature and is described by the characteristic relaxation time τ^*, whose value was proposed to be limited by the spin wave velocity. Indeed, the inelastic studies of the magnon dispersion revealed that by consideration of the sample geometry, the fastest possible domain inversion time that is calculated from the spin-wave velocity is of the same order of magnitude as the measured characteristic relaxation time. The analysis of the magnon dispersion further indicated that $NaFeGe_2O_6$ cannot be characterized as a low-dimensional system.

The multiferroic system $NaFeGe_2O_6$ displayed simple activation behavior, fast relaxation and offered a broad temperature range to investigate the multiferroic switching. It thus proposes $NaFeGe_2O_6$ to be an ideal model system to investigate the domain kinetics, for which still open questions remains. As the presence of quantum fluctuation driven domain wall tunneling for domain inversion is still not observed for multiferroics in general, it highly motivates the respective investigation in $NaFeGe_2O_6$. Due to its small coercive fields and the observed fast relaxation, respective experiment can be conducted in reasonable time and with manageable field strengths. However, lower temperatures necessitate elaborate sample environments that first need to be thoroughly tested for the utilization in high-voltage experiments. In view of the further course of this thesis, it also encouraged to study the domain relaxation in systems, which exhibits different sequences of phase transition, much higher multiferroic temperature regions or at least also a different crystallographic composition as found in molecular multiferroics. It has repeatedly stressed that it is not only of fundamental interest but in view of potential applications it is indispensable to understand how the underlying details of nuclear and magnetic structures as well as respective interactions are impacting the relaxation behavior.

Contribution to the embedded publication

Several neutron scattering experiments were conducted for the time-resolved investigation of multiferroic domain inversion. A first experiment at the triple-axis spectrometer IN12 (ILL) [114] was carried out to analyze the fast relaxation processes as well as to record the SF- and NSF-channels for a longitudinal polarization analysis and a respective thorough characterization of the low-temperature magnetic structure. This experiment was carried out on-site by the author of this thesis, M. Braden and D. Gorkov. A second experiment at IN12 [115] was also conducted by the author of this thesis to extend the recorded measurements of relaxation times to lower temperatures. Both experiments at IN12 [114, 115] were supported by the local contacts W. Schmidt and K. Schmalzl. For the investigation of very slow multiferroic relaxation, a time-resolved experiment was carried out at 4F1 (LLB). This beamtime was conducted by the author of this thesis and supported by the local contact Y. Sidis. This holds also for the experiment at 4F2, which was done for the determination of the spin-wave velocity. Both samples that were used for respective experiments were grown by P. Becker and L. Bohatý. The first draft of the paper manuscript was written by him and its completion was done in cooperation with M. Braden. The manuscript was further proofread and corrected by all named co-authors. The whole project was supervised by M. Braden.

PHYSICAL REVIEW B **104**, 174405 (2021)

Editors' Suggestion

Chiral order and multiferroic domain relaxation in $NaFeGe_2O_6$

S. Biesenkamp,[1,*] D. Gorkov,[1,2] W. Schmidt,[3] K. Schmalzl,[3] Y. Sidis,[4] P. Becker,[5] L. Bohatý,[5] and M. Braden[1,†]

[1]*II. Physikalisches Institut, Universität zu Köln, Zülpicher Straße 77, D-50937 Köln, Germany*
[2]*Heinz Maier-Leibnitz Zentrum (MLZ), Technische Universität München, Lichtenbergstr. 1, 85748 Garching, Germany*
[3]*Juelich Centre for Neutron Science JCNS, Forschungszentrum Juelich GmbH, Outstation at ILL, 38042 Grenoble, France*
[4]*UniversitéParis-Saclay, CNRS, CEA, Laboratoire Léon Brillouin, F-91191 Gif-sur-Yvette, France*
[5]*Abteilung Kristallographie, Institut für Geologie und Mineralogie, Universität zu Köln, Zülpicher Straße 49b, 50674 Köln, Germany*

(Received 17 May 2021; revised 14 October 2021; accepted 20 October 2021; published 4 November 2021)

The magnetic structure and the multiferroic relaxation dynamics of $NaFeGe_2O_6$ were studied by neutron scattering on single crystals partially utilizing polarization analysis. In addition to the previously reported transitions, the incommensurate spiral ordering of Fe^{3+} moments in the *ac* plane develops an additional component along the crystallographic *b* direction below $T \approx 5$ K, which coincides with a lock-in of the incommensurate modulation. The quasistatic control of the spin-spiral handedness, respectively of the vector chirality, by external electric fields proves the invertibility of multiferroic domains down to the lowest temperature. Time-resolved measurements of the multiferroic domain inversion in $NaFeGe_2O_6$ reveal a simple temperature and electric-field dependence of the multiferroic relaxation that is well described by a combined Arrhenius-Merz relation, as it has been observed for $TbMnO_3$. The maximum speed of domain wall motion is comparable to the spin-wave velocity deduced from an analysis of the magnon dispersion.

DOI: 10.1103/PhysRevB.104.174405

I. INTRODUCTION

The increasing power consumption due to data storage and the growing amount of information that has to be stored or buffered enforce the development of new and more effectively working memory devices [1,2]. Aside from phase-change-based devices, skyrmion racetracks, and other promising techniques [2–9], multiferroic systems are promising for designing future storage techniques [10,11].

In multiferroics at least two ferroic ordering parameters occur in the same phase and are coupled to each other [12]. Both ordering parameters can be controlled by both conjugate fields. The magnetoelectric case with ferroelectric and magnetic ordering is most prominent, as it allows for a multiferroic memory, which combines the advantages of ferroelectric (FeRAMs) and magnetic random access memories (MRAMs) [10,11,13]. In so-called type-II multiferroics the ferroelectric polarization is not only coexisting with magnetic ordering, but it is also induced by the onset of it, which hence implies strong coupling between both ferroic ordering parameters [12]. In many systems the driving mechanism for this effect is the inverse Dzyaloshinskii-Moriya interaction (DMI), for which a spin canting of neighboring spins $\boldsymbol{S}_i$ and $\boldsymbol{S}_j$ induces a ferroelectric polarization, whose direction is defined by $\boldsymbol{P} \propto \boldsymbol{e}_{ij} \times (\boldsymbol{S}_i \times \boldsymbol{S}_i)$ with $\boldsymbol{e}_{ij}$ being the connecting vector of neighboring spins [14–16].

The understanding of the read and write performance under different conditions is indispensable for the development of new memory devices. The control and the dynamics of multiferroic domain inversion were studied intensively for $TbMnO_3$ and $MnWO_4$ using neutron scattering techniques, second-harmonic generation (SHG) measurements, and dielectric spectroscopy [17–21]. The relaxation behavior in both systems differs significantly as a function of temperature and electric-field amplitude [18–20]. In $MnWO_4$ domain inversion speeds up, when cooling towards the lower commensurate magnetic phase [18,21], which is attributed to depinning of multiferroic domains by anharmonic modulations [22,23]. In $TbMnO_3$ the domain inversion can be well described by a remarkably simple law combining an Arrhenius-type activated temperature dependence with a field dependence following the Merz law established for ferroelectrics [20]. In contrast to $MnWO_4$, the incommensurate long-range order in multiferroic $TbMnO_3$ does not transform into a commensurate arrangement [24,25] but is only altered through the additional order of Tb^{3+} moments [26]. Apparently, competing incommensurate and commensurate ordering significantly influence the relaxation behavior of multiferroic domain inversion and thus complicate its description [23]. Therefore, multiferroic materials with simple phase diagrams are desirable for further investigations of multiferroic domain dynamics.

The broad class of pyroxenes with chemical formula $AMeX_2O_6$ with $A =$ Li, Na, Sr, or Ca, $X =$ Si or Ge, and *Me* a magnetic transition metal exhibit several interesting magnetic ordering phenomena, with controllable ferrotoroidicity in $LiFeSi_2O_6$ [27,28] and multiferroic phases in $NaFeSi_2O_6$ [27], in $NaFeGe_2O_6$ [29] and in $SrMnGe_2O_6$ [30] being the most prominent ones. In spite of the similar monoclinic crystal structure with magnetic zigzag chains running along the *c*

---

[*] biesenkamp@ph2.uni-koeln.de
[†] braden@ph2.uni-koeln.de

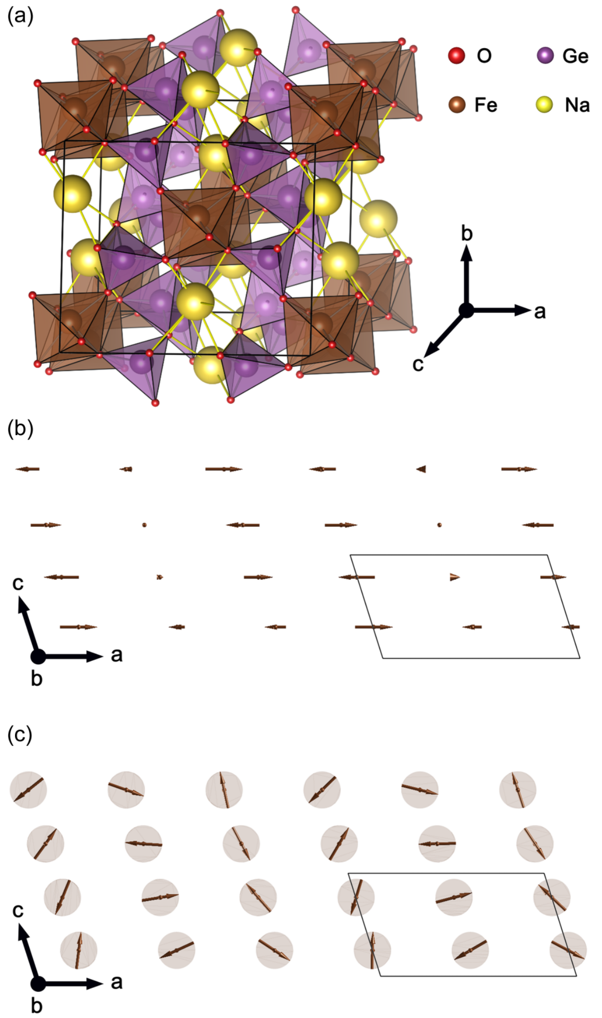

FIG. 1. The nuclear structure (with data from Ref. [35]) is shown in (a) by utilizing the crystallographic visualization software VESTA3 [38]. Both (b) and (c) sketch the magnetic structure of the intermediate SDW phase and of the low-temperature spin-spiral phase, respectively.

direction (see Fig. 1), the multiferroic mechanism is different in these three pyroxenes. In $NaFeSi_2O_6$ two successive transitions involving the same irreducible representation result in a helical structure with the propagation vector along the monoclinic axis [31]. In this material multiferroic order does not result from the spin current or inverse Dzyaloshinski-Moriya mechanism [14–16,32] but from the combination of the chiral order and the monoclinic distortion. In contrast, multiferroic order in $SrMnGe_2O_6$ [30] and in $NaFeGe_2O_6$ [33] seems to follow the most common inverse Dzyaloshinski-Moriya mechanism [14–16,32] but with differently oriented cycloidal and ferroelectric order.

$NaFeGe_2O_6$ exhibits the sequence of two incommensurate ordered phases that is characteristic for many type-II multiferroics, and there is just one magnetic site [29,33–36]. The system crystallizes in the monoclinic space group $C2/c$ with $a = 10.0073(8)$ Å, $b = 8.9382(7)$ Å, $c = 5.5184(4)$ Å, and $\beta = 107.524(1)^\circ$ [35,37]. Edge-sharing FeO_6 octahedra form zigzag chains along the c direction. These chains are separated by corner-sharing GeO_4 tetrahedra that are also stacked along the c axis (see Fig. 1). Below $T \approx 35$ K, short-range ordering was observed and two different magnetic phases with incommensurate long-range order were reported for $NaFeGe_2O_6$ with transition temperatures at $T_N \approx 13$ K and $T_{MF} \approx 11.6$ K [33–36]. First at T_N an incommensurate spin-density wave (SDW) evolves with moments pointing roughly along the a direction [33] and below T_{MF}, spins form a chiral spin structure with moments lying within the ac plane [34,35]. A small b component of the chiral structure was controversially discussed [34,35], and in [35] only a single transition is observed. Simultaneous to the onset of the chiral spin arrangement, a ferroelectric polarization ($\boldsymbol{P} \approx 32\ \mu\mathrm{C\,m}^2$) develops [29,36]. The ferroelectric polarization is confined to the ac plane as the given symmetry forbids a nonzero component of the polarization along b [33] (see Sec. III), but symmetry allows for a finite b component of the chiral spin structure.

The absence of a competing commensurate phase makes $NaFeGe_2O_6$ an ideal candidate to investigate multiferroic domain dynamics. In the following sections we will first discuss the presence of the magnetic b component utilizing neutron polarization analysis. Subsequently, we will report on our investigations of multiferroic domain inversion in $NaFeGe_2O_6$. Finally, we will discuss the measured spin-wave velocity, which is proposed to limit the inversion speed of multiferroic domains.

II. EXPERIMENTAL METHODS

A detailed description of the $NaFeGe_2O_6$ single-crystal growth by the top seeding technique can be found in Ref. [36]. For our measurements, two single crystals (SI and SII) were prepared and had been characterized by susceptibility measurements utilizing a commercial superconducting quantum interference device (SQUID) magnetometer. For both samples the transition temperatures are slightly reduced to $T_N \approx 12.5$ K and $T_{MF} \approx 11.1$ K with respect to literature [36]. In order to apply electric fields to the system, both samples were mounted between aluminium plates, which can be connected to a high-voltage setup. The ferroelectric polarization is largest along the a direction [36] and the plate normal was oriented parallel to a^*. The sample surface was thinly coated with silver paste for optimized electric contact and the aluminum plates were tightened together by insulating polytetrafluorethylene (PTFE) screws (see Ref. [20]). The plates that are cramping the respective sample were connected to sample holders defining the scattering geometry (1 0 0)/(0 0 1) for sample SI and (1 0 0)/(0 1 0) for sample SII.

Neutron polarization analysis senses the different components of the magnetic structure and the sign of the vector chirality. The respective experiments were performed at the cold three-axes spectrometer IN12 (located at the Institut Laue-Langevin) and at the cold three-axes spectrometer 4F1 (located at the Laboratoire Léon Brillouin).

At IN12, a horizontally and vertically focusing pyrolytic graphite (002) monochromator supplied $\lambda = 3$ Å and a supermirror cavity provided a highly polarized neutron beam (flipping ratio of about FR ≈ 4). Higher-order contaminations were suppressed by a velocity selector. The IN12 spectrometer was also equipped with a Helmholtz-coil setup in order to define the guide-field direction at the sample position, and spin flippers before and after the sample position enabled longitudinal polarization analysis. A curved Heusler (111) analyzer selected the final beam polarization. For studying the multiferroic domain distribution we used the full polarization analysis, although these experiments can also be performed in a half-polarized mode. However, the full analysis yields a better background. The correction for finite neutron polarization was done following [39], whereby due to the high total flipping ratio the impact of this correction is negligible.

In the absence of external electric fields, the multiferroic polarization and the chirality of the magnetic structure will not be uniform, but domains with opposite polarization and chirality will form. Multiferroics can, however, be poled by cooling in large external electric fields applied along the ferroelectric polarization [22,40,41] resulting in an almost monodomain state. In our experiments on $NaFeGe_2O_6$ we always applied the external electric field along the a^* direction.

A conventional high-voltage generator (FUG HCP 14-3500) was deployed for measurements with quasistatic electric fields ($|U| \leqslant 3.5\,\mathrm{kV}$) but a stroboscopic high-voltage setup was used for the time-resolved investigation of the multiferroic domain relaxation. This setup contains two high-voltage modules (ISEG BPP4W and ISEG BPN4W) providing high voltage ($|U| \leqslant 4\,\mathrm{kV}$) with opposite polarity and a fast MOSFET array (BEHLKE HTS-111), which is capable to switch the high-voltage output polarity with 50 μs [20]. For $TbMnO_3$ rapid electric-field-driven relaxation was indeed observed at these timescales [20].

A multichannel data collector (MESYTEC MCPD-8) records all detector events as well as a synchronization signal, when the polarity of the applied electric field is switched. All events are recorded together with a time stamp, which allows one to periodically switch the field, while summing the detected neutrons in time bins with respect to the moment when the field is reversed. This stroboscopic method thus enables one to investigate very fast relaxation processes because the width of each time bin can be arbitrarily selected, while repeating the switching periodically yields the required statistics. The time resolution is limited by the finite spreads of neutron velocities and path lengths. Reference [20] gives a detailed description of this setup and of the stroboscopic technique.

For long relaxation times above several minutes, the counting statistics obtained during a single switching period is sufficient and does not require the stroboscopic setup. The respective measurements of long relaxation times were performed at the cold three-axes spectrometer 4F1. A double pyrolytic graphite monochromator setup supplied $\lambda = 4.2$ Å and a supermirror bender polarized the neutron beam (flipping ratio of about FR ≈ 50). For polarization analysis, a MuPad system [42] and a horizontally curved Heusler analyzer were installed. In order to measure the spin-wave velocity, a polarized beam is not required and the respective experiment was conducted at the 4F2 spectrometer. The double pyrolytic-graphite monochromator provided an unpolarized neutron beam with $\lambda = 4.05$ Å and the pyrolytic-graphite analyzer enables inelastic measurements, for which a cooled Be filter was additionally inserted.

III. MAGNETIC STRUCTURE

So far, the magnetic structure of $NaFeGe_2O_6$ was not yet fully characterized as a b component of the chiral spin structure was controversially discussed [34,35] and as the reported determination of the intermediate structure was only based on neutron powder diffraction experiments [33,34]. The neutron polarization analysis on single crystals permits a precise separation of magnetic components and unambiguous identification of chiral signatures.

The symmetry conditions of incommensurate magnetic order with a propagation vector $\boldsymbol{k} = (k_h\, 0\, k_l)$ have been discussed for $NaFeGe_2O_6$ in Ref. [33]; they are furthermore identical to those in multiferroic $LiFe(WO_4)_2$ [43,44]. In space group $C2/c$ only one symmetry element has to be considered, the glide-mirror plane c, which transforms (m_x, m_y, m_z) into $(-m_x, m_y, -m_z)$. Therefore, it is obvious that magnetic x, z, and y components are separated. The character concerning this c element is ± 1 up to the phase correction. The inverse of this phase enters the basis vector components for the second site. In the magnetic superspace group formalism all magnetic moments are developed in cosine and sine series starting from the atoms in the primitive unit cell. Here we have two magnetic ions in the unit cell and the coefficients of these two are not independent but determined through the condition that the moment at $-\mathbf{r}$ and $-x_4$ (the argument of the modulation functions) is identical to the moment at $\mathbf{r}$ and x_4, which is just the inversion symmetry [45]. Therefore, only one set of cosine and sine functions is required in the harmonic description. For one-dimensional irreducible representations, as it is the case here, there is a one-to-one correspondence between irreducible representation and magnetic superspace group formalisms, but the representation analysis leaves the phases undefined, while magnetic superspace group analysis fixes these phases, leaving only three free parameters for each of the magnetic modes [45]. The symmetry of the two different incommensurate magnetic modes is given in Table I.

The magnetic superspace group analysis explains that a multiferroic cycloid cannot be obtained with a single symmetry mode, as the inversion symmetry is not broken [45]. One may also argue that in each of the two modes, the x and z components are modulated in phase, while x, z, and y components have a different character between the two sites so that any spin-current contributions cancel out, as it is also the case in the intermediate phase in $MnWO_4$ [46]. In order to generate cycloidal order, one needs to couple two magnetic modes with a phase shift of $(\frac{\pi}{2} + n\pi)$ by either combining the two different magnetic modes or by combining twice the same mode with the phase shift. In the former case, the glide-mirror symmetry is lost and ferroelectric order appears along the b direction as in $LiFe(WO_4)_2$ [43,44], while in the latter case the mirror plane persists and enforces ferroelectric polarization in the a, c plane [33]. This is the situation in the multiferroic phase of $NaFeGe_2O_6$.

Magnetic scattering will only arise from magnetic components perpendicular to the scattering vector and spin-flip (SF) processes necessitate a component of the magnetization

TABLE I. Symmetry conditions for the two incommensurate magnetic modes that can appear for a propagation vector $\boldsymbol{k} = (k_h\ 0\ k_l)$ in the space group $C2/c$ with a single magnetic ion at (0,0.904,0.25). The conditions are defined by the irreducible representation Γ_1 and Γ_2 and the corresponding basis vectors for the two Fe sites are given with $a = e^{i2\pi\delta\mathbf{r}\mathbf{q}_{\mathbf{inc}}}$. Here $\delta\mathbf{r} = \mathbf{r}_2 - \mathbf{r}_1$ and $a^* = 1/a$ is the complex conjugate of a. Representation analysis and superspace group formalism are equivalent in the case of $NaFeGe_2O_6$, but the superspace group formalism fixes the phases between modulations so that for each of the two modes the magnetic structure is described by only three parameters corresponding to either cosine or sine modulations. The resulting superspace groups for a single mode are given in the last column.

Γ	1	c	(x, y, z)	$(x, \bar{y}, z + 1/2)$	Coefficients	Character	Superspace group
Γ_1	1	$-a$	(u, v, w)	$a^*(u, -v, w)$	Re(u)Im(v)Re(w)	cos/sin/cos	$C2/c1'(\alpha 0 \gamma)0ss$
Γ_2	1	a	(u, v, w)	$a^*(-u, v, -w)$	Im(u)Re(v)Im(w)	sin/cos/sin	$C2/c1'(\alpha 0 \gamma)00s$

perpendicular to the direction of the incoming beam polarization. In contrast, non-spin-flip (NSF) processes only sense components that are aligned parallel or antiparallel to the incoming neutron beam polarization. This allows one to distinguish the different components of the $\boldsymbol{Q}$th Fourier component of the magnetization density given by

$$\boldsymbol{M}(\boldsymbol{Q}) = \int \boldsymbol{M}(\boldsymbol{Q})\exp(i\boldsymbol{Q}\boldsymbol{r})d^3r. \qquad (1)$$

For neutron polarization analysis it is convenient to define a right-handed coordinate system, where the x direction is set parallel to the scattering vector $\boldsymbol{Q}$, y is perpendicular to x but confined to the scattering plane, and z is perpendicular to both x and y. I_{ij} denotes the scattering intensity for the neutron polarization changing from i to j with $i, j = x, y, z, \bar{x}, \bar{y}, \bar{z}$ (the overbar signifies antiparallel polarization). With the longitudinal polarization setup, only the diagonal terms are accessible.

During the first part of the allocated beam time at IN12, sample SI with scattering geometry (1 0 0)/(0 0 1) was mounted. Both components of the incommensurate propagation vector $\boldsymbol{k} = (k_h\ 0\ k_l)$ could be traced as a function of temperature. For the respective measurements, Q_h and Q_l scans were executed across the magnetic reflection $\boldsymbol{Q} = (0.678\ 0\ -1.075)$ and each Q scan was fitted by a Gaussian function. Exemplary scans for different SF channels are shown in Fig. 2. It can be seen that the crystal is twinned, which, however, does not affect the following analysis as consistently only the peak from the same twin was considered during the experimental courses. The observed peak center values were considered for defining the scan of the following step in temperature. Figures 2(c) and 2(d) display the obtained temperature-dependent values for k_h and k_l, and it can be seen that both components vary with temperature but lock in a constant value at $T \approx 5$ K. The results qualitatively agree with the reported temperature dependence of the incommensurate propagation vector in Ref. [35].

The used scattering geometry entails that the SF channels are described by $I_{\bar{y}y} \propto M_b M_b^*$ and $I_{\bar{z}z} \propto M_{ac} M_{ac}^* \sin^2(\alpha)$ with M_b and M_{ac} being the complex Fourier components of the magnetization along b direction and within the ac plane, respectively, and $\sin^2(\alpha)$ being the geometry factor. a and a^* are not parallel in the monoclinic system, but in the used scattering geometry both are lying within the scattering plane. The same holds for c and c^*. Due to the incommensurability of the magnetic structure, no nuclear signal contributes to the measured intensity. The SF channels $I_{\bar{x}x}$ and $I_{x\bar{x}}$ are described by

$$I_{\bar{x}x}, I_{x\bar{x}} \propto \boldsymbol{M}_\perp \boldsymbol{M}_\perp^* \pm i(\boldsymbol{M}_\perp \times \boldsymbol{M}_\perp^*)_x, \qquad (2)$$

with $\boldsymbol{M}_\perp$ the projection of the Fourier component $\boldsymbol{M}(\boldsymbol{Q})$ perpendicular to the scattering vector, but as the scattering vector

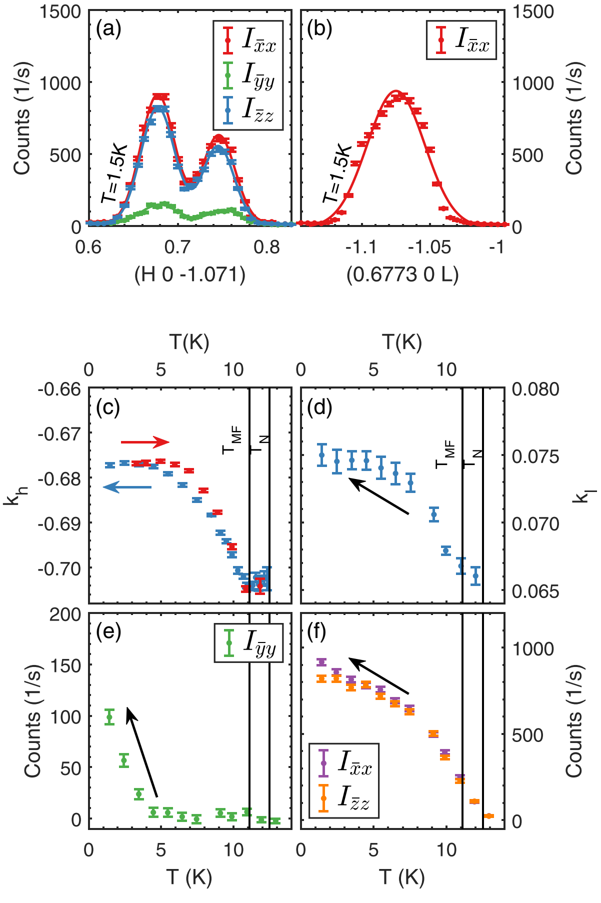

FIG. 2. (a), (b) Display exemplary Q_H and Q_L scans for different SF channels. The temperature-dependent components k_h and k_l of the propagation vector $\boldsymbol{k} = (k_h\ 0\ k_l)$ are, respectively, shown in (c) and (d). The blue and red data correspond to cooling and heating sequences, respectively. In (e) and (f) the peak intensity of reflection $\boldsymbol{Q} = (0.678\ 0\ -1.075)$ is plotted for all SF channels as function of temperature. All intensities were corrected for the finite flipping ratio and all measurements were performed on sample SI.

lies within the basal plane of the chiral spin structure the chiral term vanishes. The intensity of all three SF channels is plotted in Figs. 2(e) and 2(f). It can be clearly seen in Fig. 2(c) that $I_{\bar{y}y}$ exhibits finite intensity only below $T \approx 5$ K thus indicating the development of a finite b component of the magnetic structure within the multiferroic phase of $\mathrm{NaFeGe_2O_6}$, but exclusively at low temperature. The onset of this component coincides with the lock-in temperature of the incommensurate propagation vector. Figure 2(f) shows that below the first transition at T_N, the total magnetic scattering signal $I_{\bar{x}x}$ initially features the same amplitude as $I_{\bar{z}z}$, which senses the magnetic moments within the ac plane. This confirms that the magnetic structure is first confined to the ac plane until below $T \approx 5$ K the discrepancy between $I_{\bar{z}z}$ and $I_{\bar{x}x}$ also indicates the evolving b component of the magnetic structure. From this difference the magnitude of the b component can be estimated. A single-crystal refinement yielded $4.09(4)\mu_\mathrm{B}$ [35] for the total magnetic moment and when considering a perfect circular spiral, the averaged moment along the principal axis becomes $4.09/\sqrt{2}\mu_\mathrm{B} \approx 2.89\mu_\mathrm{B}$. Its square value is sensed by $I_{\bar{x}x}$ and as $I_{\bar{y}y} \propto m_b^2$ is approximately 10% of $I_{\bar{x}x} = I_{\bar{y}y} + I_{\bar{z}z}$ [see Figs. 2(e) and 2(f)], the magnetic component along b direction can be estimated to $m_b \approx \sqrt{0.1 \times 2.89^2}\mu_\mathrm{B} \approx 0.89\mu_\mathrm{B}$. The developing b component agrees with the discussed and underlying superspace symmetry, which confines the electric polarization to the ac plane [33].

Sample SII was mounted with scattering geometry (1 0 0)/(0 1 0) and no twinning was observed for this specimen. In this configuration the SF channels $I_{\bar{y}y}$ and $I_{\bar{z}z}$ sense the magnetization along the c direction and within the a^*, b plane, respectively. The magnetic reflection $\boldsymbol{Q} = (0.32\ 3\ 0.08)$ is not directly accessible within the given scattering plane but the finite l value can be reached by tilting the goniometer by ≈3°, which does not have significant impact on the analysis of respective SF and NSF channels. The temperature dependence of both SF channels is plotted in Fig. 3(a) and it is visible that the c component of the magnetic structure mainly develops below the second transition T_MF but, nevertheless, finite intensity and thus a nonzero component along c is also present in the intermediate phase. The chiral spin structure in the multiferroic phase thus exhibits moments in the ac plane with an additional b component, which develops below $T \approx 5$ K. In the intermediate phase between $T_\mathrm{N} = 12.5$ K and $T_\mathrm{MF} = 11.1$ K the SF channel $I_{\bar{z}z}$ possesses extensive intensity compared to $I_{\bar{y}y}$ and as the angle between $\boldsymbol{Q}$ and b amounts to approximately 6.9°, the SF channel $I_{\bar{z}z}$ essentially senses the component parallel to a^* [note that $\sin^2(6.9^\circ) \approx 0.014$]. With results from both scattering geometries it can be concluded that the SDW structure exhibits moments $\boldsymbol{m}$ that are lying essentially in the a, c plane and we determine this angle by

$$\measuredangle(\boldsymbol{m}, \boldsymbol{a}^*) = \tan^{-1}\left(\frac{m_c}{m_{a^\star}}\right) \approx \tan^{-1}\left(\sqrt{\frac{I_{\bar{y}y}}{I_{\bar{z}z}}}\right) \tag{3}$$

to amount to ≈17°.

The scattering vector in the scattering configuration of sample SII is almost perpendicular to the basal plane of the chiral structure. Therefore, the chiral term $\pm i(\boldsymbol{M}_\perp \times \boldsymbol{M}_\perp^*)_x$ is finite and contributes to both SF channels $I_{x\bar{x}}$ and $I_{\bar{x}x}$ with a different sign. Hence, the sum and the difference of $I_{x\bar{x}}$ and $I_{\bar{x}x}$ are given by $2\boldsymbol{M}_\perp\boldsymbol{M}_\perp^*$ and by the absolute value of $-2i(\boldsymbol{M}_\perp \times \boldsymbol{M}_\perp^*)_x$, respectively. Both the sum and the difference of $I_{x\bar{x}}$ and $I_{\bar{x}x}$ are plotted in Fig. 3(b) as a function of temperature and it can be seen that the chiral signal develops only below T_MF within the multiferroic phase. The chiral ratio is defined as

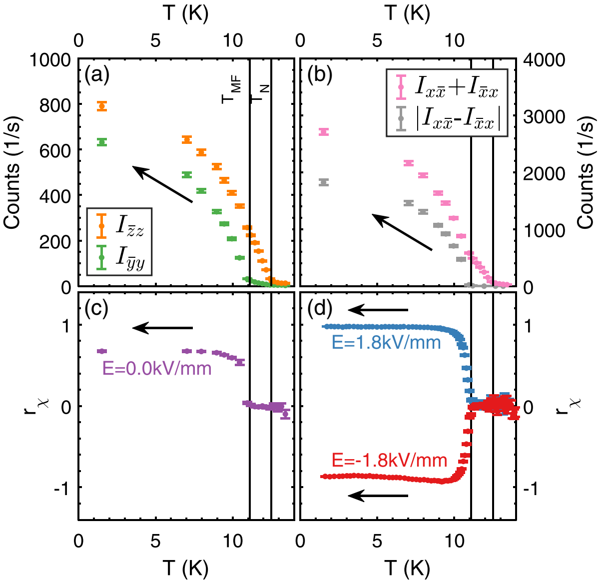

FIG. 3. Polarized neutron scattering in (1 0 0)/(0 1 0) geometry. The temperature dependence of SF channels measured at $\boldsymbol{Q} = (0.32\ 3\ 0.08)$ is shown in (a) and (b). The Q-space position was adjusted with the determined temperature-dependent values of the incommensurate propagation vector [see Figs. 2(c) and 2(d)]. In both (c) and (d) the chiral ratio is plotted as a function of temperature and for different electric-field amplitudes applied along $a^\star$.

$$r_\chi = (I_{x\bar{x}} - I_{\bar{x}x})/(I_{x\bar{x}} + I_{\bar{x}x}) \tag{4}$$

and for a monodomain sample it corresponds to $\pm i(\boldsymbol{M}_\perp \times \boldsymbol{M}_\perp^*)_x/|\boldsymbol{M}_\perp|^2$, the ratio of the chiral part with respect to the overall magnetic scattering contribution. The chiral ratio amounts to ±1 only for a completely poled multiferroic state with ideal geometry. However, as the scattering vector $\boldsymbol{Q}$ is not perfectly oriented perpendicular to the rotation plane of spins, and due to ellipticity the chiral ratio remains below one. In Fig. 3(c) the chiral ratio is plotted and it can be seen that even in the absence of an applied electric field, the chiral ratio possesses a finite value within the multiferroic phase and thus indicates an unbalanced domain distribution of multiferroic domains [22,44]. The quasistatic control of the chiral handedness and the multiferroic domain population by external electric fields is discussed in the following section.

IV. QUASISTATIC CONTROL OF MULTIFERROIC DOMAINS

A static electric field with $|E| = 1.8\ \mathrm{kV\,mm^{-1}}$ was applied, while cooling the sample. The chiral ratio was measured simultaneously and its temperature dependence is shown in

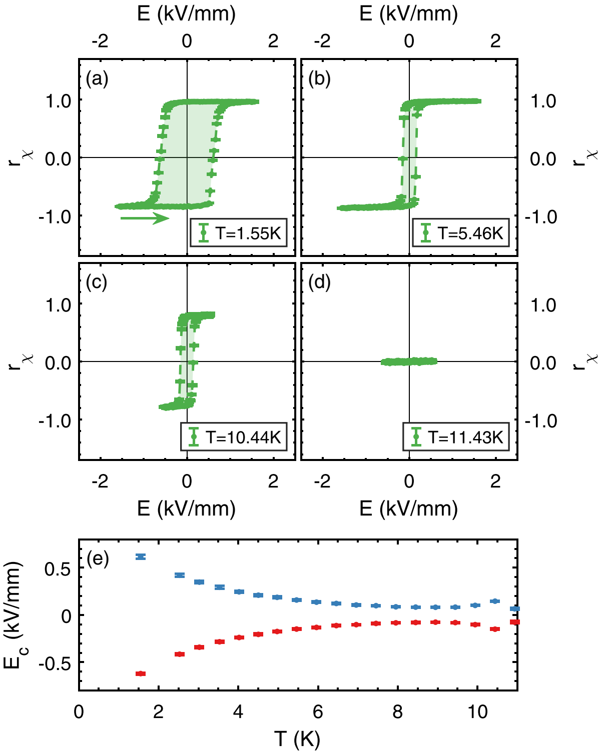

FIG. 4. All recorded hysteresis loops of the chiral ratio shown in (a)–(d) were obtained by driving the applied external electric field (along $a^\star$) slowly (with a period duration of about 45 min) between the two polarities. Both slopes of each hysteresis loop were fitted by a hyperbolic tangent in order to estimate the values of respective coercive fields, which are plotted in (e).

Fig. 3(d) for both field polarities. It can be seen that the chiral ratio reaches the maximum values of $\approx \pm 1$ already slightly below T_{MF}, which indicates a completely poled multiferroic domain distribution and a circular cycloid. This result illustrates the power of polarized neutron diffraction to solve chiral structures, as only the combination of twice the same magnetic mode can cause a chiral signal in this configuration. The chiral phase in $\mathrm{NaFeG_2O_6}$ thus must arise from a single irreducible representation similar to $\mathrm{NaFeSi_2O_6}$ [31] but the orientation of the propagation vector differs. An opposite-field polarity entails a reversed chiral ratio and an equivalent temperature dependence documenting the controllability of multiferroic domains with applied electric fields in $\mathrm{NaFeGe_2O_6}$. The behavior does not significantly change when lowering the field amplitude to $|E| = 1.2\,\mathrm{kV\,mm^{-1}}$ and $|E| = 0.6\,\mathrm{kV\,mm^{-1}}$. In order to quantify the respective values and the temperature dependence of the electric-field amplitude that is needed to reverse the chirality, quasistatic hysteresis loops have been recorded.

Figure 4 displays hysteresis loops of the chiral ratio for different temperatures. The electric field was driven quasistatically between the two polarities corresponding to a period of about 45 min for the entire hysteresis loops and $I_{x\bar{x}}$ and $I_{\bar{x}x}$ were recorded at each field value. The sign of the vector chirality is invertible down to the lowest temperature at $T = 1.55\,\mathrm{K}$. While approaching the transition to the intermediate phase, the saturation value of the chiral ratio shrinks slightly and abruptly vanishes, when heating above the multiferroic transition. This was also observed by the cooling sequences with applied static fields [see Fig. 3(d)]. The coercive fields that are needed to invert the sign of the chiral ratio in positive or negative direction were determined by fitting both slopes of the hysteresis loops with a hyperbolic tangent. The obtained coercive fields are plotted in Fig. 4(e) as a function of temperature. The coercive fields exhibit a symmetric temperature dependence with the smallest values close to the multiferroic transition.

V. MULTIFERROIC DOMAIN RELAXATION

In order to investigate the relaxation of multiferroic domains in $\mathrm{NaFeGe_2O_6}$, while triggering the inversion of domains by external electric fields, the stroboscopic setup was installed at IN12 (see Sec. II). The switching curves of the chiral ratio were recorded for different temperatures and a variety of electric-field amplitudes on sample SII. For each data set with fixed temperature and electric field, we recorded the $I_{x\bar{x}}$ and $I_{\bar{x}x}$ channels as a function of the temperature offset with respect to the field inversion. Figure 5 displays six exemplary switching curves and it can be seen by comparing the panels horizontally that the relaxation time significantly decreases when increasing the temperature. Moreover, the vertical arrangement of panels in Fig. 5 displays the field dependence of the relaxation processes. It can be seen that the electric-field strength at fixed temperature also strongly influences the relaxation processes. For all recorded curves, there is no asymmetric relaxation behavior concerning the electric field polarity.

The relaxation process can be described by an exponential relaxation in both directions [20]:

$$r_\chi(t) = r_a - (r_a - r_b)\exp\left[-\left(\frac{t}{\tau_a}\right)^{b_1}\right], \tag{5}$$

$$r_\chi(t) = r_b - (r_b - r_a)\exp\left[-\left(\frac{t - t_{1/2}}{\tau_b}\right)^{b_2}\right]. \tag{6}$$

Both parameters τ_a and τ_b are the characteristic relaxation times describing the inversion of the chiral ratio from r_a to r_b and from r_b to r_a, respectively. Here, $t_{1/2}$ accounts for the reversal of the electric field after half the period. Considering the Ishibashi-Takagi theory, which is based on the Avrami model, the stretching exponents b_1 and b_2 describe the dimensionality of the domain wall motion [47–51]. Both stretching exponents vary between 1 and 2.5, thus indicating low-dimensional domain growth. Approaching T_{MF} or enhancing the field amplitude result in larger stretching exponents, suggesting a higher growth dimensionality or possibly additional nucleation processes. A similar behavior was observed for $\mathrm{TbMnO_3}$ [20].

The investigation of long relaxation times (>1 min) does not require the stroboscopic setup, as sufficient statistics are reached during a single switching period. The respective measurements were performed at 4F1. Two switching curves are exemplarily shown in Fig. 6 for an electric-field

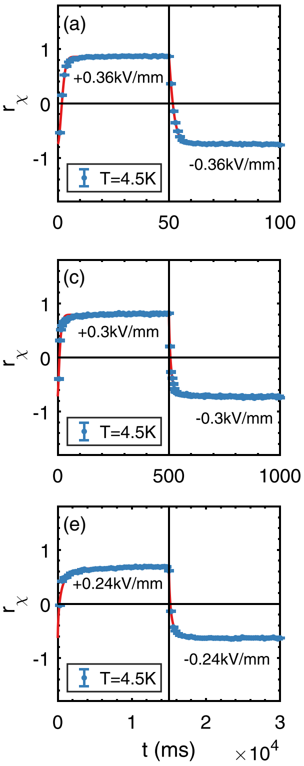

FIG. 5. All displayed switching curves in (a)–(f) were recorded by utilizing the stroboscopic method at IN12 and by measuring on sample SII. The blue data points refer to the recorded chiral ratio and the red line corresponds to the fit. The time dependence of the applied electric field follows a rectangular shape with inversion at the beginning and in the middle of each panel.

amplitude of $|E| = 0.12\,\mathrm{kV\,mm^{-1}}$. Although the experiment was performed on the same sample SII, the curves exhibit an asymmetric relaxation behavior contrary to the recorded curves from the IN12 experiment. The system was short circuited at room temperature and during the cooling procedure but nevertheless this asymmetry can be due to residual frozen-in charges or from effective pinning at defects, which provoke a preferred sign of the vector chirality in the multiferroic phase [22]. Moreover, both curves possess a kink after the second field inversion, which can be related to a time-delayed second nucleation process. However, this effect was resolvable only for the several orders of magnitude slower relaxation processes that were investigated during the 4F1 beamtime.

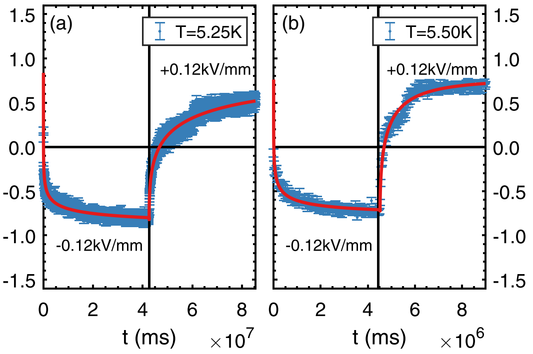

FIG. 6. At 4F1 the relaxation processes of the chiral ratio, which is plotted in (a) and (b), were recorded by counting both SF channels $I_{x\bar{x}}$ and $I_{\bar{x}x}$ as a function of time. The electric field ($|E| = 0.12\,\mathrm{kV\,mm^{-1}}$) was manually switched after the saturation of the chiral ratio for the respective handedness was reached. For both curves, sample SII was measured.

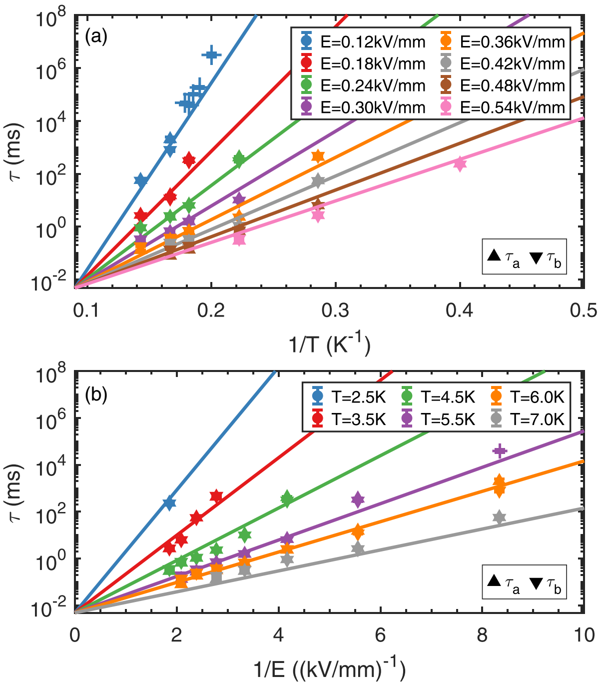

FIG. 7. (a), (b) Display the temperature- and electric-field-dependent relaxation times, respectively. Up and down triangles refer to τ_a and τ_b from IN12 data, whereas crosses correspond to τ_a from the recorded 4F1 data. The whole IN12 data set was fitted simultaneously by the combined Arrhenius-Merz law [see Eq. (7)] and the plotted colored solid lines refer to the fit results shown for fixed electric fields in (a) or fixed temperatures in (b). The 4F1 data were not included to the fit.

Figure 7 displays the fitted relaxation times τ_a and τ_b [see Eqs. (5) and (6)] as a function of inverse temperature and of inverse field with a logarithmic scaling. Up and down arrows mark the fitted relaxation time from IN12 data for switching the electric field to positive and negative values, respectively. The crosses in Figs. 7(a) and 7(b) mark the fitted relaxation times, which have been obtained from the 4F1 experiment. Combining both experiments at IN12 and 4F1 it is possible to follow the multiferroic relaxation over seven orders of magnitude in time as a function of temperature and electric field.

The multiferroic domain relaxation in TbMnO$_3$ [20] follows a combined Arrhenius-Merz law as a function of temperature and electric field:

$$\tau(E,T) = \tau^*\exp\left(\frac{A_0 T_r}{ET}\right) \quad \text{with } T_r = \frac{T_{\mathrm{MF}} - T}{T_{\mathrm{MF}}}. \tag{7}$$

Here τ^* denotes the fastest possible relaxation time that can be reached at the multiferroic phase transition T_{MF} or at infinitely large fields, and A_0 is the activation constant. Thus, τ^* and A_0 are the only two parameters needed to describe the field and temperature dependence of the relaxation. For TbMnO$_3$ the parameters amount to $\tau^* = 0.72\,\mathrm{ms}$ and $A_0 = 1483\,\mathrm{K\,kV\,mm}^{-1}$ [20]. This combined Arrhenius-Merz relation describes multiferroic relaxation in the E,T range, where it is determined by classical domain wall motion. In the studied E, T range, the multiferroic relaxation in TbMnO$_3$ deviates from the combined Arrhenius-Merz law only when approaching the multiferroic transition, as additional nucleation processes seem to accelerate the domain inversion.

For NaFeGe$_2$O$_6$ all relaxation times obtained from IN12 data were simultaneously fitted with the combined Arrhenius-Merz law. The 4F1 data were excluded from the fit as even a tiny temperature offset between both instruments due to different sample sticks and temperature calibration has significant impact on the fit result. Furthermore, the asymmetry of relaxation and the second nucleation process complicate the precise determination of relaxation times. Nevertheless, the temperature- and electric-field-dependent relaxation times τ_a from 4F1 data are included in Fig. 7 (see crosses). Due to the observed asymmetry for long relaxation times only τ_a is plotted, whereas τ_b is approximately one order of magnitude larger.

Solid lines in Figs. 7(a) and 7(b) correspond to the fit result for different temperatures and different electric-field amplitudes. It is clearly visible that the multiferroic relaxation behavior in NaFeGe$_2$O$_6$ is also well described by this combined activation law requiring only two parameters. The obtained critical relaxation time τ^* and the activation constant A_0 amount to $\tau^* = 0.0049(12)\,\mathrm{ms}$ and $A_0 = 19.5(9)\,\mathrm{K\,kV\,mm}^1$. Both values are much smaller than those observed in TbMnO$_3$ [20]. The roughly two orders of magnitude smaller τ^* value indicates a faster domain wall motion in NaFeGe$_2$O$_6$ which will be shown below to be consistent with the spin-wave velocity. The slower processes in TbMnO$_3$ can stem from the pronounced ellipticity of the chiral structure that implies anharmonicities and damping of the magnetic excitations [52]. The smaller activation parameter in NaFeGe$_2$O$_6$ indicates less pinning of the multiferroic order, which can be attributed to the much lower value of the ferroelectric polarization compared to TbMnO$_3$ [36].

During a second experiment at the IN12 spectrometer, the relaxation times at very low temperatures were further studied. Before this beam time, a tiny piece was cut from sample SII for other measurements and the sample contacts were renewed. With the restored sample setup a slightly different critical relaxation time and activation constant was observed but nevertheless both values [$\tau^* = 0.0125(18)\,\mathrm{ms}$ and $A_0 = 13.28(34)\,\mathrm{K\,kV\,mm}^{-1}$] are of the same order of magnitude compared to results from the first experiment. The measured relaxation times as well as the fit are shown in Fig. 8, and it can be seen that even at low temperature the relaxation follows the activation law indicating that no quantum effects dominate the relaxation behavior, which would lead to a saturation of the relaxation time. For fields between $E = 0.42\,\mathrm{kV\,mm}^{-1}$ and $1.02\,\mathrm{kV\,mm}^{-1}$, the domain wall motion in NaFeGe$_2$O$_6$ remains thus thermally activated and is not driven by domain wall tunneling down to $T = 1.5\,\mathrm{K}$. Domain wall tunneling was reported for magnetic and ferroelectric domain wall motion at low temperature [53–55]. In NaFeGe$_2$O$_6$, quantum effects can become relevant at even lower temperature and electric field values.

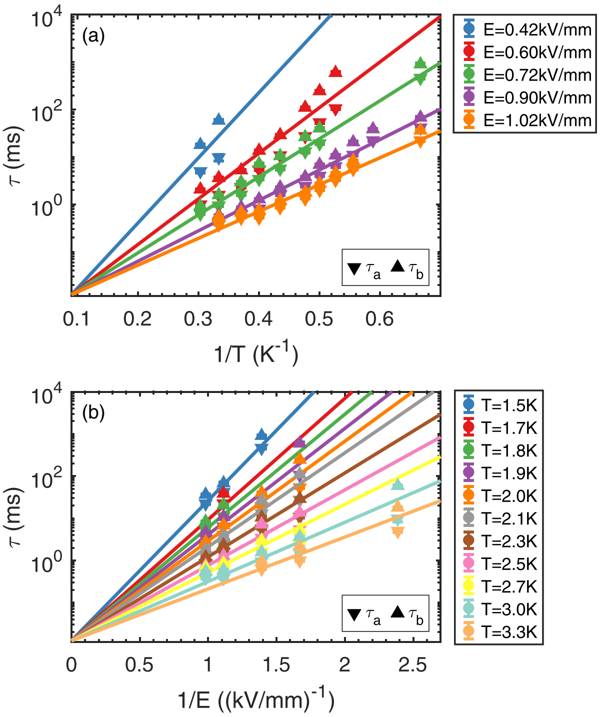

FIG. 8. Additional set of measurements of the relaxation times from a second experiment are displayed in (a) and (b). The combined Arrhenius-Merz law is valid even at very low temperatures. A slightly different activation constant and critical relaxation time with respect to results shown in Fig. 7 arise from a renewed sample setup (see text).

Some pure ferroelectrics [56,57] exhibit thermally activated relaxation following a scaling law $\tau(E, T) = \tau^*\exp(A_0 T_r/E)$, in which the relaxation only depends on the ratio T_r/E. The measurements on multiferroic TbMnO$_3$ [20] do not agree with this but follow a scaling with $T_r/(ET)$ as it results from the combined Arrhenius-Merz law. Figure 9 compares both scaling laws for NaFeGe$_2$O$_6$ and clearly shows that the combined Arrhenius-Merz law is the appropriate scaling description also for this material.

The relaxation of multiferroic domains differs from the relaxation behavior in conventional ferroelectrics [20,56,57]. In a ferroelectric material the nucleation process, the forward growth, and the subsequent sideways expansion of domains can equally contribute to the global domain relaxation process and thus render its description complicated [56,57]. In contrast, multiferroic domain inversion is dominantly determined by the slow sideways growth of domains [19,20,58,59]. Therefore, thermally activated domain wall motion and a combined Arrhenius-Merz law [20] describe the multiferroic domain inversion over a wide range of temperatures and fields, spanning over seven orders of magnitude in time. However, close to

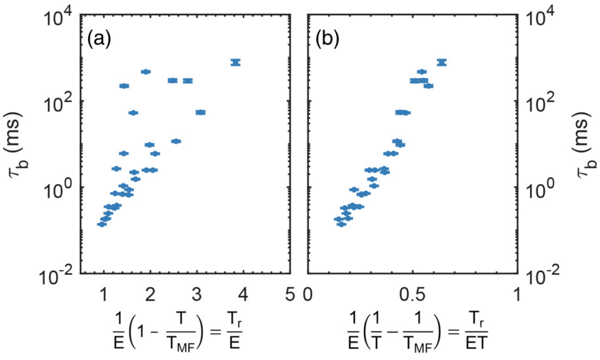

FIG. 9. The different scaling relations for the relaxation times shown in (a) and (b) clearly determine the combined Arrhenius-Merz law to be the correct description of the multiferroic domain inversion. For the comparison only IN12 data from the first experiment (see Fig. 7) were used.

the multiferroic transition and for very high fields, additional nucleation processes will accelerate the relaxation, and at very low temperatures and electric fields quantum tunneling can become relevant.

VI. SPIN-WAVE VELOCITY

Since the spin-wave velocity can limit the multiferroic domain wall motion [19,20] we analyzed the dispersion of acoustic magnon branches at the 4F2 triple-axis spectrometer. The respective measurements were carried out on sample SI, which was mounted with scattering geometry (1 0 0)/(0 0 1). For $\Delta E \geqslant 0.5$ meV, constant-energy scans were measured around the incommensurate zone center $\boldsymbol{Q} = (0.677\ \ 0\ 0.925)$ along H and L directions at $T = 3.9$ K. Below $\Delta E = 0.5$ meV it was not possible to separate the excitation from the elastic line due to the finite resolution. Figure 10 maps the measured scattering along both recorded directions. Respectively, two exemplary constant-energy scans are shown in Figs. 10(a) and 10(b). All constant-energy scans were fitted with two Gaussian functions and the obtained peak-center positions of excitations are marked by red data points in Figs. 10(c) and 10(d). The dispersion can be approximately described by $\omega(q) = \sqrt{(\Delta^2 + v_g^2 q^2)}$, with v_g the group velocity of the spin wave and Δ the gap energy. The fits for respective directions (red dashed lines in Fig. 10) yield $v_g = 662(19)\,\mathrm{m\,s^{-1}}$ along H, $v_g = 1460(36)\,\mathrm{m\,s^{-1}}$ along L and a spin gap of approximately 0.5(2) meV for both directions. The magnon dispersion is thus anisotropic with a steeper slope along the direction of zigzag chains, but this anisotropy is moderate and the material should not be considered as a low-dimensional system.

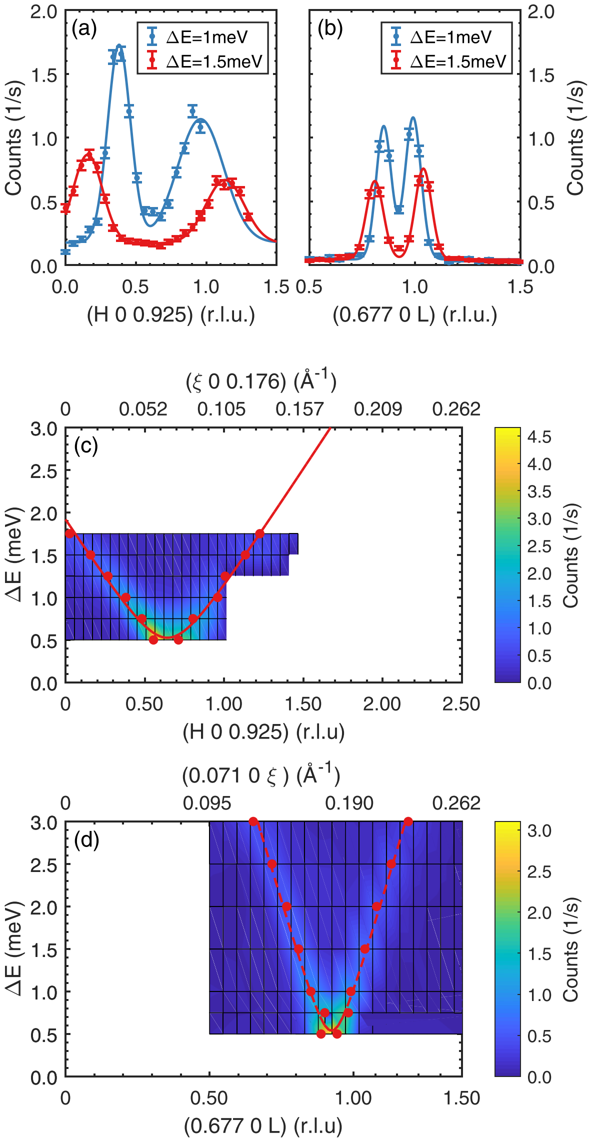

FIG. 10. The plots in a) and b) display exemplary two recorded constant-energy scans at $T = 3.9$ K around the incommensurate zone center $\boldsymbol{Q} = (0.677\ \ 0\ \ 0.9252)$ along H and L, respectively. Both panels c) and d) show the complete measured data sets, whereby red data points refer to the fitted peak maxima and the red lines correspond to fits of the respective dispersion.

We have calculated the spin-wave dispersion using the SPINW code [60], for which the result is shown in Fig. 11. So far, only for the pyroxene $\mathrm{SrMnGe_2O_6}$ a quantitative study of the magnon dispersion was reported [61] but this material exhibits already a different orientation of the propagation vector. We follow this $\mathrm{SrMnGe_2O_6}$ model, which takes three interaction parameters into account: the nearest-neighbor coupling J within the zigzag chains (distance 3.25 Å), the nearest interchain coupling J_1 (distance 5.64 Å), and the next-nearest interchain coupling J_2 [distance 6.70 Å corresponding to the (0.5 0.5 0) C translation]. All parameters correspond to the exchange interaction per bond. These interaction parameters were calculated for $\mathrm{NaFeGe_2O_6}$ by density functional theory [33]. Note that each Fe moment is coupled to two moments through J, to two moments through J_1, and to four moments through J_2. Since J_1 bases on two super-superexchange paths while J_2 bases only on a single path, one expects J_1 to be larger than J_2. Our inelastic neutron scattering data taken close to the $\mathrm{NaFeGe_2O_6}$ magnetic zone origin are not sufficient to

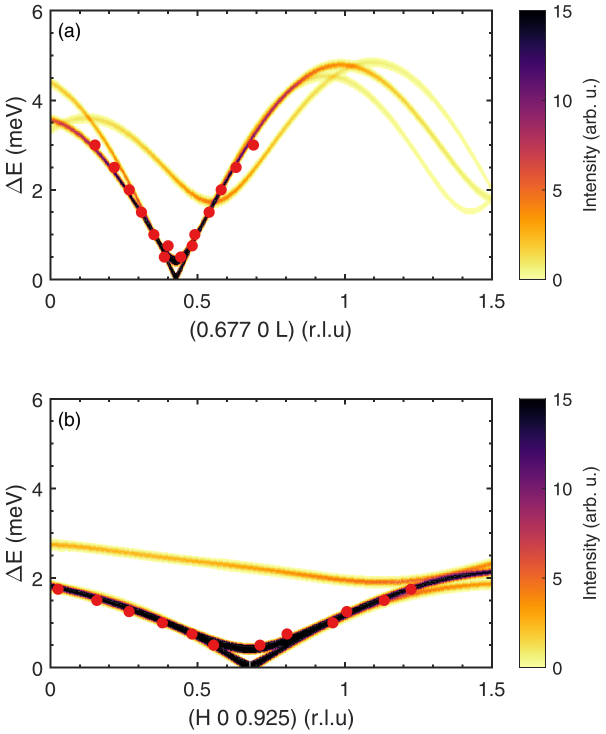

FIG. 11. Both panels show the calculated dispersion that was obatined by using *SpinW* code [60]. Hereby, the red data points correspond to the measured spin wave energies from Fig. 10.

fully solve the spin-wave dispersion of this incommensurate chiral system, for which locally transversal acoustic magnons have the character of a phason or are polarized perpendicular to the chiral plane [52,62]. Therefore, we restrict the freedom of the model. The ratio of J_1/J and J_2/J can be determined through the incommensurate propagation vector $\boldsymbol{k}_{\mathrm{inc}} = (k_h\ 0\ k_l)$ through

$$\frac{J_1}{J} = -\frac{\sin(\pi k_l)}{\sin[\pi(k_h + k_l)]}, \tag{8}$$

$$\frac{J_2}{J} = -\frac{1}{2}\frac{\sin(\pi k_l)}{\sin(\pi k_h)}. \tag{9}$$

This leaves J as the only coupling parameter to be determined; in addition, we introduce an easy-plane anisotropy term D that also stabilizes the chiral plane along the a, c plane. Figure 11 compares the calculated maps of scattering intensities with the determined spin-wave energies yielding a good description for the parameters: $J \approx 9.7$ K, $J_1 \approx 2.4$ K, and $J_2 \approx 1.3$ K and $D \approx 0.0464$ K, which qualitatively agree with the values calculated in [33]. The experimental parameters yield an antiferromagnetic Curie-Weiss temperature of 86 K in reasonable agreement with experiment. The determined J parameters reveal that the sum of interchain interaction is half as large as the intrachain interaction, which does not characterize $NaFeGe_2O_6$ as a low-dimensional system. But the interchain interaction normalized to J is even stronger for $SrMnGe_2O_6$ [61], which is thus even less low dimensional. The weakly anisotropic spin-wave dispersion seems to contrast with the magnetic susceptibility whose clear maximum at larger temperature strongly suggests a low-dimensional system. The short-range correlations are less three dimensional than the long-range order, which stems from the frustration of the two interchain interactions J_1 and J_2 [33] since these couple to the moments in the neighboring zigzag chain with and without a shift in chain direction, respectively. Since $J_2 \approx 1.3$ K coupling to twice as many sites amounts to nearly half the value of J_1, this frustration is rather perfect for a short-range correlation with strict up-down–up-down character along the chain. For the incommensurate long-range state the frustration is, however, much less effective as shown in the large spin-wave slope perpendicular to the chains. Short-range magnetic correlations and anharmonic modulation must sense a strong impact of this peculiar type of frustration.

The ferroelectric polarization is predominantly aligned along the a direction [36] and for all respective experiments on the multiferroic domain inversion, the electric field was applied parallel to a^*. In multiferroics the initial reverted regions extend along the direction of ferroelectric polarization and the subsequent sideways growth dominates the overall relaxation process [19,20]. Considering the determined spin-wave velocities, a single needle-shaped domain in the middle and the geometry of sample SII (for which the relaxation behavior was measured), the fastest possible domain relaxation is of the order of 10^{-3} ms, which agrees with the observed critical relaxation time τ^* (see Sec. V).

VII. CONCLUSION

We report investigations on the magnetic structure as well as on the multiferroic domain relaxation in $NaFeGe_2O_6$ utilizing neutron scattering experiments on single crystals. With neutron polarization analysis it is possible to separate the magnetic components of the long-range order in both phases. Thereby we can confirm the proposed incommensurate spin-density wave with moments along the a direction for the intermediate phase and a chiral spin structure with components along a and c below the multiferroic transition. In addition, there is a locking-in of the incommensurate propagation vector at $T \approx 5$ K accompanied with the emergence of a b component, whose presence was so far controversially discussed [34,35].

The multiferroic domain inversion was investigated by quasistatic as well as by time-resolved measurements of the vector chirality. Poling sequences and hysteresis loops confirm the invertibility of its sign and show low coercive fields as a function of temperature. As reported for $TbMnO_3$ [20], time-resolved measurements of the rapidly switched chiral ratio reveal the combined Arrhenius-Merz law to describe the relaxation behavior in $NaFeGe_2O_6$ over at least seven orders of magnitude in time. Even at low temperatures of the order of 1.5 K the multiferroic domain inversion is well described by thermally activated domain wall motion with only two parameters. Compared to $TbMnO_3$, $NaFeGe_2O_6$ exhibits a much shorter characteristic time corresponding to a higher domain wall velocity that is of the same order of magnitude as the spin-wave velocity. Also, the activation parameter is smaller in $NaFeGe_2O_6$ indicating weaker pinning of multiferroic order in agreement with the small value of electric polarization in this material.

Since $NaFeGe_2O_6$ allows one to study the multiferroic domain relaxation over a large temperature range (down to $T/T_{MF} \approx 0.14$), we can analyze the scaling of electric field and reduced temperature T_r. While a simple scaling $f(\frac{T_r}{E})$ can be applied to ferroelectrics [56,57], such scaling can be excluded for the multiferroic domain relaxation in $NaFeGe_2O_6$, which follows the $f(\frac{T_r}{TE})$ scaling predicted by the Arrhenius-Merz law.

In conclusion, $NaFeGe_2O_6$ exhibits similar to $TbMnO_3$ a simple field and temperature dependence of multiferroic domain inversion that is well described by thermally activated domain wall motion with an activation field given by $A_0\frac{T_r}{T}$.

The neutron scattering data from the IN12 diffractometer are available [63].

ACKNOWLEDGMENTS

This work was funded by the Deutsche Forschungsgemeinschaft (DFG, German Research Foundation), Project No. 277146847; CRC 1238, projects A02, B04; and by the Bundesministerium für Bildung und Forschung Project No. 05K19PK1. This work is partially based upon experiments performed at the IN12 instrument operated by JCNS at the Institute Laue-Langevin (ILL), Grenoble, France. The authors gratefully acknowledge the financial support provided by JCNS to perform the neutron scattering measurements at the Institute Laue-Langevin (ILL), Grenoble, France.

---

[1] N. Jones, The information factories, Nature (London) **561**, 163 (2018).

[2] J. Puebla, J. Kim, K. Kondou, and Y. Otani, Spintronic devices for energy-efficient data storage and energy harvesting, Commun. Mater **1**, 24 (2020).

[3] L. Ceze, J. Nivala, and K. Strauss, Molecular digital data storage using DNA, Nat. Rev. Genet. **20**, 456 (2019).

[4] K. N. Lin, K. Volkel, J. M. Tuck, and A. J. Keung, Dynamic and scalable DNA-based information storage, Nat. Commun. **11**, 2981 (2020).

[5] M. Wuttig and N. Yamada, Phase-change materials for rewriteable data storage, Nat. Mater. **6**, 824 (2007).

[6] R. Tomasello, E. Martinez, R. Zivieri, L. Torres, M. Carpentieri, and G. Finocchio, A strategy for the design of skyrmion racetrack memories, Sci. Rep. **4**, 6784 (2014).

[7] O. Tizno, A. R. J. Marshall, N. Fernández-Delgado, M. Herrera, S. I. Molina, and M. Hayne, Room-temperature Operation of Low-voltage, Non-volatile, Compound-semiconductor Memory Cells, Sci. Rep. **9**, 8950 (2019).

[8] A. Ghosh, G. Koster, and G. Rijnders, Multistability in bistable ferroelectric materials toward adaptive applications, Adv. Funct. Mater. **26**, 5748 (2016).

[9] M. Gu, X. Li, and Y. Cao, Optical storage arrays: a perspective for future big data storage, Light Sci. Appl. **3**, e177 (2014).

[10] J. F. Scott, Multiferroic memories, Nat. Mater. **6**, 256 (2007).

[11] N. A. Spaldin and R. Ramesh, Advances in magnetoelectric multiferroics, Nat. Mater. **18**, 203 (2019).

[12] D. Khomskii, Classifying multiferroics: Mechanisms and effects, Physics **2**, 20 (2009).

[13] M. Fiebig, T. Lottermoser, D. Meier, and M. Trassin, The evolution of multiferroics, Nat. Rev. Mater. **1**, 16046 (2016).

[14] I. E. Dzyaloshinskii, A thermodynamic theory of weak ferromagnetism of antiferromagnetics, J. Phys. Chem. Solids **4**, 241 (1958).

[15] T. Moriya, Anisotropic Superexchange Interaction and Weak Ferromagnetism, Phys. Rev. **120**, 91 (1960).

[16] M. Mostovoy, Ferroelectricity in Spiral Magnets, Phys. Rev. Lett. **96**, 067601 (2006).

[17] J. Stein, M. Baum, S. Holbein, T. Finger, T. Cronert, C. Tölzer, T. Fröhlich, S. Biesenkamp, K. Schmalzl, P. Steffens, C. H. Lee, and M. Braden, Control of Chiral Magnetism Through Electric Fields in Multiferroic Compounds Above the Long-Range Multiferroic Transition, Phys. Rev. Lett. **119**, 177201 (2017).

[18] M. Baum, J. Leist, T. Finger, K. Schmalzl, A. Hiess, L. P. Regnault, P. Becker, L. Bohatý, G. Eckold, and M. Braden, Kinetics of the multiferroic switching in $MnWO_4$, Phys. Rev. B **89**, 144406 (2014).

[19] T. Hoffmann, P. Thielen, P. Becker, L. Bohatý, and M. Fiebig, Time-resolved imaging of magnetoelectric switching in multiferroic $MnWO_4$, Phys. Rev. B **84**, 184404 (2011).

[20] J. Stein, S. Biesenkamp, T. Cronert, T. Fröhlich, J. Leist, K. Schmalzl, A. C. Komarek, and M. Braden, Combined Arrhenius-Merz Law Describing Domain Relaxation in Type-II Multiferroics, Phys. Rev. Lett. **127**, 097601 (2021).

[21] D. Niermann, C. P. Grams, M. Schalenbach, P. Becker, L. Bohatý, J. Stein, M. Braden, and J. Hemberger, Domain dynamics in the multiferroic phase of $MnWO_4$, Phys. Rev. B **89**, 134412 (2014).

[22] T. Finger, D. Senff, K. Schmalzl, W. Schmidt, L. P. Regnault, P. Becker, L. Bohatý, and M. Braden, Electric-field control of the chiral magnetism of multiferroic $MnWO_4$ as seen via polarized neutron diffraction, Phys. Rev. B **81**, 054430 (2010).

[23] S. Biesenkamp, N. Qureshi, Y. Sidis, P. Becker, L. Bohatý, and M. Braden, Structural dimerization in the commensurate magnetic phases of $NaFe(WO_4)_2$ and $MnWO_4$, Phys. Rev. B **102**, 144429 (2020).

[24] R. Kajimoto, H. Yoshizawa, H. Shintani, T. Kimura, and Y. Tokura, Magnetic structure of $TbMnO_3$ by neutron diffraction, Phys. Rev. B **70**, 012401 (2004).

[25] T. Kimura, G. Lawes, T. Goto, Y. Tokura, and A. P. Ramirez, Magnetoelectric phase diagrams of orthorhombic $RMnO_3$ ($R =$ Gd, Tb, and Dy), Phys. Rev. B **71**, 224425 (2005).

[26] O. Prokhnenko, R. Feyerherm, M. Mostovoy, N. Aliouane, E. Dudzik, A. U. B. Wolter, A. Maljuk, and D. N. Argyriou, Coupling of Frustrated Ising Spins to the Magnetic Cycloid in Multiferroic $TbMnO_3$, Phys. Rev. Lett. **99**, 177206 (2007).

[27] S. Jodlauk, P. Becker, J. A. Mydosh, D. I. Khomskii, T. Lorenz, S. V. Streltsov, D. C. Hezel, and L. Bohatý, Pyroxenes: a new class of multiferroics, J. Phys.: Condens. Matter **19**, 432201 (2007).

[28] M. Baum, K. Schmalzl, P. Steffens, A. Hiess, L. P. Regnault, M. Meven, P. Becker, L. Bohatý, and M. Braden, Controlling

toroidal moments by crossed electric and magnetic fields, Phys. Rev. B **88**, 024414 (2013).

[29] I. Kim, B.-G. Jeon, D. Patil, S. Patil, G. Nénert, and K. H. Kim, Observation of multiferroic properties in pyroxene $NaFeGe_2O_6$, J. Phys.: Condens. Matter **24**, 306001 (2012).

[30] L. Ding, C. V. Colin, C. Darie, and P. Bordet, $SrMGe_2O_6$ (M = Mn, Co): a family of pyroxene compounds displaying multiferroicity, J. Mater. Chem. C **4**, 4236 (2016).

[31] M. Baum, A. C. Komarek, S. Holbein, M. T. Fernández-Díaz, G. André, A. Hiess, Y. Sidis, P. Steffens, P. Becker, L. Bohatý, and M. Braden, Magnetic structure and multiferroic coupling in pyroxene $NaFeSi_2O_6$, Phys. Rev. B **91**, 214415 (2015).

[32] H. Katsura, N. Nagaosa, and A. V. Balatsky, Spin Current and Magnetoelectric Effect in Noncollinear Magnets, Phys. Rev. Lett. **95**, 057205 (2005).

[33] L. Ding, P. Manuel, D. D. Khalyavin, F. Orlandi, and A. A. Tsirlin, Unraveling the complex magnetic structure of multiferroic pyroxene $NaFeGe_2O_6$: A combined experimental and theoretical study, Phys. Rev. B **98**, 094416 (2018).

[34] T. V. Drokina, G. A. Petrakovskii, L. Keller, J. Schefer, A. D. Balaev, A. V. Kartashev, and D. A. Ivanov, Modulated magnetic structure in quasi-one-dimensional clinopyroxene $NaFeGe_2O_6$, J. Exp. Theor. Phys. **112**, 121 (2011).

[35] G. J. Redhammer, A. Senyshyn, M. Meven, G. Roth, S. Prinz, A. Pachler, G. Tippelt, C. Pietzonka, W. Treutmann, M. Hoelzel, B. Pedersen, and G. Amthauer, Nuclear and incommensurate magnetic structure of $NaFeGe_2O_6$ between 5 K and 298 K and new data on multiferroic $NaFeSi_2O_6$, Phys. Chem. Miner. **38**, 139 (2011).

[36] M. Ackermann, L. Andersen, T. Lorenz, L. Bohatý, and P. Becker, Anisotropy study of multiferroicity in the pyroxene $NaFeGe_2O_6$, New J. Phys. **17**, 013045 (2015).

[37] L. Solovyova and V. Bakakin, X-ray investigation of Na, Fe-metagermanate $NaFeGe_2O_6$, Krystallographiya **12**, 591 (1967).

[38] K. Momma and F. Izumi, VESTA3 for three-dimensional visualization of crystal, volumetric and morphology data, J. Appl. Crystallogr. **44**, 1272 (2011).

[39] The measured intensity I^{expt} can be corrected for the finite flipping ratio by $I_{ii}^{\text{corr}} = I_{ii}^{\text{expt}} + 1/(\text{FR} - 1)(I_{ii}^{\text{expt}} - I_{i\bar{i}}^{\text{expt}})$ and by $I_{i\bar{i}}^{\text{corr}} = I_{i\bar{i}}^{\text{expt}} - 1/(\text{FR} - 1)(I_{ii}^{\text{expt}} - I_{i\bar{i}}^{\text{expt}})$, respectively.

[40] A. Poole, P. J. Brown, and A. S. Wills, Spherical neutron polarimetry (SNP) study of magneto-electric coupling in the multiferroic $MnWO_4$, J. Phys.: Conf. Ser. **145**, 012074 (2009).

[41] Y. Yamasaki, H. Sagayama, T. Goto, M. Matsuura, K. Hirota, T. Arima, and Y. Tokura, Electric Control of Spin Helicity in a Magnetic Ferroelectric, Phys. Rev. Lett. **98**, 147204 (2007).

[42] M. Janoschek, S. Klimko, R. Gähler, B. Roessli, and P. Böni, Spherical neutron polarimetry with mupad, Phys. B (Amsterdam) **397**, 125 (2007).

[43] M. Liu, L. Lin, Y. Zhang, S. Li, Q. Huang, V. O. Garlea, T. Zou, Y. Xie, Y. Wang, C. Lu, L. Yang, Z. Yan, X. Wang, S. Dong, and J.-M. Liu, Cycloidal magnetism driven ferroelectricity in double tungstate $LiFe(WO_4)_2$, Phys. Rev. B **95**, 195134 (2017).

[44] S. Biesenkamp, D. Gorkov, D. Brüning, A. Bertin, T. Fröhlich, X. Fabrèges, A. Gukasov, M. Meven, P. Becker, L. Bohatý, T. Lorenz, and M. Braden, Single-crystal investigations on the multiferroic material $LiFe(WO_4)_2$, Phys. Rev. B **103**, 134412 (2021).

[45] J. M. Perez-Mato, J. L. Ribeiro, V. Petricek, and M. I. Aroyo, Magnetic superspace groups and symmetry constraints in incommensurate magnetic phases, J. Phys.: Condens. Matter **24**, 163201 (2012).

[46] I. Urcelay-Olabarria, J. M. Perez-Mato, J. L. Ribeiro, J. L. Garcia-Munoz, E. Ressouche, V. Skumryev, and A. A. Mukhin, Incommensurate magnetic structures of multiferroic $MnWO_4$ studied within the superspace formalism, Phys. Rev. B **87**, 014419 (2013).

[47] Y. Ishibashi and Y. Takagi, Note on ferroelectric domain switching, J. Phys. Soc. Jpn. **31**, 506 (1971).

[48] Y. Ishibashi, A model of polarization reversal in ferroelectrics, J. Phys. Soc. Jpn. **59**, 4148 (1990).

[49] M. Avrami, Kinetics of phase change. i general theory, J. Chem. Phys. **7**, 1103 (1939).

[50] M. Avrami, Kinetics of phase change. ii transformationtime relations for random distribution of nuclei, J. Chem. Phys. **8**, 212 (1940).

[51] M. Avrami, Granulation, phase change, and microstructure kinetics of phase change. III, J. Chem. Phys. **9**, 177 (1941).

[52] D. Senff, P. Link, K. Hradil, A. Hiess, L. P. Regnault, Y. Sidis, N. Aliouane, D. N. Argyriou, and M. Braden, Magnetic Excitations in Multiferroic $TbMnO_3$: Evidence for a Hybridized Soft Mode, Phys. Rev. Lett. **98**, 137206 (2007).

[53] F. Kagawa, N. Minami, S. Horiuchi, and Y. Tokura, Athermal domain-wall creep near a ferroelectric quantum critical point, Nat. Commun. **7**, 10675 (2016).

[54] J. Brooke, T. F. Rosenbaum, and G. Aeppli, Tunable quantum tunnelling of magnetic domain walls, Nature (London) **413**, 610 (2001).

[55] O. G. Shpyrko, E. D. Isaacs, J. M. Logan, Y. Feng, G. Aeppli, R. Jaramillo, H. C. Kim, T. F. Rosenbaum, P. Zschack, M. Sprung, S. Narayanan, and A. R. Sandy, Direct measurement of antiferromagnetic domain fluctuations, Nature (London) **447**, 68 (2007).

[56] R. C. Miller and A. Savage, Velocity of Sidewise 180° Domain-Wall Motion in $BaTiO_3$ as a Function of the Applied Electric Field, Phys. Rev. **112**, 755 (1958).

[57] J. F. Scott, *Ferroelectric Memories, Advanced Microelectronics* (Springer, Berlin, 2000).

[58] D. Meier, N. Leo, M. Maringer, T. Lottermoser, and M. Fiebig, Topology and manipulation of multiferroic hybrid domains in $MnWO_4$, Phys. Rev. B **80**, 224420 (2009).

[59] M. Matsubara, S. Manz, M. Mochizuki, T. Kubacka, A. Iyama, N. Aliouane, T. Kimura, S. L. Johnson, D. Meier, and M. Fiebig, Magnetoelectric domain control in multiferroic $TbMnO_3$, Science **348**, 1112 (2015).

[60] S. Toth and B. Lake, Linear spin wave theory for single-q incommensurate magnetic structures, J. Phys.: Condens. Matter **27**, 166002 (2015).

[61] C. V. Colin, L. Ding, E. Ressouche, J. Robert, N. Terada, F. Gay, P. Lejay, V. Simonet, C. Darie, P. Bordet, and S. Petit, Incommensurate spin ordering and excitations in multiferroic $SrMnGe_2O_6$, Phys. Rev. B **101**, 235109 (2020).

[62] D. Senff, N. Aliouane, D. N. Argyriou, A. Hiess, L. P. Regnault, P. Link, K. Hradil, Y. Sidis, and M. Braden, Magnetic excitations in a cycloidal magnet: the magnon spectrum of multiferroic $TbMnO_3$, J. Phys.: Condens. Matter **20**, 434212 (2008).

[63] Data are available at https://doi.ill.fr/10.5291/ILL-DATA.CRG-2439 and https://doi.ill.fr/10.5291/ILL-DATA.CRG-2757.

6. Domain kinetics in molecular $(NH_4)_2[FeCl_5\,(H_2O)]$

6.1. Motivation

The multiferroic relaxation behavior, which was reported for $TbMnO_3$ [49] and $NaFeGe_2O_6$ (see section 5 and Ref. [3]) differ fundamentally from the observed domain kinetics in $MnWO_4$ [70]. It was discussed that the complex relaxation behavior of $MnWO_4$ is caused by depinning effects, which arise from developing commensurate fragments in the multiferroic phase. The different description of domain kinetics thus motivated the investigation of multiferroic domain inversion in other materials and in particular, it is of high interest for the application potential to determine and confirm not only the appropriate law that describes the temperature- and electric-field dependent switching process but also to investigate the accessible time-range of multiferroic domain inversion in respective materials. This encouraged to expand the investigation of multiferroic domain kinetics also to molecular multiferroic compounds, whose chemical composition inherently proposes a softer lattice, which is promising for faster relaxation of multiferroic domains.

6.1.1. Crystal and magnetic structure

During the last decade, the molecular erythrosiderites $A_2[FeCl_5\,(H_2O)]$ with A being an ammonium or alkali metal ion have attracted much interest as members that belong to this material class were reported to exhibit magnetoelectric and even multiferroic behavior [116, 117]. Structurally, erythrosiderites are closely related to each other, whereby the systems crystallize in the orthorhombic space group *Pnma* and *Cmcm* for $A = NH_4$, Rb, K and $A = Cs$ respectively [118–124]. In all systems, complex groups of $[FeCl_5(H_2O)]$ form sixfold coordinated octahedra with Fe^{3+} in its center and hydrogen-bonds along the O-H-Cl path further stabilize the structure that is characterized by zigzag chains of neighboring $[FeCl_5(H_2O)]$ groups along b direction for $A = NH_4$, Rb, K and along c direction for $A = Cs$. Most erythrosiderites were reported to develop antiferromagnetic and collinear magnetic structures at low temperatures [125–127], whereby the easy-axis points along a-direction. However, this does not hold for the ammonium compound, for which no easy axis, but an ac easy plane with XY anisotropy was observed [128, 129].

The orthorhombic system $(NH_4)_2[FeCl_5\,(H_2O)]$ (space group *Pnma*) exhibits the unit cell dimensions $a = 13.706(2)\,\text{Å}$, $b = 9.924(1)\,\text{Å}$ and $c = 7.024(1)\,\text{Å}$ [116, 130] at room temperature. In zero field, at $T_S \approx 79\,\mathrm{K}$ a structurally related order-disorder transition of the $(NH)_4^+$ tetrahedra orientation leads to the loss of n and m symmetries and thus to a monoclinic distortion of the crystal lattice [131]. Below T_S the system can be described by space group $P2_1/a$ (nonstandard setting) and no further symmetry reductions are reported at low temperature [131].

At $T_N \approx 7.3\,\mathrm{K}$ long-range magnetic order in form of an incommensurate spin density wave (SDW) with moments along a direction sets in [129]. The propagation vector $\mathbf{k} = (0\ 0\ 0.23)$ displays a slight temperature dependence, but it does not reach a commensurate value [129]. Below the multiferroic transition at $T \approx 6.8\,\mathrm{K}$ a spiral spin structure forms in the ac plane [128, 129] and simultaneous to the onset of spiral ordering, a ferroelectric polarization ($P_\mathrm{ferro} \approx 3\,\mathrm{\mu C\,m^{-2}}$) develops inside the ab plane [116], which can be well explained by equation 1.8. However, Tian *et. al.* reported that the groundstate of the system is not homogeneous but consists of two soft phases in form of incommensurate and commensurate ordering [132]. In zero magnetic field, incommensurate ordering is the dominant phase but a finite magnetic field tunes the commensurate ordering until at $\approx 2.5\,\mathrm{T}$ the structure transforms into a distorted commensurate cycloid [132, 133]. The ferroelectric polarization slightly tilts away from the a axis but remains within the ac plane until at $\approx 5\,\mathrm{T}$ a spin flop transition induces a commensurate canted spin structure with moments mainly confined within the bc plane [116, 133]. Above this transition the ferroelectric polarization points along c direction, which is not confirm with equation 1.8 but is proposed to be described by the spin dependent *p*-*d* hybridization model [116, 133]. The interference of incommensurate and commensurate ordering in the multiferroic phase, as well as the molecular lattice, which promises fast relaxation processes motivated the investigation of the domain kinetics in $(NH_4)_2[FeCl_5\,(H_2O)]$.

In the following sections the experimental methods are first introduced, before time-resolved measurements of multiferroic domain inversion in $(NH_4)_2[FeCl_5\,(H_2O)]$ are presented. Subsequently, the temperature and electric-field dependence of relaxation times is discussed in view of the combined Arrhenius-Merz law that was proposed to describe the domain kinetics in multiferroics [49]. Eventually, the measured temperature dependence of higher-harmonic reflections, respectively the growing anharmonic contributions to the spiral spin-structure and their impact on the relaxation behavior is presented.

6.1.2. Experimental methods

For the investigation of the multiferroic domain dynamics and in particular for sensing the handedness of the spiral spin-structure, neutron diffraction with polarization analysis was utilized for respective experiments. As the molecular compound $(NH_4)_2[FeCl_5\,(H_2O)]$ comprises hydrogen atoms, which contribute a tremendous incoherent background to the measured signal, neutron scattering experiments were done so far only on deuterated samples [128, 129, 131–134]. The proposed experiments do not significantly profit from the reduced background signal and as the handling of deuterated samples is complicated, two non-deuterated samples SI and SII with dimensions of about $3.8\,\mathrm{mm} \times 4.8\,\mathrm{mm} \times 1.03\,\mathrm{mm}$ for SI and $5.2\,\mathrm{mm} \times 5.8\,\mathrm{mm} \times 3.1\,\mathrm{mm}$ for SII, were prepared. This also enabled an investigation of isotope effects on the magnetic structure. The samples were grown and provided by L. Bohatý and P. Becker, whereby an elaborate description of the sample growth can be found in Ref. [116]. Both samples SI and SII were respectively cramped between aluminum plates that are tightened together by insulating polytetrafluorethylen (PTFE) screws. The plate normal was oriented parallel to a so that the electric field can be applied along this direction. Both plates were mounted onto separate sample holders in the scattering geometry (0 1 0)/(0 0 1) and can be connected to the time-resolved high-voltage setup (see section 2.4 and Ref. [49]).

The time-resolved investigations of the multiferroic domain inversion were carried out during a beamtime at the triple-axis spectrometer IN12 (proposal CRG-2573 [135]), which is located at the Institute Laue-Langevin (ILL). A pyrolytic graphite (PG(0 0 2)) monochromator supplied $\lambda = 3.14\,\text{Å}$, while a cavity polarizer provided a highly polarized neutron beam. The sample was inserted in a standard orange cryostat and a helmholtz-coil setup defined the guide-field direction at the sample position. Two spin flippers that are positioned before and behind the sample as well as a Heusler (1 1 1) analyzer enabled longitudinal polarization analysis. Here, the convenient coordinate system for analyzing spin-flip (SF) and non-spin flip (NSF) processes was chosen. The x-direction is oriented parallel to the scattering vector $\mathbf{Q}$ and perpendicular to y, which are both lying in the scattering plane. Accordingly, the z-direction is perpendicular to the scattering plane. The flipping ratio (FR) was measured on the (0 2 0) nuclear reflection and amounted to $\mathrm{FR} \approx 20$.

For measuring the temperature dependence of the higher harmonics, an experiment (proposal CRG-2573 [135]) at the IN3 triple-axis spectrometer (which is also located at the ILL) was carried out. A PG (002) monochromator provided an unpolarized neutron beam with $\lambda = 2.36\,\text{Å}$ and the background signal was significantly reduced by a PG (0 0 2) analyzer. With the standard orange-cryostat, the temperature dependence of higher harmonics was measured down to $T \approx 1.5\,\mathrm{K}$.

6.1.3. Multiferroic domain control

For the temperature and electric field dependent investigation of the multiferroic domain dynamics, sample SI was measured at the IN12 triple-axis spectrometer utilizing longitudinal polarization analysis. Measuring both SF channels $I_{x\bar{x}}$ and $I_{\bar{x}x}$ along x-direction gives access to the chiral ratio r_χ. Here, the scattering geometry and the magnetic reflection (0 1 0.23) entails a scattering vector that is nearly perpendicular to the rotation plane of spins, wherefore the measured chiral ratio converges to values of ±1 for a monodomain state and by assuming absence of elliptical distortions for the spiral. In the first part of the experiment, the chiral ratio was measured at $\mathbf{Q} = (0\ 1\ 0.23)$ as function of temperature and for different applied fields. For each run, the sample was heated above the Néel temperature and subsequently cooled with an applied electric field, while recording both

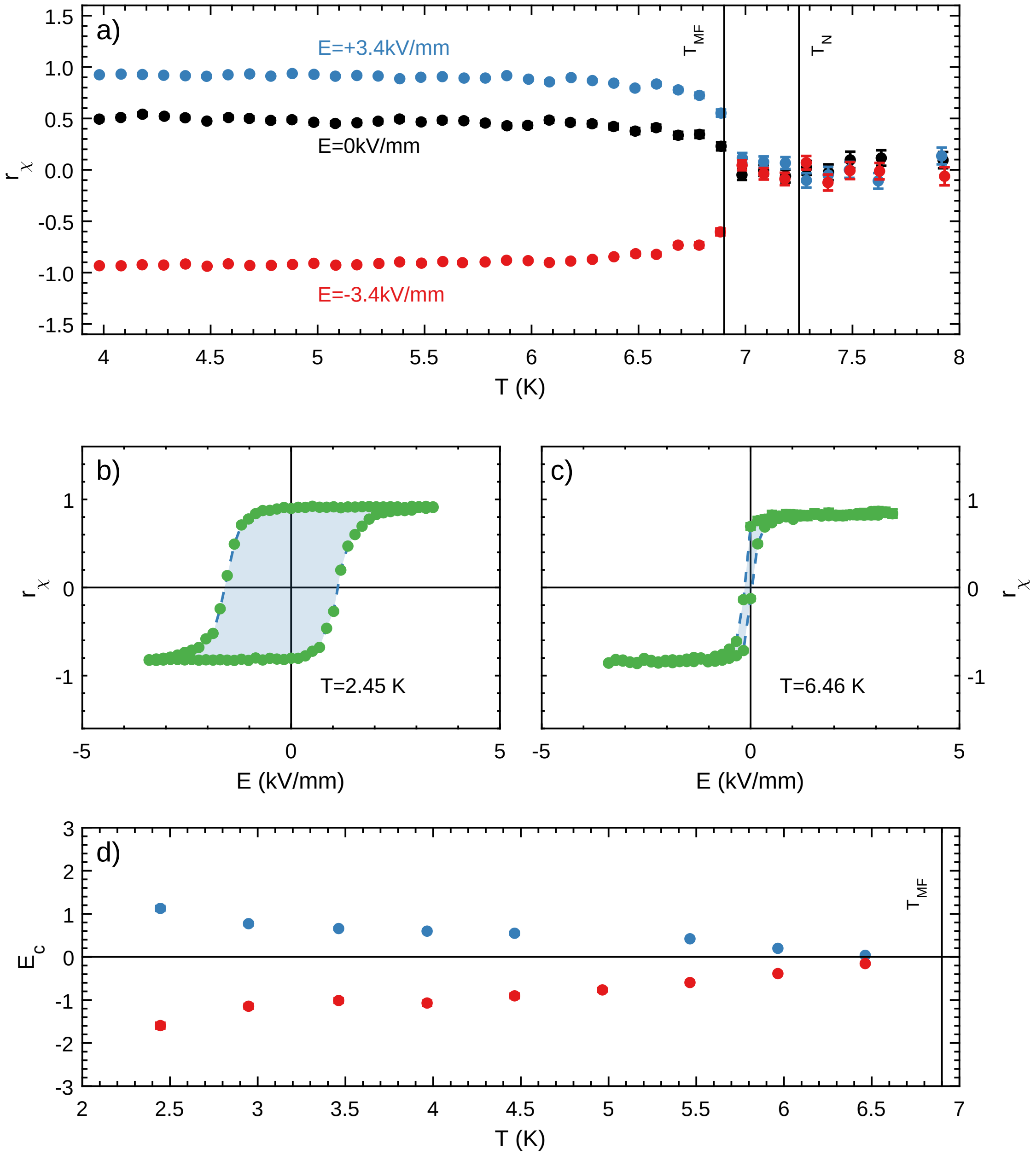

Figure 6.1.: The temperature dependence of the chiral ratio for different poling fields is displayed in a). Both panels in b) and c) show exemplary two recorded hysteresis loops at $T = 2.45\,\mathrm{K}$ and $T = 6.46\,\mathrm{K}$. The coercive fields were obtained by fitting both slopes with a hyperbolic tangent and the respective temperature dependence is shown in d). All measurements were recorded for the $\mathbf{Q} = (0\ 1\ 0.23)$ reflection.

SF channels $I_{x\bar{x}}$ and $I_{\bar{x}x}$. The temperature dependence of r_χ is shown in Fig. 6.1 a) for $E = \pm 3.4\,\mathrm{kV\,mm^{-2}}$ as well as for zero applied field. The values clearly state that the sign of the vector chirality can be poled in opposite directions depending on the applied field direction and even close to the multiferroic transition temperature the system can be poled to a monodomain. Moreover, it can be seen that in zero field a finite value for r_χ develops, which indicates a preferred state of the multiferroic domain distribution for this sample.

Hysteresis loops were recorded by quasistatically driving the applied electric field between $E = \pm 3.4\,\mathrm{kV\,mm^{-2}}$ for different temperatures, whereby one full cycle lasted approximately 70 min. Two exemplary loops are shown in Fig. 6.1 b) and c) for $T = 2.45\,\mathrm{K}$ and $T = 6.46\,\mathrm{K}$ respectively. Both hysteresis loops confirm the invertibility of the spiral handedness in $(NH_4)_2[FeCl_5\,(H_2O)]$ by external electric fields, while the visible asymmetry of the coercive fields also reproduces the results from the poling sequences. The temperature dependence of the coercive fields E_c is plotted in Fig. 6.1 d), whereby their values were obtained by fitting both slopes of the hysteresis loop by a hyperbolic tangent. The quasistatic measurements resemble the results from a deuterated sample [133].

6.1.4. Multiferroic relaxation behavior

The relaxation times of multiferroic domain inversion as a function of temperature and electric field were determined by deploying the time-resolved setup (see section 2.4 and Ref. [49]) at the IN12 spectrometer. Corresponding measurements were done on the same sample and at the same position in Q-space as for the (quasi-)static measurements that have been discussed in section 6.1.3. Figure 6.2 displays exemplary eight switching curves that were recorded for different temperatures and electric-field amplitudes. It can be seen that the inversion time for these eight switching curves cover at least one order of magnitude in time as a function of temperature and electric field. Furthermore, the observed preference of one domain type is here also visible in form of an asymmetric switching curve. Equivalent to the analysis in Ref. [3,49] and the explanation in section 2.4, the rising and falling slopes of all switching curves were fitted by stretched exponential functions (see equation 2.32).

Fitting all switching curves with equation 2.32 yields b parameters in the range between 1 and 2, which indicates low dimensional domain growth (see also Fig. 8.2). Further, the b values tend to raise for increased field or temperature, which will be referred to again in chapter 8, where the relaxation behavior of investigated multiferroics is compared. This behavior is expected, as for higher temperatures or higher fields the assumption of a single latent germ nuclei at the beginning transfers into a continuous nucleation of new germs during the switching process. An equivalent behavior was observed for $TbMnO_3$ and $NaFeGe_2O_6$ [3,49].

All fitted relaxation times are shown in Fig. 6.3 as a function of inverse temperature and inverse electric field. For the sake of simplicity, only τ_b is plotted as due to the observed asymmetry of domain inversion (see Fig. 6.2) both relaxation times τ_a and τ_b differ approximately by a factor of 2-3 from each other. However, the following discussion

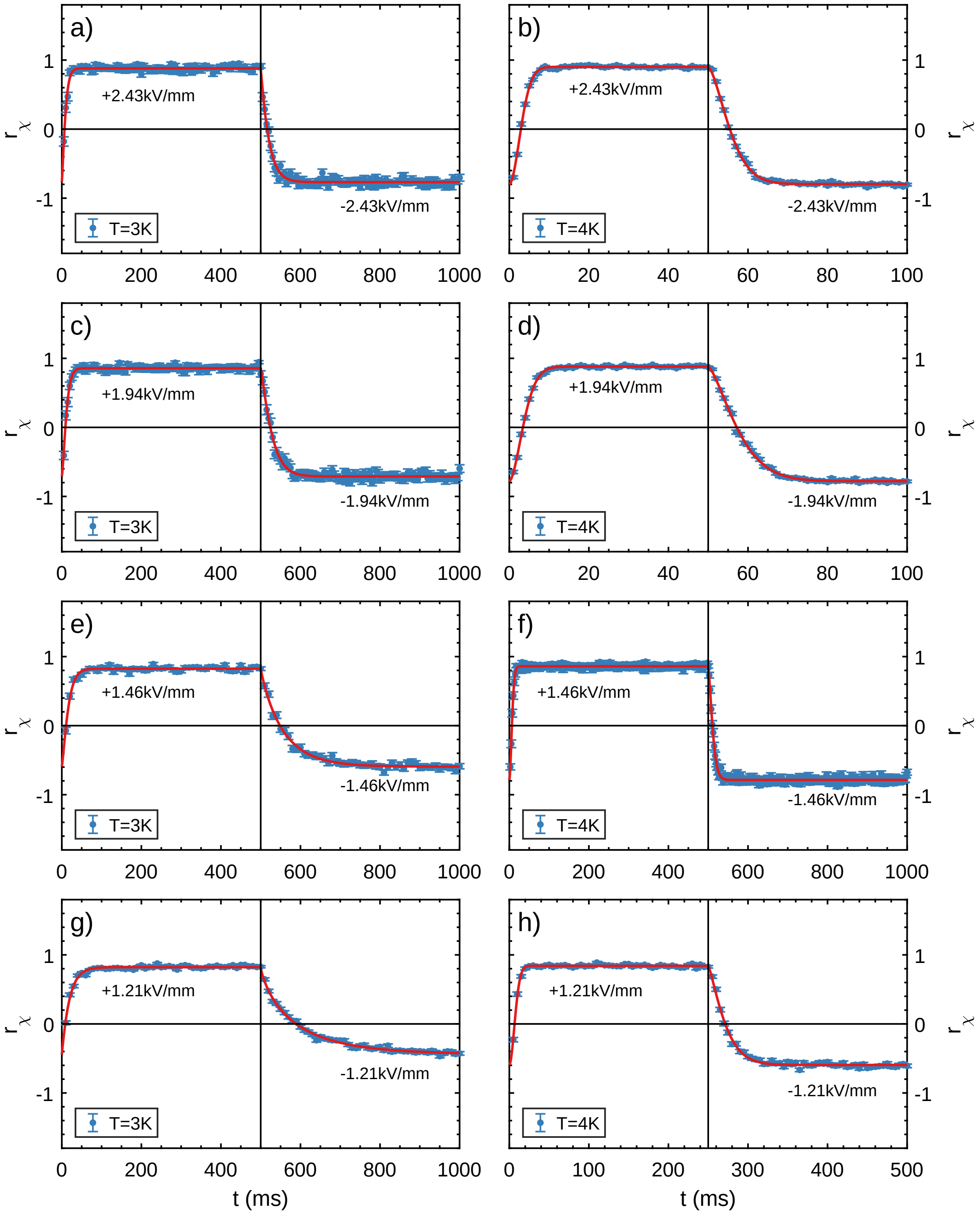

Figure 6.2.: Eight different switching curves are plotted exemplary in panels a)-h) for different temperatures and electric field amplitudes. These measurements were performed on sample SI and by recording both SF channels $I_{x\bar{x}}$ and $I_{\bar{x}x}$ for the magnetic reflection $\mathbf{Q} = (0\ 1\ 0.23)$.

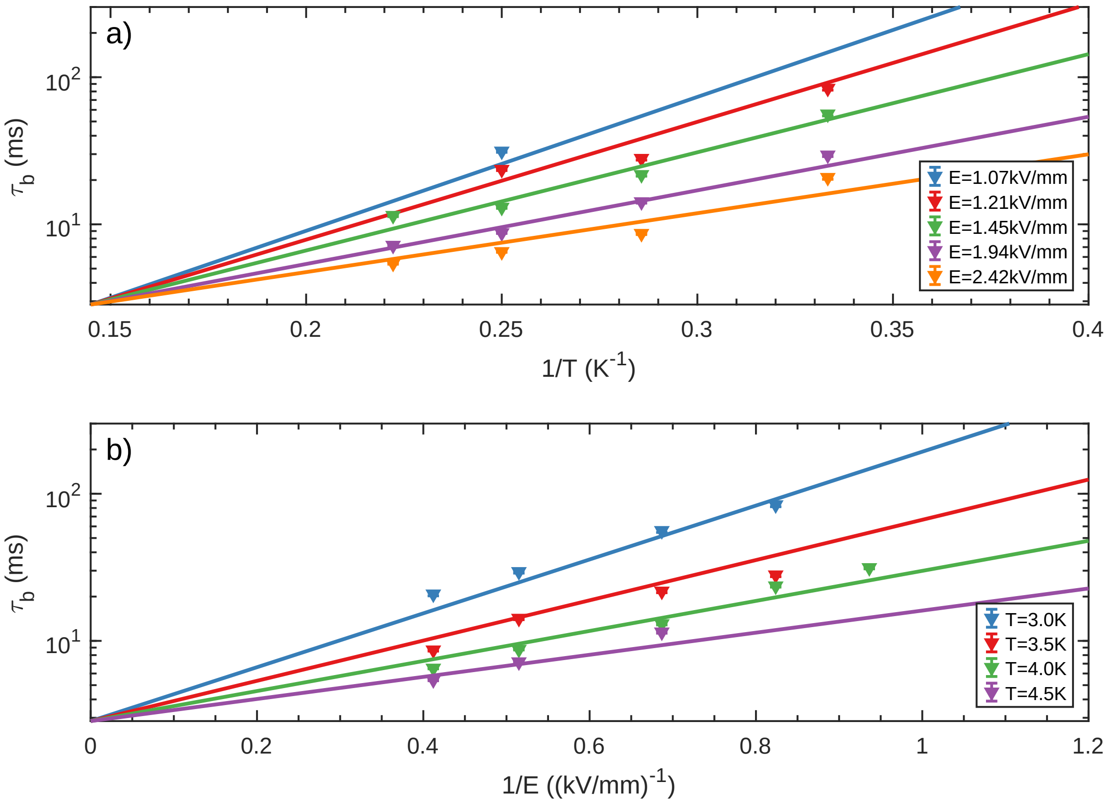

Figure 6.3.: Both panels a) and b) display the measured temperature- and electric-field dependent relaxation times. Due to the observed asymmetric switching behavior and for the sake of simplicity only τ_b is respectively plotted as a function of inverse temperature and inverse field. All solid lines refer to a fit that follows the combined Arrhenius-Merz law.

is qualitatively the same for both.

It was thoroughly discussed in Ref. [3, 49] and in section 1.2.4 that the temperature- and electric-field dependence of relaxation times for multiferroic domain inversion can be described by the simple combined Arrhenius-Merz law $\tau(E,T) = \tau^{*}\exp((A_0 T_\mathrm{r})/(ET))$ with $T_\mathrm{r} = (T_\mathrm{MF} - T)/T_\mathrm{MF}$ (see formula 1.12). In contrast to pure ferroelectric switching, where the nucleation of germs at the surface, their subsequent forward growth along the polarization direction and finally the sideways growth of needle shaped domains act on the same time scale [57], the multiferroic domain inversion is only dominated by the sideways growth of some few large domains [49, 69, 136, 137]. As only one relaxation process is relevant, it inherently forecasts a much simpler description of multiferroic domain inversion compared to the relaxation behavior in ferroelectrics. The formula that describes the combined Arrhenius-Merz law needs only two parameters for describing the thermally activated multiferroic domain wall motion as a function temperature and applied field. Fitting all determined relaxation times with the combined Arrhenius-Merz law (equation 1.12) yields the values $A_0 = 22.4(14)\,\mathrm{K\,kV\,mm^{-1}}$ and $\tau^{*} = 2.85(31)\,\mathrm{ms}$ for the multiferroic domain relaxation in $(NH_4)_2[FeCl_5\,(H_2O)]$.

The fitresult is plotted for respective temperatures and fields in Fig 6.3 and it is clearly visible that all relaxation times obey the combined Arrhenius-Merz law over a significant temperature and field range. Measurements at lower and higher temperature were hindered by the limited amount of beamtime. In this context it must be noted that measurements closer to the multiferroic transition temperature are further impacted, respectively impeded by heating effects due to the fast domain inversion. This effect can in fact be attenuated by a lowered switching frequency, but this also entails that the relaxation process covers less time-bins, respectively less data points. To maintain a sufficient amount of data points in the time-window of the relaxation process, the binning has then to be increased, which however also enforces much longer counting times for an appropriate statistic.

The measured relaxation times in the course of the conducted experiment cover only two orders of magnitude in time as a function of temperature and electric field. Astonishingly, the characteristic relaxation time in molecular $(NH_4)_2[FeCl_5\,(H_2O)]$ is one order of magnitude slower than in $TbMnO_3$ [49] and even 3 orders of magnitude slower than in $NaFeGe_2O_6$ [3]. However, this has to be set in relation to the multiferroic transition temperature and the activation constant. In $TbMnO_3$, the transition temperature is much higher and the two order of magnitude larger activation constant slows down the relaxation process tremendously with decreasing temperature. The higher activation constant of $TbMnO_3$ with respect to $(NH_4)_2[FeCl_5\,(H_2O)]$ can be related to the much larger polarization in $TbMnO_3$ ($P_{\mathrm{ferro}} \approx 800\,\mu\mathrm{C\,m^{-2}}$ [42]), which can be effectively better pinned. Eventually, in the multiferroic temperature range of $(NH_4)_2[FeCl_5\,(H_2O)]$, the domain inversion in $TbMnO_3$ is much slower compared to the molecular system. The multiferroic transition temperature of $NaFeGe_2O_6$ is also higher than in $(NH_4)_2[FeCl_5\,(H_2O)]$, whereas the activation constant is here approximately of equal size. By regarding the low characteristic relaxation time of $NaFeGe_2O_6$, it follows that the relaxation in this oxide system is thus still faster than the domain inversion in $(NH_4)_2[FeCl_5\,(H_2O)]$, while considering the same temperature range. This is surprising as the molecular constituents would actually imply a softer lattice. It was reported for $NaFeGe_2O_6$ that the characteristic relaxation time and thus the fastest possible multiferroic domain inversion is limited by the spin wave velocity [3]. From inelastic studies, which are presented in Ref. [138] it can be roughly estimated that the spin-wave velocities in $(NH_4)_2[FeCl_5\,(H_2O)]$ along b and c direction amounts to $v \approx 800\,\mathrm{m\,s^{-1}}$ and $v \approx 300\,\mathrm{m\,s^{-1}}$ respectively. With the given sample geometry, it can be thus deduced that the fastest possible inversion time for sideways domain wall motion is approximately of the order of $1 \times 10^{-3}\,\mathrm{ms}$, whereby it was assumed that a single needle-shaped domain relaxes from the middle to both sides of the sample. Hence, the relaxation time that is limited by the spin-wave velocity is several orders of magnitude faster than the measured characteristic relaxation time τ^*. However, it has to be remembered that the characteristic relaxation time in the framework of a combined Arrhenius-Merz law presumes only an initial nucleation of germs, whereas very close to the multiferroic transition temperature, the nucleation can become continuous during the switching process. This was already observed to have significant impact for $TbMnO_3$, where close to T_{MF}

the relaxation becomes much faster than predicted by the combined Arrhenius-Merz law. The determined spin-wave velocity thus sets a limit for the domain-inversion time but also highlights that the relaxation can get in principle much faster in $(NH_4)_2[FeCl_5\,(H_2O)]$, when approaching the multiferroic phase transition at which the combined Arrhenius-Merz law does not hold because of continuous germ nucleation. As noted above, the respective measurements very close to the multiferroic transition were hindered by heating effects, respectively by the limited beamtime.

The validness of the combined Arrhenius-Merz law in the predominant multiferroic temperature range of $(NH_4)_2[FeCl_5\,(H_2O)]$ can be further confirmed by the scaling of τ with $T_\mathrm{r}/(ET)$, which is discussed in chapter 8 together with the scaling behavior of other multiferroics, which were investigated within the course of this thesis. At low temperatures the thermally driven law also describes the domain inversion, which states the absence of quantum fluctuation driven domain wall tunneling in $(NH_4)_2[FeCl_5\,(H_2O)]$ at least for the investigated temperature and field range. The latter kind of domain wall motion would lead to a temperature independent relaxation behavior, which was so far only observed for pure ferroelectric and magnetic domain wall motion [72, 74]. Further, the reported interference of incommensurate and commensurate ordering also do not significantly influence the relaxation behavior down to the lowest temperature for which the domain inversion was investigated in the conducted experiment. This contrasts the situation in $MnWO_4$ and in the following section we discuss the main differences to $(NH_4)_2[FeCl_5\,(H_2O)]$ with respect to coexisting incommensurate and commensurate ordering.

6.2. Higher harmonics

Tian *et al.* reported competing incommensurate and commensurate ordering in the molecular compound $(NH_4)_2[FeCl_5\,(H_2O)]$ in form of even and odd harmonics as well as a commensurate reflection at low temperature ($T = 1.43\,\mathrm{K}$) [129, 132]. The interference of incommensurate and commensurate ordering can lead to depinning effects for multiferroic domains and was reported to cause the anomalous relaxation behavior in $MnWO_4$ [1]. In this system the domain inversion becomes faster, when approaching the lower commensurate *uudd* phase [69–71], which contrasts the simple activation law that describes the multiferroic domain inversion in $TbMnO_3$ [49], $NaFeGe_2O_6$ [3] and $(NH_4)_2[FeCl_5\,(H_2O)]$ (see section 6.1.4) in a large temperature range. In view of the observed interference of commensurate and incommensurate ordering in $(NH_4)_2[FeCl_5\,(H_2O)]$ [129, 132], it is astonishing that the domain inversion in this system nevertheless follows the combined Arrhenius-Merz law over a finite temperature range.

Tian *et al.* utilized neutron polarization analysis to separate the respective magnetic and nuclear contributions of higher harmonics [129]. They revealed that odd-order harmonics and the commensurate signal are solely of magnetic origin, whereas the second-order reflection is mainly of nuclear origin but possesses also a finite magnetic contribution. This is similar to the reported occurrence and origin of even and odd harmonics in $MnWO_4$ [1, 97].

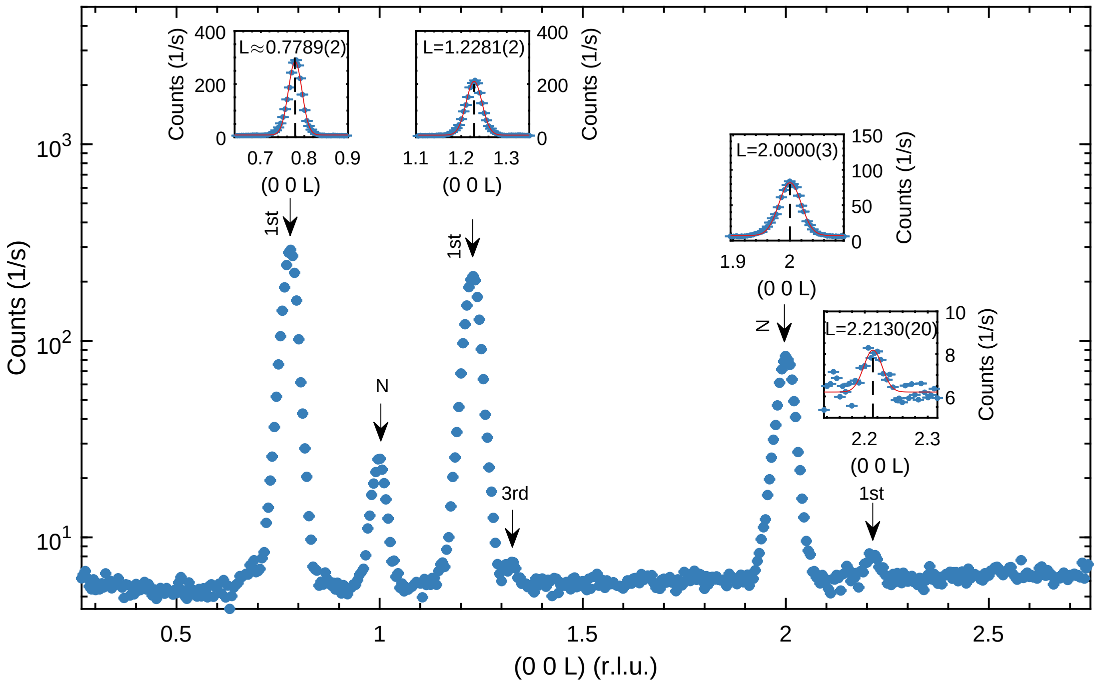

Figure 6.4.: This plot displays a Q_L-scan across (0 0 L) direction at $T = 1.48\,\mathrm{K}$. The observed nuclear (N), magnetic first order (1st) and magnetic third order (3rd) reflections are marked by arrows and the shown insets present Gaussian fits for some of the incommensurate first order and nuclear reflections, whereby the value of the fitted peak position is respectively included in all panels. An equivalent scan at $T = 1.5\,\mathrm{K}$ can be found in Ref. [129].

The appearance of second-order harmonics goes along with incommensurate ordering as in general every incommensurate magnetic modulation effects a nuclear lattice modulation of half the period in real space due to exchange striction. Moreover, in $(NH_4)_2[FeCl_5\,(H_2O)]$ and equivalent to $MnWO_4$ [1, 97] the reported temperature dependence revealed a strong enhancement of second-order intensity with the onset of ferroelectric and chiral magnetic ordering, which indicates significant magnetoelastic coupling in the multiferroic phase. The observed third and fifth order harmonics signal a squaring up of the spin spiral. This was also observed in $MnWO_4$ as a precursor of the low-temperature commensurate spin *uudd* phase, where tiny commensurate fragments in the multiferroic phase lead to depinning effects and cause the anomalous relaxation behavior [1]. In $(NH_4)_2[FeCl_5\,(H_2O)]$, no exclusive long-range ordered commensurate low-temperature phase was so far reported but odd harmonics and a sizeable peak intensity for the commensurate reflection $\mathbf{Q} = (0\,1\,0.25)$ in the incommensurate multiferroic phase indicate that commensurate order coexists and competes with the incommensurate ordering. It was reported, that the incommensurate ordering is dominant in zero field, but the coexisting commensurate ordering can be tuned with increasing magnetic field, which leads to a bicritical state between 1.5 T-2.5 T before the spin spiral becomes commensurate and distorted at 2.5 T [129, 132, 133]. So far only the temperature dependence of even harmonics was discussed [129, 132], but to appraise the impact of interfering commensurate and incommensurate ordering on the relaxation

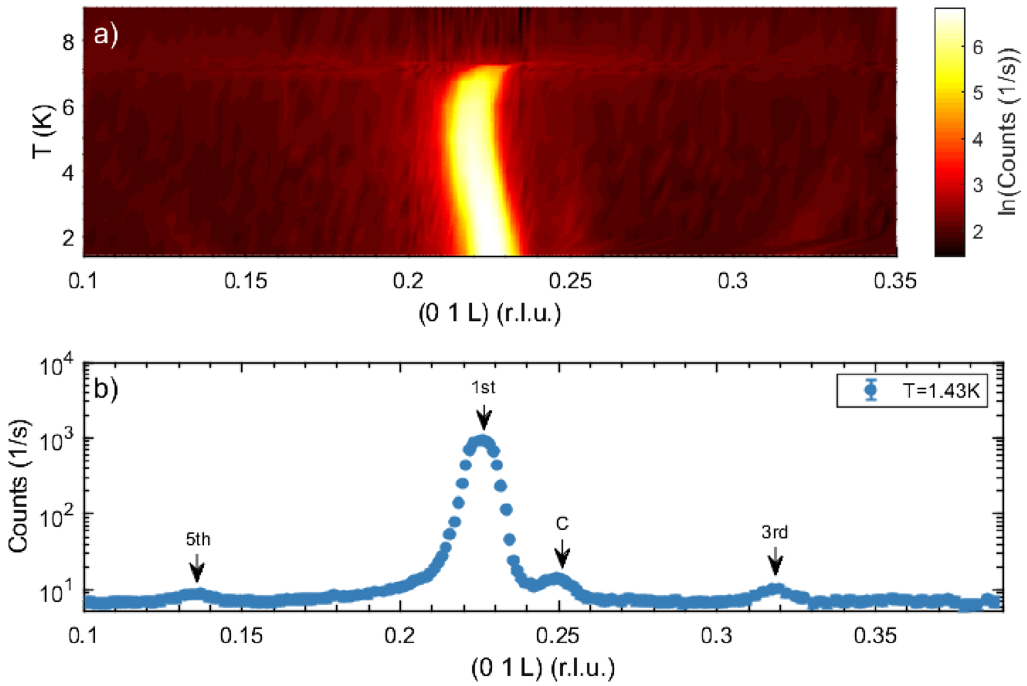

Figure 6.5.: The upper panel a) shows the temperature dependent Q_L scans across the magnetic reflection $\mathbf{Q} = (0\,1\,0.23)$. One single scan is exemplary shown in b) for $T = 1.43\,\mathrm{K}$, for which the positions of first (1st), third (3rd), fifth (5th) and commensurate reflections are marked by arrows.

behavior in zero magnetic field, temperature dependent measurements of odd harmonics and the commensurate reflection are necessary.

Figure 6.4 presents a Q_L-scan across $Q = (0\ 0\ L)$, which was measured at the lowest temperature $T = 1.48\,\mathrm{K}$ and which resembles the respective measurement from Tian *et al.* [129]. Equivalent to their result, nuclear as well as magnetic first- and third-order reflections possess finite intensity at this temperature. However, in contrast to the recorded data from Tian *et al.*, no magnetic second-order reflection can be observed in Fig. 6.4. The absence of this even harmonic and the apparent lack of some other reported first order reflections can be related to the much better signal to noise ratio in Ref. [129]. In this context it must be noted that the peak intensity of the observed second order reflection in Ref. [129] amounts approximately only 0.1% of the nuclear $\mathbf{Q} = (0\,0\,2)$ peak intensity. Considering the presented scan in Fig. 6.4, the second order reflection would possess a peak intensity of about 1 count per second, which is here not resolvable. The three incommensurate first order reflections in Fig. 6.4 are fitted by single Gaussian functions to determine their exact position and thus the incommensurability of the underlying magnetic structure. The weigthed average of determined values for the incommensurability yield the propagation vector $\mathbf{k}_{\mathrm{inc}} = (0\,0\,0.2245(1))$, which differs by approximately 2.5% from the one, which was reported for the deuterated sample [129]. This difference cannot be related to a potential misalignment of the sample as the observed nuclear reflections $(0\ 0\ 2)$ is observed exactly at the expected position $L = 2.0000(3)$ (see Gaussian fit in the right inset

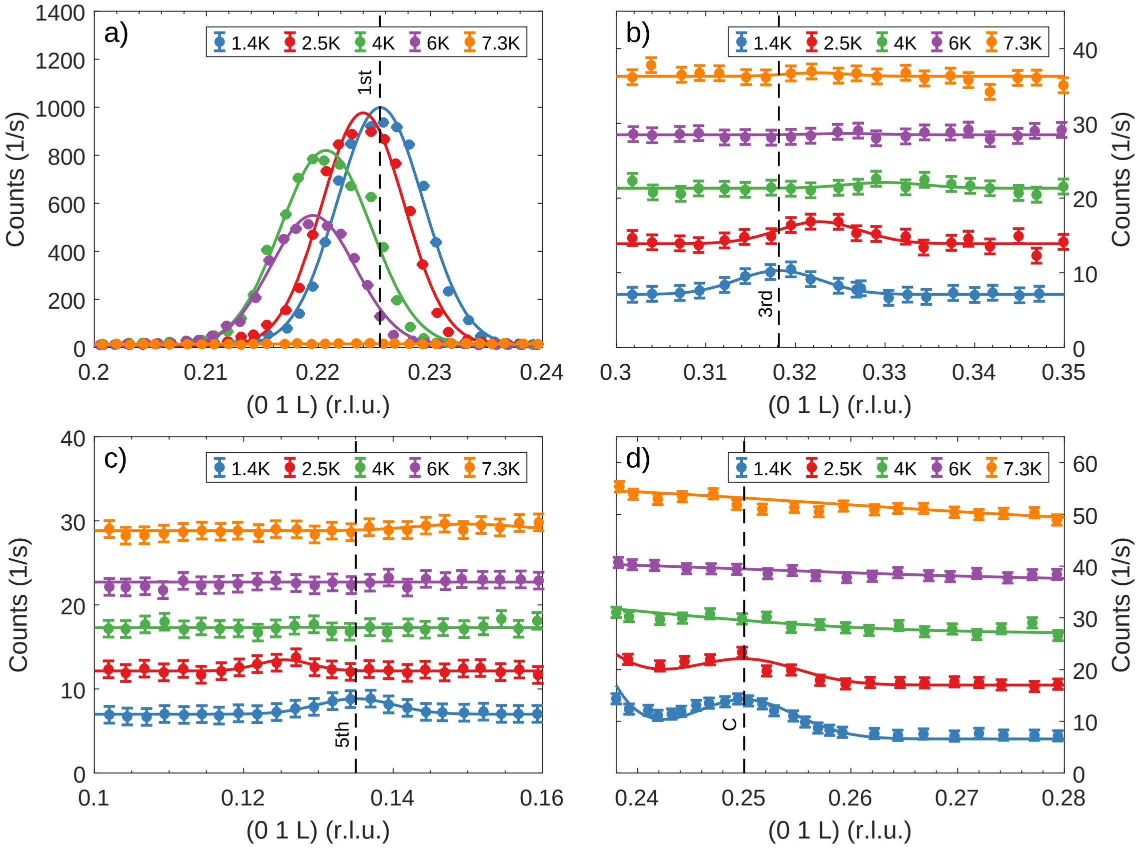

Figure 6.6.: This figure displays the observable reflections from Fig. 6.5 and the respective fits. The first, third and fifth order reflections are respectively plotted in a)-c) together with a Gaussian fit, for which a constant background was assumed. This contrasts the fit of the commensurate reflection, which is displayed in d). Here, the background was assumed to be the tail of a second Gaussian function and the commensurate peak position was fixed to $L = 0.25$. For a better view, all respective scans in b)-d) are shifted by a constant offset with respect to the y-axis.

of Fig. 6.4). This isotope dependent incommensurability will be referred to again in the context of temperature dependent measurements of first-order, third-order, fifth-order and commensurate reflections, for which it was seen promising to record Q-scans across $(0\,1\,L)$. This scan direction was chosen as a reported equivalent scan at 1.5 K [129] advertise finite and significant intensity for the commensurate and odd-harmonic reflections.

The respective recorded temperature-dependent scans are shown in Fig. 6.5 a), whereby Fig. 6.5 b) displays exemplary a single scan at $T = 1.5\,\mathrm{K}$. This scan clearly recovers the reported presence of odd harmonics and also the coexistence of incommensurate and commensurate reflections in the deuterated system [129].

All peaks were fitted separately by Gaussian functions, whereby a constant background was assumed for all higher harmonics. In contrast, for the commensurate reflection a second Gaussian function was used to describe the background, respectively the superimposed signal from the first order signal. These fits are shown in Fig. 6.6. The peak center position

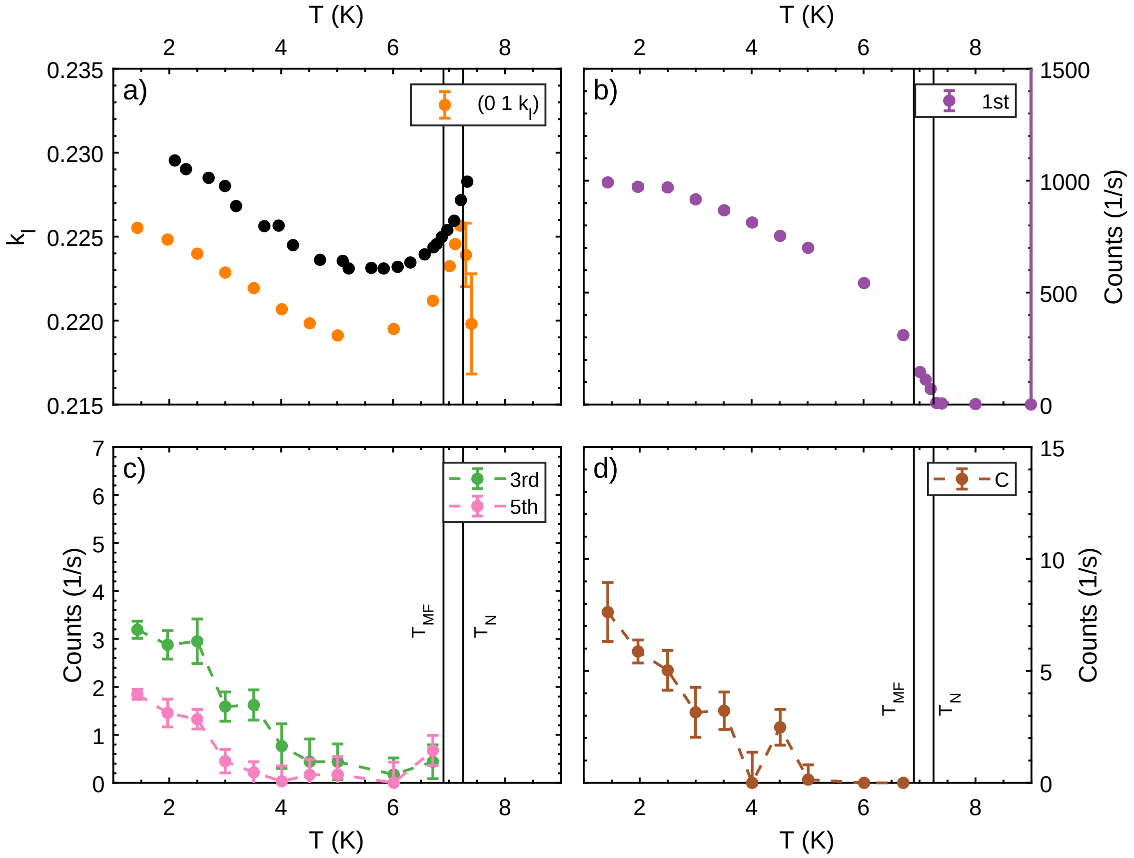

Figure 6.7.: These four panels report the obtained results from temperature dependent fits of all harmonic and commensurate reflections. Panel a) displays the obtained temperature dependence of the measured incommensurate propagation vector (orange data points) and compares it with data (black data points) from Ref. [129] in which results of a deuterated sample were discussed. The plots in b)-d) show the temperature dependent intensity of the 1st, 3rd, 5th harmonics as well as of the commensurate (C) reflection.

gives the value k_l for the incommensurate propagation vector $\mathbf{k}_{\text{inc}} = (00k_l)$. Its temperature dependence is compared with the reported values from a deuterated sample [129] in Fig 6.7 a) and obviously, both values for the incommensurability along c differ approximately by 2% at low temperature. This can be related to an isotope effect, which was so far reported to have a measurable impact only on the structural order-disorder transition at $T_S = 79\,\text{K}$ [131]. No respective effect was observed for both magnetic transitions in $(NH_4)_2[FeCl_5\,(H_2O)]$ [131]. However, from the determined temperature dependence of the incommensurability in Fig. 6.7 a) and by comparing it to the results from the deuterated sample [129] it is obvious that the isotope substitution indeed also affects the magnetic ordering in $(NH_4)_2[FeCl_5\,(H_2O)]$.

For assessing the intensity of higher harmonic reflections and hence the magnitude of anharmonic contributions to the spiral ordering, the related first order intensity is plotted in Fig. 6.7 b) as a function of temperature. In Fig. 6.7 c) the temperature dependence of both odd higher harmonics are shown. The third order reflection evolves below $T \approx 6\,\text{K}$, whereas the fifth order reflection develops only below $T \approx 4\,\mathrm{K}$. Their magnitude is of the same order of magnitude, which saturates at low temperature. By considering the geometry factor, it turns out that the peak intensity at $T = 1.5\,\mathrm{K}$ is approximately 10^{-3} of the incommensurate first order reflection, wherefore both odd harmonics can be estimated to be even larger compared to them in $MnWO_4$ [1]. The related squaring up of spins enforces tiny commensurate fragments which is further indicated by the simultaneous development of a commensurate reflection (see Fig. 6.7)). Astonishingly, the interfering commensurate ordering does not affect the relaxation behavior at $T = 3\,\mathrm{K}$ (see Fig. 6.3). Naturally, this can change at lower temperature, when the squaring up, respectively the anharmonic contributions are getting larger. As noted above, a respective collection of relaxation times at lower temperature was hindered by limited beamtime.

Nevertheless, the main difference for $(NH_4)_2[FeCl_5\,(H_2O)]$ compared to $MnWO_4$ [1] is that odd harmonics and the development of tiny commensurate fragments appear at much lower temperature. The pinning strength at lower temperature is naturally stronger and is thus capable to compensate the depinning effects from interfering commensurate ordering. Further, the intensity of odd harmonics in $MnWO_4$ diverges at the lower transition to commensurate order [1], whereas in $(NH_4)_2[FeCl_5\,(H_2O)]$ the respective intensity follows the intensity of the incommensurate first order peak and saturates at low temperature. This is also confirm with the absence of a transition to pure commensurate ordering at low temperature. It is thus expected that depinning effects do not significantly grow at much lower temperatures in $(NH_4)_2[FeCl_5\,(H_2O)]$, which explains that the relaxation behavior in $(NH_4)_2[FeCl_5\,(H_2O)]$ obeys the combined Arrhenius-Merz law even in the presence of interfering commensurate ordering at $3\,\mathrm{K}$. As mentioned, the finite amount of beamtime did not allow for a collection of relaxation times at much lower temperature, which thus motivates the continuation of this project, respectively the conduction of further time-resolved experiments on this molecular system.

6.3. Conclusion

The multiferroic domain relaxation in the molecular system $(NH_4)_2[FeCl_5\,(H_2O)]$ was discussed and in contrast to other reported neutron diffraction experiments on this system [128,129,131–134], non-deuterated samples were used, which revealed a slight isotope effect on the incommensurability of the magnetic structure. It was shown that the temperature- and electric-field dependence of multiferroic relaxation follows over a significant field and temperature range a simple combined Arrhenius-Merz law, which needs only two parameters to describe the multiferroic domain inversion. In this range, the domain kinetics in the molecular compound are described equivalent to the relaxation behavior in the oxide systems $TbMnO_3$ and $NaFeGe_2O_6$ [3,49], but astonishingly, the relaxation in the molecular system is much slower than in $NaFeGe_2O_6$ and covers only two order of magnitude in time. However, it must be noted that the limitation by the spin-wave velocity allows for much faster relaxation, which can become possible close the multiferroic phase transition, where the nucleation of germs becomes continuous and the combined Arrhenius-Merz law naturally fails. It was further shown that coexisting and competing incommensurate and commensurate ordering do not impact the relaxation behavior in the investigated temperature range, which had its lower limit at $T = 3\,\mathrm{K}$. However this does not yield evidence that the domain kinetics in $(NH_4)_2[FeCl_5\,(H_2O)]$ contrast the anomalous switching behavior in $MnWO_4$ [69–71], where tiny commensurate fragments lead to depinning effects [3]. The absence of a speeding up of domain inversion in $(NH_4)_2[FeCl_5\,(H_2O)]$ can be related to the lower multiferroic temperature range and the related stronger pinning of domains but it cannot be excluded that with decreasing temperature the growing anharmonic contribution do influence the multiferroic relaxation behavior. In this context, it must be also emphasized that at much lower temperatures quantum fluctuations can become relevant and would lead to dominating and temperature independent domain wall tunneling for the relaxation process. This temperature independent behavior was not observed in $(NH_4)_2[FeCl_5\,(H_2O)]$ or other multiferroics so far [3, 49]. Hence, it is not only desirable to investigate the potentially much faster multiferroic relaxation close to T_{MF} but it is also required to deepen the studies on the impact of interfering commensurate order and the occurrence of potential quantum fluctuation driven domain wall motion, which both necessitate the extension of time-resolved experiments to much lower temperatures. However, the presented experiments in this chapter already showed that $(NH_4)_2[FeCl_5\,(H_2O)]$ lines up with $TbMnO_3$ and $NaFeGe_2O_6$ to exhibit a finite temperature range with thermally driven relaxation behavior that is described by a combined Arrhenius-Merz law for dominating sideways motion of domains.

7. Domain relaxation in $Ni_3V_2O_8$ and CuO

7.1. Motivation

It was shown in the previous two sections that the relaxation behavior of multiferroic domains in $NaFeGe_2O_6$ and $(NH_4)_2[FeCl_5\,(H_2O)]$ obeys the same combined Arrhenius-Merz law that was observed to describe the temperature and electric field dependent multiferroic domain inversion in $TbMnO_3$ [49]. This contrasts the complex behavior in $MnWO_4$, where domain kinetics become faster, when approaching the lower transition to commensurate spin *uudd* ordering [70, 71]. It was discussed that this anomalous relaxation behavior can be related to depinning effects that are caused by tiny commensurate fragments evolving close to the transition to commensurate ordering (see chapter 3 and Ref. [1]). For both oxide systems $NaFeGe_2O_6$ and $TbMnO_3$ no such lower commensurate phase is reported [139], which explains their much simpler relaxation behavior compared to $MnWO_4$ [3, 49, 70, 71]. The molecular compound $(NH_4)_2[FeCl_5\,(H_2O)]$ exhibits dominant incommensurate order in zero magnetic field but at low temperature competing commensurate order develops and coexists with the incommensurate magnetic arrangement [132]. Nevertheless, the interfering commensurate order in the multiferroic phase does not affect the relaxation behavior in $(NH_4)_2[FeCl_5\,(H_2O)]$ at least to the lowest measured temperature ($T = 3\,\mathrm{K}$). However, it cannot be excluded that this changes at much lower temperature, where also quantum fluctuations can become relevant to impact the relaxation behavior. The systems $Ni_3V_2O_8$ and CuO exhibit both a multiferroic phase with a lower transition to commensurate ordering [140–143], wherefore they are ideally suitable to compare their relaxation behavior to the materials with much simpler phase diagrams. Moreover, CuO possesses by far the highest multiferroic transition temperature among spiral type-II multiferroics [143], which thus also enables the possibility to investigate the impact of much higher temperatures on the relaxation behavior. In the following two subsections the temperature- and electric-field dependent relaxation behavior of both compounds are presented and discussed.

7.2. $Ni_3V_2O_8$

7.2.1. Crystal and magnetic structure

$Ni_3V_2O_8$ crystallizes in the orthorhombic space group *Cmca* with lattice constants $a = 5.921\,97(3)\,\mathrm{Å}$, $b = 11.372\,13(7)\,\mathrm{Å}$ and $c = 8.224\,95(5)\,\mathrm{Å}$ (at $T = 1.5\,\mathrm{K}$) [144–146]. Edge sharing $Ni^{2+}O_6$ octahedra form a buckled Kagomé lattice in the *ac*-plane and these layers are separated by nonmagnetic $V^{5+}O_4$ tetrahedra along *b*-direction [144–146]. The two-dimensional (planar) Kagomé lattice can be described by corner sharing and isosceles triangles [147] and it can be viewed as a honeycomb lattice with additional sites on the middle point of every edge within a single honeycomb cell (decorated honeycomb lattice [147]). For this kind of lattice, the occupation of each corner by equally antiferromagnetic coupled spins yields high frustration and a highly degenerate groundstate [148–151]. Systems that belong to the family of $M_3V_2O_8$ (with M=Cu^{2+}, Co^{2+}, Zn^{2+}, Ni^{2+}, Mn^{2+} and Mg^{2+}) exhibit a modified version of the planar Kagomé lattice [145, 152–155]. In $M_3V_2O_8$ the Kagomé lattice is buckled, forming a staircase-like structure with two inequivalent sites. These two sites are named spine- (M_s) and cross-tie (M_c) sites [140], whereby the spines define the folding mark for the buckled Kagomé lattice along a straight line of neighboring triangular edges. In $M_3V_2O_8$, these spines are aligned along *a*-direction and are connected to each other via cross-ties [145, 152–155]. The occupation of inequivalent spine- and cross-tie sites by magnetic ions thus lifts the degeneracy of groundstates compared to the ideal Kagomé configuration. The magnetic structure can be still considered two-dimensional, as adjacent buckled Kagomé layers are separated by nonmagnetic $V^{5+}O_4$ layers [145, 152–155]. Nevertheless, finite interlayer interaction can stabilize three-dimensional long-range ordering in these systems [156–158]. The high frustration and inferential sensitivity on slight perturbations of magnetic interactions causes the rich phase diagrams that are found in the buckled Kagomé systems $M_3V_2O_8$ with magnetic M^{2+} ions [156–158]. However, among these materials only $Ni_3V_2O_8$ exhibits a multiferroic state at low temperature [141].

In zero magnetic field $Ni_3V_2O_8$ undergoes a sequence of phase transitions [140, 158]. First, at $T = 9.1\,\mathrm{K}$ an amplitude modulated incommensurate long-range order with $\mathbf{k}_{\mathrm{inc}} = (0.27\,0\,0)$ sets in [140, 146]. The moments are ordered along *a*-direction and only on spine sites (HTI phase) [140, 146]. Below 6.3 K an additional *b*-component develops, forming an elliptically distorted spiral along both, spine and cross-tie sites (LTI phase) [140, 146]. Simultaneous to the onset of spiral ordering on both crystallographic sites, a ferroelectric polarization ($P_{\mathrm{ferro}} \approx 100\,\mu\mathrm{C\,m^{-2}}$) along *b*-direction evolves [141]. This is confirm with the inverse DMI mechanism that was proposed to drive the multiferroic state in $Ni_3V_2O_8$ [159]. The ferroelectric polarization disappears at $T = 3.9\,\mathrm{K}$, when the magnetic structure becomes commensurate with canted moments of equal size [140, 141, 146]. Below $T = 2.3\,\mathrm{K}$ a multi-**k** structure with commensurate ($\mathbf{k} = (0\ 0\ 0)$) and incommensurate propagation vectors ($\mathbf{k} \approx (0\ 1\ 0.403)$) evolves [160]. Here, the incommensurability refers mainly to the ordering on cross-tie sites, where spin spirals evolve. However, spirals on neighboring cross-tie sites exhibits opposite helicity and no ferroelectric polarization was observed to appear in this phase [141, 160].

7.2.2. Experimental Method

The time-resolved investigation of multiferroic domain relaxation in $Ni_3V_2O_8$ was conducted at the triple-axis spectrometer IN12 (proposal CRG-2757 [115]), which is located at the Institute Laue-Langevin. The measurements were carried out with the time-resolved (high-voltage) setup that is described in section 2.4 and Ref. [49].

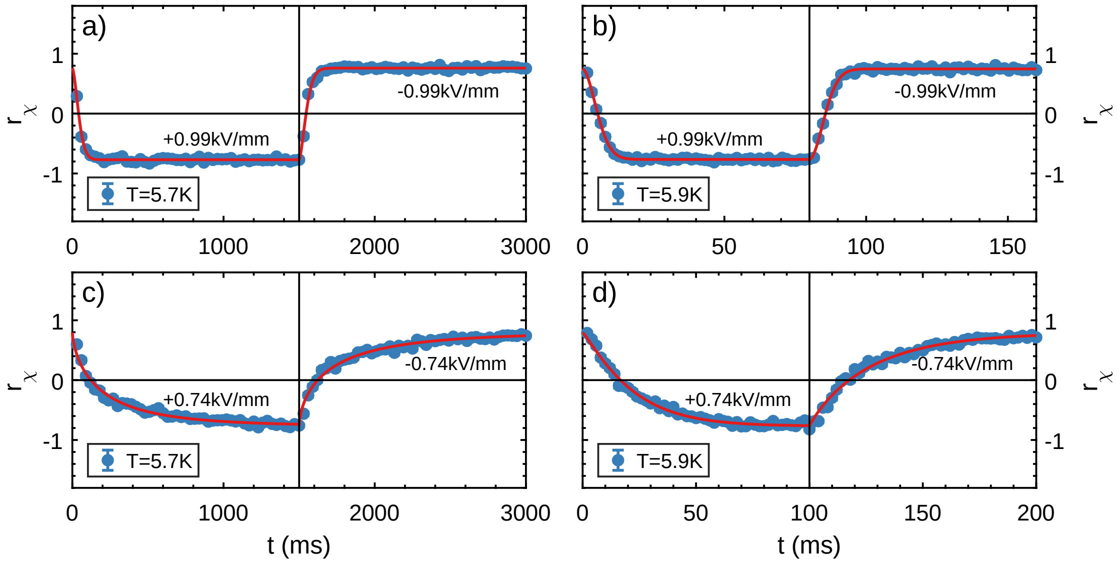

Figure 7.1.: Four exemplary switching curves are displayed in a)-d) for different temperatures and various electric field amplitudes. The relaxation process after each field inversion was fitted (red line) by a stretched exponential function (see equation 2.32).

A larger sample of $Ni_3V_2O_8$ was grown by N. Qureshi utilizing the mirror furnace. A piece of this sample with $d \approx 1\,\mathrm{mm}$ was cut and similar to previous time-resolved studies (see Ref. [3, 49, 70]) it was cramped between aluminum plates for the application of high voltage ($|U| \leq 4\,\mathrm{kV\,mm^{-1}}$). The plate normal was parallel to a direction (thus parallel to $\mathbf{P}$) and the scattering geometry for the holder was defined by (1 0 0)/(0 1 1). The neutron beam was polarized by a supermirror cavity and a pyrolytic graphite (0 0 2) monochromator supplied $\lambda = 3\,\text{Å}$. Higher-order contaminations were suppressed by a velocity selector and the instrument was further equipped with a Helmholtz-coil setup, which defines the guide field direction at the sample position. Spin-flippers before and behind the sample as well as a curved Heusler (1 1 1) analyzer were used for longitudinal polarization analysis. The flipping ratio amounted to FR$\approx$ 22 and was determined at the nuclear Bragg peak position $\mathbf{Q} = (0\,2\,2)$.

7.2.3. Multiferroic domain relaxation

Previous studies on the relaxation behavior reported the invertibility of multiferroic domains in $Ni_3V_2O_8$ [159] and an Arrhenius like dependence of the relaxation time as a function of temperature is reported in the author's master thesis [103]. However, no field dependence of the multiferroic relaxation behavior in $Ni_3V_2O_8$ was investigated during the course of the former time-resolved experiment (CRG-2290). It thus leaves the question open, whether this system can be also described by a combined Arrhenius-Merz law and motivated the continuation (proposal CRG-2757 [115]) of the previous experiment (proposal CRG-

2290 [103]) at the triple-axis spectrometer IN12. To analyze the relaxation behavior with data that were recorded under same conditions, the former temperature dependent switching curves were re-measured during this beamtime.

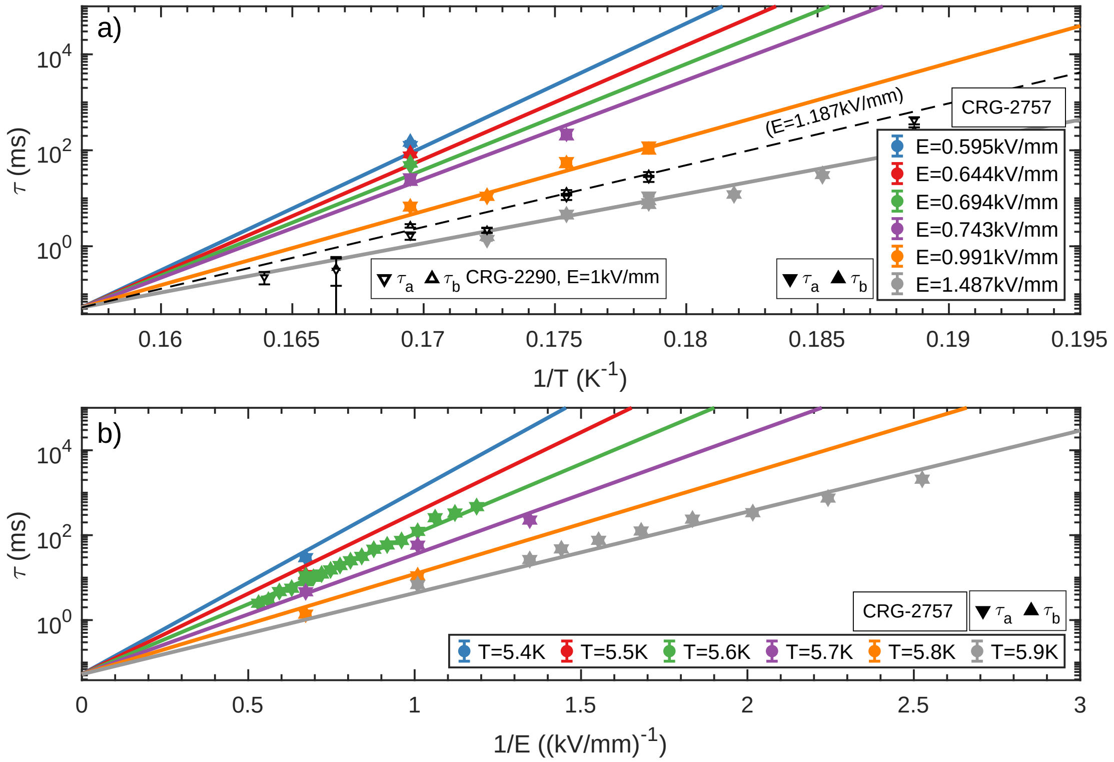

Figure 7.2.: Both panels show the determined relaxation times as a function of inverse temperature and inverse electric field, whereby the y-axis is scales logarithmically. Up and down arrows mark the relaxation times τ_a and τ_b. All solid lines in a) and b) belong to the fitted Arrhenius-Merz law for selected temperatures and electric fields. The black data points in a) refer to the experiment (CRG-2290), which was conducted within the course of the author's master thesis [103]. This data set is not included to the presented fit and obviously it does not match perfectly to the recent data that was recorded for an equivalent field magnitude (see data for $E = 0.991\,\mathrm{kV\,mm^{-1}}$). The black dashed line just indicates for which field magnitude the data would agree with the recent Arrhenius-Merz fit.

For determining the chiral ratio $r_\chi = (I_{x\bar{x}} - I_{\bar{x}x})/(I_{x\bar{x}} + I_{\bar{x}x})$, both spin-flip channels $I_{x\bar{x}}$ and $I_{\bar{x}x}$ were measured at the magnetic reflection $\mathbf{Q} = (1.27\;1\;1)$ and Fig. 7.1 displays exemplary four recorded switching curves for different fields and temperatures. It can be seen that the relaxation process significantly slows down with decreasing temperature but also with reduced electric field amplitude. Further, no asymmetry is visible, when comparing both recorded relaxation times. This indicates that the sample does not prefer a particular handedness of the spiral spin structure. The saturation value of the chiral ratio does not reach the maximum values ±1 as the scattering vector is not perfectly perpendicular to the rotation plane of spins and because of the elliptical distortion of the spiral. However, from previous poling studies on this material (with equivalent scattering geometry) it is known that a chiral ratio of $\approx \pm 0.75$ refers to a completely poled state (monodomain) [103]. Thus, it can be assumed that the multiferroic domain inversion in the field and temperature regime shown in Fig 7.1 was performed between monodomains of opposite handedness. However, close to the upper multiferroic phase transition only a smaller fraction of the system can be poled [103], which was also observed by a reduced maximum value of $|r_\chi|$ for respective switching curves.

For determining the relaxation time of each recorded switching curve, the rising and falling slopes of the inversion process were fitted by stretched exponential functions (see equation 2.32). The stretching exponents b_1 and b_2 vary between 1 and 2 (see Fig. 8.2), which thus indicates a low-dimensional domain growth (see section 1.2.4). This will be referred to again in chapter 8, where the investigations on the relaxation behavior in different multiferroic systems are summarized. All fitted relaxation times τ_a and τ_b are displayed in Fig. 7.2 as a function of inverse temperature and inverse electric field. In addition, the temperature dependent relaxation times ($E = 1\,\mathrm{kV\,mm^{-1}}$) that were recorded within the course of the author's master thesis [103] are also plotted in Fig. 7.2 (see black data points). It can be seen that the relaxation times of this data set slightly differ from the recently recorded relaxation times for an almost equal field magnitude (see relaxation times for $E = 0.991\,\mathrm{kV\,mm^{-1}}$). This slight deviation is reasonable as the recent experiment was conducted on a sample that was cut from the one, which was used for the previous experiment. Together with renewed sample contacts it justifies the observation of slightly different relaxation times. Correspondingly, the subsequently discussed fit was done only by using the recently recorded data.

The relaxation times were fitted by the combined Arrhenius-Merz law (see equation 1.12), which requires only the two fit parameters A_0 and τ^*. Solid lines in Fig. 7.2 a) and b) display the result for respective fixed temperatures and electric fields and as it can be seen from both panels, the combined activation law describes the relaxation behavior at least over the finite measured temperature and field range. It was possible to follow the relaxation of multiferroic domains in $\mathrm{Ni_3V_2O_8}$ over 4 orders of magnitude in time. The fitted activation constant amounts to $A_0 = 352(10)\,\mathrm{K\,kV\,mm^{-1}}$ and the characteristic relaxation time equals $\tau^* = 0.053(8)\,\mathrm{ms}$. Unfortunately, the sample broke during the experimental due to an electric discharge in gas and it was not possible to record relaxation times at lower temperatures. Thus, it cannot be stated, whether the simple Arrhenius-Merz law describes the multiferroic relaxation down to the lower transition to commensurate order and it also cannot be excluded that quantum fluctuation driven domain-wall tunneling becomes relevant at much lower temperature.

7.2.4. Conclusion

In conclusion, $\mathrm{Ni_3V_2O_8}$ presents another multiferroic material, whose relaxation behavior can within a finite temperature and field range be well described by the combined Arrhenius-

Merz law over 4 orders of magnitude in time. Down to the lowest measured temperature no significant deviation from this law can be observed, indicating that no interfering commensurate ordering and also no quantum fluctuation driven domain wall tunneling impacts the relaxation behavior at least in the measured temperature and field regime. The multiferroic relaxation process is thus dominated by thermally activated domain-wall motion. Unfortunately, it was not possible to investigate the relaxation closer to the lower transition to commensurate ordering, as the sample broke during the experimental course of this beamtime. Hence, it cannot be excluded that the relaxation very close to the commensurate phase disagrees with the activation law due to interfering commensurate fragments or growing quantum fluctuations.

The characteristic relaxation time that was determined for $Ni_3V_2O_8$ can be directly compared to the fastest relaxation time in $(NH_4)_2[FeCl_5\,(H_2O)]$ as both materials exhibit nearly the same multiferroic transition temperature T_{MF}. $Ni_3V_2O_8$ possesses much faster relaxation at T_{MF} but due its large activation constant and hence the strong effective pinning of domains, the relaxation slows down much more rapidly compared to the molecular compound in which relaxation becomes faster than in $Ni_3V_2O_8$ at lower temperature. This is confirm with the larger ferroelectric polarization, which can be better pinned in $Ni_3V_2O_8$ [141]. $NaFeGe_2O_6$ exhibits a higher transition temperature but because of the one order of magnitude smaller characteristic relaxation time and the one order of magnitude smaller activation constant, the relaxation time at low temperature is much faster than in $Ni_3V_2O_8$. So far only $TbMnO_3$ was reported to exhibit much slower relaxation behavior compared to $Ni_3V_2O_8$.

7.3. CuO

7.3.1. Crystal and magnetic structure

The binary system CuO crystallizes in the monoclinic space group $C2/c$ with lattice constants $a = 4.6837(5)\,\text{Å}$, $b = 3.4226(5)\,\text{Å}$, $c = 5.1288(6)\,\text{Å}$ and $\beta = 99.54(1)°$ (at $T = 293.15\,\text{Å}$) [161, 162]. Its structure consists of Cu^{2+} ions ($S = 1/2$) that are square planar coordinated by oxygen ions, which are in reverse tetrahedrally coordinated by the copper ions [161, 162]. This arrangement and the underlying symmetry in CuO forms Cu-O zigzag chains that are running along [1 0 -1] and [1 0 1] direction with Cu-O-Cu bond angles of about 146° and 109° respectively [161, 162].

Initially, CuO attracted much interest as square planar coordinated copper-oxygen planes are distinctive ingredients for the high-T_c superconducting cuprates. The magnetic superexchange interactions along Cu-O-Cu bonds in the square planar configurations were proposed to have important impact on the occurrence of superconducting phases in cuprates, wherefore the simple binary system CuO provided an ideal model system for studying these interactions isolated. It was reported that the Cu-O-Cu bond angle ϕ in cuprates is highly sensitive on the interaction parameter J, which ranges from strong antiferromagnetic exchange ($J \approx 100\,\mathrm{meV}$) for $\phi \approx 180°$ to ferromagnetic exchange ($J < 0$) for approximately $\phi < 95°$ [163–165]. In CuO, the dominant (antiferromagnetic) exchange is along [1 0 -1]-direction ($\phi \approx 146°$) with $J \approx 60\,\mathrm{meV}$ and the bond angle along [1 0 1] ($\phi \approx 109°$) results in ferromagnetic exchange [163, 165, 166]. In general, competing antiferromagnetic and ferromagnetic exchange can lead to spiral magnetic ordering and a high dominant interaction parameter promotes a high Neél temperature. It was Kimura *et al.*, who proposed the possibility of induced spiral multiferroic behavior in cuprates and in fact they observed multiferroic behavior in the spiral phase of CuO at exceptional high temperature ($T_{\mathrm{MF}} \approx 228.5\,\mathrm{K}$) [143]. The discovery of improper ferroelectricity in the spiral phase of CuO motivated further research on the underlying driving mechanism in the high temperature multiferroic compound CuO as its understanding is important for the long term goal of designing room-temperature multiferroics with application potential in memory or sensor technologies.

The sequence of magnetic transitions was subject of a controversial discussion [167–173] and only recently, it was clarified that CuO exhibits an intermediate long-range ordered phase above the multiferroic transition temperature [174]. First, in the AF3-phase below $T_{\mathrm{N}} \approx 229\,\mathrm{K}$ and within a small temperature range of about $\Delta \approx 0.5\,\mathrm{K}$ two coexisting incommensurate spin-density waves develop ($\mathbf{k}_{\mathrm{inc}} = (0.506\,0\,\text{-}0.483)$), whose moments are respectively directed along the principal axes of the spiral spin structure [174] that evolves below the multiferroic transition temperature at $T_{\mathrm{MF}} \approx 228.5\,\mathrm{K}$ in the AF2-phase [142]. Here, both principal axes of the spiral are aligned along b and $v = 0.506a^* + 1.517c^*$ direction with a^* and c^* being reciprocal lattice basis vectors [142]. Simultaneous to spiral ordering a ferroelectric polarization ($P_{\mathrm{ferro}} \approx 100\,\mathrm{\mu C\,m^{-2}}$) evolves along b-direction [143, 175] and it was proposed to be induced by inverse Dzyaloshinskii-Moriya interaction [169, 170, 175]. The ferroelectric polarization persists until below $T = 213\,\mathrm{K}$ in the AF1-phase the structure becomes commensurate ($\mathbf{k}_{\mathrm{c}} = (0.5\,0\,\text{-}0.5)$) and collinearly aligned along b-direction [142, 176, 177].

The high multiferroic transition temperature is outstanding among other spiral type-II multiferroics and together with its simple binary structure it motivated the investigation of domain dynamics in CuO.

7.3.2. Experimental Method

For the investigation of multiferroic domain relaxation, a single sample of CuO was cut from a crystal, which was grown by D. Prabhakaran utilizing the optical floating-zone method (for details see [178]). The crystal was then kindly provided for the time-resolved measurements by A. Boothroyd. Similar to previous measurements, the sample was put between aluminum plates, which are connected to the high voltage setup (see section 2.4 and Ref. [49]). The distance between both plates amounted approximately 1.3603 mm and the plate normal was aligned parallel to the ferroelectric polarization i.e. along b-direction. The scattering plane was defined by (100)/(001).

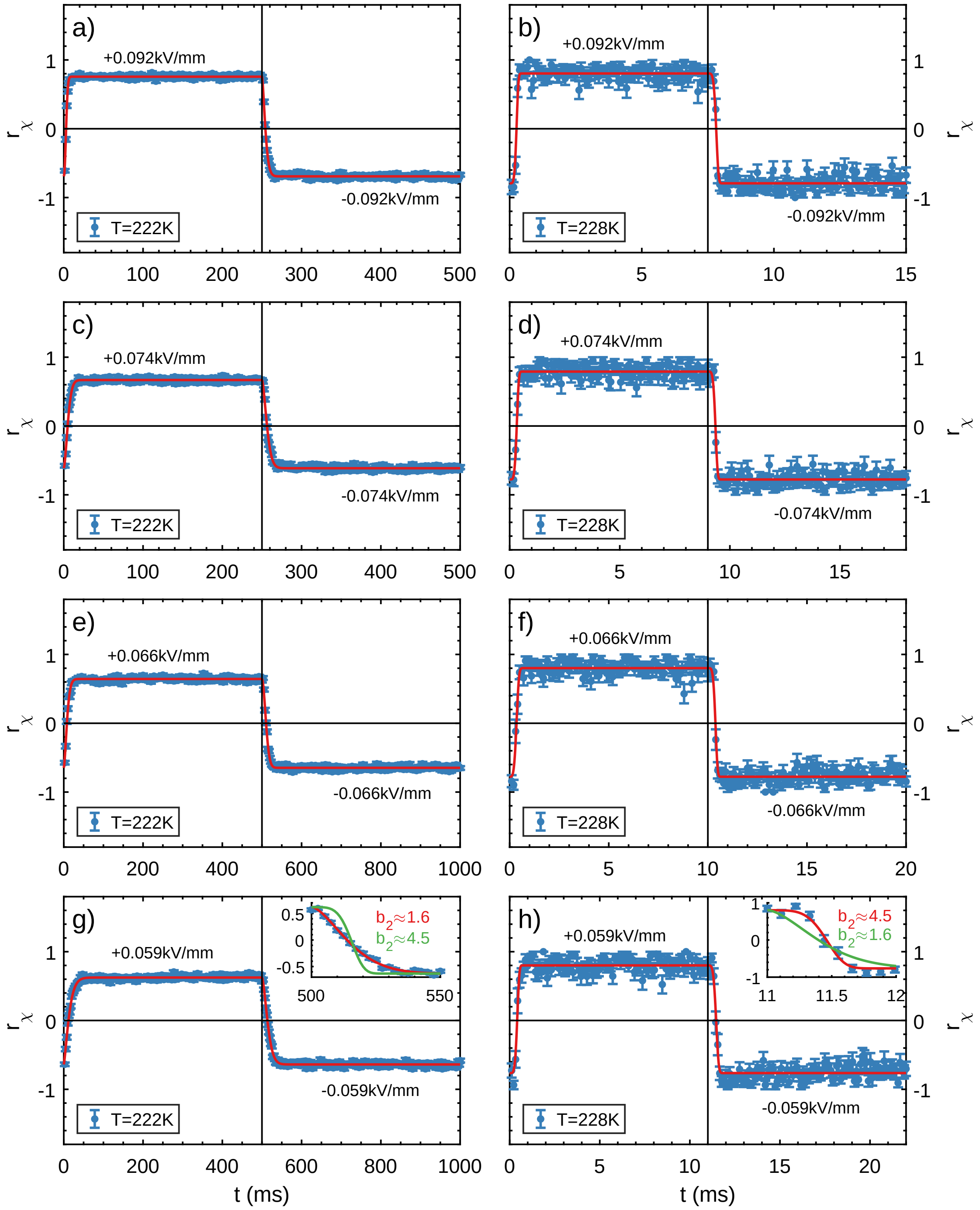

Figure 7.3.: All eight panels display recorded switching curves (blue data points) for different temperatures and various electric-field amplitudes. Vertical black lines mark the time, when the applied electric field was switched and red curves belong to the fit. In g) and h) an additional inset visualizes the impact of different b parameters on the fitted relaxation. Here, the red curve belongs to the fit for which the b_2 was not fixed and the green curve belongs to a fit, for which the b_2 parameter was fixed to a much higher or lower value.

All time-resolved measurements were also conducted at the IN12 triple-axis spectrometer (proposal 5-4-499 [179]) utilizing a similar setup compared to other discussed time-resolved experiments (see chapters 5, 6 and 7.2 and Ref. [3, 49]). A supermirror cavity polarized the incoming neutron beam and a pyrolytic graphite monochromator supplied neutrons with $\lambda = 3.49\,\text{Å}$. In contrast to the other time-resolved experiments on the multiferroic domain kinetics, the neutron polarization analysis was carried out by using a cryogenic polarization analysis device (CRYOPAD [85, 86]). However, instead of using a Helmholtz-coil setup, CRYOPAD was deployed only because it saved the time of conversion work for a successional experiment (proposal CRG-2623 [180]) that necessitated the measurements of off-diagonal terms of the polarization matrix. However, for all measurements on CuO only longitudinal spin-flip and non-spin-flip channels were recorded. The flipping ratio was measured at the nuclear reflection $\mathbf{Q} = (0\,0\,2)$ and amounted to FR ≈ 23.

7.3.3. Multiferroic domain relaxation

The chiral ratio $r_\chi = (I_{x\bar{x}} - I_{\bar{x}x})/(I_{x\bar{x}} + I_{\bar{x}x})$ was measured at the magnetic reflection $\mathbf{Q} = (0.506\,0\,\text{-}0.483)$, which entails an almost ideal scattering geometry as the scattering vector $\mathbf{Q}$ is aligned nearly perpendicular to the rotation plane of spins. In this case, chiral ratios of ±1 can be reached, representing a monodomain state. It can be seen in Fig. 7.3 that the system can be completely switched to opposite handedness over a large temperature and electric field range. Only closer to the lower transition to commensurate ordering and with reduced field amplitude less domains can be switched. From all eight panels it is further visible that similar to other spiral type-II multiferroics (see section 5, 6, 7.2 and Ref. [3, 49]) the relaxation process is highly sensitive on temperature and on the electric field amplitude. The slopes of all measured curves were fitted by stretched exponential functions (see equation 2.32), whereby the stretching exponents vary between 1 and 2 over a wide temperature an field range. This is similar compared to the domain kinetics in other multiferroic systems (see section 5, 6, 7.2 and Ref. [3, 49]) and indicates low dimensional domain growth. However, the b-parameters significantly increase and exceed values above 3, when the temperature approaches the multiferroic phase transition. This is visualized in the insets of Fig. 7.3 g) and h), where the fitted relaxation behavior is compared to a fit, for which the b_2 paramater was respectively fixed to a higher or lower value. Following the Ishibashi and Takagi theory [63–65] (see also section 1.2.4), this can be related to a crossover to continuous germ nucleation and will be referred to again in chapter 8, where the observed relaxation behavior of all discussed systems is summarized.

For CuO, all obtained relaxation times are plotted in Fig. 7.4 as a function of inverse temperature and inverse electric field. The relaxation can be followed over 3 orders of magnitude in time and it can be seen that the relaxation times for both switching directions are of equal size, indicating that the system exhibits no preferred handedness and thus a symmetric switching behavior. The relaxation times were fitted by the combined Arrhenius-Merz law and the fitresult is visualized by solid colored lines for particular temperatures or electric fields in Fig. 7.4. No speeding up of domains can be observed, when approaching the transition to commensurate ordering and it is obvious that the multiferroic domain inversion in CuO can also be well described by the combined Arrhenius-Merz law over the whole multiferroic temperature regime, indicating dominating thermally activated domain wall motion. The fitted activation constant amounts to $A_0 = 1621(32)\,\mathrm{K\,kV\,mm^{-1}}$ and the characteristic relaxation time equals $\tau^* = 0.208(10)\,\mathrm{ms}$.

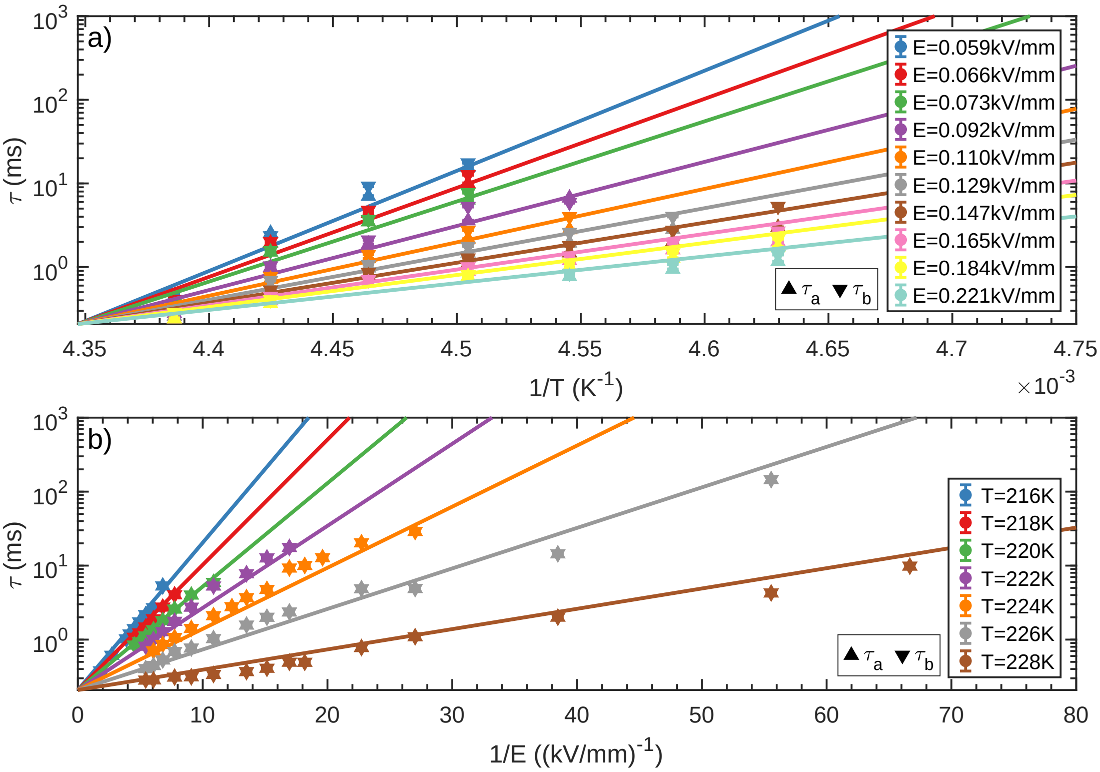

Figure 7.4.: Both plots a) and b) show the relaxation times as a function of inverse temperature and inverse electric field. Colored lines represents the Arrhenius-Merz fitresult

7.3.4. Conclusion

Similar to other multiferroics (see chapters 5, 6, 7.2 and Ref. [3, 49]), the domain kinetics in the high temperature multiferroic system CuO can be well described by the combined Arrhenius-Merz law. It must be noted that the relaxation behavior was here possible to investigate over the whole multiferroic temperature range. No domain-wall tunneling effects were observed to have measurable impact on the relaxation behavior, wherefore the relaxation behavior in CuO is solely driven by thermally activated domain-wall motion. Astonishingly, the characteristic relaxation time at T_{MF} is rather slow or of equal size, compared to the characteristic relaxation time reported for the low-temperature multiferroics $\mathrm{TbMnO_3}$, $\mathrm{NaFeGe_2O_6}$ and $\mathrm{Ni_3V_2O_8}$ (see section 5, 7.2 and Ref. [3, 49]). Only $\mathrm{(NH_4)_2[FeCl_5\,(H_2O)]}$ exhibits a one order of magnitude slower characteristic relaxation time (see section 6). As the activation constant for CuO is comparatively also largest among the studied systems, the high temperature multiferroic system possesses a strong slowing down of relaxation processes as a function of temperature and electric field. The high observed activation constant is further confirm with the very large ferroelectric polarization, which exhibits a higher magnitude compared to $NaFeGe_2O_6$, $(NH_4)_2[FeCl_5(H_2O)]$ and $Ni_3V_2O_8$. Eventually, the cupric oxide system CuO, possesses rather slow multiferroic domain kinetics similar to $TbMnO_3$ [49] but contrarily to the other reported relaxation behavior (see section 5, 6, 7.2 and Ref. [3]).

8. Summary of multiferroic relaxation behavior

The multiferroic domain kinetics were thoroughly discussed in previous chapters for different systems within the framework of quasistatic and in particular within the scope of time-resolved measurements of the electrically triggered variation of the chiral domain population. This chapter summarizes, respectively compares the obtained results that were gained within the course of these time-resolved experiments.

It was discussed that in absence of significant depinning effects, the domain relaxation in spiral type-II multiferroics follows a combined Arrhenius-Merz law, which describes thermally activated domain-wall motion. Thus, the description of temperature and electric-field dependent domain kinetics is distinct from the pure ferroelectric domain dynamics as their relaxation times scale different against temperature and field (see discussion in section 1.2.4). In general, the comparison of different scaling concepts yields a smart way to certify the appropriate model that describes the dependence of a particular quantity from different variables e.g. temperature and electric field. For multiferroic switching, it was shown that the relaxation is described by $\tau = \tau^* \exp\left(\frac{A_0 T_r}{ET}\right)$ [49], which implies that the relaxation times scale against $T_\mathrm{r}/(ET)$ with $T_\mathrm{r} = (T_\mathrm{MF} - T)/T_\mathrm{MF}$. This contrasts the behavior of pure ferroelectrics, for which the relaxation behavior and its description was reported to be more complex and not consistent among different materials [57, 61, 62, 181]. The ferroelectric relaxation times scale against a function of electric field divided by an arbitrary power of the reduced temperature T_r and for lead zirconate titanate, it was reported that the ferroelectric relaxation scales with T_r/E [62]. Both scaling laws were compared in Ref. [49] and [3] (see also chapter 5) for the measured temperature and electric-field dependence of multiferroic domain inversion. It was seen that the multiferroic domain kinetics are described by the scaling law that belongs to the combined Arrhenius-Merz description, which contrasts the scaling of relaxation times against just the quotient of electric field and a power of the reduced temperature. Within the course of this thesis it was shown that the temperature and electric field dependent domain kinetics in $\mathrm{NaFeGe_2O_6}$, $\mathrm{(NH_4)_2[FeCl_5\,(H_2O)]}$, $\mathrm{Ni_3V_2O_8}$ and CuO are also well described by the combined Arrhenius-Merz law at least in the measured temperature and field range. For the sake of completeness, the scaling of recorded relaxation times with temperature and electric field is opposed in Fig. 8.1 to the scaling that was reported for ferroelectric switching in lead zirconate titanate [62].

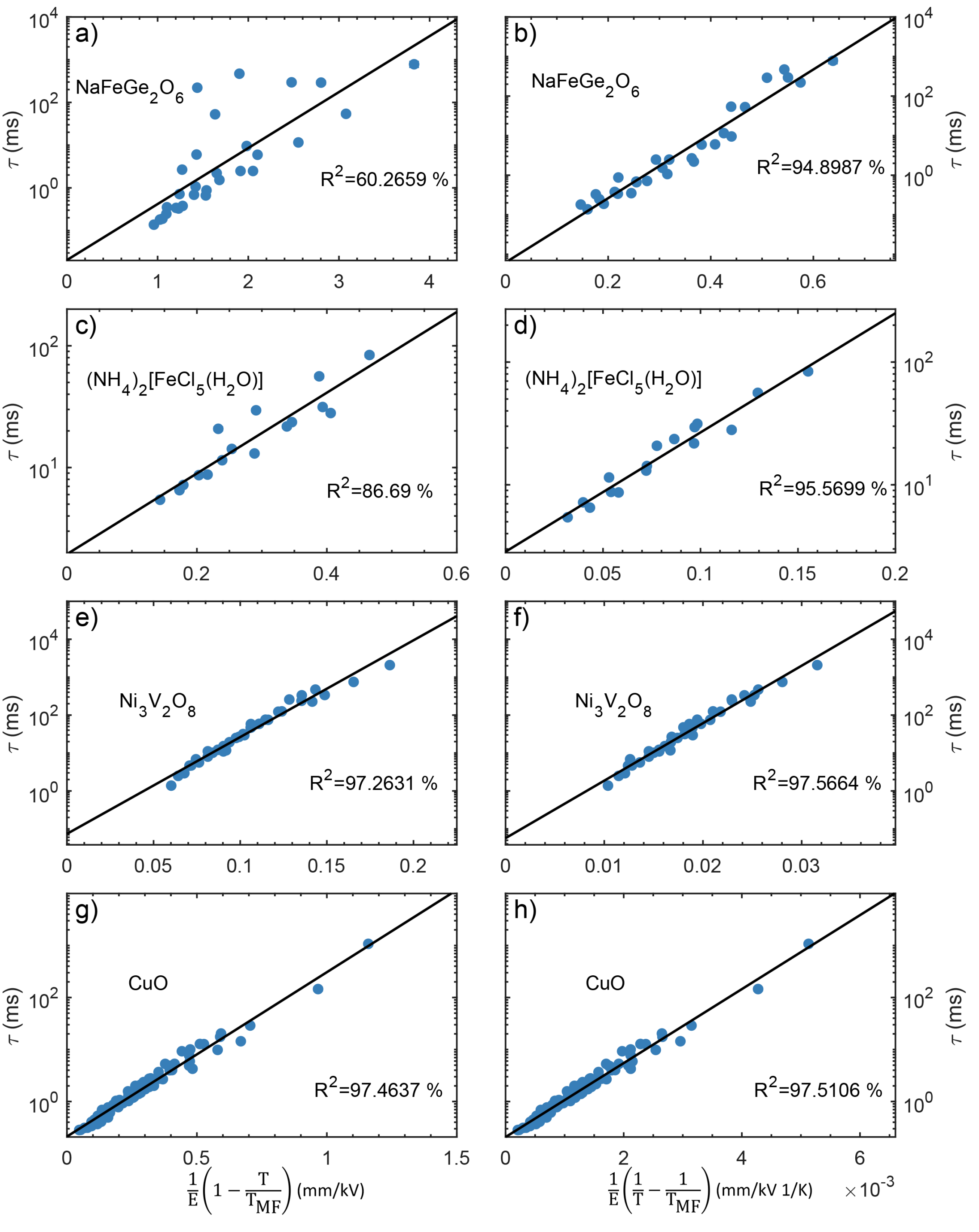

Figure 8.1.: The measured relaxation times (blue data points) for NaFeGe$_2$O$_6$ [3], (NH$_4$)$_2$[FeCl$_5$ (H$_2$O)], Ni$_3$V$_2$O$_8$ and CuO are plotted against different scaling concepts in a)-f). Plots on the left side display the scaling behavior that belongs to pure ferroelectric switching and plots on the right site oppose the scaling concept that would be expected for the combined Arrhenius-Merz law. Black lines refer to fits of the respective scaling relation $\tau = f\left(T_\mathrm{r}/E\right)$ or $\tau = f\left(T_\mathrm{r}/(ET)\right)$ with $T_\mathrm{r} = \left(T_\mathrm{MF} - T\right)/T_\mathrm{MF}$ being the reduced temperature and R^2 being the respective coefficient of determination. It must be noted that a larger R^2 value refers to a more reliable fit.

The left panels in Fig. 8.1 display the scaling against T_r/E and the right panels show the scaling that obeys the Arrhenius-Merz law, which entails an additional factor $1/T$ with respect to the ferroelectric scaling. The black lines refer to fits of respective scaling relations. For $\mathrm{NaFeGe_2O_6}$ and $\mathrm{(NH_4)_2[FeCl_5\,(H_2O)]}$ it is clearly visible that the Arrhenius-Merz description gives the appropriate scaling of relaxation times with temperature and electric field, which is also confirmed by the much higher coefficient of determination for the fit. This holds also for $\mathrm{Ni_3V_2O_8}$ and CuO, but here the difference between both scaling concepts is only marginal, which is mainly because the investigated temperature range with respect to the multiferroic transition temperature is for them much smaller ($T/T_\mathrm{MF} > 0.8$) compared to the respective range in the other investigated multiferroics (e.g. $T/T_\mathrm{MF} \approx 0.14$ for $\mathrm{NaFeGe_2O_6}$). However, the comparison of both scaling concepts further confirms the validity of the Arrhenius-Merz law to describe the relaxation in spiral type-II multiferroics, which do not show large depinning effects.

System	τ^* (ms)	v_sw (m/s)	τ_SW(ms)	A_0 (K kV/mm)	P (μC/mm^{-2})
$\mathrm{NaFeGe_2O_6}$	0.0049(12)	$1460(36)\|\|c^*$	$\approx 10^{-3}$	19.5(9)	≈32
$\mathrm{TbMnO_3}$	≈0.72	$\approx 1200\|\|b^*$	$\approx 10^{-3}$	≈1483	≈800
$\mathrm{Ni_3V_2O_8}$	0.053(8)	-	-	352(10)	≈100
CuO	0.208(10)	-	-	1621(32)	≈160
$\mathrm{(NH_4)_2[FeCl_5\,(H_2O)]}$	2.85(31)	$\approx 800\|\|b^*$ $\approx 300\|\|c^*$	$\approx 10^{-3}$	22.4(14)	≈3

Table 8.1.: This table lists the determined values of the characteristic relaxation time τ^* and the activation constant A_0, whereby the outcome of multiferroic domain inversion studies on $\mathrm{TbMnO_3}$ were taken from Ref. [49]. As noted in chapter 5, the respective outcome for $\mathrm{NaFeGe_2O_6}$ was already published in Ref. [3] by the author of this thesis. The respective literature values of the ferroelectric polarization were taken from Ref. [42, 113, 116, 141, 143] and the spin-wave velocities v_SW were estimated from inelastic neutron scattering studies, which were presented in Ref. [3, 138, 182]. The sideways enlargement time τ_SW for sideways domain-wall motion was roughly estimated from the spin-wave velocity and the sample geometry, whereby it was assumed that a single initial needle-shaped domain in the middle of the sample enlarges perpendicular to the polarization direction towards both sides.

Within the course of this thesis the relaxation behavior of several multiferroic systems were investigated and the outcome of respective Arrhenius-Merz fits are summarized in table 8.1, whereby the list is complemented by the reported results from measurements on $\mathrm{TbMnO_3}$ [49]. For a respective discussion of their magnitude and limitation, these relaxation related parameters are compared to material specific quantities, namely the ferroelectric polarization P_ferro and the spin-wave velocity v_SW perpendicular to the direction of the ferroelectric polarization.

It was already discussed that the characteristic relaxation time τ^* is limited by the spin-wave velocity for sideways-domain wall motion. From this quantity and the respective sample geometry, a sideways enlargement time τ_{SW} can be roughly estimated, when considering an initial needle-shaped domain, which starts to enlarge its size from the middle to both surfaces of the sample by sideways domain-wall motion.

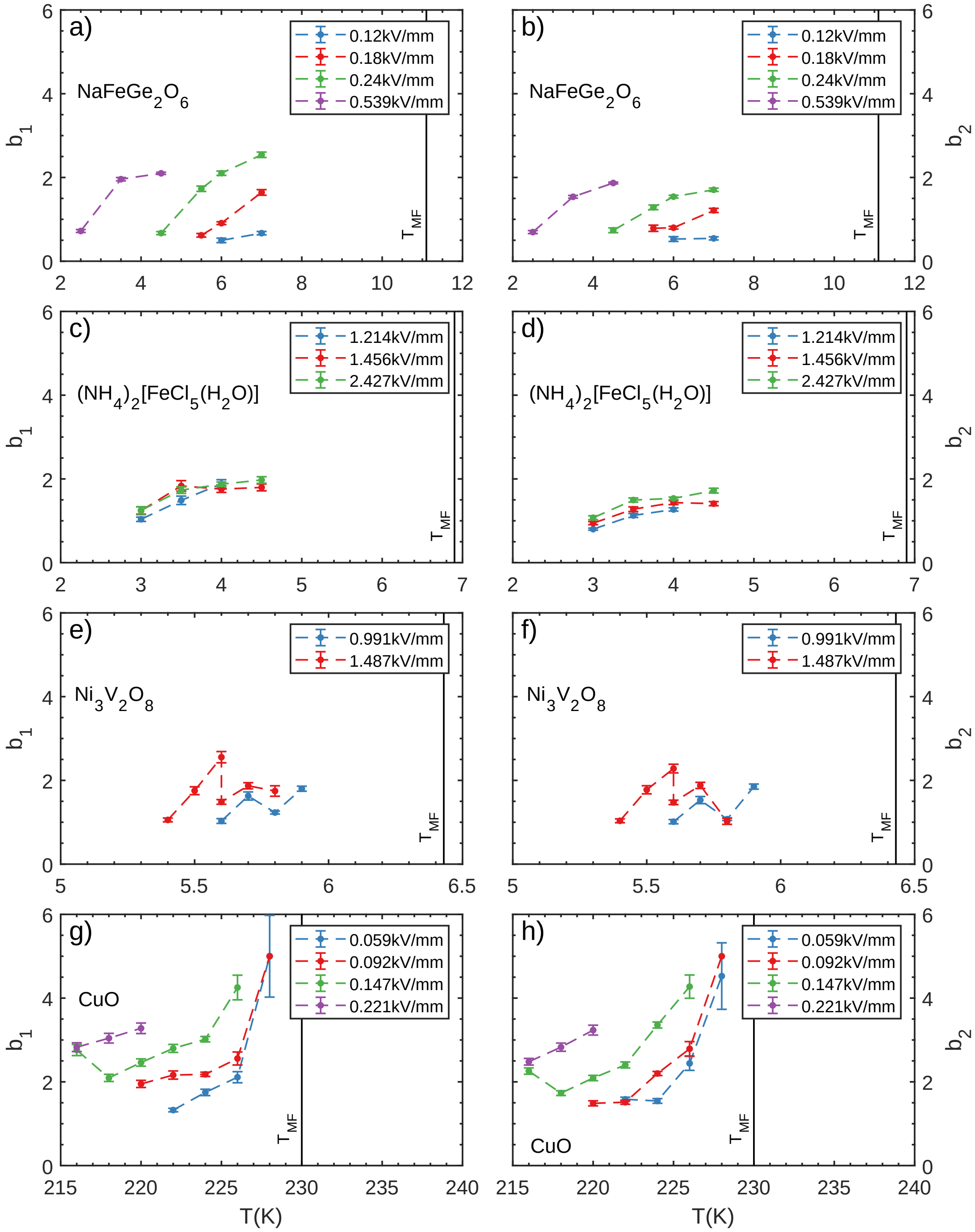

Figure 8.2.: These panels show for exemplary fields the measured temperature dependence of b_1 and b_2. Both values were obtained by fitting equation 2.32 to the recorded switching curves.

It can be read in table 8.1 that for $NaFeGe_2O_6$ the determined characteristic relaxation time is of equal size as the estimated fastest traverse time. Hence, it can be concluded that in $NaFeGe_2O_6$ the Arrhenius-Merz model describes the relaxation also very close to the multiferroic transition temperature, where the relaxation behavior becomes naturally fastest. This is however different for $TbMnO_3$ and $(NH_4)_2[FeCl_5\,(H_2O)]$ for which the determined characteristic relaxation time is much slower than the sideways enlargement time, which is limited by the spin-wave velocity.

This effect is not astonishing as the Arrhenius-Merz law presupposes a nucleation process of germs solely at the beginning of the domain inversion. However, the nucleation can become continuous close to the multiferroic transition temperature and hence also much faster than predicted by the combined Arrhenius-Merz law. In particular, for $TbMnO_3$ this was observed close to T_{MF}, where the measured relaxation times are already significantly below the value of τ^* [49]. In the framework of the Ishibashi theory [63–65], the crossover to continuous germ nucleation is accompanied by a significant enhancement, respectively a divergence of the stretching exponents b_1 and b_2 in equation 2.32. This divergence was observed at T_{MF} in $TbMnO_3$ and further indicated that the failure of the Arrhenius-Merz law close to the multiferroic transition temperature is caused by additional, respectively continuous nucleation during the switching process. Here, the relaxation times can become much faster and can eventually approach the limit that is set by the spin-wave velocity. For $Ni_3V_2O_8$ and CuO no respective inelastic studies were available to estimate the spin-wave velocity.

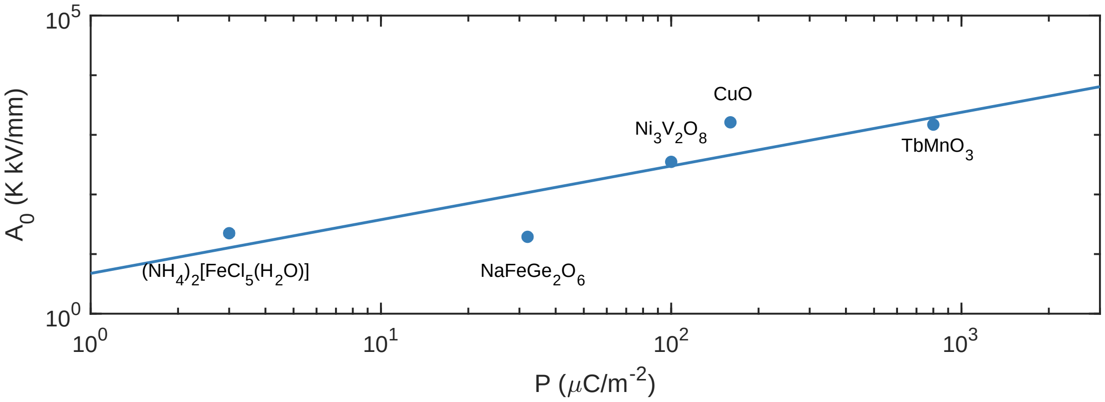

Figure 8.3.: This figure displays the measured activation constants A_0 as a function of the ferroelectric polarization. The latter values are also listed in table 8.1, whereby the literature references are listed in the respective caption.

For the sake of completeness, the determined temperature dependent stretching exponents b_1 and b_2 are also plotted in Fig. 8.2 for the materials, which were investigated within the course of this thesis. It can be seen that the temperature and electric-field dependence of b_1 and b_2 displays qualitatively the same behavior as in $TbMnO_3$ [49]. With increasing temperature or field, the stretching exponents become larger, whereby their values vary between 1 and 2. Here, it must be remembered that in the regard of the Ishibashi theory [63–65] the values indicate the growth-dimensionality. Only very close to the multiferroic transition temperature or for high fields the values for b_1 and b_2 become even larger and eventually start to diverge. This latter behavior was here seen only for CuO but should also be present for the other investigated materials. Here, it must be noted that the observation of this potential crossover to continuous nucleation of germs in CuO profited from the measurements that were possible to conduct very close to the multiferroic phase transition. In percentage, the measurements at higher temperatures were here much closer to T_{MF} than it was the case for the other investigated materials within the course of this thesis. In this context it must be also emphasized that the time-resolved measurements very close to the transition temperature were frequently hindered due to the significant amount of heat that is dissipated, when switching the field with high frequency. Reducing the frequency however goes along with a reduced amount of time-bins that are describing the relaxation process and an enhancement of time-bins entails a less number of detected neutrons in each bin and thus a worsened statistic. This can be compensated by longer counting times but this is eventually limited by the finite amount of beamtime.

As discussed, a further quantity that describes the thermally driven domain-wall motion in the framework of the combined Arrhenius-Merz law is the activation constant A_0. This constant can be related to the pinning strength of domains, which is naturally also referred to the magnitude of the ferroelectric polarization. The tendency that a large ferroelectric polarization can effectively be better pinned and thus enforces a larger activation constant can be unambiguously seen in Fig. 8.3, in which the determined activation constants are plotted against the literature values of the respective ferroelectric polarization. However, it must be emphasized that naturally all values, the ferroelectric polarization, the activation constant and also the characteristic relaxation time possess to finite extend a sample dependency. Even a dependence on the sample setup, respectively the electric contacts cannot be fully excluded. Nevertheless, it qualitatively holds that the activation constant increases for larger values of the ferroelectric polarization and that the fastest possible relaxation time is limited by the spin-wave velocity.

9. Multiferroic domain size development

9.1. Motivation

So far, the discussion of multiferroic domain kinetics was solely based on time-resolved measurements of the chiral ratio r_χ, which senses the relative population of domain types. It was shown that the temperature and electric-field dependent multiferroic domain inversion can be described by a combined Arrhenius-Merz law (see Ref. [3, 49] and chapters 5, 6, 7 and 8), whereby the simplicity of the description was proposed to be related to the different timescales of inversion processes compared to those in pure ferroelectrics [49, 57, 69]. For the latter relaxation behavior, the initial nucleation of germs, the forward and the sideways growth of domains act on the same timescale [57], whereas the description of multiferroic domain inversion is naturally simplified, as essentially only a single process, namely the sideways growth of domains, was observed to dominate the whole inversion procedure [69]. To quantify the different timescales on which forward and sideways domain growth are acting during the multiferroic domain inversion, it is thus desirable to get experimental access not only to the time dependence of the overall domain population but also to the domain size development along directions parallel and perpendicular to the applied electric field.

It was shown by SHG measurements that multiferroic domains exceed the size of several thousand ångström shortly after field inversion [69], wherefore their investigation with conventional neutron diffraction experiments is precluded as the Q-space resolution of respective diffraction instruments allows the observation of correlation lengths only up to several hundred ångström. The absolute values of domain sizes i.e. the correlation lengths along particular directions are encoded in the peak width of respective reflections and indeed it was recently documented for $TbMnO_3$ that time-resolved Q-scans at the IN12 spectrometer did not reveal a significant peak broadening after field inversion [49]. Hence, a different approach is needed to measure the time dependence of multiferroic domain sizes, complementary to the time-resolved neutron scattering studies on the multiferroic domain population development.

By considering Bragg's law, it becomes obvious that the Q-space resolution of a diffraction experiment is mainly limited by $\Delta\lambda$ and $\Delta\theta$. Hence, the resolution can only be increased by a highly monochromatic neutron beam and by high collimation. However, significant improvement of both goes along with vanishing neutron flux at the sample position, wherefore a different experimental approach is desirable. M. T. Rekveldt *et al.* proposed that much higher Q-space resolution can be gained by storing the scattering information not in the scattering angle but in the precession phase of the neutron spin, while passing through a constant magnetic field before and after the sample position [183, 184]. This experimental technique is named Larmor diffraction and is related to the spin-echo setup, which was invented by F. Mezei [185, 186]. The advantage of this procedure is that the Q-space, respectively the energy resolution, is decoupled from the monochromaticity and the beam divergence, which offers an improved precision, while still providing a high neutron flux at the sample position. Mainly the homogeneity of the magnetic field is then limiting the achievable resolution of the diffraction experiment.

In this chapter, time-resolved Larmor-diffraction studies on the multiferroic domain size development in $\mathrm{TbMnO_3}$ are reported. After summarizing the crystallographic and magnetic properties of $\mathrm{TbMnO_3}$, the basic concept of Larmor diffraction will be presented. Subsequently, the adjustments of the instrument, respectively the corrections for interfering magnetic SF-scattering processes are thoroughly discussed and eventually, the time-resolved Larmor-diffraction studies on multiferroic domain inversion in $\mathrm{TbMnO_3}$ are presented.

9.2. Crystal and magnetic structure of $\mathrm{TbMnO_3}$

The multiferroic material $\mathrm{TbMnO_3}$ crystallizes in an orthorhombically distorted perovskite structure (space group $Pbnm$) with unit cell dimensions of $a = 5.3019(1)\,\text{Å}$, $b = 5.8557(1)\,\text{Å}$ and $c = 7.4009(1)\,\text{Å}$ (at $T = 290\,\mathrm{K}$) [187]. It belongs to the family of the rare-earth manganates with chemical formula $R\mathrm{MnO_3}$ for which the rare-earth ion radius r_R determines the $\mathrm{GdFeO_3}$ like cooperative rotation of $\mathrm{MnO_6}$ octahedra [188, 189]. This rotation leads to different bond angles along Mn-O-Mn chains as a function of r_R and causes a variety of phase diagrams within this family of materials [188, 189]. For large values of r_R, an A-type antiferromagnetic structure is preferred and for smaller radii the magnetic groundstate favors E-type ordering [188, 189]. However, for intermediate values of r_R, the system forms incommensurate spiral magnetic structures, which was in particular observed for $\mathrm{TbMnO_3}$ [48, 188, 189].

In $\mathrm{TbMnO_3}$, long-range magnetic ordering evolves below $T_\mathrm{N} \approx 42\,\mathrm{K}$ in form of an incommensurate spin-density wave (SDW) with $\mathrm{Mn^{3+}}$-moments pointing along b-direction and with an incommensurate propagation vector $\mathbf{k}_\mathrm{inc} = (0\,0.28\,0)$ [48, 190]. At $T_\mathrm{MF} \approx 27.6\,\mathrm{K}$ an additional c-component arises and shapes an incommensurate spiral spin structure with moments lying within the bc-plane [48]. Simultaneous to the onset of spiral ordering, the system develops a ferroelectric polarization ($P \approx 800\,\mu\mathrm{C\,m^{-2}}$) along c-direction [42]. The underlying mechanism for the occurrence of ferroelectric ordering was proposed to be the inverse Dzyaloshinskii-Moriya interaction and it was thoroughly reported that the ferroelectric polarization is invertible by both, external electric and external magnetic fields [42, 47]. Furthermore, time-resolved neutron polarization analysis showed that the relaxation behavior of multiferroic domains follow the combined Arrhenius-Merz law, whereby the observed inversion times as a function of field and temperature are rather slow compared to other type-II multiferroics (see Ref. [3, 49] and chapters (see Ref. [3, 49] and chapters 5, 6, 7 and 8). As already noted in the motivation, time-resolved scans over the magnetic peak did not reveal indications of a peak broadening during switching sequences [49], which thus necessitate a different experimental approach to sense the multiferroic domain size development in $TbMnO_3$.

Using $TbMnO_3$ as a model system to implement the Larmor diffraction technique for investigations of time varying multiferroic domain sizes was seen to be highly attractive as its relaxation behavior is already well documented over a wide temperature and electric-field range [49]. Furthermore, SHG experiments already yielded complementary results on multiferroic domain sizes for $TbMnO_3$ [137], which is a helpful reference for the realization of time-resolved Larmor-diffraction experiments on multiferroic domain-size development.

9.3. Experimental Method

The idea of using the Larmor precession of the neutron spin in an external magnetic field as a measuring probe for high resolution neutron scattering experiments was initiated by F. Mezei in 1972 [185, 186]. The basic principle of his so called spin-echo technique is to precess the neutron spins of a polarized neutron beam before and after the scattering event in spatially equivalent field regions that are exhibiting antiparallel field alignments with respect to each other. The total precession phase of each neutron spin depends only on the time the neutron spends in the magnetic field, wherefore a finite velocity spread of the beam leads to a decay of the initial beam polarization, while passing through the first magnetic field region. However, in case of pure elastic scattering events, the reversed field in the second spectrometer arm initiate a rephasing process, which finally restores the full initial beam polarization at the detector. This is the so-called echo signal. An important feature of this process is that in contrast to a conventional triple-axis spectrometer, the neutron spin-echo experiment does not measure the dynamic scattering function $S(\mathbf{Q}, \omega)$, but the intermediate scattering function $I(\mathbf{Q}, t)$, which is the time Fourier transform of $S(\mathbf{Q}, \omega)$. This can be motivated by a consideration of the spin-echo principle within the framework of quantum mechanics. If the quantization axis is chosen to be directed along z and if the neutron beam is polarized along x-direction, then the initial state of a neutron wave-package can be described by the superposition $|+\rangle_x = (|+\rangle_z + |-\rangle_z)/\sqrt{2}$ of eigenstates. A magnetic field that is applied along the quantization axis causes a Zeeman-like splitting ($E = \pm\mu B$), wherefore both states of the initial wave package possess different velocities respectively. Consequently, the splitted parts of the initial wave package (spin up and spin down) arrive at the sample position with a delay in time. This delay $t = \tau_{\mathrm{NSE}}$ is called the neutron spin-echo time and depends only on the field integral along the neutron flight path. Because of dynamic processes, which are acting on this particular timescale, the respective energy exchange of the sample with scattered neutrons enforces that the subsequent rephasing process in the second spectrometer arm cannot not fully recover the initial polarization.

Eventually, the final polarization along x-direction is described by $\langle \cos(\omega\tau_{\mathrm{NSE}}) \rangle$, whereby the weighted average is determined by the probability distribution that describes a neutron scattering process with an energy exchange $\hbar\omega$. This is naturally described by $S(\mathbf{Q},\omega)$, wherefore the normalized final beam polarization

$$P = \frac{\int S(\mathbf{Q},\omega)\cos(\omega\tau_{\mathrm{NSE}})d\omega}{\int S(\mathbf{Q},\omega)d\omega} \tag{9.1}$$

is thus given by the cosine Fourier transformation of the dynamic scattering function, which is equal to the real part of the intermediate scattering function $I(\mathbf{Q},t)$. Hence, a typical Lorentzian lineshape $\Gamma/(\Gamma^2+\omega^2)$ for quasielastic processes leads to an exponential decay of the intermediate scattering function as a function of spin-echo time. From this decay, the excitation linewidth Γ can be obtained. It must be noted that a finite dispersion $\omega(\mathbf{q})$ of the excitation necessitates the adaption of the field boundaries, which is usually referred to as phonon focusing [191, 192]. Here, the perpendicular field boundaries (with respect to the neutron flight path) are inclined to balance a spread of the precession angle, which is purely caused by a finite slope of the dispersion [192].

The main feature of the spin-echo technique is the fact that the essential rephasing process and in particular the measured intermediate scattering function is independent of the initial velocity spread. Hence, the energy resolution of this experimental method is decoupled from the monochromaticity and collimation, which thus allows for high resolution spectroscopy, while maintaining a high neutron flux.

In simple words, each neutron independent of its initial velocity can be used to store information about an energy exchange with the specimen. With some modifications, the advantages of storing the scattering information in the precession phase, rather than in the scattering angle can be transferred to pure elastic scattering studies. It was shown by T. Rekveldt that field-boundaries parallel to the planes of the crystal lattice, a parallel field alignment and the respective cumulation of the spin precession phase in both spectrometer arms does not give information about an energy transfer but about absolute d-values and their respective variance $\Delta d/d$ [183, 184]. Despite the different field orientation, the Larmor diffraction technique in this case nevertheless also profits from the independence of the monochromaticity and the collimation of the neutron beam, which are usually the main factors that limit the diffraction resolution. In the following subsections the basic principles of both, Larmor diffraction and its implementation for multiferroic domain size determination at the three-axes spin-echo spectrometer TRISP [193] (located at the MLZ/FRMII) are elucidated. The respective explanations are based on the introductions to Larmor diffraction in Ref. [194] and Ref. [195].

9.3.1. Larmor diffraction

A typical setup for Larmor diffraction is visualized in Fig. 9.1. The neutron beam gets polarized and enters the first field region, where the neutron spins start to precess around the applied magnetic field that is oriented perpendicular to the initial polarization direction.

The precession angle $\phi = \omega_\mathrm{L} T$ of the neutron spin in a magnetic field B is given by the Larmor frequency $\omega_\mathrm{L} = 2\pi\gamma B$ with $\gamma = 2.916\,\mathrm{kHz}\,\mathrm{G}^{-1}$ and the time T in which the spin is exposed to the field. The transition time only depends on the velocity component $v_\perp$ perpendicular to the field boundaries and in contrast to neutron spin-echo spectroscopy, these boundaries are aligned parallel to the lattice planes. After leaving the first field region, the neutrons arrive a field free region, which is assembled around the sample position. For distinctive scattering angles and appropriate sample alignment the neutrons get diffracted with respect to Bragg's law, which entails that $\mathbf{G_{hkl}} = 2\mathbf{k}\sin(\theta)$ and $|\mathbf{G}| = 2\pi/d_{hkl}$. Here, $\mathbf{G_{hkl}}$ is a reciprocal lattice vector, $\mathbf{k}$ is the wave vector and d_{hkl} is the lattice spacing for the particular $(h\;k\;l)$ plane. As the field boundaries are oriented perpendicular to the reciprocal lattice vector $\mathbf{G_{hkl}}$ and parallel to the lattice plane $(h\;k\;l)$, every scattered neutron that fulfills the Bragg equation automatically possesses the same perpendicular velocity component with respect to the field boundary. Thus, the precession phase of scattered neutrons is independent of a finite wavelength spread or the beam collimation. Even for small tilts of the diffracting planes and finite mosaicity of the sample it can be shown that the precession phase remains the same at least to first order [184].

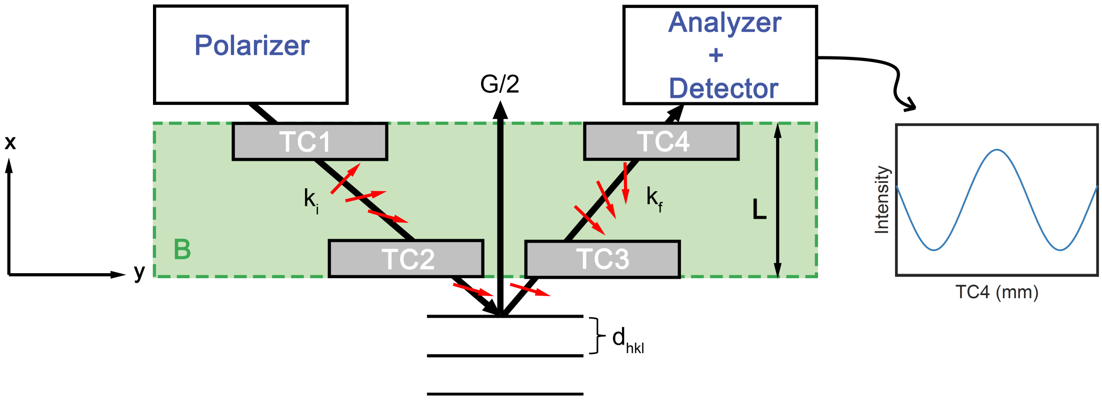

Figure 9.1.: This figure sketches the principle setup of a Larmor diffraction experiment for which a spatially symmetric magnetic field region persists along the neutron flight path before and after the scattering event. Beside the parallel field alignment in both arms, the parallel alignment of field boundaries with respect to the lattice planes is mandatory as mentioned in the text. The measured quantity in corresponding experiments is the intensity as a function of small length changes ΔL for the second field region. It must be noted that for Larmor diffraction instruments that are utilizing the NRSE technique (see section 9.3.2), the field regions are replaced by field free areas and sets of radio frequency coils (TC1-TC4), which simulate the impact of a magnetic field on the neutron spin precession. Likewise to the conventional setup, the length changes of the neutron flight path in the second precession area are realized here by small shifts ΔTC4 of the position of the last radio frequency coil TC4. For the discussion of the neutron beam polarization, the convenient coordinate system with x parallel to the scattering vector is chosen.

After the scattering process, the neutron enters a spatially symmetric field region with respect to the first one and due to the parallel field alignment, the precession phase adds up. By considering solely elastic scattering ($|\mathbf{k_{1,\perp}}| = |\mathbf{k_{2,\perp}}| = |\mathbf{k_\perp}| = \mathbf{G}/2$), the total precession phase at the analyzer/detector position is given by

$$\phi_{\text{tot}} = \omega_{\text{L}} T = \frac{\omega_{\text{L}} L m_{\text{n}}}{\hbar}\left(\frac{1}{|\mathbf{k_{1\perp}}|} + \frac{1}{|\mathbf{k_{2\perp}}|}\right) = \frac{2\omega_{\text{L}} L m_{\text{n}}}{\hbar}\frac{1}{|\mathbf{k_\perp}|} = \frac{4\omega_{\text{L}} L m_{\text{n}}}{\hbar}\frac{1}{|\mathbf{G_{hkl}}|} \tag{9.2}$$

$$= \frac{2\omega_{\text{L}} L m_{\text{n}}}{\pi\hbar} d_{hkl}. \tag{9.3}$$

Hence, the total precession phase entails the information about the lattice spacing d. Consequently a finite distribution of lattice spacings $\Delta d/d$ causes a variation of the spin precession phase $\Delta\phi = \phi_{\text{tot}}\Delta d/d$, wherefore

$$\frac{\Delta\phi}{\phi_{\text{tot}}} = \frac{\Delta d}{d} = \frac{\Delta Q}{|\mathbf{Q}|} = \epsilon. \tag{9.4}$$

A spread $\Delta\phi$ provokes a reduction of the final beam polarization $P(\phi_{\text{tot}})$, which is then given by the average of $\cos(\Delta\phi)$. Hereby, the average is described by a probability distribution $f(\epsilon)$ for the lattice spacing variation $\epsilon = \Delta d/d$. The final beam polarization $P(\phi_{\text{tot}})$ can then be expressed by

$$P(\phi_{\text{tot}}) = \langle\cos(\Delta\phi)\rangle = \int f(\epsilon)\cos(\phi_{\text{tot}}\epsilon)\,\mathrm{d}\epsilon. \tag{9.5}$$

The distribution function $f(\epsilon)$ can be assumed to possess a Gaussian character with ϵ_{FWHM} being the respective full width at half maximum (FWHM)

$$f(\epsilon) = \sqrt{\frac{4\ln(2)}{\pi}}\frac{1}{\epsilon_{\text{FWHM}}}\exp\left(-4\ln(2)\frac{\epsilon^2}{\epsilon^2_{\text{FWHM}}}\right). \tag{9.6}$$

With 9.5 and 9.6 the final beam polarization $P(\phi_{\text{tot}})$ at the detector becomes

$$P(\phi_{\text{tot}}) = P_0\exp\left(-\frac{\phi^2_{\text{tot}}}{16\ln(2)}\epsilon^2_{\text{FWHM}}\right). \tag{9.7}$$

Thus, the decay of the final beam polarization $P(\phi_{\text{tot}})$ as function of the total precession phase yields the respective peak broadening. From $\Delta Q_{\text{FWHM}} = (2\pi)/\xi$ and equation 9.4 the respective correlation length ξ can be calculated by

$$\xi = \frac{2\pi}{\epsilon_{\text{FWHM}}|\mathbf{Q}|}. \tag{9.8}$$

Hence, the polarization decay as a function of the total phase yields the correlation length and is thus the measurable quantity of interest within the course of a Larmor diffraction experiment. The value of the final beam polarization $P(\phi_{\text{tot}})$ is experimentally accessible by measuring the scattered intensity for different neutron paths lengths of the second field region. For respective scans the intensity displays a cosine dependence on small length changes ΔL, whereby the polarization can be calculated from the maximum and minimum intensity via

$$P = \frac{(I_{\max} - I_{\min})}{(I_{\max} + I_{\min})}. \tag{9.9}$$

It must be noted that one period of the cosine modulated intensity corresponds to a single precession of the neutron in the field region. Further, it is important to add that the measured final beam polarization needs to be corrected for a non-ideal performance of the individual components of the instrument. This can be incorporated by normalizing the measured raw data $P_{\mathrm{raw}}(\phi)$ with a reference data set of a perfect Ge crystal

$$P_{\mathrm{corr}}(\phi) = P_{\mathrm{raw}}(\phi) / P^{\mathrm{Ge}}(\phi). \tag{9.10}$$

The decay of the final beam polarization as a function of ϕ_{tot} is schematically sketched for different correlation lengths in Fig. 9.2 a). To measure the correlation length, respectively to fit equation 9.7 usually necessitates a finite set of data points for different total precession angles during the course of a Larmor diffraction experiment. However, to save beamtime for time-consuming temperature-, field- and time-dependent measurements, the decay of $P(\phi_{\mathrm{tot}})$ can also be deduced from a single recorded data point, when assuming the distribution function to be a Gaussian. This particular polarization value is corrected by a reference measurement on Ge (see equation 9.10) and usually this data point is measured in the range of total precession phases, where the alteration of correlation lengths comes along with a significant change of the final beam polarization. This is demonstrated in Fig. 9.2 b), in which the correlation length ξ is plotted for different total precession phases as a function of final beam polarization. From this plot it becomes obvious that low total phases are more suitable to determine small correlation lengths as a finite variation still implies a significant alteration of the finite beam polarization. This is exemplary displayed in Fig. 9.2 b) by the dashed line, which corresponds to $\xi = 1500\,\text{Å}$. For a total phase of $\phi_{\mathrm{tot}} = 1500$rd, a variation of about $\Delta\xi = 500\,\text{Å}$ is measurable by a shift of about $\Delta P \approx 0.15$. In contrast, for a total phase of about $\phi_{\mathrm{tot}} = 6000$rd, this alteration of the correlation length is not resolvable anymore. Using equivalent arguments, the opposite holds for a large correlation length e.g. $\xi \approx 8000\,\text{Å}$. A determination of it is here much more reliable, when utilizing high total precession phases. Only for a complete data set, which covers a wide range of total precession phases, very large as well as tiny correlation lengths can be sensed with equal quality. However, the main aim of this work was to study the development of multiferroic domains as a function of time and the experience from other time-resolved neutron scattering experiments on multiferroic domain kinetics showed that these time-resolved studies and in particular the binning of detected and time-stamped neutrons enforces a tremendous enhancement of counting time by a factor of approximately 100 compared to measurement sequences without time-resolution. Hence, it was considered beneficial to measure the final beam polarization only for an intermediate total phase, which is sensitive to an adequate range of correlation lengths.

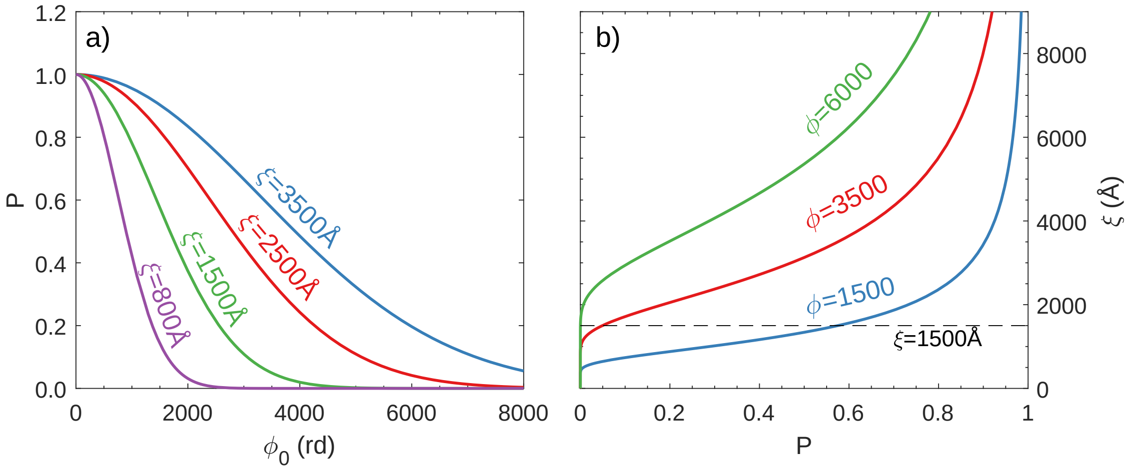

Figure 9.2.: Both panels a) and b) visualize exemplary the relationship between final beam polarization, total phase and the correlation length, whereby for the respective dependencies the lattice parameters of $\mathrm{TbMnO_3}$ as well as the scattering vector $\mathbf{Q} = (2\,0.28\,1)$ were assumed. In a) the decay of the scattered beam polarization is plotted as a function of the total precession phase and for different correlation lengths. Correspondingly, panel b) displays the correlation length as a function of the final beam polarization for different total precession phases.

9.3.2. TRISP spectrometer and setup for multiferroic domain size determination

The larmor diffraction studies for the time-resolved investigation of multiferroic domain size development were conducted at the neutron three-axes spin-echo spectrometer TRISP [193] (proposal 14858 and 16609), which is located at the FRMII in Garching. As included in its name, TRISP offers beside the spin-echo technique also the conventional triple-axis operation, which allows for a precise analysis of phonon and magnon linewidths and lifetimes. With adjusted field boundaries and an adapted field alignment for the accumulation of the precession phase in both spectrometer arms, the instrument further provides a Larmor diffraction mode for accurate measurements of lattice spacings respectively of correlation lengths. The instrument utilizes a thermal neutron beam, which gets polarized by a supermirror transmission polarizer. The initial wavelength spread is reduced by a PG monochromator ($\lambda \approx 3.69\,\text{Å}$) and an additional velocity selector blocks higher order contamination. The polarization analysis of the scattered neutron beam is done by a Heusler crystal and the intensity is detected by a ^{3}He detector.

Equivalent to other reported time-resolved neutron scattering studies on multiferroic domain dynamics (see Ref. [3, 49] and chapters 5, 6, 7 and 8), a single sample of $\mathrm{TbMnO_3}$ was placed between two alumnium plates, which were tightened together by PTFE screws. Both capacitor-like plates were connected to the high-voltage setup (see Ref. [49] and section 2.4) and the scattering geometry was chosen to be $(2\,0\,1)/(0\,1\,0)$. The scattering vector for all subsequently reported measurements was defined by $\mathbf{Q} = (2\,0.28\,1)$. The scattering configuration entails that $\mathbf{k}_\perp$ encloses an angle of about 70° with the direction of the ferroelectric polarization, wherefore the respective experiments predominantly sense the sideways enlargements of domains.

In contrast to respective experiments at IN12, the sample stick did not include a capillary, which would have offered the possibility to control the atmosphere of the nearby sample surrounding via an external valve. To avoid a gas discharge, the cryostat was thus evacuated to a very low pressure, which was possible only to finite extent as a high vacuum would entail the loss of thermal contact and thus temperature instability. During the experimental course it turned out that a pressure of the order of 5×10^{-3} mbar yield both, reasonable thermal contact and the possibility to switch an applied high-voltage without gas discharges.

A peculiarity of TRISP is its utilization of the neutron resonance spin-echo (NRSE) technique, which was invented by Golub and Gähler in 1987 [196–198]. Hereby, both field regions are replaced by radio-frequency (RF) coils, which are defining the boundaries of field-free areas before and behind the sample. At TRISP, these RF-coils are numbered by TC1-TC4 (see Fig. 9.1). To describe their operation, the usual orthogonal coordinate system is used. Both, x and y directions are lying within the scattering plane, whereby x is aligned parallel to the scattering vector. The neutron beam is polarized within the xy-plane and the z direction is oriented perpendicular to it. A single RF-coil is composed of a static magnetic field B_z, which is directed along the z-direction and an additional field $\mathbf{B}_{\mathrm{RF}}$ is rotating inside the xy-plane. The RF-frequency ω_{RF} of this rotating field is adapted to the neutron Larmor precession frequency γB_z, which is preset by the static field strength. Thus, within the reference frame of the neutron, the rotating field is static, whereby its field magnitude is regulated such that the neutron spin precesses around this field exactly by 180°. This π-flip around the rotating field thus accumulates a phase of $\phi = 2\omega_{\mathrm{RF}} t_1$ with t_1 being the time, when a neutron with velocity v enters the RF-coil TC1. While passing this first RF-coil of thickness d, the moment precesses also around B_z, wherefore the precession phase amounts in total to $\phi_1 = 2\omega_{\mathrm{RF}} t_1 + \omega_{\mathrm{RF}} d/v - \phi_0$ after leaving the first RF-coil TC1. Here, ϕ_0 is the initial precession phase of the neutron spin (with respect to the x-axis), when entering the RF-coil. For the sake of simplicity, the following explanations are based on the assumption that the beam is initially polarized in x-direction, which entails $\phi_0 = 0$. Between the first two RF-coils TC1 and TC2, the neutron does not precess, as this area is field-free, which contrasts the conventional spin-echo setup. At TRISP, this is realized by a Mu-metal shielding, which is not only covering the sample position but also the flight path of length l between the pairs of RF-coils.

The accumulation of the precession phase ϕ_2 inside the second RF-coil is equivalent to the process inside the first coil. As the time when the neutron enters this second RF-coil TC2, is determined by $t_2 = t_1 + l/v$, the overall accumulated phase in front of the sample amounts then to $\phi = 2\omega_{\mathrm{RF}} t_2 + \omega_{\mathrm{RF}} d/v - \phi_1 = 2\omega_{\mathrm{RF}}(t_2 - t_1) = 2\omega_{\mathrm{RF}} l/v$. An equivalent set of RF-coils that are enclosing a zero-field region is placed behind the sample. All four RF-coils can be moved and in particular the last coil position is scanned during the experimental course of a spin-echo, respectively a Larmor diffraction experiment. This scan yields a cosine modulated intensity, from which the final beam polarization can be calculated by using equation 9.9.

Depending on the mode of operation (spin-echo spectroscopy or Larmor diffraction), both fields in TC3 and TC4 are parallel or antiparallel aligned with respect to the alignment in TC1 and TC2. For a static magnetic field of same magnitude, the resonance technique thus provides twice the precession angle compared to the conventional spin-echo setup. The main advantage is however that the precession region of the conventional spin-echo setup can be replaced by a field free region. Hence, the resolution is significantly enhanced for the NRSE technique as it does not depend on the field homogeneity along a finite flight path but only on the precision of the adjusted radio-frequency. In view of potential stray fields and the practicability of tilts, the RF-coils further allow for a much simplified alignment of field boundaries with respect to the conventional setup. It must be noted that TRISP utilizes the so-called bootstrap method [199], which entails that each RF-Coil is complemented by a second one with opposite field orientation of the static field. The main advantage of this technique is the significant reduction of stray fields.

For Larmor diffraction, the parallel alignment of field boundaries with respect to the diffracting lattice planes is mandatory. However, the parallel or antiparallel alignment of fields for both RF-coils in the second spectrometer arm with respect to them in the first arm is not strictly determined and depends on the type of scattering. As noted, magnetic scattering potentially entails spin-flip scattering or even the modulation of the beam polarization. Hence, to guarantee the accumulation of the spin precession phase in both spectrometer arms for the Larmor diffraction technique, the appropriate mode of operation for the RF-coils in both arms need to be carefully adapted.

9.4. Results

9.4.1. Field alignment

As noted, magnetic scattering can entail SF-processes that naturally impact the accumulation of the Larmor precession phase. To operate the instrument in the demanded mode (spin-echo spectroscopy or Larmor diffraction) necessitates thus a thorough understanding of the interaction between the neutron spin and the underlying magnetic structure. In particular, the field alignment of both RF-coil sets need to be adapted to the underlying magnetic scattering process. This exigency can be deduced from the sketch in Fig. 9.3 a), in which the magnetic components are respectively directed along the axes of the conventional coordinate system for polarization analysis. It must be noted that a potential M_x component does not contribute to the scattering process as it would be aligned parallel to the scattering vector. In this example it is assumed that an incoming neutron spin $\mathbf{s_0}$ assembled a phase ϕ_0 in the first precession device and is subsequently scattered from a magnetic arrangement. Depending on the magnetic component from which the scattering is caused, the resulting orientation of the neutron spin is described either by $\mathbf{s_1}$ or $\mathbf{s_2}$. In case that the system exhibits solely a magnetic component along z-direction, the neutron spin undergoes a π-flip around M_z and is finally described by $\mathbf{s_2}$. The total precession phase thus amounts to $\phi_2 = \pi + \phi_0$ and obviously, this resembles the configuration for pure nuclear scattering. Only a phase of π is added to the neutron spin precession, which is however different for a SF-process that is caused by the M_y component. Here, the incoming spin $\mathbf{s_0}$ performs a π flip around M_y, wherefore the spin orientation after the scattering process is described by $\mathbf{s_1}$. This yields a total precession phase of $\phi_1 = \pi - \phi_0$, which implies that the operation of the first pecession device is effectively inverted. Thus, to compensate this negation for the favored instrument mode, the actual field-alignment of the second precession device needs to be inverted. This kind of treatment is distinct for magnetic arrangements with components solely aligned parallel to y, but the coexistence of finite M_y and M_z components complicates the adequate adaption of the field alignment. It is not clear which of the mentioned processes is dominating, but the appropriate field alignment can be tested experimentally by measuring the final beam polarization for different operation modes.

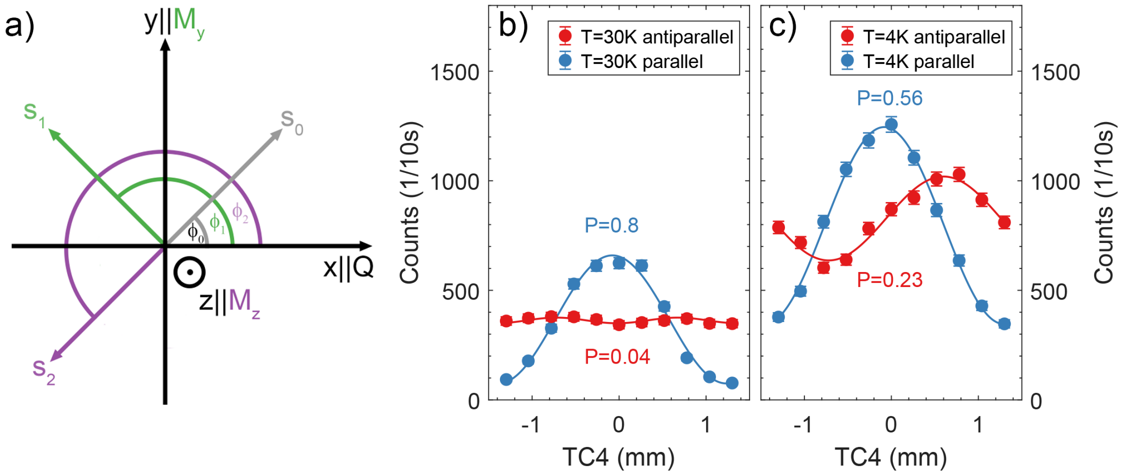

Figure 9.3.: The left panel a) sketches possible SF-processes and the respective impact on the total precession phase, whereby a similar visualization can be found in Ref. [200, 201]. Here, the common coordinate system is used and M_y and M_z denote the magnetic components that are respectively directed along y and z direction. A potential M_x component is here not relevant for the scattering process as it is aligned parallel to the scattering vector. Both plots b) and c) show the executed TC4 position scans, which were recorded on the magnetic Bragg peak $\mathbf{Q} = (2\,0.28\,1)$ to determine the appropriate field alignment for the demanded mode of operation. The field boundaries were here aligned perpendicular to the flight path of the neutron and the total precession phase amounted to $\phi_{\text{tot}} = 1914\text{rd}$.

As mentioned in section 9.3.2, the final beam polarization can be determined by scans of the TC4 position. These scans are displayed in Fig. 9.3 b) and c) for different temperatures and respectively for both kinds of field alignments. The scans were executed for a total precession phase of about $\phi_{\text{tot}} = 1914\text{rd}$, the scattering vector was chosen to be $\mathbf{Q} = (2\,0.28\,1)$ and the field boundaries were aligned perpendicular to the neutron flight path. In this context it must be remembered that the scattering geometry was chosen to be (2 0 1)/(0 1 0). The respective measurements at $T = 30\,\mathrm{K}$ are presented in Fig. 9.3 b). At this temperature, the moments are forming a SDW with moments solely directed along b and with respect to the scattering geometry, the magnetic moments are hence aligned almost parallel to the y-direction. It can be deduced from Fig. 9.3 b) that the antiparallel field alignment entails almost zero beam polarization at the detector, whereas the parallel alignment of fields yields a high final beam polarization. As the accumulation of the precession phase in both spectrometer arms naturally entails the decay of beam polarization, the recorded data in Fig. 9.3 b) clearly indicate that both precession devices need to be operated with an antiparallel field alignment for the execution of a Larmor diffraction experiment on TbMnO$_3$. By considering the chosen scattering geometry, this outcome is also conform with the theoretical consideration above (see also Fig. 9.3 a)). The accumulated precession phase in the first spectrometer arm is effectively inverted and eventually, this needs to be compensated by an opposite field alignment in the second spectrometer arm.

Astonishingly, two features of the presented coil scans at 4 K are apparently different with respect to the measurements at 30 K. First, the mean intensity I_0 of the cosine modulated intensity is significantly larger with respect to the measurements presented in Fig. 9.3 b). This can be related to the onset of chiral ordering below $T_{\mathrm{MF}} = 27.6\,\mathrm{K}$ and the underlying multiferroic domain population, which in case of an imbalanced domain distribution implies a difference between both SF channels $I_{x\bar{x}} = \mathbf{M}_\perp \mathbf{M}_\perp^* - i(\mathbf{M}_\perp \times \mathbf{M}_\perp^*)_x$ and $I_{\bar{x}x} = \mathbf{M}_\perp \mathbf{M}_\perp^* + i(\mathbf{M}_\perp \times \mathbf{M}_\perp^*)_x$. It is visualized in Fig. 9.3 a) that the SF processes that are triggered by M_y and M_z components entail a sign change of the neutron spin orientation with respect to the x-direction. However, in the presence of a chiral structure, a SF process from x to -x direction is only allowed for a particular handedness of the spiral. Of course this also holds for a flip from -x to x and respectively the opposite handedness. In case of an imbalanced population this constraint thus causes a gain, respectively a loss of averaged intensity depending on the handedness of the partially poled spiral domain structure. Therefore, the averaged intensity of TC4 coil scans in the multiferroic phase can be altered by poling the multiferroic domain distribution and the observed larger averaged intensity in Fig. 9.3 c) is thus an indication for a finite imbalance of the underlying multiferroic domain population.

The onset of chiral ordering entails also another consequence for the measured signal, as the scattering process from a chiral arrangement naturally alters the amount of beam polarization. This process is highly sensitive on the underlying domain population, the scattering geometry, elliptical distortions, the initial orientation of the incoming polarization vector. The respective dependencies will be discussed in the following course of this chapter.

It is visible in Fig. 9.3 c) that the measured final beam polarization for the parallel and antiparallel operation at $T = 4\,\mathrm{K}$ differs with respect to the coil scans at 30 K.

Nevertheless, from both tested field orientations at 4 K it can be deduced that the antiparallel field alignment is still the appropriate mode for the execution of a Larmor diffraction experiment on TbMnO$_3$. Thus, in view of the demanded Larmor diffraction experiments on multiferroic domain sizes, the precession devices in both diffractometer arms were operated with opposite field alignment for all subsequently discussed measurement. Further, the field boundaries were inclined to be parallel to the diffracting lattice planes that are sensed by the scattering vector $\mathbf{Q} = (2\,0.28\,1)$. In this configuration the signal comprises the correlation length and is to first order not affected by the mosaic spread of the sample (see section 9.3.1 and Ref. [184]).

It is obvious that the quantity of interest, namely the correlation length of a multiferroic domain is superimposed by several complex processes that need to be understood and separated in the measured signal. To understand the impact of all named effects on the final beam polarization and eventually to correct for them, it is beneficial, respectively necessary to calculate the impact of chiral scattering on the scattered beam polarization for different initial polarization alignments, respectively for different domain populations.

9.4.2. Alteration of the beam polarization

As noted in section 2.3, the orientation of the scattered beam polarization can be determined from the Blume-Maleev equations, which describe the rotation as well as the alteration of the scattered beam polarization. By considering the choosen scattering geometry (see section 9.3.2), the magnetic arrangement and the explanations that are given in [202], the outgoing beam polarization $\mathbf{P}_{\text{out}}$ can here be described by

$$\mathbf{P}_{\text{out}} = \begin{pmatrix} P_{xx} & 0 & 0 \\ 0 & P_{yy} & 0 \\ 0 & 0 & P_{zz} \end{pmatrix} \cdot \begin{pmatrix} P_x \\ P_y \\ P_z \end{pmatrix} + \begin{pmatrix} \frac{-2\text{Im}(\mathbf{M}_{\perp\mathbf{y}}\mathbf{M}^*_{\perp\mathbf{z}})}{(\mathbf{M}_\perp\mathbf{M}^*_\perp + 2P_x\text{Im}(\mathbf{M}_{\perp\mathbf{y}}\mathbf{M}^*_{\perp\mathbf{z}}))} \\ 0 \\ 0 \end{pmatrix} \tag{9.11}$$

with

$$P_{xx} = \frac{-\mathbf{M}_\perp\mathbf{M}^*_\perp}{\mathbf{M}_\perp\mathbf{M}^*_\perp + 2P_x\text{Im}(\mathbf{M}_{\perp\mathbf{y}}\mathbf{M}^*_{\perp\mathbf{z}})} = \frac{-\mathbf{M}_\perp\mathbf{M}^*_\perp}{I} \tag{9.12}$$

$$P_{yy} = \frac{-\mathbf{M}_\perp\mathbf{M}^*_\perp + 2\text{Re}(\mathbf{M}_{\perp\mathbf{y}}\mathbf{M}^*_{\perp\mathbf{y}})}{\mathbf{M}_\perp\mathbf{M}^*_\perp} \tag{9.13}$$

$$P_{zz} = \frac{-\mathbf{M}_\perp\mathbf{M}^*_\perp + 2\text{Re}(\mathbf{M}_{\perp\mathbf{z}}\mathbf{M}^*_{\perp\mathbf{z}})}{\mathbf{M}_\perp\mathbf{M}^*_\perp} \tag{9.14}$$

and

$$I = \mathbf{M}_\perp\mathbf{M}^*_\perp + 2P_x\text{Im}\left(M_{\perp y}M^*_{\perp z}\right). \tag{9.15}$$

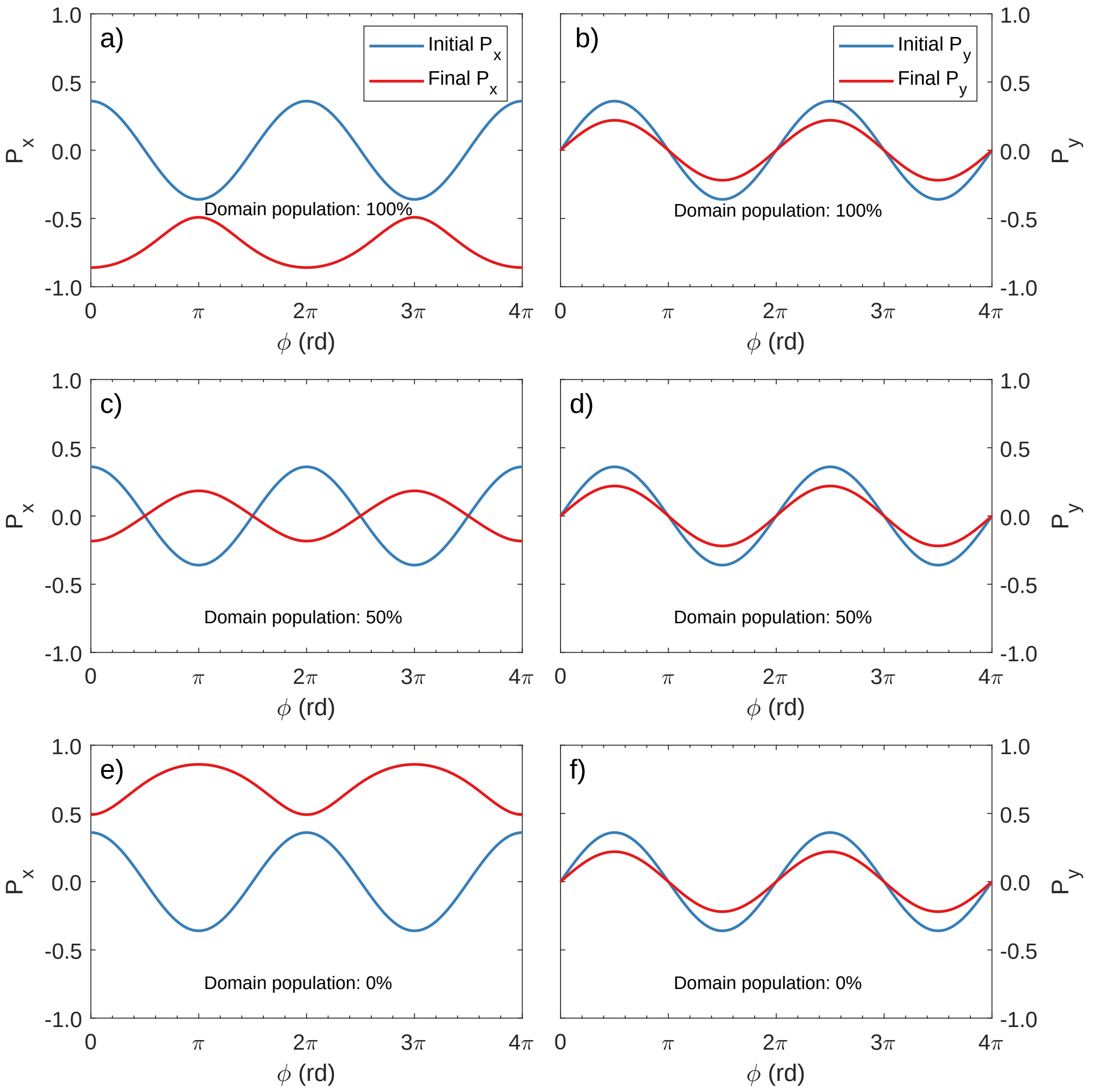

Figure 9.4.: The panels on the left and right side respectively display the x- and y-component of the initial and the referring scattered polarization vector as a function of their rotation angle in the xy-plane. Here, the angle ϕ describes the orientation of the initial polarization vector with respect to the x-axis and it was assumed that the magnitude of the initial polarization amounts approximately to $|\mathbf{P}_{\text{in}}| = 0.36$. The different rows in this figure refer to a different underlying multiferroic domain population, whereby a population of 50% refers to a chiral ratio of $r_\chi = 0$.

Figure 9.4 displays this scattering behavior exemplary for the chiral spin structure in the multiferroic phase of TbMnO$_3$. In this context it is assumed that the magnetic moment is described by $\mathbf{m} = (0, im, 0.5m)$, which takes into account the elliptical distortion of the spiral. This assumption bases on the reported chiral ratio $r_\chi \approx 0.8$, which was measured for a completely poled system that was mounted in the same scattering geometry. This observed chiral ratio for a monodomain however contrasts the calculated one ($\pm r_\chi = 0.93$ [47]), which was obtained by considering the magnetic refinement result from [48] and the underlying scattering geometry in [47]. The perpendicular component $\mathbf{M}_\perp(\mathbf{Q})$ of the magnetization with respect to $\mathbf{Q}$ can be calculated with equation 2.16, whereby the scattering vector was chosen to be $\mathbf{Q} = (2\,0.28\,1)$. To set this example also into the context of a Larmor diffraction experiment, it is further assumed that the beam polarization at the sample position is significantly decreased by the passage through the first Larmor precession region, respectively the first spectrometer arm.

The initial polarization vector is described by $\mathbf{P}_{\text{in}} = (P_x = 0.36\cos(\phi), P_y = 0.36\sin(\phi), P_z = 0)$ with ϕ being the angle between the polarization vector and the x-axis. The components P_x and P_y of the scattered beam polarization can be calculated by utilizing equation 9.11 for each value of ϕ. It can be seen in Fig. 9.4 a) that the magnitude P_x of the scattered beam is vastly different to its initial value, whereby the alteration of P_x is different for a parallel and antiparallel alignment of the initial polarization vector with respect to the x-direction (see respective values for $\phi = 0\,\text{rad}$ and $\phi = \pi$ rad). As it will be referred to in the later course of this chapter, this change of the polarization magnitude significantly adulterates the polarization decay that is measured for the determination of correlation lengths and correspondingly need to be corrected.

It can be seen in Fig. 9.4 b) that the absolute value of the P_y component of the scattered beam is always smaller than the referring value for the initial polarization vector. Hence, the chiral monodomain rotates the initial polarization vector towards x-direction, while simultaneously changing the magnitude of $|\mathbf{P}_{\text{out}}|$. It must be noted that in the particular case of a perfect scattering geometry and in case of no elliptical distortions for the chiral structure, the P_y component of the final polarization vector would always be zero so that the final polarization vector is (independent of ϕ) always perfectly polarized ($|\mathbf{P}_{\text{out}}| = 1$) and aligned parallel or antiparallel to x-direction, i.e. the chiral structure acts here as a polarizer.

It can be seen in Fig. 9.4 c) that an equal distribution of right- and left-handed monodomains yields the lowest change of $|\mathbf{P}_{\text{out}}|$, while a monodomain of opposite handedness (see Fig. 9.4 e)) entails an inverted alteration of the scattered beam polarization with respect to the initial monodomain (see a)). In the context of a varying domain population, a further key feature of the scattered beam polarization can be deduced from the right column in Fig. 9.4. Here, it becomes obvious that a change of the domain population does not have any influence at all on the P_y component of the scattered beam. Thus, for a fixed initial polarization vector in the xy-plane, the final polarization vector is rotated towards x by the same angle independent of the underlying domain population.

Obviously, the orientation of the initial polarization vector has significant influence on the alteration of the final beam polarization and hence also on the necessary correction that has to be applied for a sound and accurate determination of correlation lengths, respectively multiferroic domain sizes. Thus, to maintain coherence in view of the necessary corrections it was seen beneficial to adapt the first precession device such that the beam polarization at the sample position is always aligned parallel (respectively antiparallel) to the scattering vector.

The respective alignment of the beam polarization at the sample position can be deduced from position variations of the first RF-coil (TC1). By varying the position of TC1, the effective length of the first precession device is changed, wherefore the beam polarization changes its orientation at the sample position. This can be measured, when for each step of the TC1 position alteration, a TC4 scan is executed to determine the final beam polarization as well as the averaged intensity I_0. This process was done, respectively analyzed for the two fixed precession phases $\phi_{\text{tot}} = 1720\text{rd}$ and $\phi_{\text{tot}} = 3535\text{rd}$, while a constant electric field of about $E = 4\,\text{kV}\,\text{mm}^{-1}$ was applied to the sample, which was cooled to $T = 20\,\text{K}$. From previous experiments on the multiferroic domain population it is known that the applied field magnitude is sufficient to pole the system completely [47]. For both total precession phases the final beam polarization as well as the averaged intensity are plotted in the upper and lower panels of Fig. 9.5, respectively.

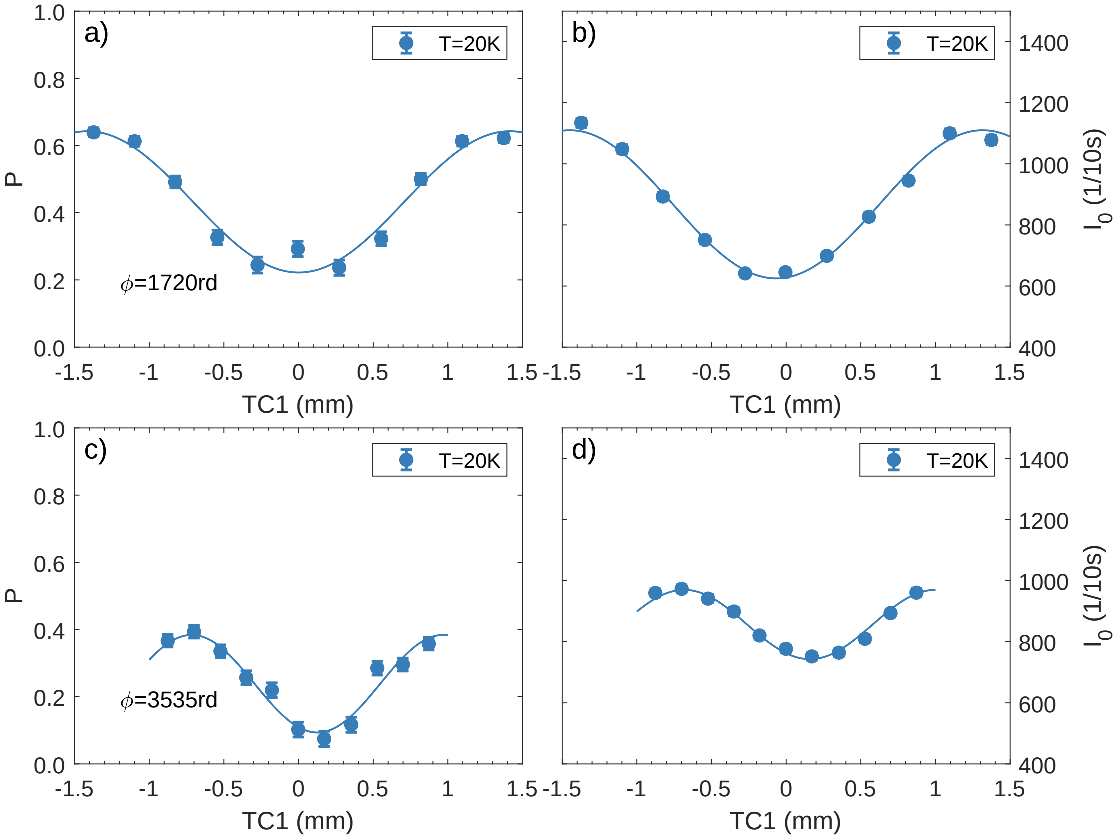

Figure 9.5.: This figure displays the impact of the polarization orientation at the sample position on the measurable quantities, when applying a constant electric field ($E = 4\,\text{kV}\,\text{mm}^{-1}$). The alignment of the beam polarization was manipulated by driving the first RF-coil (TC1), which thus alters the effective length of the first precession device. For each position of TC1, a scan of the last RF-coil position (TC4) yields the resulting final beam polarization P and the averaged intensity I_0, which are both plotted in the upper and lower panels respectively for different total precession phases. Here, a) and b) refer to a fixed total phase of about 1720 rad and c) and d) refer to a fixed total phase of about 3535 rad.

It can be seen that the final beam polarization is oscillating as a function of TC1, which can be explained by the above discussed phenomena that the scattering process from a chiral structure enforces a significant alteration of the final beam polarization as a function of the incoming polarization alignment. However, in a usual neutron polarization experiment a beam with defined polarization (direction and amplitude) reaches the sample, while in a spin-echo or Larmor diffraction experiment it is a distribution of polarization lying in the xy-plane. Simulating the referring scattering process is thus a more complex task. Without the Larmor precession device in the first spectrometer arm, the parallel and antiparallel alignment of $\mathbf{P}_{\text{in}}$ with respect to $\mathbf{Q}$ would refer to the measurable intensity SF-channels $I_{x\bar{x}}$ and $I_{\bar{x}x}$. Hence, by considering a monodomain, the parallel/antiparallel alignment of $\mathbf{P}_{\text{in}}$ with respect to $\mathbf{Q}$ would yield respectively the maximum and minimum intensity that is observable within the course of a TC1 scan. Thus, it can be concluded that the TC1 positions for the maximum and minimum values of I_0 refer to a parallel/antiparallel alignment of $\mathbf{P}_{\text{in}}$ with respect to $\mathbf{Q}$.

As noted above, if the operation of the first precession device on the beam polarization is considered, the interpretation of the maximum and minimum intensity within the course of a TC1 scan is more complex as the distribution $P_0(\phi)$ at the sample needs to be considered. For a finite velocity spread of the neutron beam, the first Larmor precession arm of the spectrometer fans out the initially polarized neutron spins in the xy plane. Hence, if a TC4 scan over a whole neutron precession period determines the averaged intensity I_0, the latter quantity equals the integrated intensity in the xy-plane. Thus, the quantity I_0 in Fig. 9.5 b) and d) refers to the scattered integrated intensity within the xy-plane as a function of TC1, respectively as a function of the initial alignment of the polarization vector at the sample position. Therefore, it still holds that both, the maxima and minima of I_0 in Fig. 9.5 refer to the TC1 position for which the initial polarization vector, respectively the center of the initial spin-distribution arrives at the sample parallel or antiparallel with respect to the scattering vector. The consideration of a fanned out spin distribution at the sample position and its impact on the change of the beam polarization by the scattering process is however important to analyze more in detail to obtain at least an estimation how the final beam polarization is altered just by the chiral scattering process.

A respective distribution of spins in the xy-plane can be described by a Gaussian probability distribution $P_0(\phi) = \exp(-\phi^2/(2\sigma)^2)$ with σ being the width. Figure 9.6 a) displays two different initial spin-distributions at the sample, which are respectively centered around $\phi_i = 0°$ and $\phi_i = 180°$. This refers to an initial polarization vector $\mathbf{P}_{\text{in}}$ that is aligned parallel or antiparallel to the x-direction and which possesses a smeared out spin-distribution in the xy-plane due to the operation of the first precession device on the polarized neutron beam. Here, it must be remembered that the averaged intensity for parallel and antiparallel alignment of $\mathbf{P}_{\text{in}}$ with respect to $\mathbf{Q}$ can be deduced from Fig. 9.5.

From equation 9.15 it can be calculated how much intensity is scattered for an initial spin orientation $P_0(\phi_i)$, respectively for an initial polarization alignment that arrives at the sample with the initial angle ϕ_i. The scattered intensity that takes into account one of the two shown probability distributions from Fig. 9.6 a) is displayed in b) as a function of ϕ_i. Here, it is further assumed that the system is completely poled to a particular type of monodomain. For a perfect spiral monodomain and a completely polarized beam it would be expected that only one of the two channels $I_{x\bar{x}}$ or $I_{\bar{x}x}$ possesses finite intensity.

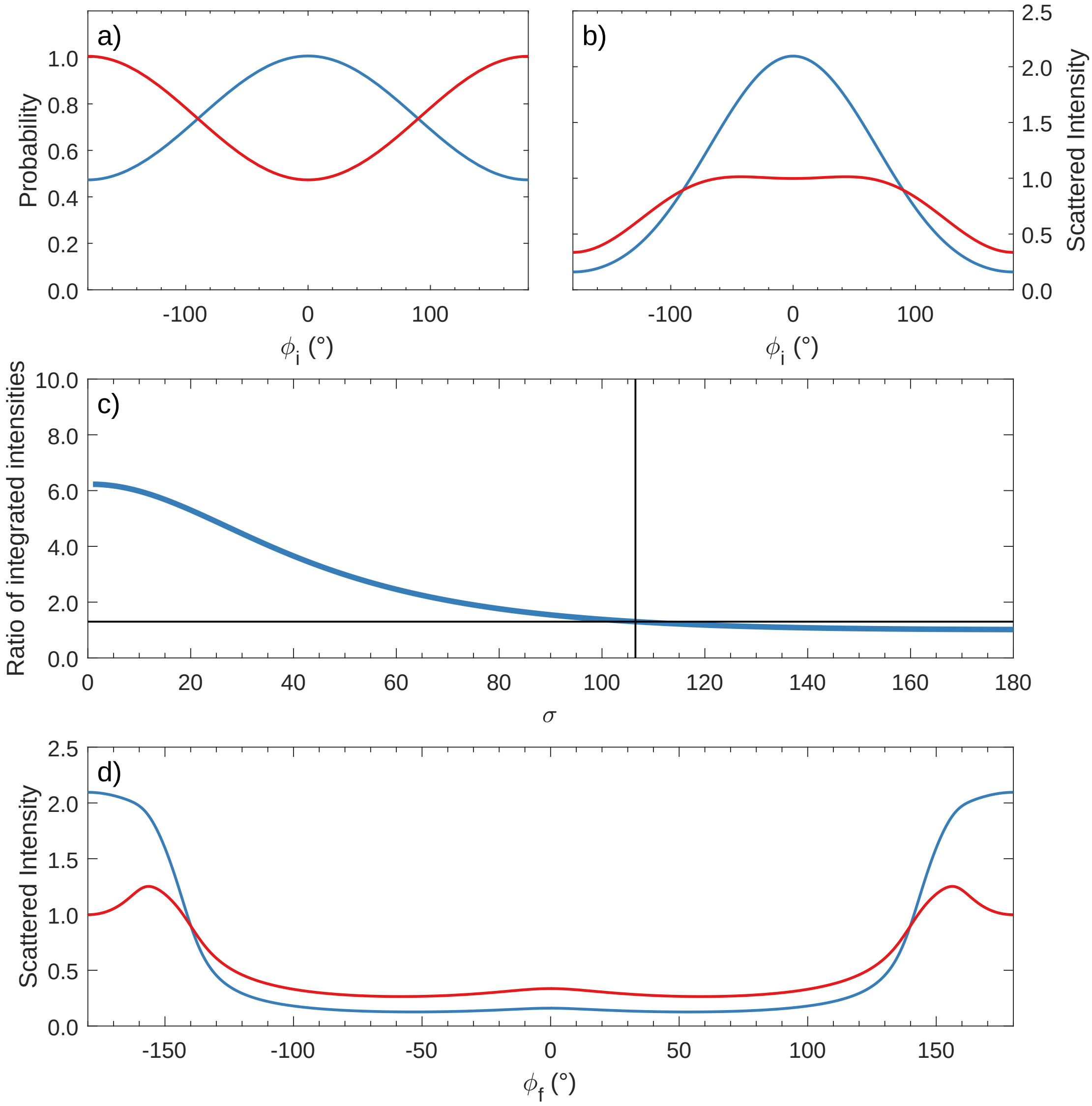

Figure 9.6.: Panel a) displays two Gaussian spin-distribution functions, whose peak center is aligned respectively parallel and antiparallel to the x-direction. Here, the respective width $\sigma = 106.5°$ is equal for both curves and the distribution functions for integer multiples of $\phi = 360°$ is backfolded. Panel b) shows the scattered intensity that can be expected with respect to the particular initial spin orientation ϕ_i, whereby the red and blue curve refer to the respective initial probability distributions from panel a). The ratio of both integrated intensities is plotted against different values for σ in c). Here, the horizontal black line refers to the observed averaged intensity ratio from the TC1 scan at 3535 rad (see Fig. 9.5 d)). Panel d) displays the calculated intensity distribution for both initial spin distributions as a function of the final polarization angle ϕ_f.

However, in the considered case of a fanned out spin-distribution, a respective center alignment of the initial spin-distribution along the non-preferred scattering direction of the respective monodomain would still result in finite scattering contributions, as spins close to the center of the probability distribution can scatter because of their finite y-component. For very broad spin-distributions, some spins are even aligned in opposite direction and thus exhibit the preferred alignment to scatter from the underlying chiral monodomain. This behavior can be well seen in Fig. 9.6 b), where for the centered probability distribution around $\phi_\mathrm{i} = 0°$, most of the neutrons are scattered for an initial orientation close to the probability distribution center. However, for the opposite initial polarization alignment only spins with a finite y-component, respectively with opposite orientation can scatter. As here most of the neutrons arrive with the non-preferred spin alignment at the sample, the scattered intensity is weaker than for the other probability distribution. A key feature of this scattered intensity as a function of ϕ_i is the fact that the integrated intensity from $-180°$ to $180°$ is related to the maximum or minimum averaged intensity that was observed in the course of the TC1 scans. This however only holds if the assumed width of the initial spin distribution function resembles the respective real spin distribution that arrived after the first precession device at the sample position. Figure 9.6 c) displays the ratio of calculated integrated intensities for an opposite spin distribution alignment as a function of the supposed width. As the respective ratio of the measured maximum and minimum averaged intensity equals approximately 1.3 (see Fig. 9.5 d)), it can be concluded that the width of the initial spin distribution at the sample position is roughly of the order of 106.5°. This width was also chosen for the Gaussian distribution function that is shown in Fig. a). It can be further deduced that the initial spin-distribution refers to a flipping ratio of about $\mathrm{FR} = 2.13$ and thus to a polarization magnitude of about $|\mathbf{P}_\mathrm{in}| = 0.36$. Hence, if a highly polarized beam ($|\mathbf{P}| = 0.95$) enters the first precession device, its polarization must decay during the passage of it by approximately 62%.

To calculate the polarization distribution $P_\mathrm{f}(\phi_\mathrm{f})$, respectively the alteration of the beam polarization after the chiral scattering process, it is necessary to determine the intensity distribution in the xy plane after the scattering event. With the knowledge how much intensity is scattered for a particular incoming spin orientation (see Fig. 9.6 b)) this can be done by utilizing equation 9.11. The respective result, namely the scattered intensity as a function of the final spin angle ϕ_f with respect to the x-axis is shown in Fig. d). It can be seen that an initial polarization distribution centered around $\phi_\mathrm{i} = 0°$ is flipped to $\phi_\mathrm{f} = 180°$ by the preferred monodomain. It is obvious that this type of monodomain is then not preferred by an opposite polarization alignment. However, the smeared out spin distribution in the xy-plane entails that a finite amount of neutrons possess a y-component for the neutron spin polarization or even the opposite alignment of it with respect to the distribution center around $\phi_\mathrm{i} = \pm 180$. This explains why the scattered polarization distribution is for this initial polarization alignment also centered around $\phi_\mathrm{f} = \pm 180°$ but with less scattered intensity than for the opposite initial polarization distribution. Further, it can be seen that for both cases, the final distribution width is significantly changed, which entails an alteration of the polarization magnitude by the chiral scattering process.

This calculation was done by considering a monodomain and oppositely oriented initial polarization distributions (see Fig. 9.6 a)). Of course, the same calculation can be done for a fixed initial spin distribution and oppositely poled monodomains. This latter consideration also reflects the experimental course in which monodomains are switched by external electric fields. The respective result is visualized in Fig. 9.7, and resembles the one, which was obtained for a fixed monodomain but oppositely aligned polarization distributions. As in Fig. 9.7 the polarization is now fixed, it is obvious that for an inverted monodomain the scattered polarization distribution is here not centered around $\phi_\mathrm{f} = \pm 180°$ but around $\phi_\mathrm{f} = 0°$. It becomes also clear that for both types of monodomains, the alteration of the scattered beam polarization is different and wherefore the respective correction is not equal for left- and right-handed monodomains, while fixing the orientation of the initial polarization distribution. As shown in c), the final spin distribution for a balanced domain distribution can be deduced from the respective mean value of the scattered intensity as a function of ϕ_f.

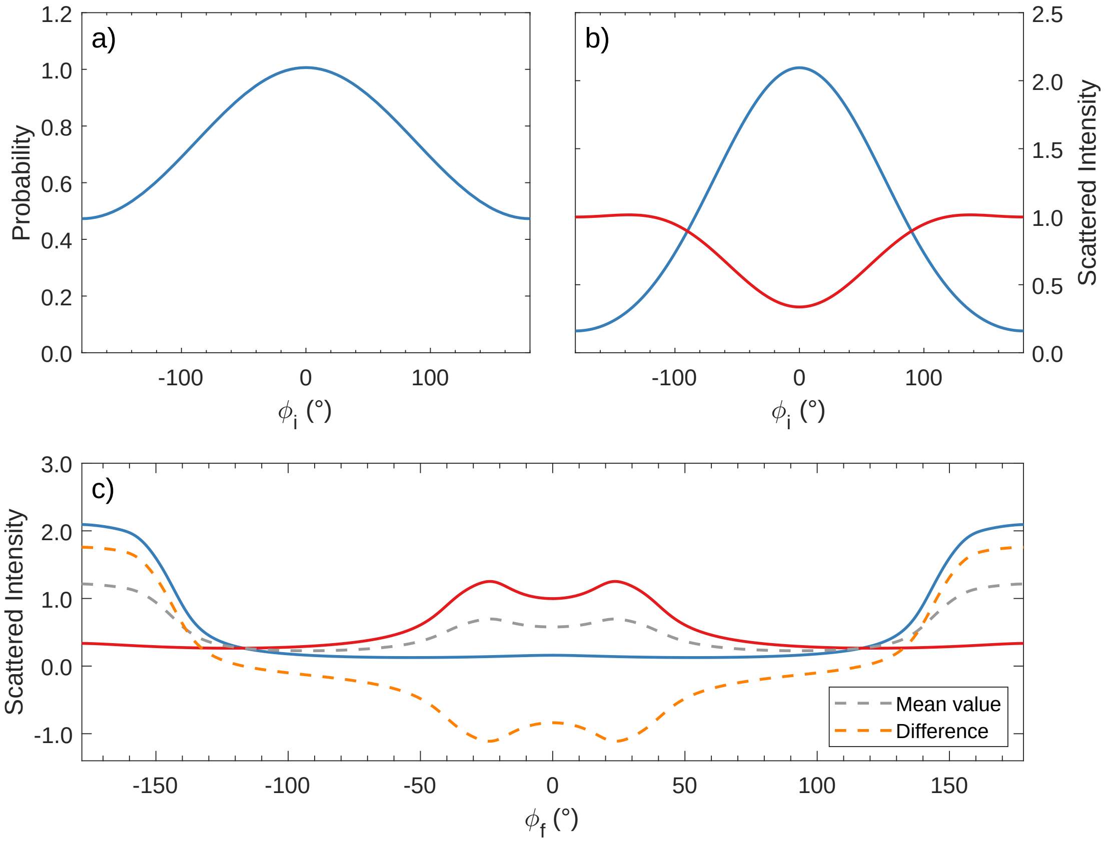

Figure 9.7.: This figure displays equivalent to Fig. 9.6 a), b) and d) the calculation of the scattered intensity distribution as a function of ϕ_f. In contrast to the calculation in Fig. 9.6, the initial spin distribution is fixed and the red and blue line differ here by the handedness of the underlying monodomain. The dashed lines in c) refer to the mean value and the difference of both curves respectively.

From Fig. 9.7 c) and by utilizing equation 2.18 it can be estimated that the scattered polarization for the preferred domain type approximately amounts to $P_{f1} = 0.86$. Hence, the polarization after the scattering process is changed by $\Delta P_{f1} \approx 0.5$ with respect to the initial polarization that arrives at the sample. This is however different and more complex for the opposite domain type. Here, the domain inversion effectively inverts the polarization distribution, which can be referred to as a negative polarization value that can be estimated with the same arguments as above to amount to $P_{f2} = -0.5$. Thus, for oppositely poled monodomains the initial polarization is changed by $\Delta P_{f1} = 0.5$ and $\Delta P_{f2} = -0.86$ respectively. The alteration of the beam polarization is thus enormous and it is obvious that this significantly impacts the quantity of interest, namely the final beam polarization that is directly related to the correlation length of multiferroic domains. It is important to note that the respective contribution from the non-preferred monodomain to the Larmor diffraction signal vanishes more or less completely after the passage trough the second arm. In principle, one senses thus only one type of domain, namely the domain, which is preferred for the respective orientation of the initial polarization distribution. Hence, if the electric field switches the handedness of the monodomain, one would measure either a large correlation length for the preferred domain or a vanishing correlation length if this type of monodomain is switched to the opposite handedness.

The altered amount of polarization ($\Delta P_{f1} = 0.5$ and $\Delta P_{f2} = -0.86$) decays in the second spectrometer arm and eventually yields an adulterated final beam polarization, which needs to be taken into account in the determination of the correlation length. For an appropriate correction of this effect, the decayed amount of the adulterated polarization must be separated from the measured final beam polarization that corresponds to the correlation length of multiferroic domains. The usual Larmor experiment aiming at the determination of correlation lengths bases on the compensation of the polarization broadenings in the two arms, which is partially lost in an experiment on a chiral structure. At first glance it seems reasonable to assume that the relative decay of beam polarization is equal to the respective decay in the first arm. However, this rough approximation has to be considered with appropriate caution. As some initial beam polarization is restored due to the chiral scattering event, the operation of the first spectrometer arm is partially resetted. This would entail that the measured signal includes also contributions from the mosaicity of the sample. Nevertheless, the subsequent discussion assumes that the decay is in percentage equal to the first arm, wherefore it has to be again emphasized that respective results have to be considered with caution. It must be also noted that the consideration, respectively the calculations above did not take into account the limited precision of the RF-coils and other instrumental parts. Thus, it is reasonable for these simplified corrections to not apply the Ge correction ($P^{\mathrm{Ge}}(\phi_{\mathrm{tot}} = 3535\,\mathrm{rad}) = 0.69$), which would compensate the impact of the non-ideal performance of the individual components of the instrument. However, in terms of the correlation length the neglected Ge correction only affects the quantitative result but not the qualitative outcome i.e. the potential observation of relative domain size variations.

For the sake of completeness the scattered intensity distribution was also calculated for the SDW phase with moments parallel to b, i.e. in the scattering plane. Figure 9.8 presents the respective results, whereby the calculation was done for a fixed monodomain and for oppositely aligned initial spin distributions. The result is trivial as the respective scattering process from a SDW just entails a π-flip for the scattered neutron spins.

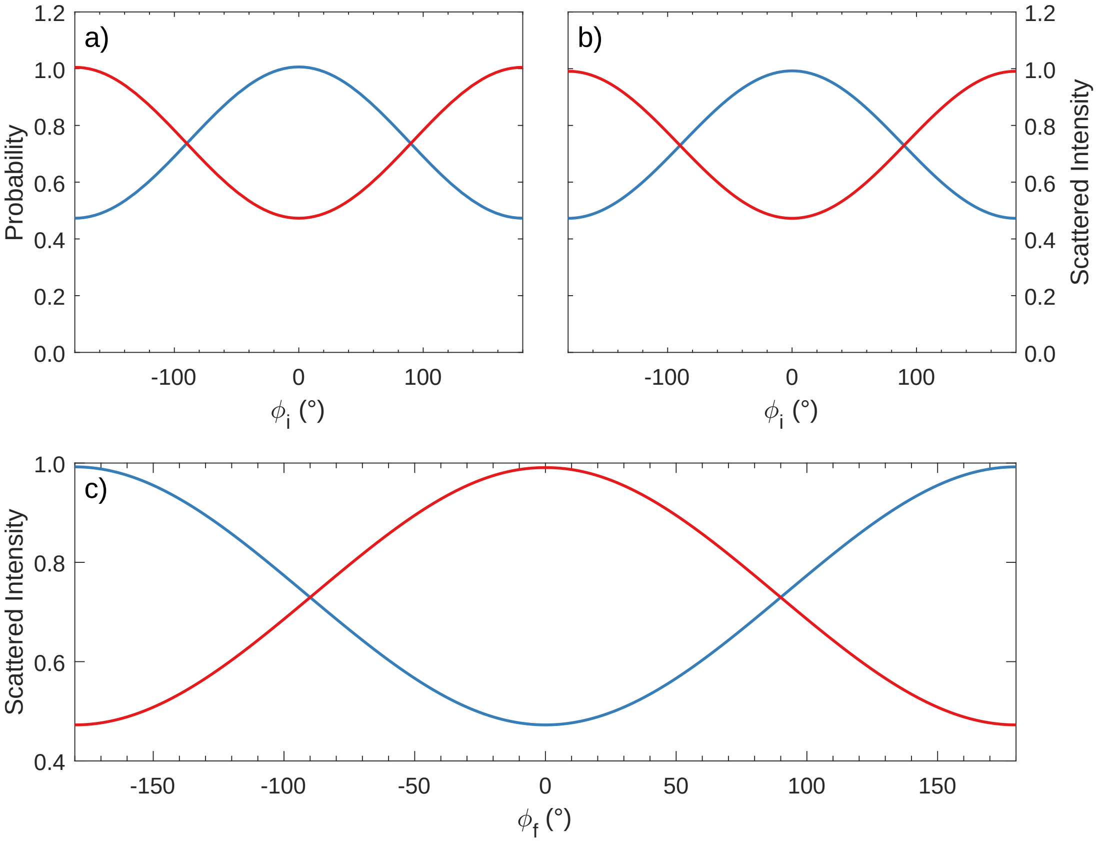

Figure 9.8.: These three panels display how opposite initial spin-distributions are scattered by a SDW with $\mathbf{m} = (0, m, 0)$, whereby the respective calculations were done equivalent to the calculations for Fig. 9.6 and Fig. 9.7.

9.4.3. Total phase scans

As discussed in the last sections, the final beam polarization is for a chiral magnetic structure impacted by different effects. To further understand their impact, it is beneficial to execute complete total phase scans of the scattered final beam polarization $P(\phi_{\text{tot}})$. Figure 9.9 displays four recorded phase scans of the final beam polarization for different temperatures and without an applied electric field. Panel a) shows the observed decay of the final beam polarization at $T = 30\,\text{K}$ and thus inside the intermediate SDW phase. As explained above, all moments are here aligned almost parallel to the y direction and the effective negation of the first precession device by the SF process from the M_y component is compensated by the antiparallel field alignment of the second precession device. The polarization decay is thus free of confounding contributions and provides direct access to the correlation length, when fitting it by equation 9.7.

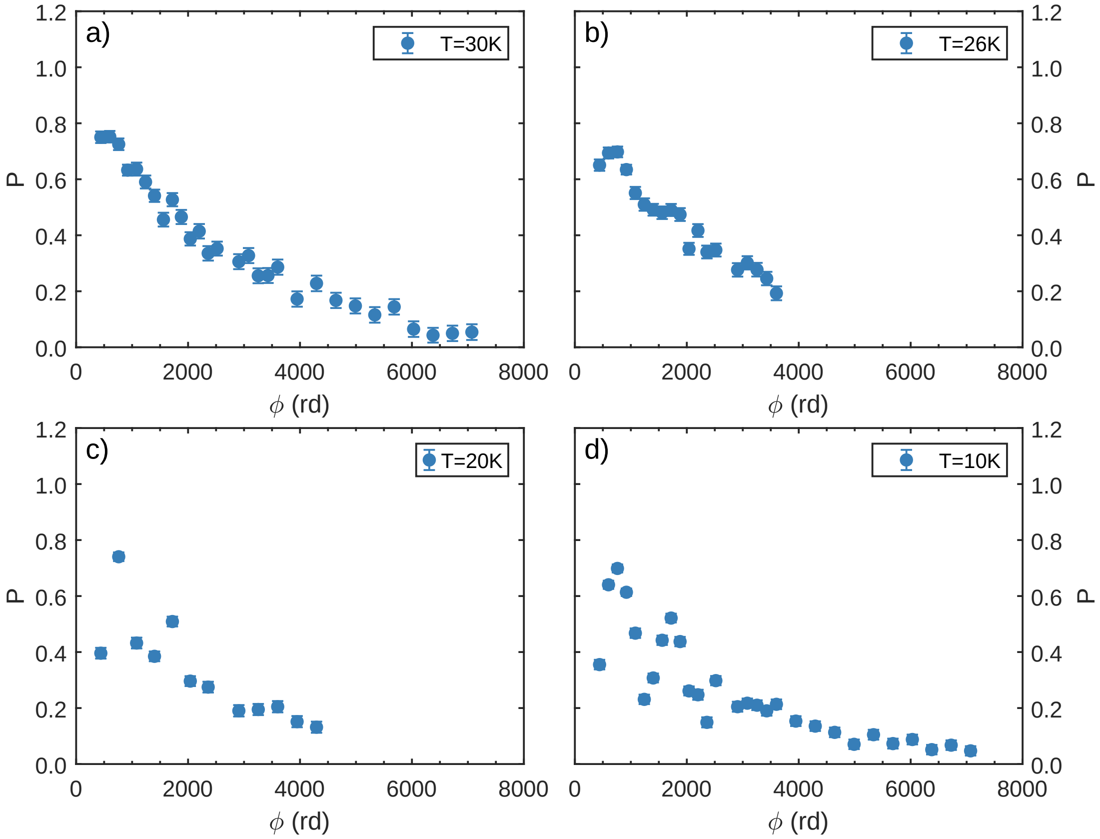

Figure 9.9.: These four panels display the phase scans for different temperatures in the intermediate as well as in the multiferroic phase. The blue data points refer to the observed final beam polarization.

This situation significantly changes, when reducing the temperature below the multiferroic transition temperature at $T_{\mathrm{MF}} = 27.6\,\mathrm{K}$. This can be unambiguously seen in panel b), in which the polarization decay at $T = 26\,\mathrm{K}$ is plotted. It is obvious that the recorded decay of $P(\phi_{\mathrm{tot}})$ is superimposed by a pronounced oscillation of the signal and as it can be seen in both panels c) and d), the oscillation amplitude becomes even more enhanced, when reducing the temperature further. The general reason for these observed oscillations can be explained by the calculations that were made in the previous section. It was shown that the parallel or antiparallel alignment of $P_i(\phi)$ with respect to the scattering vector entails for a chiral structure a different final polarization, respectively a different final polarization distribution after the scattering event. As the initial polarization distribution is here rotating in the xy-plane as a function of ϕ_{tot} it explains the pronounced oscillation below T_{MF}.

It is important to emphasize that the frequency of the visible oscillation in Fig. b)-d) is actually much smaller than pretended by the shown data. This is because the rotation of $P_i(\phi)$ possesses the periodicity of the neutron Larmor precession, which naturally entails a faster oscillation than visible in Fig 9.9. The periodicity that is visible for the oscillations in these panels is deceptive and originates from the experimental procedure that all data points (at least for low values of ϕ_{tot}) were measured with the same step size, which is much larger than the actual period of a single oscillation. This of course pretends an oscillating signal with much larger periodicity.

With an increasing width of the initial polarization distribution in the xy-plane at the sample position, the oscillations become damped, which justifies the description of the polarization decay for respective high total precession phases by equation 9.7. It was already mentioned in section 9.3.1 that due to finite beamtime and in view of the time-consuming and time-resolved measurements on the multiferroic domain size development, the final beam polarization will be measured only for a single fixed total precession phase. In this context it was also discussed that an intermediate value of the total precession phase is the best choice, because here the correlation length can be sensed over a broad range (see also Fig. 9.2). Fortunately, it can be seen in panels b)-d) that the oscillations are already exhaustively damped for these intermediate values, wherefore the total precession phase of about $\phi_{\text{tot}} = 3535\text{rd}$ was seen to be a good choice for measurements of the final beam polarization and the respective fit of its decay.

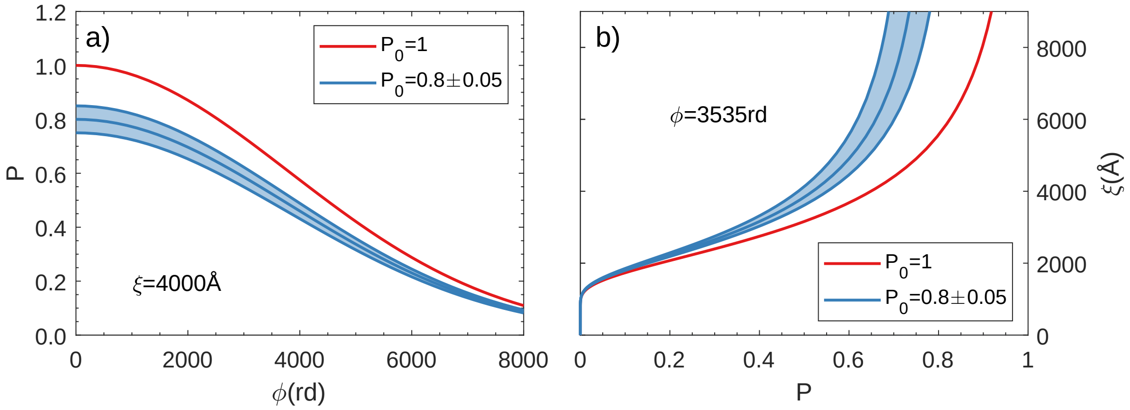

Figure 9.10.: Both panels a) and b) visualize the impact of P_0 on the polarization decay, when assuming a particular correlation length. In a) the decay of the final beam polarization is plotted as a function of the total precession phase for $\xi = 4000\,\text{Å}$ and for different values of P_0. Panel b) displays the relation between correlation length and the corresponding final beam polarization for $\phi_{\text{tot}} = 3535\text{rd}$ and also for different values of P_0. In both panels a) and b), the blue shaded area refers to a variation of P_0 by $\Delta P_0 = 0.05$. It must be further noted that here the lattice parameters of TbMnO_3 as well as the scattering vector $\mathbf{Q} = (2\,0.28\,1)$ were assumed for the visualization of the dependencies between the different quantities.

The oscillating decay of the final beam polarization can in principle be also simulated by a ray-tracing model, which was also utilized in the course of a spin-echo experiment on the critical dynamics in MnF_2 and Rb_2MnF_4 [200]. However, the adaption of this simulation necessitates much more data points and must further take into account the polarizing contribution from a finite multiferroic domain distribution. This tremendously complicates the data analysis, whereas the description of the polarization decay by equation 9.7 is valid and adequate.

Without the Ge correction it is obvious, that the value of P_0 does not equal $P_0 = 1$ because the non-ideal performances of the different components of the instrument are not corrected. By considering the phase scans in 9.9 it can be assumed that P_0 amounts approximately to $P_0 = 0.8$, which is reasonable because it can be shown that even a finite variation of P_0 has only negligible impact on the fit result, when measuring at high precession phases. This is exemplary sketched in Fig. 9.10 for a deviation of about $\Delta P_0 = \pm 0.05$. First, it is visible in panel a) that the reduction of $P_0 = 1$ to $P_0 = 0.8$ leads to a significant discrepancy in view of the respective polarization decay. It can be seen that in particular for intermediate total precession phases, the final beam polarization does not differ much if $P_0 = 0.8$ is varied. The respective impact of ΔP_0 on the determination of correlation lengths is visualized in panel b) for a fixed total precession phase of about $\phi_{\text{tot}} = 3535$rd. For very small correlation lengths ξ, there is even no difference between the curve for $P_0 = 1$ and $P_0 = 0.8$. In contrast, above $\xi \approx 2000\,\text{Å}$, the correlation length starts to differ significantly between both initial polarization values, but it can be also seen that up to $\xi \approx 5000\,\text{Å}$ a variation of $P_0 = 0.8$ by $\Delta P_0 = \pm 0.05$ is accompanied only by a small variation of the correlation length. Thus, the assumption, respectively the simplification that the reduced value of P_0 in the multiferroic phase remains constant is reasonable for values up to $\xi \approx 5000\,\text{Å}$ and does not lead to a significant deviation of determined correlation lengths. It must be further noted that in the extreme case of a strongly deviating P_0, the respective value only falsifies the quantitative result i.e. the determined absolute domain size. However, the qualitative outcome in form of potential relative domain size variations is still valid.

9.4.4. Temperature dependent correlation length

The setup for the multiferroic domain size investigation was eventually adjusted such that a single final polarization value was only measured for the intermediate total precession phase $\phi_{\text{tot}} = 3535$ and fitted by equation 9.7. The TC1 position was set to TC1=-0.702 mm to provide approximately a parallel alignment of $P_{\text{i}}(\phi_{\text{i}})$ with respect to $\mathbf{Q}$ at the sample position (see Fig. 9.5).

The respective poling sequences as a function of temperature were done for different electric-field amplitudes as well as for static and frequently switched fields. For all runs, the sample was initially heated up to $T = 80\,\text{K}$ and subsequently short circuited, while cooling to the start temperature of the respective measurements. All sequences were executed for the cooling and heating direction and the results are displayed in Fig. 9.11.

The averaged intensity is plotted in panel a) of Fig. 9.11 and its temperature dependence reveals both magnetic transitions. First, at $T = 42\,\text{K}$ the development of finite intensity coincides with the onset of magnetic ordering in the SDW phase and a kink at $T = 27.6\,\text{K}$ signals the transition to the multiferroic phase. It was already shown in section 9.4.2 that the beam polarization for $\phi_{\text{tot}} = 3535\,\text{rad}$ has already significantly decayed after the first precession device. This can also be deduced from the averaged intensity in Fig. 9.11 a) as the observed averaged intensity I_0 for oppositely poled fields is only slightly differing. For a poled monodomain, a perfect beam polarization and its respective alignment parallel to x-direction at the sample position, it would entail zero intensity for one of the two applied static field polarities. In contrast, all measured averaged intensities are only slightly differing, which further proves in additon to the explanations in 9.4.2 that the beam is significantly depolarized at the sample position.

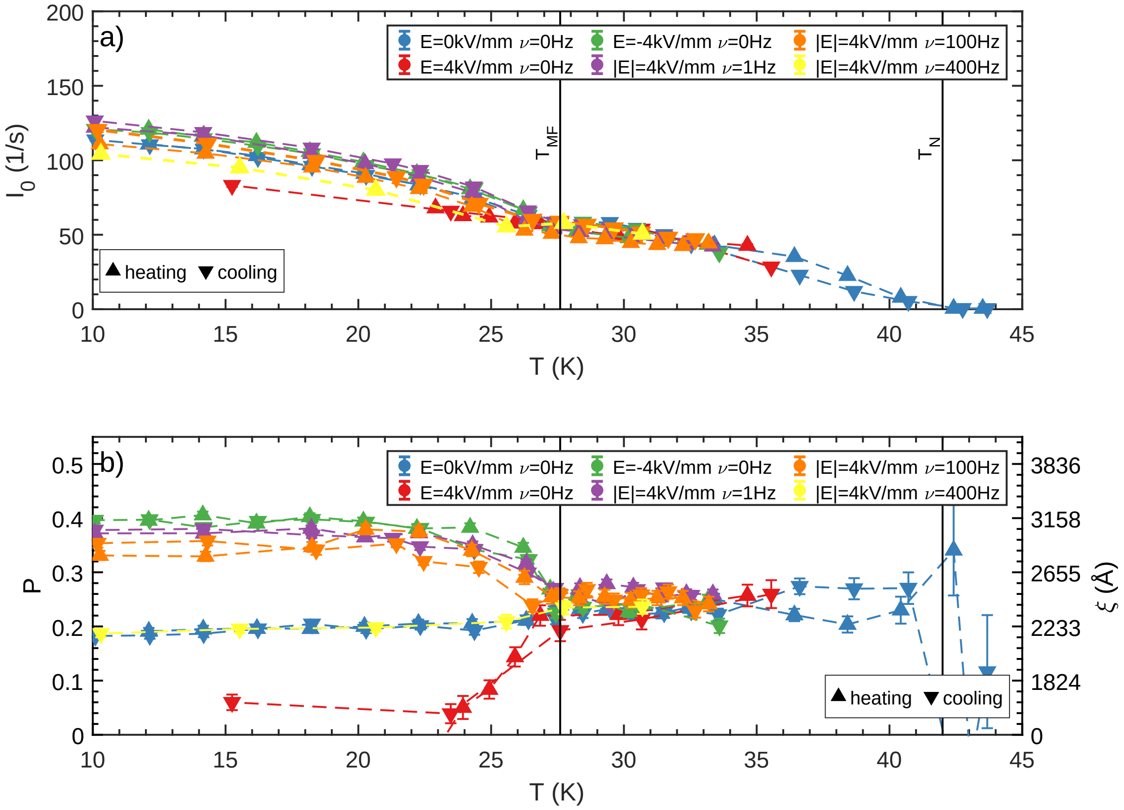

Figure 9.11.: The figure displays the obtained results from temperature dependent TC4 coil scans for different applied static and periodically switched electric-fields. For all sequences the sample was initially heated to $T \approx 80\,\mathrm{K}$ and subsequently short-circuited, while cooling the system towards the start temperature of the measurement sequence. The measurements were done for cooling and heating direction. Panel a) shows the recorded averaged intensity I_0 and panel b) displays the measured final beam polarization P and the calculated correlation length ξ. The latter quantity is plotted on the right y-axis, which does not scale linearly as the polarization has an exponential dependence on the correlation length. The measured final beam polarization however scales linearly on the left y-axis.

The measured final beam polarization and the respective calculated correlation length are plotted as a function of temperature in panel b) of Fig. 9.11. Above T_{MF} and within the intermediate SDW phase, the determined correlation length was determined to amount 2500 Å for all applied static and periodically switched fields. Here, the correlation length describes the domains that are differing by a phase shift of the antiferromagnetic structure and it must be emphasized that the measured quantities in the SDW phase are not superimposed by disruptive effects. This however changes for the multiferroic phase for which a thorough discussion in section 9.4.2 revealed a significant rotation and in particular a generation of beam polarization by the chiral scattering processes. The discussion of respective sequences, for which the field was periodically switched is difficult as the imbalance of the domain distribution cannot be estimated. The lack of this knowledge however hinders a precise correction of the correlation length as even a slight variation of an imbalanced domain distribution can have significant impact on the generated beam polarization (see section 9.4.2). Therefore, the respective correction is impossible to apply if the exact population of domains is not known. Unfortunately this also holds for the zero-field curve, when the temperature is lowered below the multiferroic phase transition. This is because it cannot be excluded that even in zero-field the domain distribution is slightly imbalanced.

For both sequences, for which oppositely poled field were applied, it is known that the respective field amplitude is sufficient to pole the system completely. If the assumption holds that the system is switchable, respectively polarizable with respective field amplitudes, both sequences for E =-4 kV mm^{-1} and $E = 4\,\mathrm{kV\,mm^{-1}}$ can be roughly corrected by the considerations that werde made in section 9.4.2. Following the respective explanations, the recorded final beam polarization for E =-4 kV mm^{-1} need to be subtracted by 0.19. This shifts the saturated value at low temperature to approximately $P \approx 0.21$, which then almost equals the measured final beam polarization of the zero field sequence. As discussed in 9.4.2, the correction of the measured final beam polarization for $E = 4\,\mathrm{kV\,mm^{-1}}$ is more complex. As the domain inversion effectively inverts the polarization distribution, the measured value of about $P \approx 0.06$ at $T \approx 15\,\mathrm{K}$ needs to be considered as a negative polarization. The respective correction by +0.32 would then shift the measured final beam polarization to 0.26, which also very close to the results of the sequences for E =-4 kV mm^{-1} and $E = 0\,\mathrm{kV\,mm^{-1}}$. Hence, from the respective data and with the highly simplified correction that bases on the assumption of an equal polarization decay in both spectrometer arms, a variation of the correlation length cannot be observed. The quantity of interest, namely the domain size is here heavily superimposed by the polarization alteration that is varied by the external electric field, which at least proves that the domain population was altered by the external stimulus. However, as noted above, these results have to be considered with appropriate caution as the respective corrections are based on oversimplified assumptions (see 9.4.2).

Another quantity that can be obtained from the temperature dependent TC4 scans is the position x_0 and the respective shift of the cosine function that describes the intensity at the detector depending on the TC4 position. Figure 9.12 displays the determined values of x_0 as function of temperature and for oppositely poled fields as well as for the zero field sequence. Following the explanations in 9.4.2, both types of monodomains entail a different center position for the final polarization distribution in the xy-plane. As the initial center position was aligned parallel to **Q**, respectively x-direction by TC1-TC4 scans at $T = 20\,\mathrm{K}$ (see 9.5), it is expected that depending on the type of monodomain, the final polarization distribution is centered either around 0° or around ±180°. Depending on the scattering process this is obviously related to a phase shift of the cosine modulated intensity as a function of TC4, which is well observable in Fig 9.12. In the multiferroic phase, the measured values of x_0 are clearly differing for E =-4 kV mm^{-1} and $E = 4\,\mathrm{kV\,mm^{-1}}$. However, for a balanced domain distribution the dominant y-component determines whether the center is aligned around 0° or around ±180°. Hence, for the zero-field sequence, the measured values of x_0 must equal either the sequence with E =-4 kV mm^{-1} or the sequence with $E = 4\,\mathrm{kV\,mm^{-1}}$. Here, it can be seen that the zero-field sequence resembles the temperature dependence of the sequence with E =-4 kV mm^{-1}.

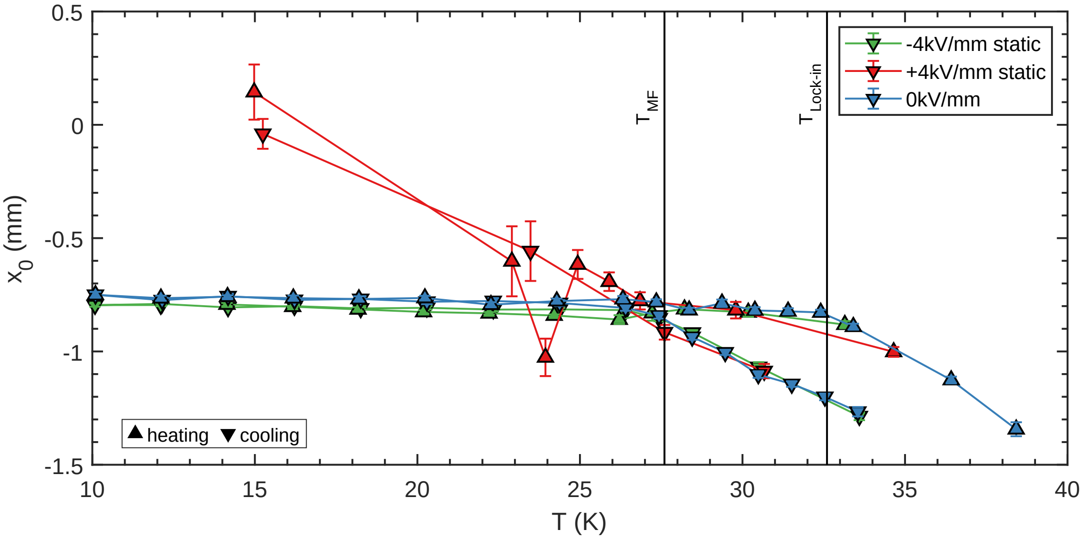

Figure 9.12.: This figure displays the x_0 position of the cosine modulated intensity that was obtained by TC4 scans and for different applied fields.

Astonishingly, the temperature dependence of x_0 in the SDW phase differs for the cooling and heating sequences. This can be related to a temperature-dependent variation of the incommensurability in TbMnO$_3$. The alignment of the initial polarization distribution parallel to **Q** was done only at $T = 20\,\mathrm{K}$, whereby the respective TC1 position was then fixed for all subsequent measurements. It is known for heating sequences from very low temperature to above the multiferroic transition that the incommensurability $\delta_k = 0.28$ of the magnetic structure is not changing until the lock-in transition of the incommensurate propagation vector $k_{\text{inc}} = (0\ 0.28\ 0)$ at $T_{\text{lock-in}} = 31.6\,\mathrm{K}$ [203]. Above this temperature, the incommensurability is varying with temperature, which obviously also entails that the scattering vector is changing. Hence, the alignment of the polarization distribution at the sample position is also altered with respect to the direction of **Q**. This enforces a phase shift of TC4, which is visible by the temperature dependent variation of x_0 above the reported lock-in transition, which is here observed at approximately $T_{\text{lock-in}} = 32.6\,\mathrm{K}$. Surprisingly, the cooling sequence reveals a hysteresis, as the lock-in transition is shifted to a lower temperature, respectively to the multiferroic phase transition. This potentially explains why the lock-in, respectively the stabilization of δ_k is reported in literature either at $T = 31.6\,\mathrm{K}$ or at T_{MF} [203–205].

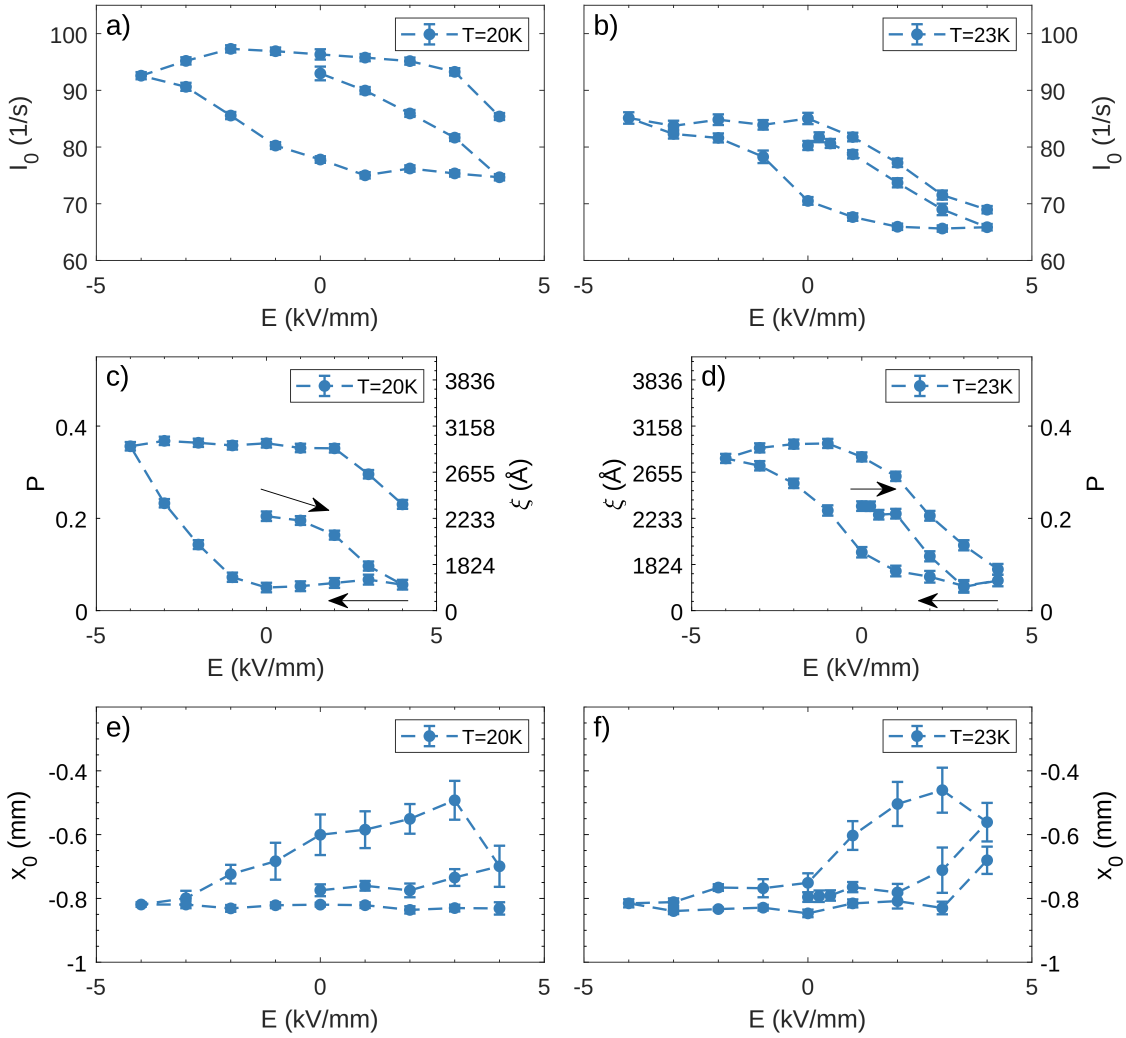

Figure 9.13.: These panels display the temperature dependent hysteresis loops of the averaged intensity, the final beam polarization, the correlation length and x_0. A single loop was measured within 4 h and the sweep direction was clockwise as indicated by the arrows and the dashed lines. Before the respective hysteresis loops were recorded, the system was heated above approximately 80 K and short circuited until the sample was cooled to the demanded temperature for the measurement sequence.

9.4.5. Hysteresis loops of the correlation length

For each recorded hysteresis loop, the sample was heated and short-circuited above the transition temperature to magnetic three-dimensional ordering. Subsequently the sample was cooled to the temperature of interest and the field was then driven between its polarities. One cycle lasted approximately 4 h and the absolute value of the maximum field amounted to $|E| = 4\,\mathrm{kV\,mm^{-1}}$ for both field polarities. The recorded hysteresis loops, respectively the recorded averaged intensity, the measured final beam polarization, the calculated correlation length and the determined values of x_0 are displayed in Fig. 9.13, in which the sweep direction is marked by the arrows.

Both observables, the averaged intensity and the final beam polarization approximately resemble the results that were gained from poling sequences for different applied fields (see Fig. 9.11). It is clearly visible that the hysteresis loop at 20 K exhibits a pronounced asymmetry, as the cycle cannot be closed at 20 K and accordingly the multiferroic domain population cannot be inverted by the applied field. This is slightly different for the hysteresis loop at 23 K, for which the higher temperature obviously entails weaker domain pinning. The loop is closed but nevertheless, the asymmetry of the coercive fields is still visible. It can be also observed that the maximum and the minimum polarization values in both panels c) and d) are slightly smaller, respectively larger than the maximum and minimum values that are presented in Fig. 9.11 b) for the static poling sequences. This is potentially reasoned by the fact that the electric-field sweep between both field polarities was also still too fast for the domains to fully relax towards a monodomain. This is further indicated by the pronounced humps that are developing for the hysteresis at $T = 23\,\mathrm{K}$, when the field is decreased after it has reached its maximum value. The field dependence of x_0 also fits to the observed temperature dependence of x_0 for different fields (see Fig. 9.12).

Even though the reported results and the performed corrections did not show a variation of the correlation length (see discussion in 9.4.4), it was seen beneficial to conduct time-resolved measurements, which are reported in the next section. In this context, it must be noted that the time-dependent variation of the final beam polarization is indeed mainly caused by the explained nature of chiral scattering (see 9.4.2), which depends on the domain distribution. As the variation of the final beam polarization as a function of field is solely dominated by the alteration of the spin distribution by the chiral scattering process, the respective time-resolved switching experiments give thus at least an information about a variation of the underlying domain population.

9.4.6. Time-resolved measurements of the correlation length

The conduction of a time-resolved Larmor diffraction experiment was done within the course of a second beamtime at TRISP (proposal 16609). Similar to the first beamtime (proposal 14858), the final beam polarization was measured and fitted for the single total precession phase $\phi_{\mathrm{tot}} = 3535\mathrm{rd}$, whereby the TC1 position was shifted to -0.620 mm to guarantee a parallel alignment of $P_{\mathrm{i}}(\phi_{\mathrm{i}})$ with respect to the scattering vector $\mathbf{Q}$ at the sample position. The measurements were done on the same sample, for which only the electric contacts were renewed

It was already mentioned that time-resolved coil scans and in particular the respective binning of detected neutrons into time-bins with respect to the time-dependence of the electric field necessitate long counting times for an appropriate statistic. It must be further remembered that the time-resolved measurements are based on the idea to improve the statistic of each bin by periodically repeating the switching process many times. However, within the course of the Larmor diffraction experiment, first test sequences revealed that a tremendous amount of repeated switching cycles gradually freezes the domain distribution towards the preferred handedness, which was observed to be present in this sample (see discussion above). In the extreme case of very long sequences i.e. counting times of the order of 24 h, the domain distribution was finally even not alterable anymore. Thus, to avoid the scenario of gradually pushing the domain distribution to a well pinned and not modifiable state, the time-resolved measurements were splitted into smaller sequences of about $2\,\mathrm{h} - 4\,\mathrm{h}$ counting time and after each run the sample was heated above 80 K and short-circuited, while cooling the system back to the temperature of interest. Eventually, the measured intensity for time-bins of each sequence were summed up to obtain an appropriate statistic. Utilizing this procedure provides both, high statistic as well as the guarantee that the multiferroic domain distribution can be altered for both field directions. It must be noted that this course of action was not needed for the reported time-resolved measurements of the chiral ratio (see Ref. [3, 49] and chapters 5, 6, 7 and 8), as here only two intensity channels (i.e. $I_{x\bar{x}}$ and $I_{\bar{x}x}$) were necessary to record for the respective analysis. This of course entails a much lower counting time for the respective measurements, when comparing it to the coil scans, which are composed of at least a dozen of different TC4 positions. Eventually, it was seen promising to execute the time-resolved Larmor diffraction experiment closer to the multiferroic transition temperature i.e. at 24 K, as here the pinning is effectively weaker than for very low temperature. The applied field was switched every second to the opposite polarity.

The time-resolved TC4 coils scans are visualized in Fig. 9.14 and it can be seen in a) that the amplitude of the cosine modulated intensity varies as a function of time. More precisely, it can be observed that the amplitude drops, respectively increases, when the applied field polarity is suddenly switched after each second. Thus, the final beam polarization, which is plotted in 9.14 b), displays a pronounced time-dependence with respect to the field inversion. The obtained final beam polarization was fitted by equation 9.7, while assuming $P_0 = 0.8$ and the resulting correlation length refers to the right axis in Fig. 9.14 b). The grey dashed square function does not belong to a particular axis but only visualizes the time dependence of the applied field. As already explained in section 9.4.4, the alteration of the beam polarization is here only caused by the varying domain population and not by a variation of the correlation length. However, from this outcome it is also clear that the domain population of respective domain types increases not to the full extent, when comparing the measured maximum and minimum value of the final beam polarization to the respective results from static poling sequences (see Fig. 9.4.4).

The red solid line in Fig. 9.14 b) corresponds to a fit of the time-dependent beam polarization, which was done equivalent to the fits of the time-dependent chiral ratio (see Ref. [3, 49] and chapters 5, 6, 7 and 8). The fit yields non-symmetric relaxation times $\tau_1 = 0.170(26)\,\mathrm{s}$ and $\tau_2 = 0.046(6)\,\mathrm{s}$ for both switching directions respectively. The relaxation time τ_2 is thus only slightly slower but still in the range of the reported inversion time for $|E| = 4\,\mathrm{kV\,mm^{-1}}$ at $T = 24\,\mathrm{K}$ [49], whereas the relaxation time τ_1 is already one order of magnitude slower than reported. However, this is still reasonable because of the observed preferred handedness and the fact that the relaxation time naturally depends on the activation constant, which is sensitive to the pinning strength and which is thus slightly sample dependent. Further, it has to be remembered that the exchange gas in the sample surrounding had to be reduced to a minimum to avoid gas discharges. Hence, all reported values of the temperatures are thus naturally assigned with a finite error and as known from Ref. [49], even small temperature variations have significant impact on the relaxation time. Hence, the finding that the obtained relaxation times are slightly larger with respect to them in Ref. [47] is reasonable.

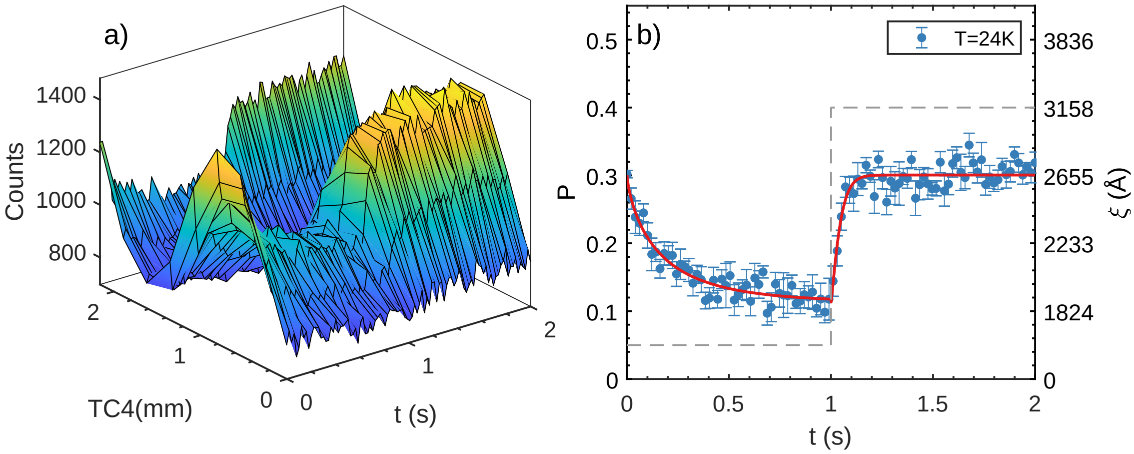

Figure 9.14.: This figure shows the results of a time-resolved Larmor diffraction sequence. In a), the TC4-coil scan is plotted as a function of time and the final beam polarization that can be determined from each coil-scan is plotted in b), whereby the right y-axis refers to the respective correlation length. Here, the grey dashed line visualizes the time-dependence of the applied field and the moment, when its polarity is switched. It must be noted that the inversion time of the electric field is in the range of μs, wherefore here the time-dependence of the field can be assumed to be described by a perfect rectangular function. The red-line in b) corresponds to a continuous approximation of the heavy-side function, which was fitted to the recorded time-dependent correlation length.

9.5. Conclusion

The last sections thoroughly discussed the setup, the adjustments that are needed and the implications that interfere with the conduction of a Larmor diffraction experiment on multiferroic domain dynamics. In particular, it was shown that the procedure needs to be adapted to the underlying magnetic structure, which provokes here the rotation as well as the alteration of the scattered beam polarization. It was shown in detail how the chiral scattering is capable to impact the quantity of interest, namely the correlation length of multiferroic domains. Eventually, it turned out that the calculation of respective correlation lengths can only be done with oversimplified assumptions concerning the decay of the altered beam polarization in the second spectrometer arm. Hence, the respective results have to be considered with appropriate caution. For a more reliable correction of the polarization modulation that is caused by chiral scattering, it seems beneficial to simulate also the polarization decay as a function of the total neutron precession phase, which however necessitate more data than shown in Fig. 9.9. For these measurements it would be also desirable to align the initial polarization distribution for each value of the total precession phases. Obviously, this is hindered by the finite amount of beamtime. Another approach would be the operation of the Larmor diffraction instrument only with the second Larmor precession device. Then the beam would arrive still completely polarized at the sample and is thus not impacted by generation of additional beam polarization. However, the missing operation of the first arm entails that the mosaicity of the sample significantly contributes to the signal.

With all adjustments of the instrumental setup and the simplified assumptions concerning the polarization decay in the second spectrometer arm, it was unfortunately not possible to observe an alteration of the domain sizes by varying external electric fields. The observed variation of the final beam polarization can only be related to the varying domain population, which impacts the alteration of the scattered beam polarization differently depending on the predominant domain type (left- or right-handed domains). The discussed shift of TC4 as a function of temperature and field revealed a hysteresis for the temperature dependence of the incommensurability, for which the lock-in was observed either at $T_{\mathrm{MF}} = 32.6$ for the heating sequence or at $T_{\mathrm{MF}} = 27.6$ for the cooling sequence. With the given setup, the conducted time-resolved measurements sensed the time-varying domain population, for which the observed relaxation times approximately agree to the reported values in literature [49].

Eventually, it is important to highlight the perspective of utilizing the Larmor diffraction technique for investigating domain dynamics in systems, which exhibit a different driving mechanism for the multiferroic behavior. So far, the neutron scattering studies on the domain dynamics were restricted to materials, in which the multiferroic phase was induced by chiral ordering, respectively by the inverse Dzyaloshinskii-Moriya interaction. Here, the respective investigations benefited from the fact that the handedness of the spiral structure can be sensed by polarization analysis. The distinction between different magnetic domains in systems with a different microscopic driving mechanism is however not so obvious. For example, the domains that are related to an exchange striction based multiferroic system cannot be sensed separately by neutron polarization analysis. This chapter thoroughly presented the potential application of the Larmor diffraction technique to sense the variation of multiferroic domain sizes, respectively correlation lengths and can be applied in principal to all kind of magnetic arrangements. Obviously, the absence of chiral magnetic structures would significantly facilitate the feasibility of the experiment and in particular the data analysis of respective measurements. Thus, this experimental approach is very promising for investigations of the domain size development, respectively the multiferroic relaxation behavior in multiferroics that exhibits a different driving mechanisms, which thus highly motivates the continuation of this project. Further, also the investigation of toroidal domains seems promising, which will be referred to again in the context of ferrotoroidal domain dynamics (see appendix A).

10. Ising-like spin-1/2 chain material $BaCo_2V_2O_8$

10.1. Motivation

An isolated Ising spin-1/2 antiferromagnetic chain, which is expelled to a transverse magnetic field is of considerable interest, as the underlying theoretical model can be exactly solved and yields an accurate description of a quantum phase transition [206–210]. The quantum critical cone extends from the quantum critical point up to finite temperatures and defines the region in the phase diagram, where thermal and quantum fluctuations are equally weighted. This provokes the occurrence of peculiar new phases [206–208], wherefore the exactly solvable transverse-field Ising (TFI) model is highly attractive to further understand and investigate the exotic phenomena that can arise from the competition of thermal and quantum fluctuations [206–208].

The advantage of its exact theoretical solution is however interfered by the lack of its experimental accessibility, as appropriate model systems can be hardly realized. This is because finite interchain interactions commonly hinder the presence of isolated one-dimensional ordering along a magnetic spin-chain but rather promotes the development of three-dimensional long-range ordering at low temperature.

In the last decade, the system $BaCo_2V_2O_8$ was established as an ideal playground for the investigation of quantum phase transitions, as this system hosts effective spin-1/2 XXZ chains with strong Ising anisotropy [211–217]. However, also for this system finite interchain interactions enforce the development of three-dimensional ordering at low temperature [214, 218] and it was further seen that the system exhibits a strong in-plane anisotropy [211]. For a transverse field applied along [1 0 0] direction, the Néel ordering is completely suppressed at $\mu_0 H = 10\,\mathrm{T}$ [211, 219], which was proposed to be described by a topological quantum phase transition [216]. In contrast, for a transverse field that is directed along [1 1 0], the Néel ordering persists above $\mu_0 H = 10\,\mathrm{T}$ until the system becomes quantum disordered at the quantum critical point at $\mu_0 H = 40\,\mathrm{T}$ [219]. For the latter mentioned field direction, a recent work from Z. Wang *et al.* [212] reported sound velocity and magnetization measurements, which both revealed an additional anomaly at $\mu_0 H = 21.4\,\mathrm{T}$ (at $T = 1.3\,\mathrm{K}$). This anomaly in the magnetization data was also reported in a subsequent publication of A. Okutani *et al.* [220], but they observed it at a higher field of about $\mu_0 H \approx 30\,\mathrm{T}$ (at $T = 1.3\,\mathrm{K}$).

Z. Wang et al. [212] proposed this anomaly to mark a suppression of three-dimensional ordering above the critical field value $\mu_0 H^{3\text{D}}$. This potential realization of a quasi isolated Ising spin-1/2 chain system would enable the experimental investigation of an ideal TFI configuration. However, the results from sound velocity and magnetization measurements are not adequate to fully characterize the magnetic structure in terms of moment orientation, commensurate or incommensurate arrangements and correlation lengths. Beyond that it will be discussed in the following course that also a potential high-field Tomonaga-Luttinger liquid (TLL) phase can be induced by staggered fields. Because neutron diffraction offers a unique tool to sense the details of magnetic ordering, it thus motivated the respective investigation of the reported transition in $\text{BaCo}_2\text{V}_2\text{O}_8$.

The following section reports neutron diffraction experiments on $\text{BaCo}_2\text{V}_2\text{O}_8$, whereby, the high-field neutron scattering studies were conducted at the state-of-the-art high-field magnet (HFM), which is operated at the extreme environment diffractometer (EXED) at the Helmholtz-Zentrum Berlin (HZB) and which provides continuous fields up to 26 T [221–224]. A second neutron scattering experiment for a magnetic peak width analysis was performed at the diffractometer D23, which was operated at lower fields ($\mu_0 H \leq 15\,\text{T}$) but which instead offered a high Q-space resolution for the peak profile investigation. Before the respective results are discussed, the following sections first provide a brief overview of the structural information of $\text{BaCo}_2\text{V}_2\text{O}_8$ and the experimental method, before subsequently the results of conducted experiments are presented.

10.2. Crystal and magnetic structure of $\text{BaCo}_2\text{V}_2\text{O}_8$

The effective spin-1/2 XXZ chain system $\text{BaCo}_2\text{V}_2\text{O}_8$ crystallizes in the tetragonal space-group $I4_1/acd$ with lattice constants $a = 12.444(1)$ Å and $c = 8.415(3)$ Å [214, 225]. In view of the magnetic arrangement in $\text{BaCo}_2\text{V}_2\text{O}_8$, the main building block of the crystallographic structure is provided by the only magnetic element Co^{2+} ($S = 3/2$), which is octahedrally coordinated by oxygen ions. These CoO_6 octahedra form edge sharing screw chains that are propagating along the crystallographic c-direction (see Fig. 10.1 a)) and which are separated by nonmagnetic VO_3 tetrahedra and BaO_{12} cuboctahedra. Due to the reported high Ising-anisotropy of the Co^{2+} moments [213], the magnetic CoO_6 chain can thus be described by an effective spin $S = 1/2$ XXZ-chain system.

As it will be discussed below, the magnetism of $\text{BaCo}_2\text{V}_2\text{O}_8$ is strongly affected by the distortion of the magnetic CoO_6 environment [219]. The determined shortest Co-O bond is directed along c-direction, which implies a compression of the octahedral environment along the chain direction and further to this, opposite Co-O bonds along c direction do not enclose an angle of 180°, wherefore the local axis c' of the octahedra is slightly tilted away from the global c-axis. As a consequence of the underlying rotational symmetry elements, the local c' axis of the CoO_6 octahedra rotates around the global c-axis with respect to the neighboring CoO_6 octahedra along the chain. However, the sense of rotation strongly depends on the location of the chain in the crystallographic unit cell, as two different types of screw chains are present. The CoO_6 chains that are generated by 4_1 and 4_3 symmetries possess respectively a different sense of rotation (see Fig. 10.1 a)) and it will be discussed below that in particular the tilt of the rotating $\mathrm{CoO_6}$ octahedra along the c-axis causes the different magnetic behavior in transverse fields applied along [1 0 0] or [1 1 0] direction [219].

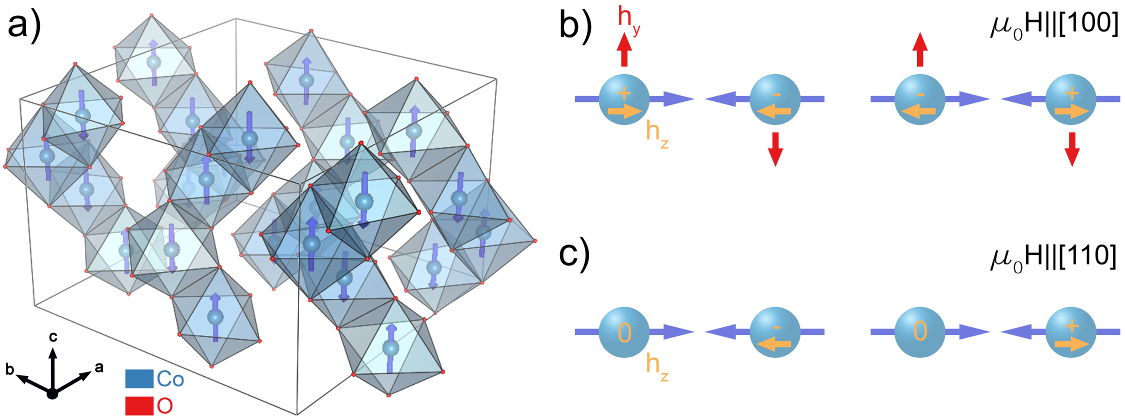

Figure 10.1.: The left side of this figure visualizes the magnetic $\mathrm{Co^{2+}}$ chains that are running along c-direction. For the sake of simplicity, the non-magnetic $\mathrm{VO_3}$ tetrahedra and non-magnetic $\mathrm{BaO_{12}}$ cuboctahedra are hidden. The illustration was done utilizing VESTA [226]. Both panels b) and c) sketch a one-dimensional mapping of the magnetic chain (blue arrows indicate the orientation of magnetic moments) and illustrate the induced staggered fields h_y and h_z (red and yellow arrows) for a field H_0 applied along [1 0 0] and [1 1 0] direction respectively. In both cases, the orthogonal coordinate system is chosen in a way that the applied field H_0 is parallel to x, h_z parallel to c and consequently y perpendicular to the latter mentioned directions. The field strength of the longitudinal and the transverse staggered field was respectively reported to amount $h_y = 0.4 g_{xx} H_0$ and $h_z = 0.14 g_{xx} H_0$ with $g_{xx} = 2.75$ for $H_0 || [1\,0\,0]$ and $g_{xx} = 2.95$ for $H_0 || [1\,1\,0]$ [219].

Strong intrachain interaction and finite but weaker interchain interaction cause the development of three-dimensional long-range ordering of the $\mathrm{Co^{2+}}$ moments at $T_\mathrm{N} = 5.5\,\mathrm{K}$ in zero field [214]. The c-direction is here the easy axis of the system [214, 215] and the commensurate propagation vector of magnetic ordering was determined to be $\mathbf{k} = (1\,0\,0)$ [218, 227, 228]. The moments are antiferromagnetically aligned along the chain, but the orientation of neighboring moments within the same [1 0 0]/[0 1 0] plane is respectively parallel or antiparallel [218, 227, 228], wherefore the magnetic structure does not follow the tetragonal symmetry but rather possesses a lower one, which enforces the formation of magnetic domains [211].

The application of a magnetic field along the easy axis revealed a second order transition at $\mu_0 H \approx 3.9\,\mathrm{T}$ to a paramagnetic and disordered phase, whereas at lower temperature ($T < 1.8\,\mathrm{K}$) the magnetic field triggers a first-order transition to incommensurate magnetic ordering [218, 227, 228]. It first coexists with the commensurate ordering in a tiny field range ($\Delta(\mu_0 H) \approx 0.2\,\mathrm{T}$) before the latter ordering type is completely suppressed [228]. The incommensurate magnetic structure is described by a longitudinal spin-density wave, for which the incommensurability δ of the incommensurate propagation vector $\mathbf{k}_\mathrm{inc} = (1\,0\,\delta)$

increases from ≈ 0.03 up to ≈ 0.3 with increasing field [218, 227, 228]. It was observed that above $\mu_0 H \approx 8.5\,\mathrm{T}$ commensurate ordering with $\mathbf{k}_\mathrm{c} = (1\,0\,0)$ is developing and is coexisting to the intermediate incommensurate phase [229]. Only above $\mu_0 H \approx 9.25\,\mathrm{T}$ the incommensurate fraction vanishes and a canted transverse antiferromagnetic structure is stabilized [229]. The sequence of field-induced transitions in $\mathrm{BaCo_2V_2O_8}$ with $\mu_0 H || c$ is well described by the Tomonaga-Luttinger liquid (TLL) model [230–234]. For a 1D spin-1/2 Ising system it proposes the dominance of incommensurate and longitudinal spin-spin correlations over staggered correlations transverse to the spin-chain, whereby the latter ones are prevalent for a spin-1/2 Heisenberg chain [234]. As finite interchain interactions stabilize the appearance of long-range 3D ordering at low temperature in the quasi 1D Ising-like system $\mathrm{BaCo_2V_2O_8}$ [214], it hinders the emergence of a TLL phase in zero field [234]. However, the application of an external field reinforces the quantum fluctuations and prompts the system towards the transition to a TLL phase [234, 235]. This is manifested by the observed field-induced transition to incommensurate ordering above the critical field at $\mu_0 H \approx 3.9\,\mathrm{T}$ [218, 227, 228]. The observed incommensurability exhibits a pronounced field dependence, which is also confirm with the TLL model as it proposes a proportionality between the incommensurate magnetic propagation vector and the field-induced magnetization [233, 234].

In the framework of the TLL theory it was also proposed that transverse correlations are adequately boosted in $\mathrm{BaCo_2V_2O_8}$ at higher fields and become even larger than the longitudinal ones, which suggests the crossover to staggered and transverse commensurate order [234]. As already mentioned, a second transition to a commensurate canted antiferromagnetic structure was indeed observed above $\mu_0 H \approx 8.9\,\mathrm{T}$ [229]. The transverse antiferromagnetic structure first coexists to the incommensurate ordering, which disappears at $\mu_0 H \approx 8.9\,\mathrm{T}$ [229]. However, concurrent dominance of both, longitudinal and transverse correlations in a finite crossover region is also confirm with the proposed TLL physics in $\mathrm{BaCo_2V_2O_8}$ [234].

The magnetic behavior under the influence of transverse fields in $\mathrm{BaCo_2V_2O_8}$ is even more complex due to the reported *ab* in-plane anisotropy of the system [211, 219]. Following the explanations in [219], the effective Hamiltonian for applied transverse fields can be written as

$$\begin{aligned}\mathcal{H} =& J\sum_j \left(S_{j,z}S_{j+1,z} + \epsilon\left(S_{j,x}S_{j+1,x} + S_{j,y}S_{j+1,y}\right)\right)\\ &- \mu_\mathrm{B}\sum_j (g_{xx}H_0 S_{j,x} + h_y S_{j,y}\sin\left(2\phi_1 + \pi\left(j-1\right)\right)\\ &+ h_z S_{j,z}\cos\left(\phi_1 + \frac{\pi(j-1)}{2}\right)).\end{aligned} \tag{10.1}$$

Here, the angle $\phi_1 = 0°$ and $\phi_1 = 45°$ refer to $H_0||(1\,1\,0)$ and $H_0||(1\,0\,0)$ respectively. The effective fields fields along y- and z-direction are described by $h_y = C_y g_{xx} H_0$ and $h_z = C_z g_{xx} H_0$, whereby the constants are given by $C_y = 0.4$ and $C_z = 0.1\sqrt{2}$. Depending on the angle ϕ_1, the g-values amount to $g_{xx} = 2.95$ (for $\phi_1 = 0°$) or $g_{xx} = 2.75$ (for $\phi_1 = 45°$). The other parameters in the Hamiltonian were calculated [219] to amount

$\epsilon = 0.46$ and $J/k_\mathrm{B} = 65\,\mathrm{K}$.

As already mentioned, the in-plane anisotropy arises from the tilted octahedra with respect to the global c-axis [219]. Due to this tilt and the symmetry constrained rotation of the local octahedra axes around the global c-axis, the effective g-tensor obtains finite off-diagonal entries, which cause the development of staggered fields depending on the applied transverse field direction [211, 219]. This is visualized in Fig. 10.1 and can be derived from the Hamiltonian by considering the angles $\phi_1 = 0°$ and $\phi_1 = 45°$ for $H_0||(1\,1\,0)$ and $H_0||(1\,0\,0)$ respectively. In the particular case of $\mathrm{BaCo_2V_2O_8}$, the applied field H_0 along [1 0 0] direction induces the presence of perpendicular staggered fields $h_y = 0.4 g_{xx} H_0$ and $h_z \approx 0.14 g_{xx} H_0$ along b and c respectively, whereas a transverse field along [1 1 0] direction causes a staggered field $h_z \approx 0.14 g_{xx} H_0$ only along c and thus parallel to the chain direction [211, 219]. This field dependent development of staggered fields is reinforced by the experimental observation of different critical fields for the complete suppression of long-range Néel-ordering [211, 219]. A transversal field along [1 0 0] direction promotes the elimination of Néel ordering at a much weaker field compared to the case of an applied field along [1 1 0] direction [211, 219]. For this field alignment the Néel temperature is only reduced by 25% at $\mu_0 H = 10\,\mathrm{T}$ and only above the critical field $\mu_0 H = 40\,\mathrm{T}$ the Néel ordering is entirely suppressed [219]. This much higher value for the critical field along [1 1 0] is confirm with the fact that the effective g tensor implies only staggered fields along the chain direction [219].

Recently, the transverse field direction along [110]-direction attracted again special attention as sound velocity and magnetization measurements in Ref. [212] and Ref. [220] revealed an additional anomaly at $\mu_0 H = 21.4\,\mathrm{T}$ [212], respectively at $\mu_0 H = 30\,\mathrm{T}$ [220]. The anomaly was proposed to signal the suppression of three-dimensional ordering below the quantum critical point and as already discussed, this can be viewed as a realization of an isolated effective spin-1/2 chain that can be described by the TFI model in a finite field range above the three-dimensional ordered phase and below the quantum critical point [212]. It is worth mentioning that this realization of the TFI model would offer experimental access to the underlying physics and its further investigation in a real system. Nevertheless, the magnetization and sound-velocity measurements are not sufficient to characterize the nature of magnetic ordering to the full extent. Furthermore, a staggered-field induced TLL phase cannot be excluded to appear in finite transverse fields. Therefore, a profound analysis and characterization of this high-field transition is highly desirable.

10.3. Experimental method

The investigation of the proposed field induced transition in $\mathrm{BaCo_2V_2O_8}$ is well suited to neutron scattering experiments, as the magnetic structure components can easily be sensed by it. However, conventional diffraction instruments are limited in the accessible field range, as common cryomagnets provide continuous fields only up to 15 T at maximum. The phase region, in which the suppression of three-dimensional ordering was proposed by Z. Wang *et* *al.* [212] can be reached by utilizing the high-field magnet (HFM) at the Helmholtz-Zentrum Berlin (HZB) [222,224] (proposal HFM-183-00001-IN/HT). This world-wide unique magnet for neutron diffraction is capable to operate continuously at 26 T, which is the current record for a continuous field that can be applied at a neutron scattering instrument. The magnet is built as a hybrid system, which consists of an outer superconducting coil that covers two resistive coils in the inner part of the magnet. These two resistive coils are built such that at opposite sides and parallel to the field, the cusps of conical openings (respectively 30° opening angle) are directed to the center position of the magnet. The sample is mounted at this center position and the conical opening can be filled by a cryogenic environment. For the experiment that is discussed below, a horizontal continuous flow ^{3}He cryostat with a base temperature of 0.6 K was used. The tremendous accessible field range goes along with an enhanced infrastructure for the magnet, which consequently limits the mobility of the whole instrument. In particular, it highly restricts the accessible Q-space range for a scattering experiment and limits the number of measurable reflections. To enable the observation of reflections at low scattering angles, the HFM was adapted to the extreme environment diffractometer (EXED), which utilizes the neutron time-of-flight technique for scattering experiments [221, 223, 224]. The reduction and treatment of the time-of-flight data was done utilizing Mantid [236]. Neutrons are guided by supermirrors from the thermal and cold source to the chopper system that defines the time of the neutron pulse and the subsequent time-of-flight analysis allows for a broad accessible wavelength range of 0.7 Å-15 Å for the incoming neutron beam. The conical openings before and behind the sample together with a possible rotation of the magnet by 12° at maximum allows for a scattering angle up to $2\theta = 27°$. Four detector banks that comprise in total 192 position sensitive ^{3}He detectors are placed before and behind the sample for respectively recording the backward and forward scattering.

For the investigation of the potential field dependent suppression of three-dimensional long-range ordering in $BaCo_2V_2O_8$, it is necessary to sense the magnetic c component of the structure, which thus requires a scattering vector with perpendicular components to the [0 0 1] direction. This is because only perpendicular components of the magnetization with respect to the scattering vector can be sensed (see section 2.2). A further restriction for the scattering setup is provided by the magnetic field, which is horizontally aligned within the scattering plane and must be directed along the TFI direction [1 1 0]. The available reflections with respect to different scattering geometries were determined by the EXEQ software that offers the experiment planning for EXED beamtime [237]. From different tested scattering planes, it became obvious that only the scattering plane (1 1 0)/(1 -1 0) with $(1 1 0)||\mu_0 H$ provides a scattering geometry that allows for the observation of magnetic reflections with a finite perpendicular component with respect to the scattering vector. Thus, a single sample of $BaCo_2V_2O_8$ was prepared in scattering geometry (1 1 0)/(1 -1 0), but it has to be noted that the instrumental setup at HFM/EXED does not allow for sample rotations once the sample is inserted into the magnet. Therefore, an exact alignment of the [1 1 0] direction along the field direction was needed. The sample was grown by

S. Niesen utilizing the mirror furnace and details about the sample growth can be found in [238].

The high-field experiment at the HFM/EXED instrument profited from the accessible high-fields up to 26 T, but the instrumental Q-space resolution did not allow for a precise peak profile analysis of the magnetic reflection. Therefore, a second experiment (proposal 5-41-1032) at the conventional two-axis diffractometer D23 was conducted. The D23 diffractometer is located at the ILL and can be operated together with a 15 T cryomagnet, which thus yields a much lower field compared to the HFM/EXED experiment. However, from the HFM/EXED output it was observed that a potential transition is resolvable also at lower fields, when measuring at higher temperatures. The D23 diffractometer was operated at 14.9 T and an additional 10' collimation was inserted in front of the sample to further improve the resolution in Q-space. Due to the resulting shortage of space in front of the cryomagnet, an aperture was only possible to place behind the sample position. As a vertical cryomagnet was used, the sample of the HFM/EXED experiment was reoriented to the (1 -1 0)/(0 0 1) plane with $[1\,1\,0]||\mu_0 H$. For all reported scans, a Cu (2 0 0) monochromator supplied an incoming beam with $\lambda = 3$ Å.

10.4. Results

10.4.1. High-field studies at HFM/EXED

As a collapse of magnetic ordering is related to the disappearance of intensity for the respective magnetic reflections, the main goal of the conducted experiment at the HFM/EXED instrument was to record the intensity of magnetic reflections across the proposed transition as a function of field and temperature.

Here, the experimental procedure was to ramp the applied field between zero field and its maximum value at $\mu_0 H = 25.9$ T, while recording neutron time-of-flight data for different fixed fields. This sequence was repeated for different sample temperatures and eventually, several cuts along particular Q-directions were extracted from the position sensitive detector, respectively the time-of flight data to obtain Q-scans across the magnetic reflections. These cuts were extracted for $\mathbf{Q} = (\text{-}H\ H\ \pm 1)$ direction, which entails scattering vectors that possess perpendicular components with respect to the easy axis. Thus, the corresponding magnetic reflections can signal the suppression of the three-dimensional ordering of Co^{2+} moments that are pointing along c-direction. The respective scattering was recorded only in forward direction, as the finite wavelength band and the limited scattering angle prohibited the observation of reflections in the backward scattering channel. All extracted intensities were normalized to the monitor value to facilitate the comparability of the signal strength between different data sets, respectively different fields and temperatures.

The left panels of figure 10.2 display exemplary the $\mathbf{Q} = (\text{-}H\ H\ \text{-}1)$ cuts as a function of magnetic field strength, whereby each panel comprises the cuts for a different sample temperature.

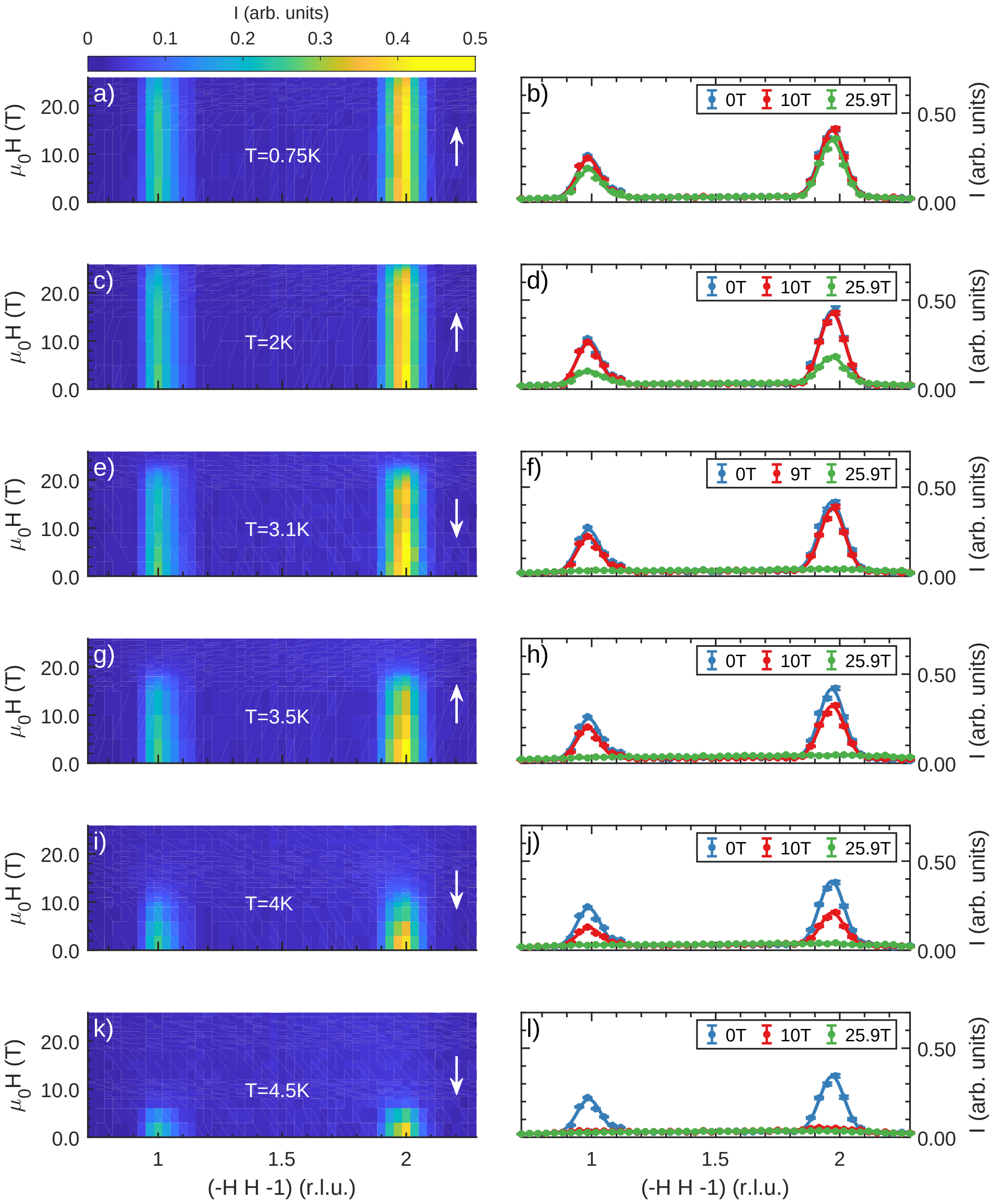

Figure 10.2.: The left panels of this figure display the temperature and magnetic field dependent intensity for extracted cuts along $\mathbf{Q} = (\text{-}H\ H\ \text{-}1)$. White arrows mark the direction of the field sweep and all intensities are normalized to the monitor. For each panel on the left side, three cuts for different fields are respectively displayed in the neighboring right panel. The colored solid lines refer to Gaussian fits, whereby it must be noted that both reflections were fitted separately.

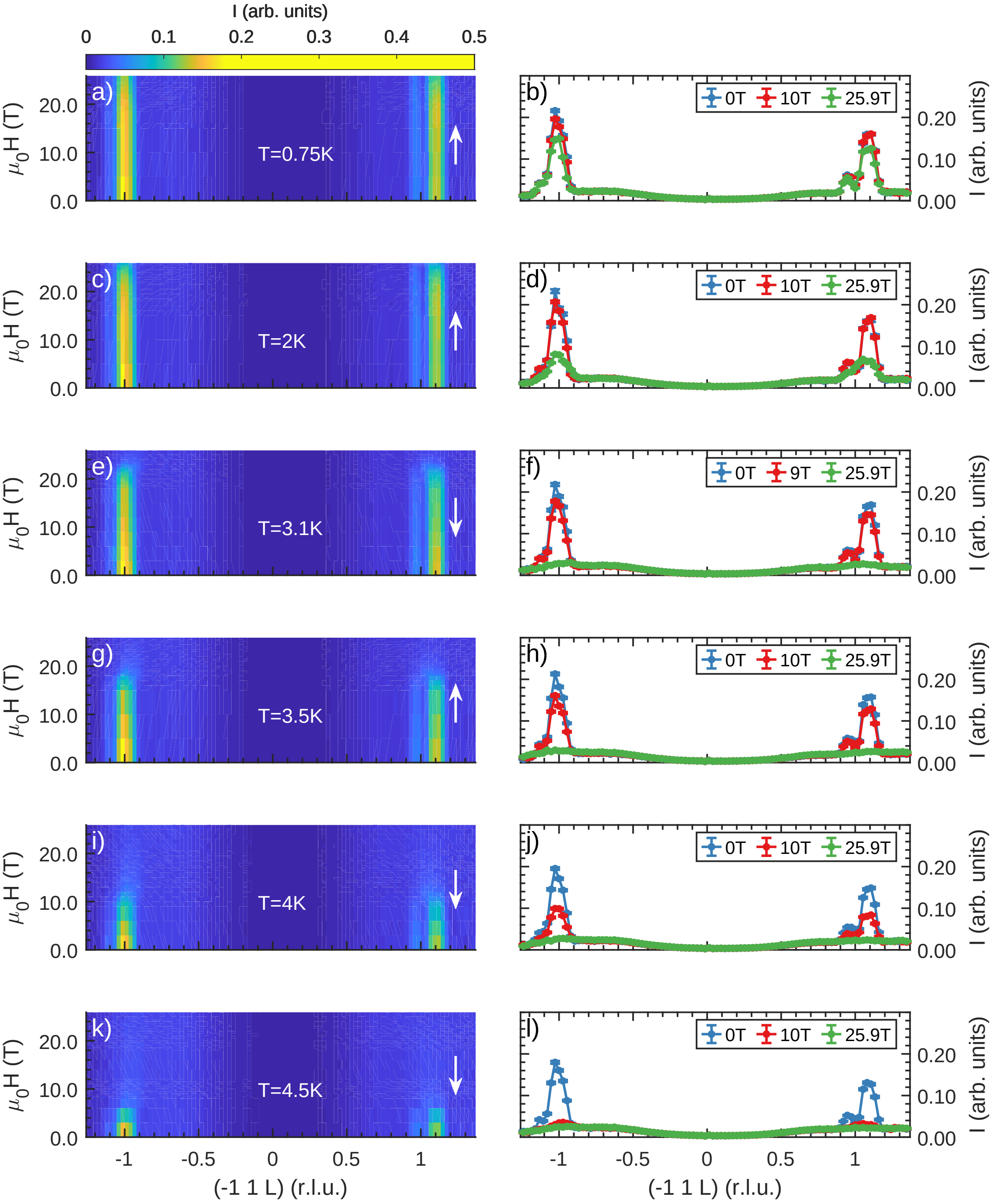

Figure 10.3.: The left panels show the reduced temperature and field dependent cuts across $Q = (\text{-}1\ 1\ L)$. The observed field and temperature independent splitting (see individual cuts in the right panels) of the reflection is not caused by the sample but by an instrumental effect for scans out of the horizontal scattering plane. Solid lines in all right plots are just guide to the eyes and do not belong to a fit.

With these exemplary cuts along ($\text{-}H\ H\ \text{-}1$) direction, both magnetic reflections (-1 1 -1) and (-2 2 -1) are accessible and also clearly observable at zero field and below the transition temperature to the long-range ordered phase. Astonishingly, at the lowest measured temperature ($T = 0.75\,\mathrm{K}$), the magnetic reflections are still observable above the proposed transition field at $\mu_0 H_{\perp}^{\mathrm{3D}} = 21.4\,\mathrm{T}$ and even at $T = 2\,\mathrm{K}$ the magnetic reflections persist above $\mu_0 H_{\perp}^{\mathrm{3D}}$. This contrasts the proposed suppression of three-dimensional ordering, which was related to the observed anomaly in the sound-velocity and magnetization data in Ref. [212]. The surface plots in Fig. 10.2 reveal that the field dependent intensity does not vanish at very low temperature and high fields but rather exhibits a kink, which is followed by a moderate decay of intensity (see also exemplary cuts in the right panels of Fig. 10.2). This could also indicate the appearance of a second phase with an altered magnetic structure rather than completely suppressed three-dimensional ordering below the QCP. In the following, the proposed field value for the kink and the field magnitude for which the intensity disappears are respectively called H_{C1} and H_{C2}. With increasing temperature, the kink and the disappearance of the magnetic intensity shifts to lower field values. Qualitatively the same behavior can be observed for cuts along Q_L direction (see Fig. 10.3), but here it must be noted that a temperature and field independent peak splitting arises from an instrumental artifact for scans out of the horizontal scattering plane. As mentioned, the fact that significant intensity is still observable above the reported anomaly from sound velocity and magnetization measurements in Ref. [212] potentially indicate that the magnetic three-dimensional ordering is not suppressed but persists above the proposed transition. Due to the observed kink, there is rather some evidence that the anomaly signals a modification of the magnetic arrangement i.e. a second long-range ordered high-field phase. To clarify the potential appearance of a second long-range ordered high-field phase, a precise analysis of the field dependent peak intensity and peak width is necessary.

For this purpose, all magnetic reflections were fitted by a Gaussian function to obtain a precise temperature and field dependence of the peak intensity and peak width. These fits are exemplary shown (solid lines) in the right panels of Fig. 10.2 for selected field magnitudes. It must be noted that due to the bad peak shape along Q_L direction only $Q = (\text{-}H\ H\ \pm 1)$ cuts were fitted and wherefore solid lines in Fig. 10.3 are just guide to the eyes.

All fitresults i.e. peak intensity and peak width are visualized in Fig. 10.4. It can be seen that the plotted temperature and field dependence of the peak amplitude in the left panels of Fig. 10.4 confirm qualitatively the observation from surface plots in Fig. 10.2. Indeed, two subsequent transitions can be observed in a finite temperature and field range. At $4.5\,\mathrm{K}$ and $4\,\mathrm{K}$, both transitions are not resolvable separately, but for temperatures below, the field dependent intensity exhibits first a kink at H_{C1} until it vanishes at H_{C2}. It is clear to see that above H_{C1}, the peak width increases significantly inside the proposed second high-field phase. The fact that the enhancement of the peak width does not exactly coincides with the transition at H_{C1} can be related to insufficient Q-space resolution.

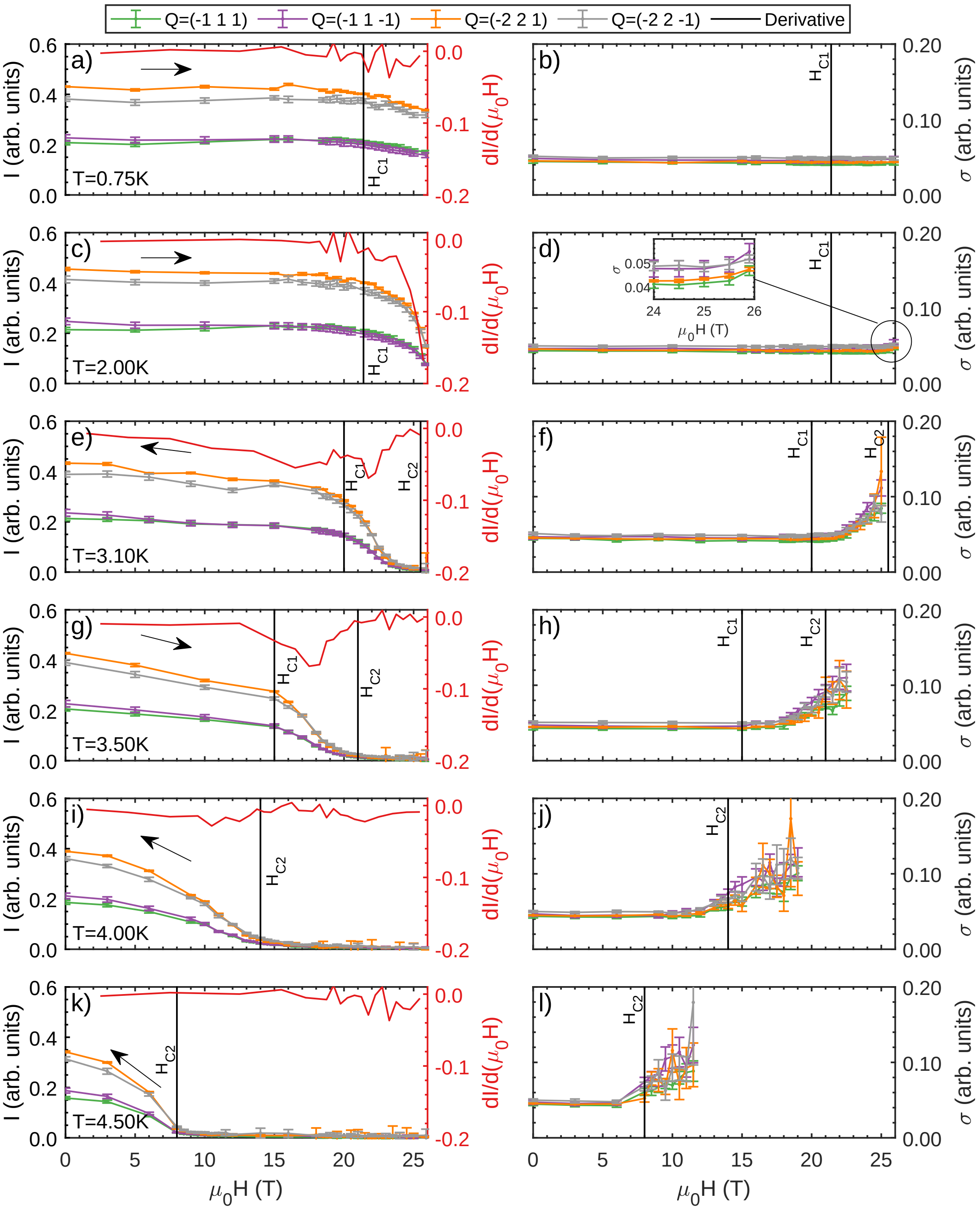

Figure 10.4.: The temperature and field dependent peak intensity I and peak width σ are plotted in a)-l) for the magnetic reflections (-1 1 1), (-1 1 -1), (-2 2 1) and (-2 2 -1). The red solid line in the left panels refers to the mean derivative of the temperature dependent intensity for the equivalent reflections (-2 2 1) and (-2 2 -1). Its temperature dependent value belongs to the right y-axis. All corresponding peaks were fitted separately by single Gaussian functions and all other displayed lines are only guides to the eyes. The black arrows indicate the sweep direction of the applied magnetic field.

The results confirm a second field induced phase, which exhibits long-range ordering. However, a further characterization of this high field phase is highly desirable to understand the physics that drives this transition. A possible scenario for the second long-range ordered phase, which is triggered by a transverse field along [110] direction, can be deduced from the same TLL model that was used to explain the field-induced transition to incommensurate ordering for an external field parallel to the chain direction.

The idea of a potential crossover to a TLL phase for the transverse field with $\mu_0 H||[1\,1\,0]$ is rooted in the reported emergence of staggered fields along c (see Fig. 10.1 c)). In view of the TLL physics, the peculiarity of the staggered field arrangement (i.e. $h_z =$"+ 0 - 0", see Fig. 10.1 a)) is that the alignment of Co^{2+} moments and staggered fields in relation to each other resembles an equivalent arrangement that would be achieved with an external field applied along the easy-axis. In the latter case the field orientation with respect to the antiferromagnetically aligned Co^{2+} moments alternates at each site along the chain from parallel to antiparallel. Qualitatively the same situation is also obtained for the staggered fields that are induced by the transverse field along [1 1 0] direction. The only difference is that the equivalent mutual orientation of staggered field and moment is fulfilled only at every second site. In between, the staggered field is zero. Thus, in contrast to the field-induced TLL phase that is reported for an applied external field parallel to the easy axis, the effective field that can drive the TLL phase amounts here to $h_z^{\mathrm{eff}} = h_z/2 \approx (0.14 g_{xx} H_0)/2$. The factor 1/2 arises from the fact that the staggered field vanishes at every second site. Thus, the effective field strength along c is only a small fraction of the applied transverse field H_0 and in view of the TLL phase, it explains the much higher value of the proposed transition field compared to the reported one for fields applied along the easy axis.

In case that the transverse field indeed drives the system to a TLL phase via longitudinal staggered fields, the magnetic arrangement must become incommensurate along the chain direction. As noted above, the instrumentally caused peak splitting for Q_L scans as well as the low Q-space resolution hindered the search for a field-induced incommensurate splitting of magnetic reflections. However, the HFM/EXED experiment revealed that the transition is also well observable at lower transverse fields but higher temperature within a range of a few mK. Following these results, it was thus seen promising to characterize the transition by utilizing a conventional vertical 15T cryomagnet and the much higher Q-space resolution that is provided at the D23 diffractometer.

10.4.2. High-resolution peak shape analysis at D23

The main goal of the conducted experiment was to resolve a potential transition to incommensurate order, which is proposed to arise from the TLL physics and for which a thorough peak shape investigation is needed. Temperature dependent Q-scans were done along L direction and as noted in section 10.3, the Q-space resolution was significantly enhanced by a 10' collimation in front of the sample.

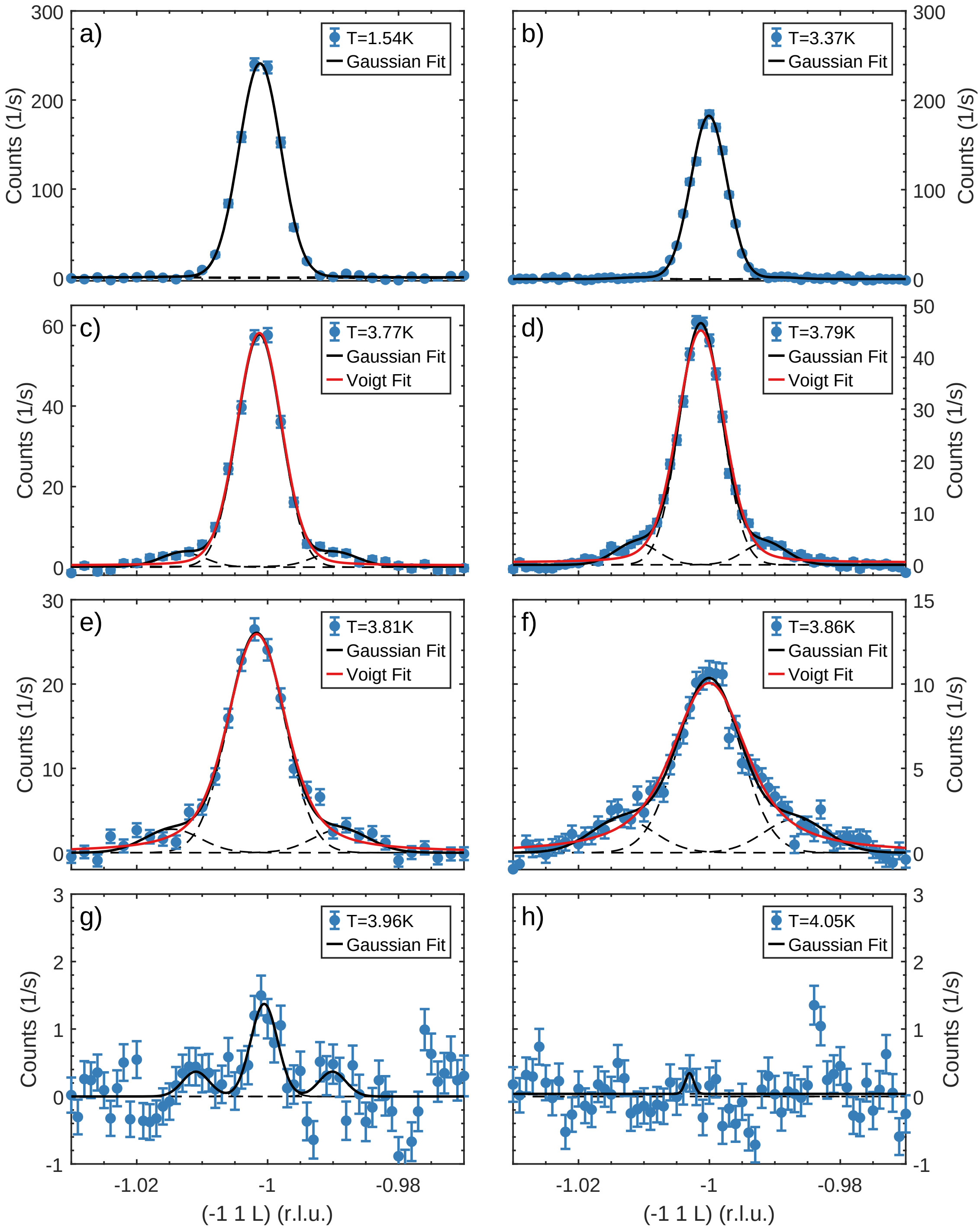

Figure 10.5.: The panels a)-h) display exemplary background corrected Q_L-scans across the magnetic reflection (-1 1 -1) for different temperatures at 14.9 T. All scans were fitted by the sum of three Gaussian functions, whereby the width of each Gaussian was fixed to the same value and the potential incommensurate satellites were constrained to have the same intensity as well as the same distance to the commensurate peak. The fitted sum is visualized as a black solid line and the three Gaussian functions are separately plotted as dashed lines. Further to this, in c)-f) a red solid curve visualizes the fitted convolution of a Gaussian function with a Lorentzian one (Voigt fit).

Due to the space that is taken by the collimation, an aperture was only placed behind the sample position, which caused a slightly increased background. Figure 10.5 displays exemplary several recorded Q_L-scans with subtracted background contribution for different temperatures at $\mu_0 H = 14.9\,\mathrm{T}$. At first glance, it seems that the peak shape is changing from pure Gaussian to a Lorentzian line shape, when the temperature is heated above approximately 3.7 K. In general, the Gaussian peak shape is inherent to the instrumental resolution, whereby the Lorentzian width is inversely related to the correlation length of the structure along the respective scan-direction. The peak shape can thus potentially be described by a convolution of a Gaussian function with a Lorentzian one. The red solid line in Fig. 10.5 c)-f) displays a corresponding fit of the significantly broadened magnetic reflection. As the instrumental resolution does not change with temperature, the Gaussian width was fixed to the value that was obtained at the lowest temperature, where only the instrumental resolution determines the peak width. A field dependent broadening of the fitted Lorentzian width would thus refer to a decreasing correlation length and hence a transition to short-range ordering.

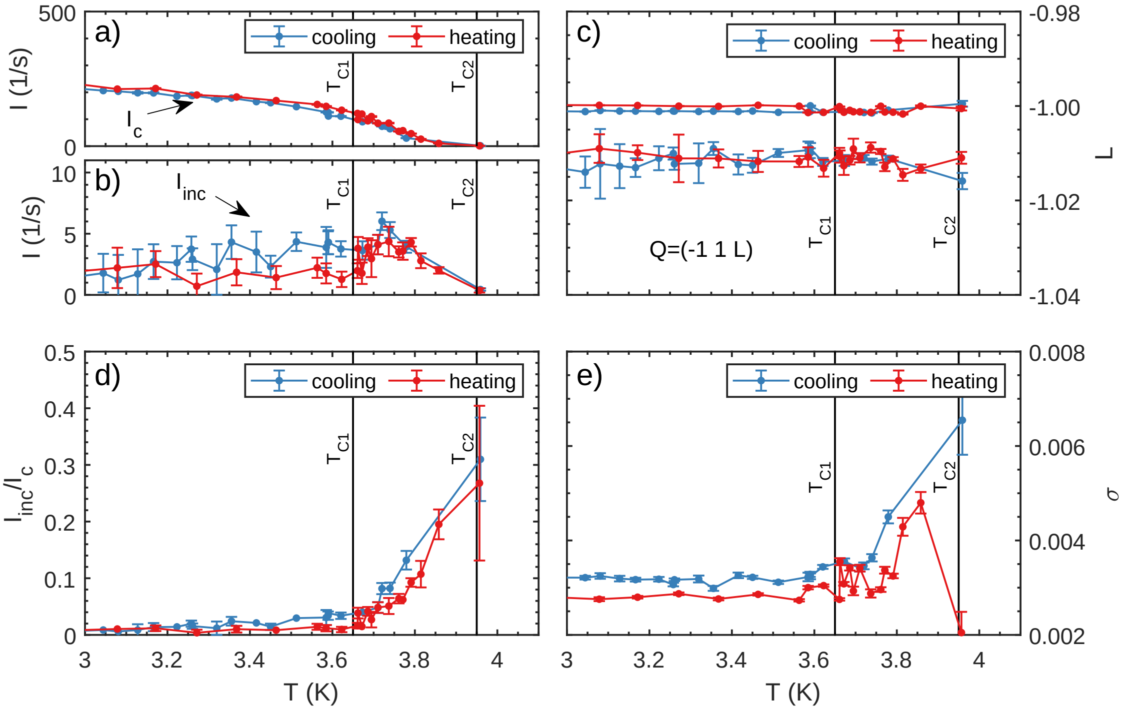

Figure 10.6.: The fitted incommensurate and commensurate peak amplitudes I_{inc} and I_{c} are plotted in a) and b) as a function of temperature. The y-axis scales logarithmically, wherefore some large errorbars cannot be plotted. Panel c) displays the obtained peak position of the commensurate and incommensurate reflection. It must be noted that the peak position is shown only for one incommensurate reflection, as the equivalent satellite was constrained to follow the same incommensurability. Both panels d) and e) show the ratio of peak intensities and peak widths σ (standard deviation) respectively as a function of temperature.

However, it is obvious that the fitted convolution (see Fig. c)-f)) does not well describe the measured peaks above $T \approx 3.7\,\mathrm{K}$ as two shoulders of the reflection significantly exceed the fitted peak shape of the convolution. Instead of a crossover to short-range ordering, this deviation from the fitted convolution indicates the appearance of coexisting incommensurate satellites, which are causing the observed peak broadening. To verify this, all recorded scans were also fitted by three Gaussian functions, which are constrained to possess the same width. Further, the amplitude of both potential incommensurate satellites were fixed to the same value and their peak position was constrained to be symmetrically distributed around the commensurate one. These fits are visualized as black solid lines for the reflections that are exemplary shown in Fig 10.5 a)-h). Dashed lines show the individual Gaussian peaks that assemble the whole fit function and it can be unambiguously seen that the mixture of incommensurate satellites together with a dominant commensurate reflection describes the measured peaks very well and thus much better than the convolution. This is a sound indication that incommensurate ordering is indeed emerging and coexisting to the commensurate one above the critical transverse field H_{C1} that is applied along [1 1 0] direction.

Figure 10.6 displays the obtained fit results for the temperature dependent Q_L-scans, which were performed at $\mu_0 H = 14.9\,\mathrm{T}$. The determined peak intensity of both, of the commensurate as well as of the incommensurate reflection further confirms the above discussed observation for the field induced transition to incommensurate ordering. Simultaneously to the kink of the commensurate peak amplitude, the incommensurate intensity becomes finite until the amplitude of both, commensurate and incommensurate reflections vanishes. Only between H_{C1} and H_{C2} the peak exhibits significant intensity within the given error range. The fitted peak position is shown in c) and reveals a finite but tiny incommensurability ($L \neq 1$) above the proposed transition. The finite value for the incommensurate peak position below H_{C1} is only because a Gaussian peak with almost zero intensity (see Fig. 10.5) is fitted to the background and pretends the existence of incommensurate ordering below H_{C1} A better estimation of the phase boundaries can be obtained from the ratio of incommensurate and commensurate peak intensity, which is visualized in Fig. 10.6 d). It can be seen that coexisting incommensurate ordering is developing at $T \approx 3.7\,\mathrm{K}$ until the long-range ordered structure is completely suppressed at $T \approx 4\,\mathrm{K}$. The first transition is also accompanied by a significant broadening of the Gaussian peak width (see Fig. 10.6 e)), which was fixed to the same value for the commensurate reflection and the incommensurate satellites. These results and in particular the values for the transitions H_{C1} and H_{C2} agree very well to the outcome of the HFM/EXED experiment. In the last part of the experiment Q_L scans were recorded at $4\,\mathrm{K}$, while reducing the applied field towards $0\,\mathrm{T}$. The respective fit results are visualized in Fig. 10.7 and also acknowledge the presence of a second field-induced phase with coexisting commensurate and incommensurate ordering for a transverse field applied along [1 1 0] direction. The transition to the low-field commensurate phase appears at approximately $11\,\mathrm{T}$, which is confirm with the observed kink in the field dependent data of the HFM/EXED experiment at $4\,\mathrm{K}$.

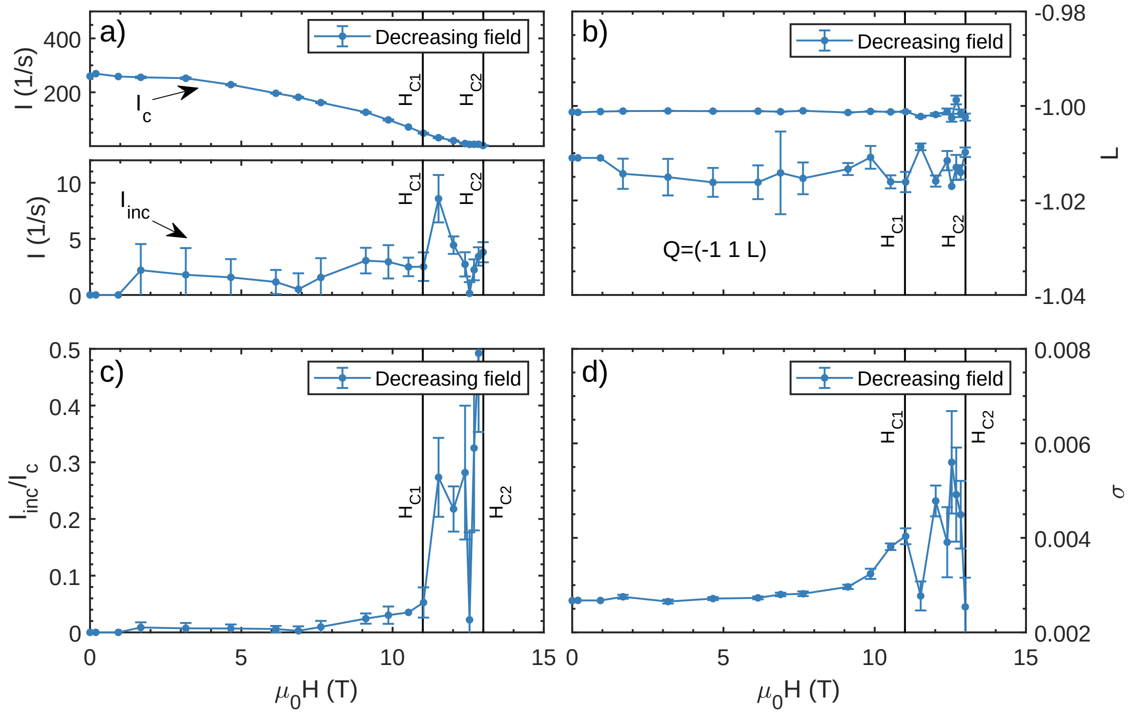

Figure 10.7.: All four panels present the obtained field-dependent fit results equivalent to the temperature dependent data in Fig. 10.6. The data was recorded at 4 K, while decreasing the field.

10.5. Conclusion

Both neutron scattering experiments on $BaCo_2V_2O_8$ unambiguously showed that a transverse field along [1 1 0] direction does not suppress the three-dimensional ordering below the QCP but triggers a transition to a second long-range ordered phase at H_{C1}. The discussed high-resolution Q_L scans across magnetic reflections revealed that this second phase is accompanied by the appearance of incommensurate satellites ($\mathbf{k} = (1\,0\,\delta)$) exhibiting a small incommensurability of about $\delta \approx 0.012$. They coexist with the commensurate peak until both kind of reflections vanish at H_{C2}. The measured transitions are documented in the phase diagram in Fig. 10.8 in which also the reported anomalies from magnetization and sound-velocity measurements (see Ref. [212]) are included. Solid lines are just guides to the eyes and represent a rough estimation of the respective phase boundaries. It can be seen that the determined transitions from the HFM/EXED and D23 experiment nicely agree to the reported transitions that were observed by Z. Wang *et al.* [212]. However, this does not hold for the reported anomaly in [220]. Here, the first anomaly as a function of field was seen at $\mu_0 H \approx 30\,\mathrm{T}$ (at $T = 1.3\,\mathrm{K}$), which obviously does not fit to the presented data and the approximate phase boundaries in Fig. 10.8.

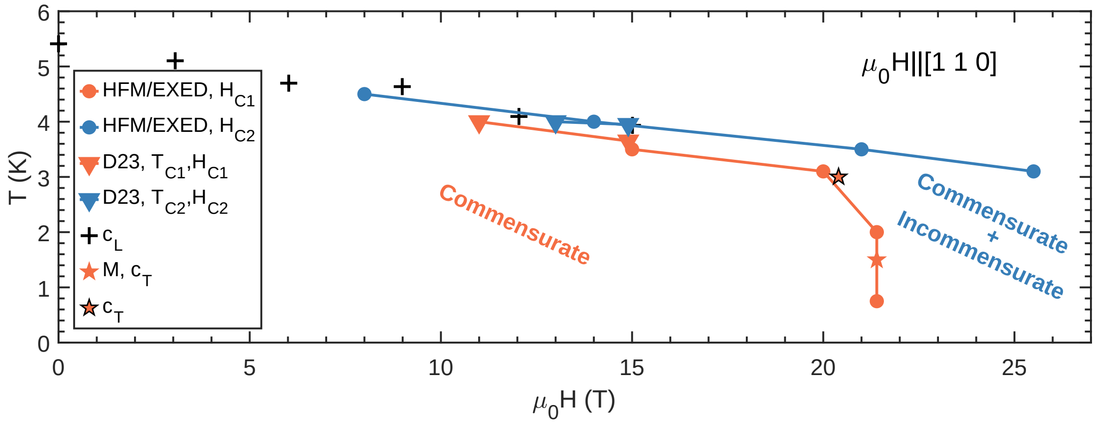

Figure 10.8.: This figure displays the proposed H-T phase diagram of $BaCo_2V_2O_8$ for an applied external field along [1 1 0] direction. Circles and triangles refer to the determined transitions from the HFM/EXED and D23 experiment respectively. Further, the reported anomalies from magnetization (M) and sound-velocity (c_L,c_T) measurements [212] are included in this diagram. Solid lines are just guides to the eyes and depict the expected phase boundary of the low-field commensurate phase as well as of the high-field phase with coexisting commensurate and incommensurate order.

It was mentioned that the appearance of incommensurate ordering can here potentially be related to a TLL phase, which is not directly driven by the transverse field but by the induced staggered fields along the magnetic chain direction. It would thus resemble the TLL phase, which was reported for an external field applied longitudinal to the easy axis [234, 235]. However, in this context, it must be considered to what extend the effective field along z is respectively generated by the external transverse or external longitudinal field. For $\mu_0 H||[1\,1\,0]$ the Hamiltonian in equation 10.1 yields the Zeeman term

$$\pm\mu_\mathrm{B}\underbrace{C_z g_{xx} H_0}_{h_z} S_{j,z} \qquad \text{or } 0 \text{ for } j = \text{odd} \tag{10.2}$$

and for $\mu_0 H||[0\,0\,1]$ the Zeeman term for an effective field along z-direction is described by

$$\pm\mu_\mathrm{B}\underbrace{g_{zz} H_0}_{h'_z} S_{j,z}. \tag{10.3}$$

Here, the respective g-values are reported to amount $g_{xx} = 2.95$ (for $\mu_0 H||[1\,1\,0]$) [219] and $g_{zz} = 6.3$ (for $\mu_0 H||[0\,0\,1]$) [213]. Consequently, the ratio of both effective fields h_z and h'_z becomes

$$\frac{1}{2} C_z \frac{g_{xx}}{g_{zz}} H_0 S_{j,z} \approx 0.033, \tag{10.4}$$

whereby the factor 1/2 arises from the fact that the staggered field vanishes (for $\mu_0 H||[1\,1\,0]$) at every second Co site. Hence, an applied external field of about 14.9 T along [1 1 0] would generate the same effective field along c as an applied field of approximately 0.49 T along the easy axis. However, for an applied field along [0 0 1]-direction, the transition to a TLL phase was reported to be approximately at $\mu_0 H = 3.8\,\mathrm{T}$ [227,228,239], wherefore an applied transverse field ($\mu_0 H || [1\,1\,0]$) of about 14.9 T is not enough to induce sufficiently strong staggered fields that can exceed this transition to a TLL phase. But in this context, it must be kept in mind that the intense transverse field impacts the magnetization differently with respect to an external field that is applied longitudinal to the easy axis. To understand this impact on the TLL-physics and to clarify the physics that drives the system towards an incommensurability necessitate thus elaborate theoretical studies. From the experimental point of view, it can only be stated that the system exhibits a transition to coexisting commensurate and incommensurate order but the clarification, whether this transition can be related to a TLL phase needs more theoretical studies on the transverse and longitudinal spin-spin correlation functions that are impacted by the magnetization of the system. It would be further beneficial to intensify the studies on the field dependency of the incommensurability but the respective experiments are unfortunately limited by the accessible field range and the necessity of high Q-space resolution.

A. Switching of toroidal moments

A.1. Motivation

The well-known ferroic ordering types, namely ferroelasticity, ferroelectricity and ferromagnetism differ explicitly by their respective behavior under space-inversion and time-reversal [11, 23]. On the basis of these symmetry considerations, toroidal ordering was intensively discussed to represent a fourth ferroic ordering type, which exclusively changes sign under both, space-inversion and time-reversal [240, 240–242]. The definition of the toroidal moment stems from the multipole expansion of the electromagnetic vector potential and a typical composition that generates such a toroidal moment is given by an electric current that circulates around a solenoid, which generates a magnetic field that rotates through the solenoid [243, 244]. In this case, the toroidal moment is oriented perpendicular to the rotating magnetic field and its sign is determined by the handedness of the magnetic field. An equivalent situation can be gained by a head-to-tail arrangement of localized spins in a periodic crystal, whereby the toroidal moment is then defined by $\mathbf{t} = \frac{1}{2}\sum_i \mathbf{r_i} \times \mathbf{s_i}$ with $\mathbf{r_i}$ being the space position and $\mathbf{s_i}$ being the magnetic moment of the i_{th} atom [241–244]. Hence, the direction of $\mathbf{t}$ is here determined by the handedness of the spin arrangement and it was further shown that the toroidal moment $\mathbf{t}$ couples to the curl of a magnetic field [241–244]. The spontaneous toroidization of a system was defined as toroidal moment per unit volume V_{cell}, thus given by $\mathbf{T} = \mathbf{t}/V_{\text{cell}}$ [241, 242]. Similar to the calculation of a ferroelectric polarization, the absolute value of $\mathbf{T}$ depends on the chosen origin, wherefore it is convenient to calculate rather the change of toroidization $\Delta\mathbf{T}$ with respect to a respective non-centrosymmetric system in which no toroidal order is allowed [241, 242].

Beside the onset of spontaneous long-range order, a further required attribute for ferroic ordering is the formation of switchable domains in the respective system [240]. Using the curl of a magnetic field as the conjugate field to reverse toroidal domains seems to be the obvious approach but is experimentally unfeasible, as it requires a finite current flowing through systems that are mostly insulating and moreover, producing a finite curl of the magnetic field is also challenging in complex experimental environments. However, it was reported that toroidal order enforces asymmetric components of the magnetoelectric tensor [241–244], which entails a coupling of the toroidal moment to crossed magnetic- and electric-fields. It has to be noted that the other way around does not hold. The presence of antisymmetric components for the magnetoelectric tensor does not obligatory entails the existence of toroidal order [241].

The presence of toroidal domains, as well as their controllability with crossed electric-and magnetic-fields was proven by second harmonic generation spectroscopy and spherical neutron polarimetry [24, 245, 246]. The latter method was utilized to investigate the poling of toroidal domains in $LiFeSi_2O_6$ [24] and with second harmonic generation spectroscopy it was possible to prove hysteric behavior of toroidal domain inversion in $LiCoPO_4$ [245, 246]. Thus, toroidal ordering indeed fulfills the criteria for a ferroic state but a thorough study of temperature and electric-field dependent toroidal domain dynamics i.e. the investigation of the relaxation behavior of toroidal domains is still missing and motivates further studies on toroidal materials. However, the application of crossed electric- and magnetic-fields hinders rapid switching of the toroidal field and moreover conflicts with in-situ studies of domain kinetics, when utilizing spherical neutron polarimetry. Hence, a different approach for the switching of toroidal domains is desirable.

In the following, a first attempt of time-resolved toroidal domain inversion studies on $LiFeSi_2O_6$ is described. Here, rapid electric-field inversion was utilized to generate a finite value for the curl of the magnetic field as a consequence of Ampère's circuital law. The induced curl of the magnetic field was exerted as the driving field for toroidal domain inversion and the time-resolved data collection technique utilizing neutron-polarimetry was adapted from respective experiments on multiferroic domain inversion (see section 2.4 and Ref. [49]).

A.2. Crystal and magnetic structure of $LiFeSi_2O_6$

The pyroxene system $LiFeSi_2O_6$ exhibits at monoclinic unit cell (space group $C2/c$) with lattice constants $a = 9.6641(8)\,\text{Å}$, $b = 8.6612(8)\,\text{Å}$, $c = 5.2924(4)\,\text{Å}$ and $\beta = 110.12°$ at $T = 298\,\text{K}$ [247, 248]. The crystal structure is composed of edge-sharing FeO_6 octahedra, which are forming zigzag chains along c-direction and which are separated by corner sharing SiO_4 tetrahedra chains that are also propagating along c [247, 248]. At $T_\text{S} = 229\,\text{K}$ a structural transition to space group $P2_1/c$ is induced by a kinking of the SiO_4 chains [248, 249]. Hereby, neighboring chains are buckled differently at different angle and are thus inequivalent below T_S [248]. As it will be explained below, most important for the development of toroidal order is the shift of Fe ions, which becomes possible after the symmetry reduction. The Fe ions within a chain shift in the same direction, but opposite to the Fe ions in neighboring chains [24]. At $T_\text{N} = 18.1\,\text{K}$, the Fe^{3+} moments develop commensurate collinear long-range ordering within the ac plane ($\mathbf{k}_\text{c} = (0\,0\,0)$), whereby an additional b-component forms a canted magnetic structure [250–253]. However, it must be noted that the reported Neél temperature varies slightly in literature [250–253]. The magnetic space group was determined to be $P2_1/c'$, which entails that neighboring moments are oriented parallel within a chain and antiparallel along neighboring chains in $LiFeSi_2O_6$ [24]. As the structural displacements of all four Fe ions within a single unit cell and the respective magnetic moment orientations possess the same relative phase, a finite value for $\mathbf{T}$ evolves. This finally leads to the formation of toroidal domains in the magnetically long-range ordered phase of $LiFeSi_2O_6$ [24]. Considering symmetry arguments, Tolédano *et. al.* further showed that toroidal ordering drives the antiferromagnetic ordering, wherefore the toroidal moment in $\mathrm{LiFeSi_2O_6}$ can be identified as a primary ferroic ordering parameter [254]. As already mentioned, the chosen basis determines the value for the toroidal moment, but nevertheless, the difference $\Delta\mathbf{T}$ with respect to a non-centrosymmetric reference system, in which all Fe ions are not shifted, is invariant concerning the chosen basis and amounts to $|\Delta\mathbf{T}| = 0.00025(3)\ \mu_\mathrm{B}\text{Å}^{-2}$ for $\mathrm{LiFeSi_2O_6}$ [24].

A.3. Experimental Method

The sign of the ferrotoroidal moment depends on the respective orientation of structural displacements and magnetic moments to each other in a single unit cell. Hence, it can be concluded that four types of toroidal domains are forming in the magnetically long-range ordered phase of $\mathrm{LiFeSi_2O_6}$. It is clear that phase shifts of 0° and 180° between magnetic moment orientation and structural displacement determine the plus or minus sign of the toroidal moment respectively. Considering spherical neutron polarimetry, the phase difference and thus the sign of the toroidal moment can be sensed by the nuclear-magnetic interference terms as they contain the product of the nuclear F_N and magnetic structure factor F_M and not the square of them, which thus preserves the phase of both. Accordingly, the measurements necessitate a reflection, which contains both magnetic, as well as nuclear scattering contributions and it has to be noted that in this scattering configuration only the z component of $\mathbf{M}$ contributes to the signal, wherefore $\mathbf{M} = m_z$. Baum *et al.* determined the reflections with the largest nuclear-magnetic interference contribution for $\mathrm{LiFeSi_2O_6}$ and calculated the entries of the polarization matrix, while considering the convenient coordinate system for polarization analysis (see section 2.3) and the scattering geometry (1 0 0)/(0 1 0) [24]. The polarization matrix then equals

$$\mathbf{P}^{\text{theo}}_{(\mathbf{3\,0\,0})} = \begin{pmatrix} \frac{F_\mathrm{N}^2 - m_z^2}{F_\mathrm{N}^2 + m_z^2} & -\frac{2F_\mathrm{N} m_z}{F_\mathrm{N}^2 + m_z^2} & 0 \\ \frac{2F_\mathrm{N} m_z}{F_\mathrm{N}^2 + m_z^2} & \frac{F_\mathrm{N}^2 - m_z^2}{F_\mathrm{N}^2 + m_z^2} & 0 \\ 0 & 0 & \frac{F_\mathrm{N}^2 + m_z^2}{F_\mathrm{N}^2 + m_z^2} \end{pmatrix} = \begin{pmatrix} -0.997 & \mp 0.077 & 0 \\ \pm 0.077 & -0.997 & 0 \\ 0 & 0 & 1 \end{pmatrix}. \qquad \text{(A.1)}$$

From the calculated polarization matrix $\mathbf{P}^{\text{theo}}_{(\mathbf{3\,0\,0})}$ it was seen that the inversion of toroidal domains would lead to an opposite sign change in the off-diagonal polarization channels P_{xy} and P_{yx}, which was experimentally proven by Baum *et. al.* [24]. As the application of magnetic fields conflicts with the usage of polarized neutron scattering as the measuring probe, the system $\mathrm{LiFeSi_2O_6}$ was cooled and poled in a separate cryomagnet for different sign permutations of the applied crossed electric and magnetic fields until afterwards the sample was inserted in a CRYOPAD setup that enabled the measurements of P_{xy} and P_{yx} for each previously defined field-sign permutation [24]. In situ application of both, magnetic and electric fields in CRYOPAD is not possible, wherefore a different method was needed to investigate not only the poling of toroidal domains but also the relaxation behavior.

The idea behind the recent and subsequently discussed experiment was to utilize Ampère's circuital law for switching the toroidal moment. Considering this Maxwell equation, the curl of the magnetic field is determined by $\mu_0 \left(\mathbf{j} + \epsilon_0 \frac{\mathrm{d}E}{\mathrm{d}t}\right)$, whereby in insulating materials $\epsilon_0 \frac{\mathrm{d}E}{\mathrm{d}t}$ can replace the current density $\mathbf{j}$ to generate a finite curl of the magnetic field. Hence, driving the applied electric field fast and continuously between both polarities can produce the conjugate field that is needed to invert the toroidal moment. The desirable advantage of this method is that it allows for in-situ studies of toroidal switching using spherical neutron polarimetry as it does not necessitate the simultaneous application of a crossed magnetic field.

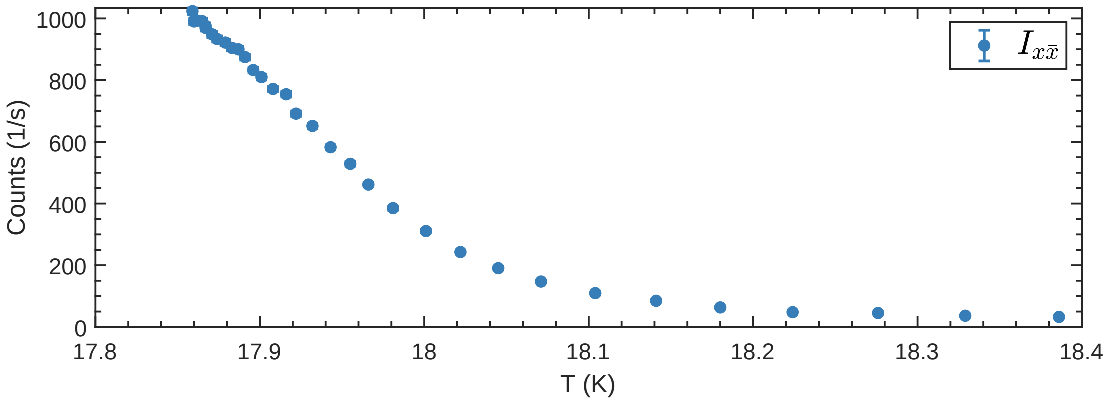

Figure A.1.: The measured intensity at $\mathbf{Q} = (3\,0\,0)$ for the spin-flip channel $I_{x\bar{x}}$ is displayed as a function of temperature. No field was applied and the data was recorded while cooling the system. Each data point was measured 10 s to obtain good statistic and in particular temperature stability for each step in temperature.

For respective measurements a single sample of $\mathrm{LiFeSi_2O_6}$ was prepared and mounted between two aluminum electrodes, whose plate normals were oriented parallel to the b direction and thus along the toroidal moment. It has to be noted that it is the same sample that was used for measurements presented in Ref. [24]. The whole sample holder was installed in $(1\,0\,0)/(0\,1\,0)$ scattering geometry to measure the $\mathbf{Q} = (3\,0\,0)$ reflection equivalent to the experiment executed by Baum *et al.* [24]. The distance between both plates amounted approximately to $d \approx 1.8215\,\mathrm{mm}$. With equivalent arguments that are described in Ref. [24], the inversion of the toroidal moment is indicated by a sign change of the off-diagonal components P_{xy} and P_{yx}. The time-resolved experiment (proposal CRG-2623 [180]) was conducted at the IN12 triple axis spectrometer at the ILL and for the determination of off-diagonal elements of the polarization matrix $\mathbf{P}$, spherical neutron polarimetry was utilized by deploying a CRYOPAD system. The neutron beam was initially polarized by a supermirror cavity and the pyrolytic graphite $(0\,0\,2)$ monochromator filtered neutrons with $\lambda = 3.49\,\text{Å}$. For the application of time-varying electric fields, the sample holder was connected to the time-resolved high-voltage setup described in Ref. [49] and section 2.4. However, in contrast to former described time-resolved experiments, the fast high-voltage switch for rectangular shaped field inversion was replaced by a Trek Model 609E-6 high voltage amplifier to drive the field linearly from peak to peak thus forming a triangular shaped field inversion. At each maximum and minimum position of the field inversion, the derivative $\mathrm{d}E/\mathrm{d}t$ changes its sign, which thus inverts the toroidal field orientation. The flipping ratio was measured at $\mathbf{Q} = (4\,0\,0)$ and amounted to $\mathrm{FR} \approx 20$.

A.4. Time-resolved measurements

Previous measurements on the same sample (see Ref. [24]) revealed the transition temperature $T_\mathrm{N} = 18.1\,\mathrm{K}$, which is slightly different to other reported values [250–253]. As also a different temperature sensor calibration could cause different observed transition temperatures and as the subsequently discussed measurements close to the phase transition required the exact knowledge of its value, a determination of T_N during the experimental course was necessary. For this purpose, the spin-flip channel $I_{x\bar{x}}$ was recorded as a function of temperature at $\mathbf{Q} = (3\,0\,0)$ because here $I_{x\bar{x}}$ senses the perpendicular component of the magnetization and thus, for the given scattering geometry, the development of magnetic long-range ordering in $\mathrm{LiFeSi_2O_6}$. In Fig. A.1 the respective measured temperature dependence of this channel is plotted and it can be seen that the observed phase transition temperature amounts approximately to $T_\mathrm{N} \approx 18.2\,\mathrm{K}$.

The time-resolved measurements of the off-diagonal term P_{xy}, whose sign senses the orientation of the toroidization, were also done at $\mathbf{Q} = (3\,0\,0)$, while periodically driving the applied high voltage with a triangular shape between $\pm 4\,\mathrm{kV}$. It holds that higher switching frequencies result in much higher values for $\mathrm{d}E/\mathrm{d}t$ and thus stronger toroidal fields, but it also entails that the system has less time for complete relaxation. Thus, for very fast switching and in spite of resulting larger toroidal fields, the induced alteration of the toroidal domain distribution is potentially not large enough to be observable with reasonable statistic. Hence, several combinations of field strengths and temperatures were tested during the experimental course, for which the measured switching curves are presented in Fig. A.2. As mentioned in section A.3 the finite field derivative replaces the current density in an insulator, but its equivalent value j is nevertheless displayed for each switching curve in Fig. A.2.

Most of the switching curves were recorded at higher temperature close to the transition temperature as it is naturally expected that domain pinning is weaker close to the transition, which enables easier domain inversion with less field. However, measurements close to T_N suffer from less intensity and thus from poor statistics. It can be seen in Fig. A.2 that none of the measured switching curves reveal a sign change of P_{xy} or at least a finite alteration of its absolute value with respect to the time after the field inversion. Even a reduction of the binning, which leads to better statistics does not bare a very small but finite value for dP_{xy}/dt after field inversion. The observed average value of P_{xy} amounts approximately to -0.04 and its absolute value is thus less than the predicted value for a toroidal monodomain (see equation A.1) [24].

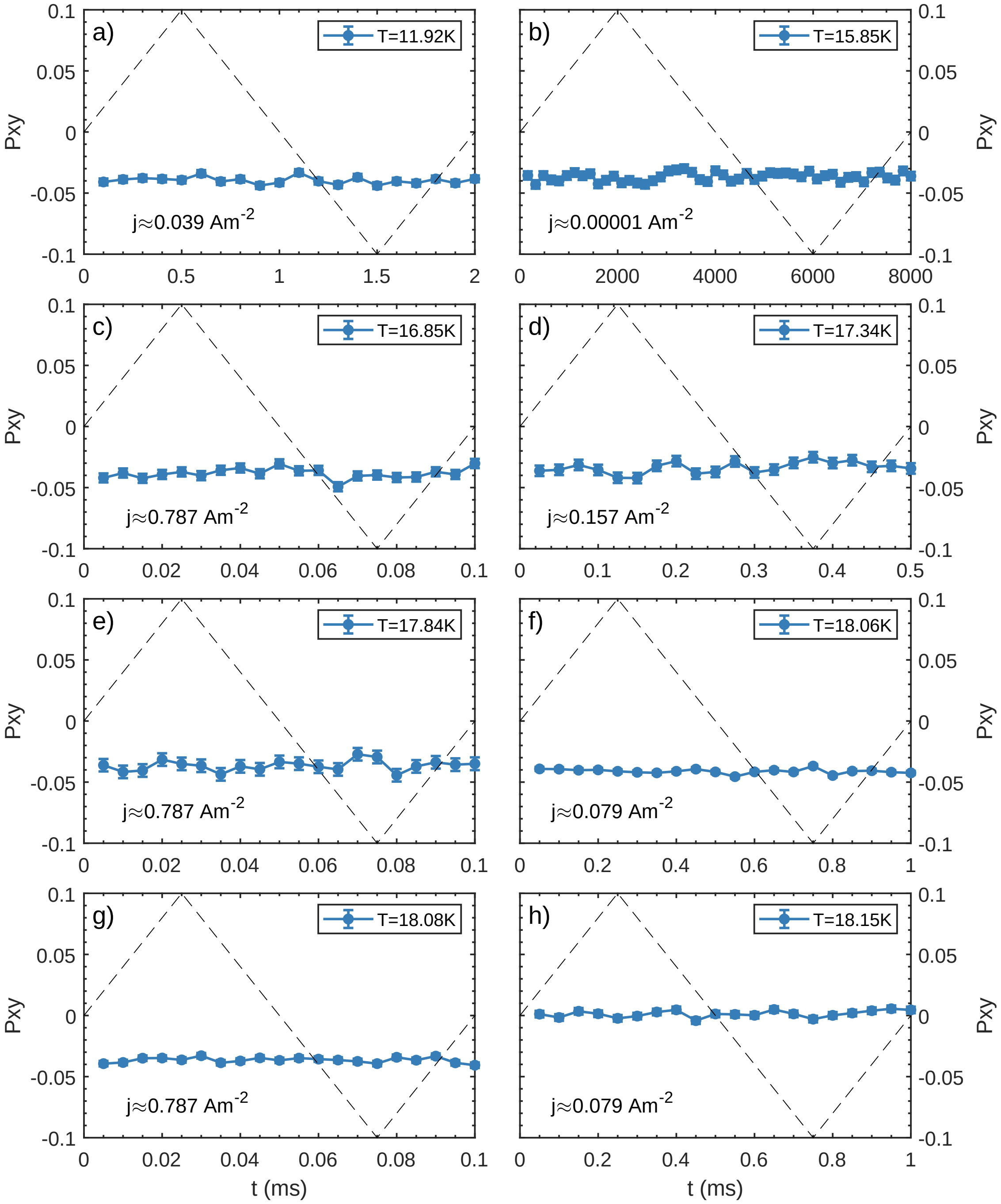

Figure A.2.: All six panels a)-h) display recorded time-resolved switching curves for different temperatures and switching frequencies. The data in blue correspond to the measured $P_{xy} = (I_{xy} - I_{x\bar{y}})/(I_{xy} - I_{x\bar{y}})$ channel and the black dashed line visualizes the triangular waveform of the time-dependent electric field. All shown data sets were recorded, while driving the applied high voltage between $\pm 4\,\mathrm{kV}$. At each peak maxima and minima the field derivative changes its sign, wherefore the toroidal field is inverted at that time. It has to be noted that in this insulator, the field derivative replaces the current density j in Ampère's circuital law. However, its equivalent value is shown in each panel.

Moreover the absolute value is also slightly smaller compared to the respective measured value [24] after crossed field poling and vanishes above T_N. However, it is known that a finite value of P_{xy} only appears, when entering the toroidal phase and when toroidal domains of opposite orientation are not equally distributed [24]. Hence, from the data in Fig. A.2 it can be concluded that the system is already partially poled inside the toroidal phase, but no domain inversion was triggered by the applied toroidal field strength as a function of time.

It appears obvious that the toroidal field is even close to the transition too small to trigger a domain imbalance in reasonable time before a subsequent field inversion restores the initial state. As already mentioned, stronger toroidal fields are here provoked by larger values for $\epsilon_0 \frac{\mathrm{d}E}{\mathrm{d}t}$ and thus faster switching processes which is counterproductive for potentially slower relaxation of toroidal domains.

It has to be noted that the largest value of $\epsilon_0 \frac{\mathrm{d}E}{\mathrm{d}t}$ is equivalent to a current density of about $0.787\,\mathrm{A\,m^{-2}}$ and considering the sample surface $A \approx 11\,\mathrm{mm} \times 9\,\mathrm{mm}$, whose normal is parallel to the toroidal field, it thus refers to very small current values of the order of only several microamperes. It is obvious that the direct application of a current would enable a much higher magnitude but however this is hindered by the absence of finite conductivity in the toroidal phase of insulating $\mathrm{LiFeSi_2O_6}$.

A.5. Conclusion

A first approach for time-resolved measurements of toroidal domain switching utilizing spherical neutron polarimetry was presented in this chapter. It was assumed that a finite electric-field derivative replaces the current density in insulators to induce a finite curl of a magnetic field. Such a time-varying field was applied parallel to *b*-direction to produce a toroidal field that couples to the toroidal order in $\mathrm{LiFeSi_2O_6}$. Unfortunately, it was not possible to observe any change of the toroidal domain distribution, while inverting the field derivative an thus the toroidal field periodically. Even close to the phase transition, where less pinning is expected, no sign change or variation of toroidal ordering was detected. As discussed, it seems likely that the applied toroidal-field strength is too weak and the referring switching frequency too fast to resolve domain inversion in this system.

Nevertheless, for future investigations of toroidal domain dynamics it is recommendable to study further toroidal phases of different systems utilizing the finite electric-field derivative for producing the toroidal field. In spite of the small toroidal-field strength that can be obtained by time varying electric fields, potentially smaller coercive fields in other systems could promote domain inversion with less field strength and reasonable relaxation time. However, most promising for future studies of toroidal relaxation behavior is the investigation of systems exhibiting finite conductivity in their toroidal phase, as it would allow for the direct application of currents. It is much easier to generate several order of magnitude higher current densities compared to the value that was replaced by $\epsilon_0 \frac{\mathrm{d}E}{\mathrm{d}t}$ in the insulator $LiFeSi_2O_6$ to generate the finite curl of the magnetic field.

Another promising project in the context of ferrotoroidal domain dynamics would be the utilization of the Larmor diffraction technique (see chapter 9). The advantage is here that the observation of the toroidal domain dynamics does not necessitate spherical polarization analysis but rather the investigation of the decaying beam polarization. This naturally entails much higher intensity at the detector and thus significantly improved statistic in reasonable beamtime. A more detailed description of the experimental procedure is found in chapter 9. A significantly improved statistic would then allow for sensing even very small variations of the ferrotoroidal domain distributions close to the transition temperature. In this context, it must be remembered that the respective investigations close to the phase transition via spherical neutron polarimetry were hindered by the lack of intensity for sufficient statistic in finite beamtime. Thus, the Larmor diffraction technique can support the measurements of potential ferrotoroidal domain size variations close to the transition temperature. However, it must be kept in mind that Larmor diffraction is highly affected by the generation of additional beam polarization due to respective SF-scattering processes. In particular, nuclear-magnetic interference effects will here significantly perturb the measured signal, which necessitate a careful analysis, respectively an accurate correction. Nevertheless, it seems promising to utilize the Larmor diffraction technique for the time-resolved observation of varying ferrotoroidal domain sizes.

B. Spin-flip and non-spin-flip channels

	nuclear	magnetic	chiral magn.	nucl. magn.
$xx =$	NN^*			
$x\bar{x} =$		$\mathbf{M}_\perp \mathbf{M}_\perp^*$	$-\ i\,(\mathbf{M}_\perp \times \mathbf{M}_\perp^*)_\mathbf{x}$	
$\bar{x}x =$		$\mathbf{M}_\perp \mathbf{M}_\perp^*$	$+\ i\,(\mathbf{M}_\perp \times \mathbf{M}_\perp^*)_\mathbf{x}$	
$xx =$	NN^*			
$yy =$	NN^*	$+\ M_y M_y^*$		$+2\,\mathrm{Re}(M_y^* N)$
$y\bar{y} =$		$M_z M_z^*$		
$\bar{y}y =$		$M_z M_z^*$		
$\bar{y}\bar{y} =$	NN^*	$+\ M_y M_y^*$		$-\,2\,\mathrm{Re}(M_y^* N)$
$zz =$	NN^*	$+\ M_z M_z^*$		$+2\,\mathrm{Re}(M_z^* N)$
$z\bar{z} =$		$M_y M_y^*$		
$\bar{z}z =$		$M_y M_y^*$		
$\bar{z}\bar{z} =$	NN^*	$+\ M_z M_z^*$		$-\,2\,\mathrm{Re}(M_z^* N)$
$2xy = 2y\bar{x} =$	NN^*	$+\mathbf{M}_\perp \mathbf{M}_\perp^*$	$-\ i\,(\mathbf{M}_\perp \times \mathbf{M}_\perp^*)_\mathbf{x}$	$+2\,\mathrm{Re}(M_y^* N) + 2\,\mathrm{Im}(M_z^* N)$
$2x\bar{y} = 2\bar{y}\bar{x} =$	NN^*	$+\mathbf{M}_\perp \mathbf{M}_\perp^*$	$-\ i\,(\mathbf{M}_\perp \times \mathbf{M}_\perp^*)_\mathbf{x}$	$-\,2\,\mathrm{Re}(M_y^* N) -\,2\,\mathrm{Im}(M_z^* N)$
$2\bar{x}y = 2yx =$	NN^*	$+\mathbf{M}_\perp \mathbf{M}_\perp^*$	$+\ i\,(\mathbf{M}_\perp \times \mathbf{M}_\perp^*)_\mathbf{x}$	$+2\,\mathrm{Re}(M_y^* N) -\,2\,\mathrm{Im}(M_z^* N)$
$2\bar{x}\bar{y} = 2\bar{y}x =$	NN^*	$+\mathbf{M}_\perp \mathbf{M}_\perp^*$	$+\ i\,(\mathbf{M}_\perp \times \mathbf{M}_\perp^*)_\mathbf{x}$	$-\,2\,\mathrm{Re}(M_y^* N) + 2\,\mathrm{Im}(M_z^* N)$
$2xz = 2z\bar{x} =$	NN^*	$+\mathbf{M}_\perp \mathbf{M}_\perp^*$	$-\ i\,(\mathbf{M}_\perp \times \mathbf{M}_\perp^*)_\mathbf{x}$	$+2\,\mathrm{Re}(M_z^* N) -\,2\,\mathrm{Im}(M_y^* N)$
$2x\bar{z} = 2\bar{z}\bar{x} =$	NN^*	$+\mathbf{M}_\perp \mathbf{M}_\perp^*$	$-\ i\,(\mathbf{M}_\perp \times \mathbf{M}_\perp^*)_\mathbf{x}$	$-\,2\,\mathrm{Re}(M_z^* N) + 2\,\mathrm{Im}(M_y^* N)$
$2\bar{x}z = 2zx =$	NN^*	$+\mathbf{M}_\perp \mathbf{M}_\perp^*$	$+\ i\,(\mathbf{M}_\perp \times \mathbf{M}_\perp^*)_\mathbf{x}$	$+2\,\mathrm{Re}(M_z^* N) + 2\,\mathrm{Im}(M_y^* N)$
$2\bar{x}\bar{z} = 2\bar{z}x =$	NN^*	$+\mathbf{M}_\perp \mathbf{M}_\perp^*$	$+\ i\,(\mathbf{M}_\perp \times \mathbf{M}_\perp^*)_\mathbf{x}$	$-\,2\,\mathrm{Re}(M_z^* N) -\,2\,\mathrm{Im}(M_y^* N)$
$2yz = 2zy =$	NN^*	$+\mathbf{M}_\perp \mathbf{M}_\perp^* + 2\,\mathrm{Re}(M_y M_z^*)$		$+2\,\mathrm{Re}(M_y^* N) + 2\,\mathrm{Im}(M_z^* N)$
$2y\bar{z} = 2\bar{z}y =$	NN^*	$+\mathbf{M}_\perp \mathbf{M}_\perp^* -\,2\,\mathrm{Re}(M_y M_z^*)$		$+2\,\mathrm{Re}(M_y^* N) -\,2\,\mathrm{Im}(M_z^* N)$
$2\bar{y}z = 2z\bar{y} =$	NN^*	$+\mathbf{M}_\perp \mathbf{M}_\perp^* -\,2\,\mathrm{Re}(M_y M_z^*)$		$-\,2\,\mathrm{Re}(M_y^* N) + 2\,\mathrm{Im}(M_z^* N)$
$2\bar{y}\bar{z} = 2\bar{z}\bar{y} =$	NN^*	$+\mathbf{M}_\perp \mathbf{M}_\perp^* + 2\,\mathrm{Re}(M_y M_z^*)$		$-\,2\,\mathrm{Re}(M_y^* N) -\,2\,\mathrm{Im}(M_z^* N)$

Table B.1.: This table lists all 36 spin-flip and non-spin-flip channels, which can be derived from the Blume-Maleev equations [82, 83]. An equivalent presentation is given in [182] and [255].

List of Figures

List of Tables

Bibliography

[1] S. Biesenkamp, N. Qureshi, Y. Sidis, P. Becker, L. Bohatý & M. Braden: Structural dimerization in the commensurate magnetic phases of $NaFe(WO_4)_2$ and $MnWO_4$, *Phys. Rev. B* **102**, 144429 (2020)

[2] S. Biesenkamp, D. Gorkov, D. Brüning, A. Bertin, T. Fröhlich, X. Fabrèges, A. Gukasov, M. Meven, P. Becker, L. Bohatý, T. Lorenz & M. Braden: Single-crystal investigations on the multiferroic material $LiFe(WO_4)_2$, *Phys. Rev. B* **103**, 134412 (2021)

[3] S. Biesenkamp, D. Gorkov, W. Schmidt, K. Schmalzl, Y. Sidis, P. Becker, L. Bohatý & M. Braden: Chiral order and multiferroic domain relaxation in $NaFeGe_2O_6$, *Phys. Rev. B* **104**, 174405 (2021)

[4] W. C. Röntgen: Ueber die durch Bewegung eines im homogenen electrischen Felde befindlichen Dielectricums hervorgerufene electrodynamische Kraft, *Annalen der Physik* **271**, 264 (1888)

[5] H. A. Wilson & J. J. Thomson: On the electric effect of rotating a dielectric in a magnetic field, *Proceedings of the Royal Society of London* **73**, 490 (1904)

[6] P. Debye: Bemerkung zu einigen neuen Versuchen über einen magneto-elektrischen Richteffekt, *Zeitschrift für Physik* **36**, 300 (1926)

[7] P. Curie: Sur la symétrie dans les phénomènes physiques, symétrie d'un champ électrique et d'un champ magnétique, *J. Phys. Theor. Appl.* **3**, 393 (1894)

[8] L. Landau, E. Lifshitz & L. Pitaevskii: Electrodynamics of continuous media, course of theoretical physics (1960)

[9] A. V. Šubnikov: Symmetry and Antisymmetry of Finite Figures, *U.S.S.R. Academy of Sciences, Moscow* (1951)

[10] E. Ascher *et al.*: Kineto-electric and kinetomagnetic effects in crystals, *Int. J. Magn* **5**, 287 (1974)

[11] H. Schmid: Some symmetry aspects of ferroics and single phase multiferroics*, *Journal of Physics: Condensed Matter* **20**, 434201 (2008)

[12] S. L. Hou & N. Bloembergen: Paramagnetoelectric Effects in $NiSO_4 \cdot 6H_2O$, *Phys. Rev.* **138**, A1218 (1965)

[13] T. H. O'Dell: An induced magneto-electric effect in yttrium iron garnet, *The Philosophical Magazine: A Journal of Theoretical Experimental and Applied Physics* **16**, 487 (1967)

[14] E. Ascher: Higher-order magneto-electric effects, *The Philosophical Magazine: A Journal of Theoretical Experimental and Applied Physics* **17**, 149 (1968)

[15] G. T. Rado & J. M. Ferrari: Linear and bilinear magnetoelectric effects in magnetically biased magnetite (Fe_3O_4), *Phys. Rev. B* **15**, 290 (1977)

[16] I. E. Dzyaloshinskii: On the magneto-electrical effects in antiferromagnets, *Sov. Phys. JETP* **10**, 628 (1960)

[17] D. N. Astrov: Magnetoelectric effect in chromium oxide, *Sov. Phys. JETP* **13**, 729 (1961)

[18] V. E. Wood & A. E. Austin: Possible applications for magnetoelectric materials, *Int. J. Magn.* **5**, 303–315 (1974)

[19] M. Fiebig: Revival of the magnetoelectric effect, *Journal of Physics D: Applied Physics* **38**, R123 (2005)

[20] G. A. Gehring: On the microscopic theory of the magnetoelectric effect, *Ferroelectrics* **161**, 275 (1994)

[21] W. F. Brown, R. M. Hornreich & S. Shtrikman: Upper Bound on the Magnetoelectric Susceptibility, *Phys. Rev.* **168**, 574 (1968)

[22] K. Aizu: Possible Species of “Ferroelastic” Crystals and of Simultaneously Ferroelectric and Ferroelastic Crystals, *Journal of the Physical Society of Japan* **27**, 387 (1969)

[23] K. Aizu: Possible Species of Ferromagnetic, Ferroelectric, and Ferroelastic Crystals, *Phys. Rev. B* **2**, 754 (1970)

[24] M. Baum, K. Schmalzl, P. Steffens, A. Hiess, L. P. Regnault, M. Meven, P. Becker, L. Bohatý & M. Braden: Controlling toroidal moments by crossed electric and magnetic fields, *Phys. Rev. B* **88**, 024414 (2013)

[25] H. Schmid: Multi-ferroic magnetoelectrics, *Ferroelectrics* **162**, 317 (1994)

[26] D. Khomskii: Classifying multiferroics: Mechanisms and effects, *Physics* **2**, 20 (2009)

[27] J. Goodenough & J. Longo: Landolt–Bornstein, Group III, in *Magnetic and other properties of oxides and related compounds*, vol. 4, Springer-Verlag New York (1970)

[28] T. Mitsui: Ferroelectric and related substances, *Landolt-Bornstein, Series* **16**, 99 (1982)

[29] B. T. Matthias: New Ferroelectric Crystals, *Phys. Rev.* **75**, 1771 (1949)

[30] R. E. Cohen: Origin of ferroelectricity in perovskite oxides, *Nature* **358**, 136 (1992)

[31] N. A. Hill: Why Are There so Few Magnetic Ferroelectrics?, *The Journal of Physical Chemistry B* **104**, 6694 (2000)

[32] G. A. Smolenskii, V. A. Isupov & A. I. Agranovskaya: A new group of ferroelectrics-(with layered structure), *Soviet Physics-Solid State* **1**, 149 (1959)

[33] G. A. Smolenskii, V. A. Isupov, N. N. Krainik & A. I. Agranovskaya: Concerning

the coexistence of the ferroelectric and ferrimagnetic states, *Izv. Akad. Nauk SSSR, Ser. Fiz* **25**, 1 (1961)

[34] J. B. Neaton, C. Ederer, U. V. Waghmare, N. A. Spaldin & K. M. Rabe: First-principles study of spontaneous polarization in multiferroic $BiFeO_3$, *Phys. Rev. B* **71**, 014113 (2005)

[35] P. Ravindran, R. Vidya, A. Kjekshus, H. Fjellvåg & O. Eriksson: Theoretical investigation of magnetoelectric behavior in $BiFeO_3$, *Phys. Rev. B* **74**, 224412 (2006)

[36] J. R. Teague, R. Gerson & W. James: Dielectric hysteresis in single crystal $BiFeO_3$, *Solid State Communications* **8**, 1073 (1970)

[37] D. C. Arnold, K. S. Knight, F. D. Morrison & P. Lightfoot: Ferroelectric-Paraelectric Transition in $BiFeO_3$: Crystal Structure of the Orthorhombic β Phase, *Phys. Rev. Lett.* **102**, 027602 (2009)

[38] J. Wang, J. B. Neaton, H. Zheng, V. Nagarajan, S. B. Ogale, B. Liu, D. Viehland, V. Vaithyanathan, D. G. Schlom, U. V. Waghmare, N. A. Spaldin, K. M. Rabe, M. Wuttig & R. Ramesh: Epitaxial $BiFeO_3$ Multiferroic Thin Film Heterostructures, *Science* **299**, 1719 (2003)

[39] D. Lebeugle, D. Colson, A. Forget, M. Viret, P. Bonville, J. F. Marucco & S. Fusil: Room-temperature coexistence of large electric polarization and magnetic order in $BiFeO_3$ single crystals, *Phys. Rev. B* **76**, 024116 (2007)

[40] D. Khomskii: Multiferroics: Different ways to combine magnetism and ferroelectricity, *Journal of Magnetism and Magnetic Materials* **306**, 1 (2006)

[41] M. Fiebig, T. Lottermoser, D. Meier & M. Trassin: The evolution of multiferroics, *Nature Reviews Materials* **1**, 16046 (2016)

[42] T. Kimura, T. Goto, H. Shintani, K. Ishizaka, T. Arima & Y. Tokura: Magnetic control of ferroelectric polarization, *Nature* **426**, 55 (2003)

[43] P. Wang, X. Lu, X. Gong & H. Xiang: Microscopic mechanism of spin-order induced improper ferroelectric polarization, *Computational Materials Science* **112**, 448 (2016)

[44] I. E. Dzyaloshinskii: A thermodynamic theory of "weak" ferromagnetism of antiferromagnetics, *J. Phys. Chem. Solids* **4**, 241 (1958)

[45] T. Moriya: Anisotropic Superexchange Interaction and Weak Ferromagnetism, *Phys. Rev.* **120**, 91 (1960)

[46] M. Mostovoy: Ferroelectricity in Spiral Magnets, *Phys. Rev. Lett.* **96**, 067601 (2006)

[47] J. Stein, M. Baum, S. Holbein, T. Cronert, V. Hutanu, A. C. Komarek & M. Braden: Control of multiferroic domains by external electric fields in $TbMnO_3$, *Journal of Physics: Condensed Matter* **27**, 446001 (2015)

[48] M. Kenzelmann, A. B. Harris, S. Jonas, C. Broholm, J. Schefer, S. B. Kim, C. L. Zhang, S.-W. Cheong, O. P. Vajk & J. W. Lynn: Magnetic Inversion Symmetry Breaking and Ferroelectricity in $TbMnO_3$, *Phys. Rev. Lett.* **95**, 087206 (2005)

[49] J. Stein, S. Biesenkamp, T. Cronert, T. Fröhlich, J. Leist, K. Schmalzl, A. C. Komarek & M. Braden: Combined Arrhenius-Merz Law Describing Domain Relaxation in Type-II Multiferroics, *Phys. Rev. Lett.* **127**, 097601 (2021)

[50] H. Katsura, N. Nagaosa & A. V. Balatsky: Spin Current and Magnetoelectric Effect in Noncollinear Magnets, *Phys. Rev. Lett.* **95**, 057205 (2005)

[51] T. Arima: Ferroelectricity Induced by Proper-Screw Type Magnetic Order, *Journal of the Physical Society of Japan* **76**, 073702 (2007)

[52] H. Murakawa, Y. Onose, S. Miyahara, N. Furukawa & Y. Tokura: Ferroelectricity Induced by Spin-Dependent Metal-Ligand Hybridization in $Ba_2CoGe_2O_7$, *Phys. Rev. Lett.* **105**, 137202 (2010)

[53] I. A. Sergienko, C. Şen & E. Dagotto: Ferroelectricity in the Magnetic E-Phase of Orthorhombic Perovskites, *Phys. Rev. Lett.* **97**, 227204 (2006)

[54] J. B. Goodenough: Theory of the Role of Covalence in the Perovskite-Type Manganites $[\mathrm{La}, M(\mathrm{II})]\mathrm{MnO}_3$, *Phys. Rev.* **100**, 564 (1955)

[55] J. B. Goodenough: An interpretation of the magnetic properties of the perovskite-type mixed crystals $\mathrm{La}_{1-x}\mathrm{Sr}_x\mathrm{CoO}_{3-\lambda}$, *Journal of Physics and Chemistry of Solids* **6**, 287 (1958)

[56] J. Kanamori: Superexchange interaction and symmetry properties of electron orbitals, *Journal of Physics and Chemistry of Solids* **10**, 87 (1959)

[57] J. F. Scott: *Ferroelectric Memories*, Advanced microelectronics, Springer (2000)

[58] W. J. Merz: Domain Formation and Domain Wall Motions in Ferroelectric $BaTiO_3$ Single Crystals, *Phys. Rev.* **95**, 690 (1954)

[59] M. Hayashi: Kinetics of Domain Wall Motion in Ferroelectric Switching. I. General Formulation, *Journal of the Physical Society of Japan* **33**, 616 (1972)

[60] M. E. Lines & A. M. Glass: *Principles and applications of ferroelectrics and related materials*, Oxford University Press, New York (1977)

[61] H. Orihara & Y. Ishibashi: Switching Characteristics of Ferroelectric Liquid Crystal DOBAMBC (II)–Temperature Dependence and Scaling Rule–, *Japanese Journal of Applied Physics* **24**, 902 (1985)

[62] J. F. Scott, L. Kammerdiner, M. Parris, S. Traynor, V. Ottenbacher, A. Shawabkeh & W. F. Oliver: Switching kinetics of lead zirconate titanate submicron thin-film memories, *Journal of Applied Physics* **64**, 787 (1988)

[63] Y. Ishibashi & Y. Takagi: Note on Ferroelectric Domain Switching, *Journal of the Physical Society of Japan* **31**, 506 (1971)

[64] Y. Ishibashi: Polarization Reversal Kinetics in Ferroelectric Liquid Crystals, *Japanese Journal of Applied Physics* **24**, 126 (1985)

[65] Y. Ishibashi: A Model of Polarization Reversal in Ferroelectrics, *Journal of the Physical Society of Japan* **59**, 4148 (1990)

[66] M. Avrami: Kinetics of Phase Change. I General Theory, *The Journal of Chemical Physics* **7**, 1103 (1939)

[67] M. Avrami: Kinetics of Phase Change. II Transformation-Time Relations for Random Distribution of Nuclei, *The Journal of Chemical Physics* **8**, 212 (1940)

[68] M. Avrami: Granulation, Phase Change, and Microstructure Kinetics of Phase Change. III, *The Journal of Chemical Physics* **9**, 177 (1941)

[69] T. Hoffmann, P. Thielen, P. Becker, L. Bohatý & M. Fiebig: Time-resolved imaging of magnetoelectric switching in multiferroic $MnWO_4$, *Phys. Rev. B* **84**, 184404 (2011)

[70] M. Baum, J. Leist, T. Finger, K. Schmalzl, A. Hiess, L. P. Regnault, P. Becker, L. Bohatý, G. Eckold & M. Braden: Kinetics of the multiferroic switching in $MnWO_4$, *Phys. Rev. B* **89**, 144406 (2014)

[71] D. Niermann, C. P. Grams, M. Schalenbach, P. Becker, L. Bohatý, J. Stein, M. Braden & J. Hemberger: Domain dynamics in the multiferroic phase of $MnWO_4$, *Phys. Rev. B* **89**, 134412 (2014)

[72] J. Brooke, T. F. Rosenbaum & G. Aeppli: Tunable quantum tunnelling of magnetic domain walls, *Nature* **413**, 610 (2001)

[73] O. G. Shpyrko, E. D. Isaacs, J. M. Logan, Y. Feng, G. Aeppli, R. Jaramillo, H. C. Kim, T. F. Rosenbaum, P. Zschack, M. Sprung, S. Narayanan & A. R. Sandy: Direct measurement of antiferromagnetic domain fluctuations, *Nature* **447**, 68 (2007)

[74] F. Kagawa, N. Minami, S. Horiuchi & Y. Tokura: Athermal domain-wall creep near a ferroelectric quantum critical point, *The Journal of Chemical Physics* **7**, 10675 (2016)

[75] J. Chadwick: The existence of a neutron, *Proceedings of the Royal Society of London. Series A, Containing Papers of a Mathematical and Physical Character* **136**, 692 (1932)

[76] B. Willis, B. Willis & C. Carlile: *Experimental Neutron Scattering*, Oxford University Press (2013)

[77] G. Shirane, S. Shapiro & J. Tranquada: *Neutron Scattering with a Triple-Axis Spectrometer: Basic Techniques*, Cambridge University Press (2002)

[78] G. L. Squires: *Introduction to the theory of thermal neutron scattering*, Cambridge University Press (2012)

[79] D. S. Sivia: *Elementary scattering theory: for X-ray and neutron users*, Oxford University Press (2011)

[80] T. Chatterji: *Neutron Scattering from Magnetic Materials*, Elsevier Science (2005)

[81] A.-J. Dianoux & G. Lander: *Neutron data booklet*, Published by licence under the OCP Science imprint. Institut Laue-Langevin, BP 156, 38042 Grenoble Cedex 9, France, 2003. (2003)

[82] M. Blume: Polarization Effects in the Magnetic Elastic Scattering of Slow Neutrons,

Phys. Rev. **130**, 1670 (1963)

[83] S. V. Maleev, V. G. Bar'yakhtar & R. A. Suris: The scattering of slow neutrons by complex magnetic structures, *Soviet Phys.-Solid State (English Transl.)* **4** (1963)

[84] R. M. Moon, T. Riste & W. C. Koehler: Polarization Analysis of Thermal-Neutron Scattering, *Phys. Rev.* **181**, 920 (1969)

[85] F. Tasset: Zero field neutron polarimetry, *Physica B: Condensed Matter* **156-157**, 627 (1989)

[86] E. Lelièvre-Berna, E. Bourgeat-Lami, P. Fouilloux, B. Geffray, Y. Gibert, K. Kakurai, N. Kernavanois, B. Longuet, F. Mantegezza, M. Nakamura, S. Pujol, L.-P. Regnault, F. Tasset, M. Takeda, M. Thomas & X. Tonon: Advances in spherical neutron polarimetry with Cryopad, *Physica B: Condensed Matter* **356**, 131 (2005), proceedings of the Fifth International Workshop on Polarised Neutrons in Condensed Matter Investigations

[87] M. Janoschek, S. Klimko, R. Gähler, B. Roessli & P. Böni: Spherical neutron polarimetry with MuPAD, *Physica B: Condensed Matter* **397**, 125 (2007)

[88] G. Eckold: Time-resolved triple-axis spectroscopy — A new method for real-time neutron scattering, *Nuclear Instruments and Methods in Physics Research Section A: Accelerators, Spectrometers, Detectors and Associated Equipment* **289**, 221 (1990)

[89] J. Stein, Ph.D. thesis (in preparation).

[90] J. A. Alonso, M. J. Martínez-Lope, M. T. Casais & M. T. Fernández-Díaz: Evolution of the Jahn-Teller Distortion of MnO_6 Octahedra in $R$$MnO_3$ Perovskites (R = Pr, Nd, Dy, Tb, Ho, Er, Y): A Neutron Diffraction Study, *Inorganic Chemistry* **39**, 917 (2000)

[91] H. Weitzel: Kristallstrukturverfeinerung von Wolframiten und Columbiten, *Zeitschrift für Kristallographie - Crystalline Materials* **144**, 238 (1976)

[92] G. Lautenschläger, H. Weitzel, T. Vogt, R. Hock, A. Böhm, M. Bonnet & H. Fuess: Magnetic phase transitions of $MnWO_4$ studied by the use of neutron diffraction, *Phys. Rev. B* **48**, 6087 (1993)

[93] O. Prokhnenko, R. Feyerherm, M. Mostovoy, N. Aliouane, E. Dudzik, A. U. B. Wolter, A. Maljuk & D. N. Argyriou: Coupling of Frustrated Ising Spins to the Magnetic Cycloid in Multiferroic $TbMnO_3$, *Phys. Rev. Lett.* **99**, 177206 (2007)

[94] H. Ehrenberg, H. Weitzel, C. Heid, H. Fuess, G. Wltschek, T. Kroener, J. van Tol & M. Bonnet: Magnetic phase diagrams of $MnWO_4$, *J. Phys.: Condens. Matter* **9**, 3189 (1997)

[95] A. H. Arkenbout, T. T. M. Palstra, T. Siegrist & T. Kimura: Ferroelectricity in the cycloidal spiral magnetic phase of $MnWO_4$, *Phys. Rev. B* **74**, 184431 (2006)

[96] R. P. Chaudhury, F. Yen, C. R. dela Cruz, B. Lorenz, Y. Q. Wang, Y. Y. Sun & C. W. Chu: Thermal expansion and pressure effect in $MnWO_4$, *Phys. B Condens.*

Matter **403**, 1428 (2008)

[97] T. Finger, D. Senff, K. Schmalzl, W. Schmidt, L. P. Regnault, P. Becker, L. Bohatý & M. Braden: Polarized-neutron-scattering studies on the chiral magnetism in multiferroic $MnWO_4$, *Journal of Physics: Conference Series* **211**, 012001 (2010)

[98] T. Finger, D. Senff, K. Schmalzl, W. Schmidt, L. P. Regnault, P. Becker, L. Bohatý & M. Braden: Electric-field control of the chiral magnetism of multiferroic $MnWO_4$ as seen via polarized neutron diffraction, *Phys. Rev. B - Condens. Matter Mater. Phys.* **81**, 1 (2010)

[99] S. Holbein, M. Ackermann, L. Chapon, P. Steffens, A. Gukasov, A. Sazonov, O. Breunig, Y. Sanders, P. Becker, L. Bohatý, T. Lorenz & M. Braden: Strong magnetoelastic coupling at the transition from harmonic to anharmonic order in $NaFe(WO_4)_2$ with $3d^5$ configuration, *Phys. Rev. B* **94**, 104423 (2016)

[100] M. Braden, G. Wilkendorf, J. Lorenzana, M. Aïn, G. J. McIntyre, M. Behruzi, G. Heger, G. Dhalenne & A. Revcolevschi: Structural analysis of $CuGeO_3$: Relation between nuclear structure and magnetic interaction, *Phys. Rev. B* **54**, 1105 (1996)

[101] Data are available at `https://doi.ill.fr/10.5291/ILL-DATA.5-41-911` and it must be noted that the respective experiment was carried out during the course of the author's master thesis.

[102] Data are available at `https://doi.ill.fr/10.5291/ILL-DATA.5-41-983`.

[103] S. Biesenkamp: *Neutron scattering studies of magnetoelectric materials*, Master thesis, University of Cologne (2018)

[104] M. Liu, L. Lin, Y. Zhang, S. Li, Q. Huang, V. O. Garlea, T. Zou, Y. Xie, Y. Wang, C. Lu, L. Yang, Z. Yan, X. Wang, S. Dong & J.-M. Liu: Cycloidal magnetism driven ferroelectricity in double tungstate $LiFe(WO_4)_2$, *Phys. Rev. B* **95**, 195134 (2017)

[105] P. V. Klevtsov & R. F. Klevtsova: Crystallographic investigation of a double tungstate $LiFe(WO_4)_2$, *Sov. Phys. Crystallogr.* **15**, 294 (1970)

[106] G. Le Flem, R. Salmon & P. Hagenmuller: Sur quelques nouveaux tungstates doubles de structure wolframite, *C. R. Acad. Sci. Paris* **268**, 1431–1434 (1969)

[107] P. Tolédano: Pseudo-proper ferroelectricity and magnetoelectric effects in $TbMnO_3$, *Phys. Rev. B* **79**, 094416 (2009)

[108] P. Tolédano, B. Mettout, W. Schranz & G. Krexner: Directional magnetoelectric effects in $MnWO_4$: magnetic sources of the electric polarization, *Journal of Physics: Condensed Matter* **22**, 065901 (2010)

[109] L. Ding, P. Manuel, D. D. Khalyavin, F. Orlandi & A. A. Tsirlin: Unraveling the complex magnetic structure of multiferroic pyroxene $NaFeGe_2O_6$: A combined experimental and theoretical study, *Phys. Rev. B* **98**, 094416 (2018)

[110] I. Kim, B.-G. Jeon, D. Patil, S. Patil, G. Nénert & K. H. Kim: Observation of multiferroic properties in pyroxene $NaFeGe_2O_6$, *Journal of Physics: Condensed*

Matter **24**, 306001 (2012)

[111] T. V. Drokina, G. A. Petrakovskii, L. Keller, J. Schefer, A. D. Balaev, A. V. Kartashev & D. A. Ivanov: Modulated magnetic structure in quasi-one-dimensional clinopyroxene $NaFeGe_2O_6$, *Journal of Experimental and Theoretical Physics* **112**, 121 (2011)

[112] G. J. Redhammer, A. Senyshyn, M. Meven, G. Roth, S. Prinz, A. Pachler, G. Tippelt, C. Pietzonka, W. Treutmann, M. Hoelzel, B. Pedersen & G. Amthauer: Nuclear and incommensurate magnetic structure of $NaFeGe_2O_6$ between 5 K and 298 K and new data on multiferroic $NaFeSi_2O_6$, *Physics and Chemistry of Minerals* **38**, 139 (2011)

[113] M. Ackermann, L. Andersen, T. Lorenz, L. Bohatý & P. Becker: Anisotropy study of multiferroicity in the pyroxene $NaFeGe_2O_6$, *New Journal of Physics* **17**, 013045 (2015)

[114] Data are available at `https://doi.ill.fr/10.5291/ILL-DATA.CRG-2439`.

[115] Data are available at `https://doi.ill.fr/10.5291/ILL-DATA.CRG-2757`. Here, it must be noted that this beamtime was initally allocated for a time-resolved study of domain dynamics in $Ni_3V_2O_8$. As the respective sample broke during the experimental course, the remaining beamtime was used for measurements on $NaFeGe_2O_8$.

[116] M. Ackermann, D. Brüning, T. Lorenz, P. Becker & L. Bohatý: Thermodynamic properties of the new multiferroic material $(NH_4)_2[FeCl_5(H_2O)]$, *New Journal of Physics* **15**, 123001 (2013)

[117] M. Ackermann, T. Lorenz, P. Becker & L. Bohatý: Magnetoelectric properties of $A_2[FeCl_5(H_2O)]$ with A= K, Rb, Cs, *Journal of Physics: Condensed Matter* **26**, 506002 (2014)

[118] I. Lindqvist: *Ark, Kemi. Mineral.* **24**, 1 (1947)

[119] A. Bellanca: *Period. Mineral.* **17**, 59 (1948)

[120] B. N. Figgis, R. C. L. & W. A. H.: *Aust. J. Chem.* **70**, 5161 (1977)

[121] C. J. O'Connor, B. S. Deaver & E. Sinn: Crystal structures of $A_2FeCl_5 \times H_2O$ (A=Rb^+, Cs^+) and field dependent superconducting susceptometer measurements, *The Journal of Chemical Physics* **70**, 5161 (1979)

[122] J. E. Greedan, D. C. Hewitt, R. Faggiani & I. D. Brown: Structure of and hydrogen bonding in dicaesium aquapentachloroferrate(III), *Acta Crystallographica Section B* **36**, 1927 (1980)

[123] A. J. Schultz & R. L. Carlin: Single-crystal pulsed neutron diffraction structure of the antiferromagnet $K_2[FeCl_5(H_2O)]$ with and without applied pressure, *Acta Crystallographica Section B* **51**, 43 (1995)

[124] D. Lacková, I. Ondrejkovičová & M. Koman: A new pathway of preparation and refined structure of $(NH_4)_2[FeCl_5(H_2O)]$, *Acta Chimica Slovaca* **6**, 129 (2013)

[125] M. Gabas, F. Palacio, J. Rodriguez-Carvajal & D. Visser: Magnetic structures of the

three-dimensional Heisenberg antiferromagnets $K_2FeCl_5{\cdot}D_2O$ and $Rb_2FeCl_5{\cdot}D_2O$, *Journal of Physics: Condensed Matter* **7**, 4725 (1995)

[126] J. Campo, J. Luzón, F. Palacio, G. J. McIntyre, A. Millán & A. R. Wildes: Understanding magnetic interactions in the series $A_2FeX_5 \cdot H_2O$ (A = K, Rb; X = Cl, Br). II. Inelastic neutron scattering and DFT studies, *Phys. Rev. B* **78**, 054415 (2008)

[127] J. Luzón, J. Campo, F. Palacio, G. J. McIntyre & A. Millán: Understanding magnetic interactions in the series $A_2FeX_5 \cdot H_2O$ (A = K, Rb; X = Cl, Br). I. Spin densities by polarized neutron diffraction and DFT calculations, *Phys. Rev. B* **78**, 054414 (2008)

[128] J. Alberto Rodríguez-Velamazán, O. Fabelo, A. Millán, J. Campo, R. D. Johnson & L. Chapon: Magnetically-induced ferroelectricity in the $(ND_4)_2[FeCl_5(D_2O)]$ molecular compound, *Scientific Reports* **5**, 14475 (2015)

[129] W. Tian, H. Cao, J. Wang, F. Ye, M. Matsuda, J.-Q. Yan, Y. Liu, V. O. Garlea, H. K. Agrawal, B. C. Chakoumakos, B. C. Sales, R. S. Fishman & J. A. Fernandez-Baca: Spin-lattice coupling mediated multiferroicity in $(ND_4)_2FeCl_5 \cdot D_2O$, *Phys. Rev. B* **94**, 214405 (2016)

[130] J. N. McElearney & S. Merchant: Nonisomorphic antiferromagnetic behavior of two isomorphic salts: low-temperature heat capacities and magnetic susceptibilities of diammonium iron pentachloride monohydrate and dipotassium iron pentachloride monohydrate, *Inorganic Chemistry* **17**, 1207 (1978)

[131] D. Brüning, T. Fröhlich, M. Langenbach, T. Leich, M. Meven, P. Becker, L. Bohatý, M. Grüninger, M. Braden & T. Lorenz: Magnetoelectric coupling in the mixed erythrosiderite $[(NH_4)_{1-x}K_x]_2[FeCl_5(H_2O)]$, *Phys. Rev. B* **102**, 054413 (2020)

[132] W. Tian, H. B. Cao, A. J. Clune, K. D. Hughey, T. Hong, J.-Q. Yan, H. K. Agrawal, J. Singleton, B. C. Sales, R. S. Fishman, J. L. Musfeldt & J. A. Fernandez-Baca: Electronic phase separation and magnetic-field-induced phenomena in molecular multiferroic $(ND_4)_2FeCl_5 \cdot D_2O$, *Phys. Rev. B* **98**, 054407 (2018)

[133] J. A. Rodríguez-Velamazán, O. Fabelo, J. Campo, J. Rodríguez-Carvajal, N. Qureshi & L. C. Chapon: Switching of the Chiral Magnetic Domains in the Hybrid Molecular/Inorganic Multiferroic $(ND_4)_2[FeCl_5(D_2O)]$, *Scientific Reports* **8**, 174439 (2018)

[134] J. A. Rodríguez-Velamazán, O. Fabelo, J. Campo, A. Millán, J. Rodríguez-Carvajal & L. C. Chapon: Magnetic-field-induced change of magnetoelectric coupling in the hybrid multiferroic $(ND_4)_2[FeCl_5(D_2O)]$, *Phys. Rev. B* **95**, 174439 (2017)

[135] Data are available at `https://doi.ill.fr/10.5291/ILL-DATA.CRG-2573`. The proposal CRG-2573 includes both experiments at IN12 and IN3, which were conducted for the investigation of multferroic domain inversion and the temperature dependence of higher harmonics in $(NH_4)_2[FeCl_5\,(H_2O)]$.

[136] D. Meier, N. Leo, M. Maringer, T. Lottermoser, M. Fiebig, P. Becker & L. Bohatý: Topology and manipulation of multiferroic hybrid domains in $MnWO_4$, *Phys. Rev. B*

80, 224420 (2009)

[137] M. Matsubara, S. Manz, M. Mochizuki, T. Kubacka, A. Iyama, N. Aliouane, T. Kimura, S. L. Johnson, D. Meier & M. Fiebig: Magnetoelectric domain control in multiferroic $TbMnO_3$, *Science* **348**, 1112 (2015)

[138] X. Bai, R. S. Fishman, G. Sala, D. M. Pajerowski, V. O. Garlea, T. Hong, M. Lee, J. A. Fernandez-Baca, H. Cao & W. Tian: Magnetic excitations of the hybrid multiferroic $(ND_4)_2[FeCl_5(D_2O)]$, *Phys. Rev. B* **103**, 224411 (2021)

[139] T. Kimura, G. Lawes, T. Goto, Y. Tokura & A. P. Ramirez: Magnetoelectric phase diagrams of orthorhombic RMnO$_3$ (R = Gd, Tb, and Dy), *Phys. Rev. B* **71**, 224425 (2005)

[140] G. Lawes, M. Kenzelmann, N. Rogado, K. H. Kim, G. A. Jorge, R. J. Cava, A. Aharony, O. Entin-Wohlman, A. B. Harris, T. Yildirim, Q. Z. Huang, S. Park, C. Broholm & A. P. Ramirez: Competing Magnetic Phases on a Kagomé Staircase, *Phys. Rev. Lett.* **93**, 247201 (2004)

[141] G. Lawes, A. B. Harris, T. Kimura, N. Rogado, R. J. Cava, A. Aharony, O. Entin-Wohlman, T. Yildirim, M. Kenzelmann, C. Broholm & A. P. Ramirez: Magnetically Driven Ferroelectric Order in $Ni_3V_2O_8$, *Phys. Rev. Lett.* **95**, 087205 (2005)

[142] M. Ain, A. Menelle, B. M. Wanklyn & E. F. Bertaut: Magnetic structure of CuO by neutron diffraction with polarization analysis, *Journal of Physics: Condensed Matter* **4**, 5327 (1992)

[143] T. Kimura, Y. Sekio, H. Nakamura, T. Siegrist & A. P. Ramirez: Cupric oxide as an induced-multiferroic with high-T_C, *Nature Materials* **7**, 291 (2008)

[144] H. Fuess, E. F. Bertaut, R. Pauthenet & A. Durif: Structure aux rayons X, neutrons et propriétés magnétiques des orthovanadates de nickel et de cobalt, *Acta Crystallographica Section B* **26**, 2036 (1970)

[145] E. E. Sauerbrei, R. Faggiani & C. Calvo: Refinement of the crystal structure of $Co_3V_2O_8$ and $Ni_3V_2O_8$, *Acta Crystallographica Section B* **29**, 2304 (1973)

[146] M. Kenzelmann, A. B. Harris, A. Aharony, O. Entin-Wohlman, T. Yildirim, Q. Huang, S. Park, G. Lawes, C. Broholm, N. Rogado, R. J. Cava, K. H. Kim, G. Jorge & A. P. Ramirez: Field dependence of magnetic ordering in Kagomé-staircase compound $Ni_3V_2O_8$, *Phys. Rev. B* **74**, 014429 (2006)

[147] I. Syôzi: Statistics of Kagomé Lattice, *Progress of Theoretical Physics* **6**, 306 (1951)

[148] A. P. Ramirez, G. P. Espinosa & A. S. Cooper: Strong frustration and dilution-enhanced order in a quasi-2D spin glass, *Phys. Rev. Lett.* **64**, 2070 (1990)

[149] D. A. Huse & A. D. Rutenberg: Classical antiferromagnets on the Kagomé lattice, *Phys. Rev. B* **45**, 7536 (1992)

[150] J. T. Chalker, P. C. W. Holdsworth & E. F. Shender: Hidden order in a frustrated system: Properties of the Heisenberg Kagomé antiferromagnet, *Phys. Rev. Lett.* **68**,

855 (1992)

[151] J. N. Reimers & A. J. Berlinsky: Order by disorder in the classical Heisenberg kagomé antiferromagnet, *Phys. Rev. B* **48**, 9539 (1993)

[152] R. D. Shannon & C. Calvo: Crystal Structure of a New Form of $Cu_3V_2O_8$, *Canadian Journal of Chemistry* **50**, 3944 (1972)

[153] R. Gopal & C. Calvo: Crystal Structure of α-$Zn_3(VO_4)_2$, *Canadian Journal of Chemistry* **49**, 3056 (1971)

[154] X. Wang, Z. Liu, A. Ambrosini, A. Maignan, C. L. Stern, K. R. Poeppelmeier & V. P. Dravid: Crystal growth, structure, and properties of manganese orthovanadate $Mn_3(VO_4)_2$, *Solid State Sciences* **2**, 99 (2000)

[155] N. Krishnamachari & C. Calvo: Refinement of the Structure of $Mg_3(VO_4)_2$, *Canadian Journal of Chemistry* **49**, 1629 (1971)

[156] N. Rogado, M. K. Haas, G. Lawes, D. A. Huse, A. P. Ramirez & R. J. Cava: β-$Cu_3V_2O_8$: magnetic ordering in a spin-1/2 Kagomé-staircase lattice, *Journal of Physics: Condensed Matter* **15**, 907 (2003)

[157] Y. Chen, J. W. Lynn, Q. Huang, F. M. Woodward, T. Yildirim, G. Lawes, A. P. Ramirez, N. Rogado, R. J. Cava, A. Aharony, O. Entin-Wohlman & A. B. Harris: Complex magnetic order in the kagomé staircase compound $Co_3V_2O_8$, *Phys. Rev. B* **74**, 014430 (2006)

[158] N. Rogado, G. Lawes, D. Huse, A. Ramirez & R. Cava: The Kagomé-staircase lattice: magnetic ordering in $Ni_3V_2O_8$ and $Co_3V_2O_8$, *Solid State Communications* **124**, 229 (2002)

[159] I. Cabrera, M. Kenzelmann, G. Lawes, Y. Chen, W. C. Chen, R. Erwin, T. R. Gentile, J. B. Leão, J. W. Lynn, N. Rogado, R. J. Cava & C. Broholm: Coupled Magnetic and Ferroelectric Domains in Multiferroic $Ni_3V_2O_8$, *Phys. Rev. Lett.* **103**, 087201 (2009)

[160] G. Ehlers, A. A. Podlesnyak, S. E. Hahn, R. S. Fishman, O. Zaharko, M. Frontzek, M. Kenzelmann, A. V. Pushkarev, S. V. Shiryaev & S. Barilo: Incommensurability and spin dynamics in the low-temperature phases of $Ni_3V_2O_8$, *Phys. Rev. B* **87**, 214418 (2013)

[161] G. Tunell, E. Posnjak & C. J. Ksanda: Geometrical and Optical Properties, and Crystal Structure of Tenorite, *Zeitschrift für Kristallographie - Crystalline Materials* **90**, 120 (1935)

[162] S. Åsbrink & L.-J. Norrby: A refinement of the crystal structure of copper(II) oxide with a discussion of some exceptional e.s.d.'s, *Acta Crystallographica Section B* **26**, 8 (1970)

[163] T. Shimizu, T. Matsumoto, A. Goto, K. Yoshimura & K. Kosuge: Magnetic Dimensionality of the Antiferromagnet CuO, *Journal of the Physical Society of Japan* **72**,

2165 (2003)

[164] M. A. Kastner, R. J. Birgeneau, G. Shirane & Y. Endoh: Magnetic, transport, and optical properties of monolayer copper oxides, *Rev. Mod. Phys.* **70**, 897 (1998)

[165] Y. Mizuno, T. Tohyama, S. Maekawa, T. Osafune, N. Motoyama, H. Eisaki & S. Uchida: Electronic states and magnetic properties of edge-sharing Cu-O chains, *Phys. Rev. B* **57**, 5326 (1998)

[166] B. X. Yang, T. R. Thurston, J. M. Tranquada & G. Shirane: Magnetic neutron scattering study of single-crystal cupric oxide, *Phys. Rev. B* **39**, 4343 (1989)

[167] V. P. Sakhnenko & N. V. Ter-Oganessian: Praphase concept for the phenomenological description of magnetoelectrics, *Crystallography Reports* **57**, 112 (2012)

[168] R. Villarreal, G. Quirion, M. L. Plumer, M. Poirier, T. Usui & T. Kimura: Magnetic Phase Diagram of CuO via High-Resolution Ultrasonic Velocity Measurements, *Phys. Rev. Lett.* **109**, 167206 (2012)

[169] G. Giovannetti, S. Kumar, A. Stroppa, J. van den Brink, S. Picozzi & J. Lorenzana: High-T_c Ferroelectricity Emerging from Magnetic Degeneracy in Cupric Oxide, *Phys. Rev. Lett.* **106**, 026401 (2011)

[170] G. Jin, K. Cao, G.-C. Guo & L. He: Origin of Ferroelectricity in High-T_c Magnetic Ferroelectric CuO, *Phys. Rev. Lett.* **108**, 187205 (2012)

[171] P. Tolédano, N. Leo, D. D. Khalyavin, L. C. Chapon, T. Hoffmann, D. Meier & M. Fiebig: Theory of High-Temperature Multiferroicity in Cupric Oxide, *Phys. Rev. Lett.* **106**, 257601 (2011)

[172] Z. Wang, N. Qureshi, S. Yasin, A. Mukhin, E. Ressouche, S. Zherlitsyn, Y. Skourski, J. Geshev, V. Ivanov, M. Gospodinov & V. Skumryev: Magnetoelectric effect and phase transitions in CuO in external magnetic fields, *Nature Communications* **7**, 10295 (2011)

[173] A. Rebello, Z. C. M. Winter, S. Viall & J. J. Neumeier: Multiple phase transitions in CuO observed with thermal expansion, *Phys. Rev. B* **88**, 094420 (2013)

[174] N. Qureshi, E. Ressouche, A. Mukhin, M. Gospodinov & V. Skumryev: Proof of the elusive high-temperature incommensurate phase in CuO by spherical neutron polarimetry, *Science Advances* **6** (2020)

[175] P. Babkevich, A. Poole, R. D. Johnson, B. Roessli, D. Prabhakaran & A. T. Boothroyd: Electric field control of chiral magnetic domains in the high-temperature multiferroic CuO, *Phys. Rev. B* **85**, 134428 (2012)

[176] J. B. Forsyth, P. J. Brown & B. M. Wanklyn: Magnetism in cupric oxide, *Journal of Physics C: Solid State Physics* **21**, 2917 (1988)

[177] P. J. Brown, T. Chattopadhyay, J. B. Forsyth & V. Nunez: Antiferromagnetism in CuO studied by neutron polarimetry, *Journal of Physics: Condensed Matter* **3**, 4281 (1991)

[178] D. Prabhakaran & A. Boothroyd: Single crystal growth of Zn-doped CuO by the floating-zone method, *Journal of Crystal Growth* **250**, 77 (2003), proceedings of the Fourteenth American Conference on Crystal Grow th and Epitaxy

[179] Data are available at `https://doi.ill.fr/10.5291/ILL-DATA.5-42-499`.

[180] Data are available at `https://doi.ill.fr/10.5291/ILL-DATA.CRG-2623`.

[181] R. C. Miller & A. Savage: Velocity of Sidewise 180° Domain-Wall Motion in $BaTiO_3$ as a Function of the Applied Electric Field, *Phys. Rev.* **112**, 755 (1958)

[182] S. Holbein: *Neutron Scattering Studies on Complex Magnetic Structures in Magnetoelectric Materials*, Ph.D. thesis, Universität zu Köln (2016)

[183] M. H. Rekveldt & W. H. Kraan: High-resolution neutron diffraction using larmor precession for angular and wavelength labelling, *Journal of Neutron Research* **8**, 53 (1999)

[184] M. T. Rekveldt, T. Keller & R. Golub: Larmor precession, a technique for high-sensitivity neutron diffraction, *Europhysics Letters (EPL)* **54**, 342 (2001)

[185] F. Mezei: Neutron spin echo: A new concept in polarized thermal neutron techniques, *Zeitschrift für Physik A Hadrons and nuclei* **255**, 146 (1972)

[186] F. Mezei, C. Pappas & T. Gutberlet: *Neutron spin echo spectroscopy: Basics, trends and applications*, vol. 601, Springer Science & Business Media (2002)

[187] J. Blasco, C. Ritter, J. García, J. M. de Teresa, J. Pérez-Cacho & M. R. Ibarra: Structural and magnetic study of $Tb_{1-x}Ca_xMnO_3$ perovskites, *Phys. Rev. B* **62**, 5609 (2000)

[188] T. Kimura, S. Ishihara, H. Shintani, T. Arima, K. T. Takahashi, K. Ishizaka & Y. Tokura: Distorted perovskite with e_g^1 configuration as a frustrated spin system, *Phys. Rev. B* **68**, 060403 (2003)

[189] R. Kajimoto, H. Mochizuki, H. Yoshizawa, H. Shintani, T. Kimura & Y. Tokura: R-Dependence of Spin Exchange Interactions in RMnO$_3$ (R = Rare-Earth Ions), *Journal of the Physical Society of Japan* **74**, 2430 (2005)

[190] S. Quezel, F. Tcheou, J. Rossat-Mignod, G. Quezel & E. Roudaut: Magnetic structure of the perovskite-like compound $TbMnO_3$, *Physica B+C* **86-88**, 916 (1977)

[191] R. Pynn: Neutron spin-echo and three-axis spectrometers, *Journal of Physics E: Scientific Instruments* **11**, 1133 (1978)

[192] F. Mezei: Neutron spin echo: Ten years after, *Physica B+C* **120**, 51 (1983)

[193] H. M.-L. Zentrum: TRISP: Three axes spin echo spectrometer, *Journal of large-scale research facilities* **1**, A37 (2015)

[194] T. Keller, R. Golub & R. Gähler: Chapter 2.8.6 - Neutron Spin Echo—A Technique for High-Resolution Neutron Scattering, in R. Pike & P. Sabatier, eds., *Scattering*, 1264–1286, Academic Press, London (2002)

[195] J. Repper, T. Keller, M. Hofmann, C. Krempaszky, W. Petry & E. Werner: Neutron Larmor diffraction measurements for materials science, *Acta Materialia* **58**, 3459 (2010)

[196] R. Golub & R. Gähler: A neutron resonance spin echo spectrometer for quasi-elastic and inelastic scattering, *Physics Letters A* **123**, 43 (1987)

[197] R. Gähler & R. Golub: A high resolution neutron spectrometer for quasielastic scattering on the basis of spin-echo and magnetic resonance, *Zeitschrift für Physik B Condensed Matter* **65**, 269 (1987)

[198] R. Gähler, R. Golub & T. Keller: Neutron resonance spin echo—a new tool for high resolution spectroscopy, *Physica B: Condensed Matter* **180-181**, 899 (1992)

[199] Gähler, R. & Golub, R.: Neutron resonance spin echo, bootstrap method for increasing the effective magnetic field, *J. Phys. France* **49**, 1195 (1988)

[200] K. F. Tseng, T. Keller, A. C. Walters, R. J. Birgeneau & B. Keimer: Neutron spin-echo study of the critical dynamics of spin-$\frac{5}{2}$ antiferromagnets in two and three dimensions, *Phys. Rev. B* **94**, 014424 (2016)

[201] F. Groitl, T. Keller, K. Rolfs, D. A. Tennant & K. Habicht: Anomalous thermal decoherence in a quantum magnet measured with neutron spin echo spectroscopy, *Phys. Rev. B* **93**, 134404 (2016)

[202] P. Brown: CHAPTER 5 - Spherical Neutron Polarimetry, in T. Chatterji, ed., *Neutron Scattering from Magnetic Materials*, 215–244, Elsevier Science, Amsterdam (2006)

[203] J. Stein, M. Baum, S. Holbein, T. Finger, T. Cronert, C. Tölzer, T. Fröhlich, S. Biesenkamp, K. Schmalzl, P. Steffens, C. H. Lee & M. Braden: Control of Chiral Magnetism Through Electric Fields in Multiferroic Compounds above the Long-Range Multiferroic Transition, *Phys. Rev. Lett.* **119**, 177201 (2017)

[204] R. Kajimoto, H. Yoshizawa, H. Shintani, T. Kimura & Y. Tokura: Magnetic structure of $TbMnO_3$ by neutron diffraction, *Phys. Rev. B* **70**, 012401 (2004)

[205] S. B. Wilkins, T. R. Forrest, T. A. W. Beale, S. R. Bland, H. C. Walker, D. Mannix, F. Yakhou, D. Prabhakaran, A. T. Boothroyd, J. P. Hill, P. D. Hatton & D. F. McMorrow: Nature of the Magnetic Order and Origin of Induced Ferroelectricity in $TbMnO_3$, *Phys. Rev. Lett.* **103**, 207602 (2009)

[206] M. Vojta: Quantum phase transitions, *Rep. Prog. Phys.* **66**, 2069 (2003)

[207] S. Sachdev: Quantum phase transitions, *Phys. World* **12**, 33 (1999)

[208] S. Sachdev & B. Keimer: Quantum criticality, *Physics Today* **64**, 29 (2011)

[209] P. Pfeuty: The one-dimensional Ising model with a transverse field, *Annals of Physics* **57**, 79 (1970)

[210] E. Ising: Beitrag zur Theorie des Ferromagnetismus, *Zeitschrift für Physik* **31**, 253 (1925)

[211] S. K. Niesen, G. Kolland, M. Seher, O. Breunig, M. Valldor, M. Braden, B. Grenier & T. Lorenz: Magnetic phase diagrams, domain switching, and quantum phase transition of the quasi-one-dimensional Ising-like antiferromagnet $BaCo_2V_2O_8$, *Phys. Rev. B* **87**, 224413 (2013)

[212] Z. Wang, T. Lorenz, D. I. Gorbunov, P. T. Cong, Y. Kohama, S. Niesen, O. Breunig, J. Engelmayer, A. Herman, J. Wu, K. Kindo, J. Wosnitza, S. Zherlitsyn & A. Loidl: Quantum Criticality of an Ising-like Spin-1/2 Antiferromagnetic Chain in a Transverse Magnetic Field, *Phys. Rev. Lett.* **120**, 207205 (2018)

[213] S. Kimura, H. Yashiro, M. Hagiwara, K. Okunishi, K. Kindo, Z. He, T. Taniyama & M. Itoh: High field magnetism of the quasi one-dimensional anisotropic antiferromagnet $BaCo_2V_2O_8$, *J. Phys.: Conf. Ser.* **51**, 99 (2006)

[214] Z. He, D. Fu, T. Kyômen, T. Taniyama & M. Itoh: Crystal Growth and Magnetic Properties of $BaCo_2V_2O_8$, *Chemistry of Materials* **17**, 2924 (2005)

[215] Z. He, T. Taniyama & M. Itoh: Large magnetic anisotropy in the quasi-one-dimensional system $BaCo_2V_2O_8$, *Applied Physics Letters* **88**, 132504 (2006)

[216] Q. Faure, S. Takayoshi, S. Petit, V. Simonet, S. Raymond, L.-P. Regnault, M. Boehm, J. S. White, M. Månsson, C. Rüegg, P. Lejay, B. Canals, T. Lorenz, S. C. Furuya, T. Giamarchi & B. Grenier: Topological quantum phase transition in the Ising-like antiferromagnetic spin chain $BaCo_2V_2O_8$, *Nature Physics* **14**, 716 (2018)

[217] Z. Wang, M. Schmidt, A. Loidl, J. Wu, H. Zou, W. Yang, C. Dong, Y. Kohama, K. Kindo, D. I. Gorbunov, S. Niesen, O. Breunig, J. Engelmayer & T. Lorenz: Quantum Critical Dynamics of a Heisenberg-Ising Chain in a Longitudinal Field: Many-Body Strings versus Fractional Excitations, *Phys. Rev. Lett.* **123**, 067202 (2019)

[218] Y. Kawasaki, J. L. Gavilano, L. Keller, J. Schefer, N. B. Christensen, A. Amato, T. Ohno, Y. Kishimoto, Z. He, Y. Ueda & M. Itoh: Magnetic structure and spin dynamics of the quasi-one-dimensional spin-chain antiferromagnet $BaCo_2V_2O_8$, *Phys. Rev. B* **83**, 064421 (2011)

[219] S. Kimura, K. Okunishi, M. Hagiwara, K. Kindo, Z. He, T. Taniyama, M. Itoh, K. Koyama & K. Watanabe: Collapse of Magnetic Order of the Quasi One-Dimensional Ising-Like Antiferromagnet $BaCo_2V_2O_8$ in Transverse Fields, *Journal of the Physical Society of Japan* **82**, 033706 (2013)

[220] A. Okutani, H. Onishi, S. Kimura, T. Takeuchi, T. Kida, M. Mori, A. Miyake, M. Tokunaga, K. Kindo & M. Hagiwara: Spin Excitations of the $S = 1/2$ One-Dimensional Ising-Like Antiferromagnet $BaCo_2V_2O_8$ in Transverse Magnetic Fields, *Journal of the Physical Society of Japan* **90**, 044704 (2021)

[221] O. Prokhnenko, W.-D. Stein, H.-J. Bleif, M. Fromme, M. Bartkowiak & T. Wilpert: Time-of-flight Extreme Environment Diffractometer at the Helmholtz-Zentrum Berlin, *Review of Scientific Instruments* **86**, 033102 (2015)

[222] P. Smeibidl, M. Bird, H. Ehmler, I. Dixon, J. Heinrich, M. Hoffmann, S. Kempfer, S. Bole, J. Toth, O. Prokhnenko & B. Lake: First Hybrid Magnet for Neutron Scattering at Helmholtz-Zentrum Berlin, *IEEE Transactions on Applied Superconductivity* **26**, 1 (2016)

[223] M. Bartkowiak, N. Stüßer & O. Prokhnenko: The design of the inelastic neutron scattering mode for the Extreme Environment Diffractometer with the 26T High Field Magnet, *Nuclear Instruments and Methods in Physics Research Section A: Accelerators, Spectrometers, Detectors and Associated Equipment* **797**, 121 (2015)

[224] O. Prokhnenko, P. Smeibidl, W.-D. Stein, M. Bartowiak & N. Stüsser: HFM/EXED: The High Magnetic Field Facility for Neutron Scattering at BER II, *Journal of large-scale research facilities* **3** (2017)

[225] R. Wichmann & H. Müller-Buschbaum: Neue Verbindungen mit $SrNi_2V_2O_8$-Struktur: $BaCo_2V_2O_8$ und $BaMg_2V_2O_8$, *Zeitschrift für anorganische und allgemeine Chemie* **534**, 153 (1986)

[226] K. Momma & F. Izumi: *VESTA3* for three-dimensional visualization of crystal, volumetric and morphology data, *Journal of Applied Crystallography* **44**, 1272 (2011)

[227] S. Kimura, M. Matsuda, T. Masuda, S. Hondo, K. Kaneko, N. Metoki, M. Hagiwara, T. Takeuchi, K. Okunishi, Z. He, K. Kindo, T. Taniyama & M. Itoh: Longitudinal Spin Density Wave Order in a Quasi-1D Ising-like Quantum Antiferromagnet, *Phys. Rev. Lett.* **101**, 207201 (2008)

[228] E. Canévet, B. Grenier, M. Klanjšek, C. Berthier, M. Horvatić, V. Simonet & P. Lejay: Field-induced magnetic behavior in quasi-one-dimensional Ising-like antiferromagnet $BaCo_2V_2O_8$: A single-crystal neutron diffraction study, *Phys. Rev. B* **87**, 054408 (2013)

[229] B. Grenier, V. Simonet, B. Canals, P. Lejay, M. Klanjšek, M. Horvatić & C. Berthier: Neutron diffraction investigation of the $H-T$ phase diagram above the longitudinal incommensurate phase of $BaCo_2V_2O_8$, *Phys. Rev. B* **92**, 134416 (2015)

[230] S. Tomonaga: Remarks on Bloch's Method of Sound Waves applied to Many-Fermion Problems, *Progress of Theoretical Physics* **5**, 544 (1950)

[231] J. M. Luttinger: An Exactly Soluble Model of a Many-Fermion System, *Journal of Mathematical Physics* **4**, 1154 (1963)

[232] A. Luther & I. Peschel: Calculation of critical exponents in two dimensions from quantum field theory in one dimension, *Phys. Rev. B* **12**, 3908 (1975)

[233] F. D. M. Haldane: General Relation of Correlation Exponents and Spectral Properties of One-Dimensional Fermi Systems: Application to the Anisotropic $S = \frac{1}{2}$ Heisenberg Chain, *Phys. Rev. Lett.* **45**, 1358 (1980)

[234] K. Okunishi & T. Suzuki: Field-induced incommensurate order for the quasi-one-dimensional XXZ model in a magnetic field, *Phys. Rev. B* **76**, 224411 (2007)

[235] S. Kimura, T. Takeuchi, K. Okunishi, M. Hagiwara, Z. He, K. Kindo, T. Taniyama & M. Itoh: Novel Ordering of an $S = 1/2$ Quasi-1d Ising-Like Antiferromagnet in Magnetic Field, *Phys. Rev. Lett.* **100**, 057202 (2008)

[236] O. Arnold, J. Bilheux, J. Borreguero, A. Buts, S. Campbell, L. Chapon, M. Doucet, N. Draper, R. Ferraz Leal, M. Gigg, V. Lynch, A. Markvardsen, D. Mikkelson, R. Mikkelson, R. Miller, K. Palmen, P. Parker, G. Passos, T. Perring, P. Peterson, S. Ren, M. Reuter, A. Savici, J. Taylor, R. Taylor, R. Tolchenov, W. Zhou & J. Zikovsky: Mantid—Data analysis and visualization package for neutron scattering and μ SR experiments, *Nuclear Instruments and Methods in Physics Research Section A: Accelerators, Spectrometers, Detectors and Associated Equipment* **764**, 156 (2014)

[237] M. Bartkowiak, K. Prokeš, M. Fromme, A. Budack, J. Dirlick & O. Prokhnenko: *EXEQ* and *InEXEQ*: software tools for experiment planning at the Extreme Environment Diffractometer, *Journal of Applied Crystallography* **53**, 1613 (2020)

[238] S. K. Niesen: *Synthesis and Characterizatin of Spin-Chain Compounds of the* $AM_2V_2O_8$ *Type*, Ph.D. thesis, Universität zu Köln (2015)

[239] Q. Faure, S. Takayoshi, V. Simonet, B. Grenier, M. Månsson, J. S. White, G. S. Tucker, C. Rüegg, P. Lejay, T. Giamarchi & S. Petit: Tomonaga-Luttinger Liquid Spin Dynamics in the Quasi-One-Dimensional Ising-Like Antiferromagnet $\mathrm{BaCo_2V_2O_8}$, *Phys. Rev. Lett.* **123**, 027204 (2019)

[240] H. Schmid: On ferrotoroidics and electrotoroidic, magnetotoroidic and piezotoroidic effects*, *Ferroelectrics* **252**, 41 (2001)

[241] N. A. Spaldin, M. Fiebig & M. Mostovoy: The toroidal moment in condensed-matter physics and its relation to the magnetoelectric effect, *Journal of Physics: Condensed Matter* **20**, 434203 (2008)

[242] C. Ederer & N. A. Spaldin: Towards a microscopic theory of toroidal moments in bulk periodic crystals, *Phys. Rev. B* **76**, 214404 (2007)

[243] V. Dubovik & V. Tugushev: Toroid moments in electrodynamics and solid-state physics, *Physics Reports* **187**, 145 (1990)

[244] A. A. Gorbatsevich & Y. V. Kopaev: Toroidal order in crystals, *Ferroelectrics* **161**, 321 (1994)

[245] B. B. Van Aken, J.-P. Rivera, H. Schmid & M. Fiebig: Observation of ferrotoroidic domains, *Nature* **449**, 702—705 (2007)

[246] A. S. Zimmermann, D. Meier & M. Fiebig: Ferroic nature of magnetic toroidal order, *Nature communications* **5**, 4796 (2014)

[247] J. Clark, D. Appleman & J. Papike: Crystal-chemical characterization of clinopyroxenes based on eight new structure refinements, *Mineral. Soc. Am. Spec. Pap.* **2**, 31 (1969)

[248] G. Redhammer, G. Roth, W. Paulus, G. André, W. Lottermoser, G. Amthauer,

W. Treutmann & B. Bitschnau: The crystal and magnetic structure of Li-aegirine $LiFe^{3+}Si_2O_6$: A temperature-dependent study, *Physics and Chemistry of Minerals* **28**, 337 (2001)

[249] M. Behruzi, T. Hahn, C. T. Prewitt & K. Baldwin: Low- and high-temperature crystal structures of $LiFeGe_2O_6$, $LiFeSi_2O_6$ and $LiCrSi_2O_6$, *Acta Crystallographica Section A* **40**, C247 (1984)

[250] E. Baum, W. Treutmann, . Behruzi, W. Lottermoser & G. Amthauer: Structural and magnetic properties of the clinopyroxenes $NaFeSi_2O_6$ and $LiFeSi_2O_6$, *Zeitschrift für Kristallographie - Crystalline Materials* **183**, 273 (1988)

[251] W. Lottermoser, G. Redhammer, K. Forcher, G. Amthauer, W. Paulus, G. Andre & W. Treutmann: Single crystal Mössbauer and neutron powder diffraction measurements on the synthetic clinopyroxene Li-acmite $LiFeSi_2O_6$, *Zeitschfrift für Kristallographie* **213**, 101 (1998)

[252] S. Jodlauk, P. Becker, J. A. Mydosh, D. I. Khomskii, T. Lorenz, S. V. Streltsov, D. C. Hezel & L. Bohatý: Pyroxenes: a new class of multiferroics, *Journal of Physics: Condensed Matter* **19**, 432201 (2007)

[253] G. J. Redhammer, G. Roth, W. Treutmann, M. Hoelzel, W. Paulus, G. André, C. Pietzonka & G. Amthauer: The magnetic structure of clinopyroxene-type $LiFeGe_2O_6$ and revised data on multiferroic $LiFeSi_2O_6$, *Journal of Solid State Chemistry* **182**, 2374 (2009)

[254] P. Tolédano, M. Ackermann, L. Bohatý, P. Becker, T. Lorenz, N. Leo & M. Fiebig: Primary ferrotoroidicity in antiferromagnets, *Phys. Rev. B* **92**, 094431 (2015)

[255] M. M. Baum: *Neutron-Scattering Studies on Chiral Multiferroics*, Ph.D. thesis, Universität zu Köln (2013)

Abstract

This thesis reports thorough studies on multiferroic and frustrated systems, whereby specific focus was put on the investigation of multiferroic domain dynamics. For the respective experiments mainly neutron scattering techniques ranging from conventional diffraction, inelastic scattering, neutron polarization analysis to Larmor diffraction were utilized.

The well-known multiferroic tungstate $MnWO_4$ and the structurally related double-tungstate system $NaFe(WO_4)_2$ both exhibit competing commensurate and incommensurate order at low temperature. Within the course of this thesis, it was possible to observe a structural dimerization in the respective commensurate spin up-up-down-down phases, which is caused by a bond-angle modulation due to the alternating ferro- and antiferromagnetic exchange along the Fe^{3+}, respectively Mn^{2+} chain. A structural refinement yielded a bond-angle modulation of about $\pm 1.15(16)^\circ$ in the *ac*-plane for $NaFe(WO_4)_2$, which is however estimated to be of similar size in $MnWO_4$. For $MnWO_4$ it was further seen that second and third harmonic reflections evolve in the incommensurate multiferroic phase, whereby the odd harmonic reflection diverges in contrast to the even one, when approaching the lower transition to commensurate spin up-up-down-down ordering. The developing third harmonic and the related squaring up of spins can hence be seen as precursor of the lower commensurate phase and refers to tiny commensurate fragments that evolve already in the multiferroic phase. They are capable to effectively depin multiferroic domains and in view of the investigation of the multiferroic relaxation behavior it was thus seen beneficial to study multiferroic spiral type-II systems that exhibit simple phase diagrams, which do not exhibit an interference of incommensurate and commensurate ordering.

A potential candidate was considered to be $LiFe(WO_4)_2$, which is so far the only multiferroic double-tungstate system. In this thesis, a thorough single-crystal study and the respective characterization of both low-temperature phases are presented. The magnetic refinements yielded that the system first develops below $T = 22.2\,\mathrm{K}$ a spin-density wave with moments that are lying within the *ac*-plane. Further, the refinement of a low-temperature data set showed that below $T = 19\,\mathrm{K}$ the magnetic arrangement in the multiferroic phase transforms into a spiral-spin structure, which exhibits an additional *b*-component. Hence, $LiFe(WO_4)_2$ possesses a typical and simple sequence of magnetic phases for a spiral type-II multiferroic, whose ferroelectric polarization can be well described in the framework of the Dzyaloshinskii-Moriya interaction. Temperature dependent measurements of the chiral ratio by neutron polarization analysis further revealed a finite value of it at low temperature, which thus implies an imbalanced multiferroic domain distribution even in zero-field.

Another multiferroic system that exhibits an equivalent simple phase diagram is $NaFeGe_2O_6$.

This thesis reports studies on the magnetic structure and the multiferroic domain dynamics. The respective investigation showed that the system does not possess solely magnetic components in the *ac*-plane but simultaneous to the lock-in of the incommensurate modulation it develops an additional *b*-component in the multiferroic phase. The time-resolved analysis of the multiferroic domain inversion revealed that the relaxation behavior can be well described by a combined Arrhenius-Merz law over a broad temperature and field range. Even at very low temperature the relaxation behavior follows the description for thermally activated domain-wall motion, whereby no indication of emerging quantum driven domain wall tunneling processes was seen. Unpolarized inelastic neutron scattering experiments further showed that the fasted speed of domain inversion, respectively of domain-wall motion at the multiferroic transition temperature is comparable to the spin-wave velocity.

In the further course of this thesis also the relaxation behavior of other multiferroic systems is reported. In this context it was possible to observe that the molecular system $(NH_4)_2[FeCl_5\,(H_2O)]$, the Kagomé staircase material $Ni_3V_2O_8$ and the high-temperature multiferroic compound CuO also follow the combined Arrhenius-Merz law for thermally activated multiferroic domain inversion over a finite field and temperature range.

The investigations of relaxation times in the course of this thesis were performed by time-resolved studies of the domain population, whose magnitude is encoded in the chiral ratio. Complementary, the time-resolved domain size development can be deduced from the correlation length, which can be deduced from the respective peak widths. The observation of increasing domain sizes during a multiferroic inversion process is however commonly hindered by the finite Q-space resolution at conventional diffraction instruments. This thesis documents time-resolved Larmor diffraction experiments, which represent a different approach to sense the correlation length. Here, the respective scattering information is not encoded in the scattering angle but in the Larmor precession phase of the neutron spin, when it transits magnetic-field regions before and behind the sample. This makes the demanded scattering information independent of a finite beam collimation or a finite wavelength spread, which thus tremendously enhances the achievable resolution in the course of scattering experiments. However, it turned out that the alteration of the beam polarization by chiral scattering processes enormously impacts the Larmor diffraction signal and thus necessitates appropriate corrections.

Apart from the studies on multiferroic systems, this thesis reports also on a detailed investigation of the magnetic structure in the Ising-like spin-1/2 chain material $BaCo_2V_2O_8$, when a transverse magnetic-field is applied along [1 1 0] direction. In this context, it was possible to observe a finite peak splitting of the commensurate magnetic reflection at finite field, whereby the onset of this high-field incommensurate order is discussed within the framework of a Tomonaga-Luttinger phase, which is potentially driven by longitudinal staggered fields along the easy-axis.

Kurzzusammenfassung

Diese Arbeit berichtet über ausführliche Studien an multiferroischen und frustrierten Systemen, wobei der Fokus auf Untersuchungen der multiferroischen Domänendynamik gelegt wurde. Für die entsprechenden Experimente wurden überwiegend Techniken der Neutronenstreuung, angefangen von konventioneller Diffraktion, inelastischer Streuung, Neutronen Polarisationsanalyse, bis hin zur Larmordiffraktion genutzt.

Das bekannte multiferroische Wolframat $MnWO_4$ und das strukturell verwandte Doppelwolframat $NaFe(WO_4)_2$ weisen beide konkurrierende kommensurable und inkommensurable Ordnungen bei tiefen Temperaturen auf. Im Rahmen dieser Arbeit war es möglich, in den entsprechenden kommensurablen Spin up-up-down-down Phasen eine strukturelle Dimerisierung nachzuweisen, die aufgrund einer Bindungswinkelmodulation durch den alternierenden ferro- und antiferromagnetischen Austausch entlang der Fe^{3+} bzw. Mn^{2+} Ketten hervorgerufen wird. Eine strukturelle Verfeinerung ergab eine Bindungswinkelmodulation von ungefähr $\pm 1.15°$ in der ac-Ebene für $NaFe(WO_4)_2$, was jedoch schätzungsweise von gleicher Größe auch in $MnWO_4$ vorliegt. Bei $MnWO_4$ konnte außerdem beobachtet werden, dass sich die zweite und dritte höhere harmonische Ordnung der Reflexe in der inkommensurablen Phase entwickelt, wobei die ungerade höhere Ordnung im Gegensatz zur geraden Ordnung divergiert, wenn sich dem unteren Übergang zur kommensurablen Spin up-up-down-down Phase angenähert wird. Die sich entwickelnde dritte harmonische Ordnung und die zugehörige Aufrichtung der Spins kann somit als Vorläufer der tiefer liegenden kommensurablen Phase gesehen werden und bezieht sich auf kleine kommensurable Fragmente, die sich schon in der multiferroischen Phase entwickeln. Diese sind in der Lage, die multiferroischen Domänen effektiv zu entfestigen. In Anbetracht der Untersuchungen der multiferroischen Domänendynamik wurde es als vorteilhaft angesehen, multiferroische Typ-II Systeme zu untersuchen, die ein einfaches Phasendiagram ohne konkurrierende inkommensurable und kommensurable Ordnung aufweisen.

Als potentieller Kandidat wurde $LiFe(WO_4)_2$ gesehen, welches bisher das einzige multiferroische Doppelwolframat System ist. Diese Arbeit präsentiert eine gründliche Einkristall-Studie und die entsprechende Charakterisierung der beiden Tieftemperaturphasen. Die magnetischen Verfeinerungen ergaben, dass das System zunächst unterhalb $T = 22.2\,\mathrm{K}$ eine Spin-Dichte Welle mit Momenten in der ac-Ebene entwickelt. Außerdem zeigte die Verfeinerung eines Datensatzes bei tiefer Temperatur, dass die Magnetstruktur unterhalb von $T = 19\,\mathrm{K}$ und somit in der multiferroischen Phase in eine Spirale mit zusätzlicher b-Komponente übergeht. Somit weist $LiFe(WO_4)_2$ eine typische und einfache Abfolge von magnetischen Phasen für ein Typ-II Multiferroika mit spiraler Magnetstruktur auf. Die

auftretende ferroelektrische Polarisation kann gut im Rahmen der Dzyaloshinskii-Moriya Wechselwirkung beschrieben werden. Temperaturabhängige Messungen des chiralen Verhältnis mittels Neutronen Polarisationsanalyse zeigten eine unausgeglichene Domänenverteilung, sogar ohne angelegtes elektrisches Feld.

Ein weiteres multiferroisches System, dass ein äquivalentes Phasendiagram aufweist, ist $NaFeGe_2O_6$. Diese Arbeit berichtet von Studien der Magnetstruktur und der multiferroischen Domänendynamik. Die entsprechenden Untersuchungen zeigten, dass das System nicht nur magnetische Komponenten in der ac-Ebene aufweist, sondern simultan zum lock-in der Inkommensurabilität auch eine entwickelnde b-Komponente in der multiferroischen Phase offenbart. Die zeitaufgelöste Analyse der multiferroischen Domäneninversion zeigte, dass das Relaxationsverhalten über einen breiten Temperatur- und elektrischen Feldbereich durch ein kombiniertes Arrhenius-Merz Gesetz beschrieben werden kann. Sogar bei sehr tiefen Temperaturen folgt das Relaxationsverhalten der Beschreibung für thermisch aktivierte Domänenwandbewegung, wobei es keine Anzeichen für ein sich entwickelndes Domänentunneln durch Quantenfluktuationen gab. Unpolarisierte inelastische Neutronenstreuung zeigte außerdem, dass die Geschwindigkeit der Domäneninversion am multiferroischen Übergang mit der Spinwellengeschwindigkeit vergleichbar ist.

Im weiteren Verlauf dieser Arbeit wird auch das Relaxationsverhalten anderer multiferroischer Systeme diskutiert. In diesem Zusammenhang konnte beobachtet werden, dass das molekulare System $(NH_4)_2[FeCl_5\,(H_2O)]$, das Kagomé staircase Material $Ni_3V_2O_8$ und das Hochtemperatur-Multiferroika CuO auch dem kombinierten Arrhenius-Merz Gesetz für thermisch aktivierte multiferroische Domäneninversion über einen endlichen Temperatur- und Feldbereich folgen.

Die Untersuchung von Relaxationszeiten im Verlauf dieser Arbeit sind mittels zeitaufgelöster Messungen der Domänenpopulation, deren Größe im chiralen Verhältnis steckt, durchgeführt worden. Ergänzend dazu kann die zeitaufgelöste Untersuchung der Domänengrößenentwicklung von der entsprechenden Peakbreite abgeleitet werden. Die Beobachtung von wachsenden Domänengrößen während des multiferroischen Inversionsprozesses ist jedoch durch die endliche Q-Raum Auflösung bei konventionellen Diffraktionsinstrumenten erschwert. Diese Arbeit dokumentiert zeitaufgelöste Larmordiffraktions-Experimente, welche einen anderen Zugang zum Messen von Korrelationslängen darstellen. Dabei steckt die entsprechende Streuinformation nicht im Streuwinkel, sondern in der Larmorpräzession des Neutronenspins, wenn es ein Magnetfeld vor und nach der Probe durchquert. Das macht die gefragte Streuinformation unabhängig von der Strahlkollimation oder einer endlichen Wellenlängenverteilung, was die erreichbare Auflösung deutlich steigert. Es stellte sich jedoch heraus, dass die Änderung der gestreuten Strahlpolarisation durch den chiralen Streuprozess signifikant das Larmordiffraktionssignal beeinflusst und entsprechende Korrekturen des Signals dringend nötig macht.

Neben den Studien an multiferroischen Systemen berichtet diese Arbeit auch von detaillierten Untersuchungen zu der Magnetstruktur des Ising ähnlichen Spin 1/2 Ketten Material $BaCo_2V_2O_8$, wenn dieses einem transversalen Feld entlang der [1 1 0] Richtung ausgesetzt ist. In diesem Zusammenhang war es möglich, eine endliche Aufspaltung des kommensurablen Peaks im endlichen Feld zu beobachten. Das Auftreten dieser inkommensurablen Ordnung bei hohen transversalen Feldern wird im Bezug zu einer möglichen Tomonaga-Luttinger Flüssigkeitsphase, die mit longitudinal versetzten Feldern entlang der easy-Achse induziert wird, diskutiert.

Danksagung

Die mit dieser Doktorarbeit verbundenen Forschungsarbeiten, die Vorbereitung und Durchführung von Neutronenstreuexperimenten, sowie die alltägliche Laborarbeit wurden regelmäßig begleitet von neuen experimentellen Herausforderungen und neuen Fragestellungen. Ich möchte mich besonders bei den Personen bedanken, die mich während dieser Doktorandenzeit begleitet und in unterschiedlicher Form unterstützt haben.

Als erstes möchte ich mich bei meinem Doktorvater Herrn Prof. Dr. Markus Braden für die Betreuung meiner Arbeit bedanken. Durch die Ermöglichung vieler Messzeiten, einer Vielzahl an Konferenzbesuchen und Workshopteilnahmen konnte ich viele wertvolle Erfahrungen und neues Wissen ansammeln. Der regelmäßige Austausch über die einzelnen Themen und die verschiedenen Messtechniken, insbesondere bei gemeinsamen Messzeiten, waren von unschätzbarem Wert für mich. Die sehr angenehme Zeit, die ich in der Arbeitsgruppe Braden verbracht habe, werde ich immer in sehr guter Erinnerung behalten.

Bei Herrn Prof. Dr. Markus Grüninger bedanke ich mich für die Begutachtung der Arbeit und bei Herrn Prof. Dr. Stephan Schlemmer bedanke ich mich für die Übernahme des Vorsitzes der Prüfungskommission. Bei Dr. Jens Brede möchte ich mich für die Übernahme des Prüfungsbeisitzes bedanken.

Ich möchte mich auch bei allen aktuellen und ehemaligen Mitgliedern der Arbeitsgruppe, sowie dem gesamten II. Physikalischen Institut der Universität zu Köln für die angenehme und konstruktive Zusammenarbeit bedanken! Bei Dr. Tobias Fröhlich und Jonas Stein möchte ich mich an dieser Stelle jeweils besonders für die Einweisung zur Röntgendiffraktometrie und zur zeitaufgelösten Messtechnik bedanken. Außerdem gilt mein Dank Dr. Alexandre Bertin für die Unterstützung bei den APEX Tieftemperaturmessungen und Susanne Heijligen für den Support bei SQUID-Messungen.

Alle Messungen und die durchgeführten Experimente sind immer maßgeblich von einer guten Probenqualität abhängig. Die meisten Proben, die für diese Arbeit verwendet wurden, sind von Frau Prof. Dr. Petra Becker-Bohatý und Herrn Prof. Dr. Ladislav Bohatý gezüchtet und für Messungen bereitgestellt worden. Bei beiden möchte ich mich sehr für die durchgehend exzellenten Proben und auch für die interessanten und sehr aufschlussreichen Gespräche zu den verschiedenen Kristallsystemen bedanken. Herrn Prof. Dr. Ladislav Bohatý möchte ich zusätzlich für die Beteiligung an meinem Thesis Advisory Committee danken.

Herrn Prof. Dr. Andrew Boothroyd und Dr. Dharmalingam Prabhakaran danke ich für das bereitgestellte Probenmaterial von CuO und bei Dr. Navid Qureshi möchte ich

mich für Bereitstellung von Probenmaterial von $Ni_3V_2O_8$ bedanken. Herrn Prof. Dr. Thomas Lorenz danke ich sehr, dass er mir Proben von dem $BaCo_2V_2O_8$ System für die Neutronemessungen zu Verfügung gestellt hat, und ich möchte mich außerdem sehr herzlich bei ihm für die Beteiligung an meinem Thesis Advisory Committee, sowie für die hilfreichen Gespräche und den Austausch zu diversen Fragestellungen bei $BaCo_2V_2O_8$ und $LiFe(WO_4)_2$ bedanken. Bezüglich des letzten Systems möchte ich mich auch sehr bei Dr. Daniel Brüning für die Durchführung von Wärmekapazitätsmessungen bedanken.

Der Erfolg von Neutronenstreuexperimenten ist erheblich von der Verlässlichkeit und Genauigkeit der Instrumente abhängig. Beides war während meiner Messzeiten immer gewährleistet und kurzfristige Änderungen an den Aufbauten wurden schnell und unkompliziert durchgeführt. Dies verdanke ich insbesondere der großartigen Arbeit der entsprechenden Local Contacts, die mich während meiner Messzeiten am ILL, am FRMII, am HZB, und am LLB betreut haben. Dafür möchte ich mich sehr herzlich bei Dr. Navid Qureshi, Dr. Yvan Sidis, Dr. Martin Meven, Dr. Arsen Gukasov, Dr. Xavier Fabrèges, Dr. Dmitry Gorkov, Dr. Karin Schmalzl, Dr. Wolfgang Schmidt, Dr. Paul Steffens, Dr. Ketty Beauvois, Dr. Thomas Hansen, Dr. Eric Ressouche, Dr. Thomas Keller und Dr. Oleksandr Prokhnenko bedanken.

Die Vorbereitung der Messzeiten bedurfte oftmals die Konstruktion neuer Probenhalterungen, neuer Elektronik oder der Reperatur letzterer. Für die immer schnelle und oft kurzfristige Umsetzung möchte ich mich sehr herzlich bei der mechanischen und elektrischen Werkstatt des II. Physikalischen Instituts bedanken.

Bei meinen Bürokollegen und Freunden Philipp Warzanowski, David Maluski und Kevin Jenni möchte ich mich für die wunderbaren gemeinsamen Jahre im Büro 208 bedanken. Neben dem Austausch über physikalische Themen waren die gemeinsamen Freizeitaktivitäten abseits der Arbeit immer eine große Freude. Zum Glück haben wir es aus allen Escape-Rooms geschafft.

Ich möchte hier auch die Gelegenheit nutzen, um meinem ehemaligen Physiklehrer Herrn Ulrich Kloppenburg meinen Dank auszusprechen. Er hat mich für die Physik begeistert und der Physik Leistungskurs wird mir immer in besonderer Erinnerung bleiben.

Schließlich gilt der größte Dank meinen Eltern, ohne deren Unterstützung das Studium und die Arbeit in dieser Form nicht möglich gewesen wäre. Danke Mama und Papa!

Publikationen

Teilpublikationen

- S. Biesenkamp, N. Qureshi, Y. Sidis, P. Becker, L. Bohatý, and M. Braden, *Structural dimerization in the commensurate magnetic phases of* $NaFe(WO_4)_2$ *and* $MnWO_4$*,* Phys. Rev. B **102**, 144429 (2020),
- S. Biesenkamp, D. Gorkov, D. Brüning, A. Bertin, T. Fröhlich, X. Fabrèges, A. Gukasov, M. Meven, P. Becker, L. Bohatý, T. Lorenz, and M. Braden, *Single-crystal investigations on the multiferroic material* $LiFe(WO_4)_2$*,* Phys. Rev. B **103**, 134412 (2021),
- S. Biesenkamp, D. Gorkov, W. Schmidt, K. Schmalzl, Y. Sidis, P. Becker, L. Bohatý and M. Braden, *Chiral order and multiferroic domain relaxation in* $NaFeGe_2O_6$*,* Phys. Rev. B **104**, 174405 (2021),

Weitere Publikationen

- J. Stein, M. Baum, S. Holbein, T. Finger, T. Cronert, C. Tölzer, T. Fröhlich, S. Biesenkamp, K. Schmalzl, P. Steffens, C.H. Lee, and M. Braden, *Control of Chiral Magnetism Through Electric Fields in Multiferroic Compounds above the Long-Range Multiferroic Transition*, Phys. Rev. Lett. **119**, 177201 (2017),
- C.P. Grams, S. Kopatz, D. Brüning, S. Biesenkamp, P. Becker, L. Bohatý, Thomas Lorenz and J. Hemberger. *Evidence for polarized nanoregions from the domain dynamics in multiferroic* $LiCuVO_4$, Sci Rep 9, 4391 (2019)
- J. Stein, S. Biesenkamp, T. Cronert, T. Fröhlich, J. Leist, K. Schmalzl, A.C. Komarek, and M. Braden, *Combined Arrhenius-Merz Law Describing Domain Relaxation in Type-II Multiferroics*, Phys. Rev. Lett. **127**, 097601 (2021),
- Y. Wang, H. F. Legg, T. Boemerich, J. Park, S. Biesenkamp, A. A. Taskin, M. Braden, A. Rosch, Y. Ando, *Gigantic Magnetochiral Anisotropy in the Topological Semimetal* $ZrTe_5$, Phys. Rev. Lett. **128**, 176602 (2022),

Sample and data availability

Beside some exceptions that are listed below, all samples are available and were transferred to M. Braden. This does not hold for $BaCo_2V_2O_8$, for which the activated sample is stored at the Institut Laue-Langevin due to radio protection. The samples of $(NH_4)_2[FeCl_5(H_2O)]$ are also not available because they have been destroyed during the experimental course as a consequence of their sensibility against water and humidity. The sample of $Ni_3V_2O_8$ broke as a consequence of a gas discharge.

All data, files and codes that are mandatory for the reported results and evaluations in this thesis are stored on the servers of the II. Institute of Physics, which belongs to the University of Cologne. All files are also backed by the author of this thesis and the raw data that were collected during neutron scattering experiments are further saved at the respective facility. In case that a digital object identifier (doi) was assigned to the data by the neutron scattering facility, the citation is given in the respective chapter.

Selbstständigkeitserklärung

Hiermit versichere ich an Eides statt, dass ich die vorliegende Dissertation selbstständig und ohne die Benutzung anderer als der angegebenen Hilfsmittel und Literatur angefertigt habe. Alle Stellen, die wörtlich oder sinngemäß aus veröffentlichten und nicht veröffentlichten Werken dem Wortlaut oder dem Sinn nach entnommen wurden, sind als solche kenntlich gemacht. Ich versichere an Eides statt, dass diese Dissertation noch keiner anderen Fakultät oder Universität zur Prüfung vorgelegen hat; dass sie - abgesehen von unten angegebenen Teilpublikationen und eingebundenen Artikeln und Manuskripten - noch nicht veröffentlicht worden ist sowie, dass ich eine Veröffentlichung der Dissertation vor Abschluss der Promotion nicht ohne Genehmigung des Promotionsausschusses vornehmen werde. Die Bestimmungen dieser Ordnung sind mir bekannt. Darüber hinaus erkläre ich hiermit, dass ich die Ordnung zur Sicherung guter wissenschaftlicher Praxis und zum Umgang mit wissenschaftlichem Fehlverhalten der Universität zu Köln gelesen und sie bei der Durchführung der Dissertation zugrundeliegenden Arbeiten und der schriftlich verfassten Dissertation beachtet habe und verpflichte mich hiermit, die dort genannten Vorgaben bei allen wissenschaftlichen Tätigkeiten zu beachten und umzusetzen. Ich versichere, dass die eingereichte elektronische Fassung der eingereichten Druckfassung vollständig entspricht.

Teilpublikationen

- S. Biesenkamp, N. Qureshi, Y. Sidis, P. Becker, L. Bohatý, and M. Braden, *Structural dimerization in the commensurate magnetic phases of* $NaFe(WO_4)_2$ *and* $MnWO_4$, Phys. Rev. B **102**, 144429 (2020),
- S. Biesenkamp, D. Gorkov, D. Brüning, A. Bertin, T. Fröhlich, X. Fabrèges, A. Gukasov, M. Meven, P. Becker, L. Bohatý, T. Lorenz, and M. Braden, *Single-crystal investigations on the multiferroic material* $LiFe(WO_4)_2$, Phys. Rev. B **103**, 134412 (2021),
- S. Biesenkamp, D. Gorkov, W. Schmidt, K. Schmalzl, Y. Sidis, P. Becker, L. Bohatý and M. Braden, *Chiral order and multiferroic domain relaxation in* $NaFeGe_2O_6$, Phys. Rev. B **104**, 174405 (2021),

Köln, 9th September 2022

Sebastian Biesenkamp